Effect of ceramic breeder environment on low-cycle fatigue of EUROFER97

Zur Erlangung des akademischen Grades einer
DOKTORIN DER INGENIEURWISSENSCHAFTEN (Dr.-Ing.)

von der KIT-Fakultät für Maschinenbau des
Karlsruher Instituts für Technologie (KIT)
angenommene

DISSERTATION

von

Dipl.-Ing. Elvina Gaisina

Tag der mündlichen Prüfung: 08. Oktober 2024

Hauptreferent: Prof. Dr.-Ing. Jarir Aktaa
Korreferent: Prof. Dr. Anton Möslang

Acknowledgments

I would like to express my deepest gratitude to my supervisor, Prof. Dr.-Ing. Jarir Aktaa, for providing me with this incredible opportunity to conduct my doctoral thesis in his department. I am truly grateful for his exceptional commitment, unwavering support, continuous supervision, and the numerous scientific discussions we have had, which have significantly contributed to the completion of this work.

I would like to extend my heartfelt gratitude to Dr.-Ing. Mario Walter for his exceptional supervision, invaluable guidance in the methodology of mechanical testing, and his continuous support throughout this research. I am truly grateful for his insightful suggestions, which have greatly enhanced the quality of my work, as well as the fruitful discussions we have had that have expanded my understanding of the subject matter.

I would also like to thank Prof. Dr. Anton Möslang for reviewing this thesis and serving as my co-referent during the Ph.D. defence, providing valuable insights and feedback.

I would like to express my heartfelt gratitude to Dr. Julia Leys and Dr. Regina Knitter for their invaluable contributions throughout the conduction of pre-corrosion experiments. Their expertise, insightful discussions, and meticulous analysis have greatly enriched our understanding of the experimental results. I am deeply appreciative of Dr. Michael Dürrschnabel for his comprehensive TEM studies and his guidance in handling and investigating TEM samples. His expertise and attention to detail have significantly enhanced the quality of our research findings. I would also like to extend my thanks to Dr. Ramil Gaisin for his valuable support with SEM and FIB studies, and to Dr. Klaus Seemann for his expertise in X-ray diffraction studies. Their contributions and insights have enriched our understanding of the materials under investigation. Furthermore, I would like to express my gratitude to Dr. Thomas Bergfeldt for his diligent work in conducting carrier gas hot extraction measurements. I would also like to acknowledge the technical support provided by Melina Blem during the performance of mechanical tests. Her assistance ensured the accuracy and reliability of our experimental data. Lastly, I would like to thank Dr. Guangming Zhou for his continuous support and for providing updated information on the latest design of blankets.

This work has been carried out within the framework of the EUROfusion Consortium and has received funding from the Euratom research and training programme 2014–2018 and 2019–2020 under grant agreement No 633053 and Grant Agreement No 101052200 — EUROfusion. Views and opinions expressed are however those of the author(s) only and do not necessarily reflect those of the European Union or the European Commission. Neither the European Union nor the European Commission can be held responsible for them.

Abstract

EUROFER97 is a promising reduced-activation ferritic-martensitic steel for components of nuclear fusion reactors, specifically as a structural material for the breeder blanket. In the advanced helium-cooled pebble bed blanket concept of DEMO, EUROFER97 will be subjected to a harsh environment, including high temperatures, rapid heating and cooling cycles, high neutron fluxes of high energy, and exposure to lithium-ceramics pebbles in a purge gas atmosphere. This environment can have a significant impact on the material's microstructure and mechanical properties, particularly on its fatigue properties, which are of primary interest due to the cyclic operation of the reactor and the resulting alternating thermomechanical loads. As a result, two main questions arise: i) how does the microstructure of EUROFER97 evolve under these conditions, and ii) to what extent are the material's fatigue properties affected.

Currently, it is not possible to accurately replicate the operating conditions of EUROFER97 in a blanket at least due to the lack of powerful sources of high-energy neutrons. However, an experiment was proposed to provide a preliminary answer to the research questions above. In this experiment, EUROFER97 samples were exposed to pre-corrosion in the ceramic breeder environment, namely contact with lithium-ceramics pebbles in a purge gas atmosphere at 550°C for various durations. The microstructure was then analysed on the surface and in the cross-section to evaluate the effect of exposure duration. The key experiments in this study involve conducting low cycle fatigue tests to determine how the pre-corrosion affects the fatigue life of EUROFER97.

For the first time, a comprehensive study of the evolution of the microstructure and fatigue properties of EUROFER97 was carried out after its exposure to the ceramic breeder environment for 8–128 days. Results demonstrate that this exposure leads to the formation of a complex three-layered surface corrosion of EUROFER97, with imprints of lithium-ceramics pebbles as the main feature. The thickness and phase composition of the layers vary up to about 16–32 days of corrosion and then do not change significantly any longer. The primary cause of corrosion is the presence of impurities, specifically oxygen and water vapor, in the purge gas. The main focus of this study was to investigate the effect of pre-corrosion on the low cycle fatigue properties of EUROFER97. Findings show a significant decrease in the number of cycles to failure, up to 60% and 35% for sub-sized and standard samples, respectively. Careful analysis of the structure before, during, and after testing strongly suggests that a rough, corroded surface on EUROFER97 samples, with imprints of lithium-ceramics pebbles, contains imprints and cracks from which fatigue cracks develop. The maximum allowable total strain range of EUROFER97 components for 2 years of operation in blanket were estimated as 0.25%. The study found that the components cannot meet the required number of cycles, even without taking into account the effects of strong neutron irradiation and creep. The ways of mitigation of the problem and possible solutions are discussed.

Kurzfassung

EUROFER97 ist ein vielversprechender ferritisch-martensitischer Stahl mit reduzierter Aktivierung für Kernfusionsreaktoren, insbesondere als Strukturmaterial für den Bau des Brutblankets. Im fortschrittlichen Helium-Cooled Pebble-Bed Design Konzept von DEMO wird EUROFER97 einer rauen Umgebung ausgesetzt sein, einschließlich hoher Temperaturen, schneller Heiz- und Kühlzyklen, hoher Neutronenflüsse hoher Energie und der Einwirkung von Lithium-Keramik-Kügelchen und einem Spülgas Atmosphäre. Diese Umgebung kann erhebliche Auswirkungen auf die Mikrostruktur und die mechanischen Eigenschaften des Materials haben, insbesondere auf seine Ermüdungseigenschaften, die aufgrund des zyklischen Betriebs des Reaktors und der daraus resultierenden wechselnden thermomechanischen Belastungen von vorrangigem Interesse sind. Daraus ergeben sich zwei Hauptfragen: i) Wie entwickelt sich die Mikrostruktur von EUROFER97 unter diesen Bedingungen und ii) inwieweit werden die Ermüdungseigenschaften des Materials dadurch beeinflusst.

Derzeit ist es zumindest aufgrund des Mangels an leistungsstarken Quellen für hochenergetische Neutronen nicht möglich, die Betriebsbedingungen von EUROFER97 in einem Blanket genau nachzubilden. Es wurde jedoch ein Experiment vorgeschlagen, um eine vorläufige Antwort auf die oben genannten Forschungsfragen zu geben. In diesem Experiment wurden EUROFER97-Proben einer Vorkorrosion in der Keramikbrüterumgebung ausgesetzt, nämlich dem Kontakt mit Lithium-Keramik-Kügelchen in einer Spülgasatmosphäre bei 550°C für verschiedene Zeiträume. Anschließend wurde die Mikrostruktur auf der Oberfläche und im Querschnitt analysiert, um den Einfluss der Expositionsdauer zu bewerten. Die Experimente in dieser Studie umfassen die Durchführung von Kurzzeitermüdungstests um festzustellen, wie sich die Vorkorrosion auf die Ermüdungslebensdauer von EUROFER97 auswirkt.

Zum ersten Mal wurde eine umfassende Studie zur Entwicklung der Mikrostruktur und der Ermüdungseigenschaften von EUROFER97 durchgeführt, nachdem der Stahl 8 bis 128 Tage lang der Keramikbrüterumgebung ausgesetzt war. Die Ergebnisse zeigen, dass diese Exposition zu einer komplexen dreischichtigen Oberflächenkorrosion von EUROFER97 führt, mit Abdrücken von Lithium-Keramik-Kügelchen als Hauptmerkmal. Die Dicke und Phasenzusammensetzung der Schichten variiert bis etwa 16–32 Tage und ändert sich anschließend nicht mehr wesentlich. Die Hauptursache der Korrosion ist das Vorhandensein von Verunreinigungen, insbesondere Sauerstoff und Wasserdampf, im Spülgas. Das Hauptaugenmerk dieser Studie lag auf der Untersuchung der Auswirkung der Vorkorrosion auf die Kurzzeitermüdungseigenschaften von EUROFER97. Die Ergebnisse zeigen eine signifikante Verringerung der Anzahl der Zyklen bis zum Versagen, bis zu 60 % bzw. 35 % bei Klein- bzw. Standardproben. Eine sorgfältige Analyse der Struktur vor, während und nach den Tests weist stark darauf hin, dass die raue, korrodierte, mit Abdrücken der Lithium-Keramik-Kügelchen dekorierte Oberfläche der EUROFER97-Proben Risse enthält, aus denen sich Ermüdungsrisse entwickeln. Der maximal zulässige Gesamtdehnungsbereich der EUROFER-Komponenten für einen zweijährigen Betrieb im Blanket wurde auf 0,25 % geschätzt. Eine weiterführende Auswertung ergab, dass die Komponenten die geforderte Zyklenzahl, auch ohne

Berücksichtigung der Auswirkungen starker Neutronenbestrahlung und Kriechen, nicht erreichen können. Es werden daher Möglichkeiten zur Eindämmung sowie Lösungen des Problems diskutiert.

Contents

Terminology, abbreviations, and symbols

Terminology

ceramic breeder environment	environment implying contact with lithium-ceramics pebbles in purge gas atmosphere at a temperature of 550°C to simulate the operating conditions in a blanket of nuclear fusion reactor
imprint	a visible mark or interaction left on the surface of EUROFER97 steel as a result of contact with lithium-ceramics pebbles
lithium-ceramics pebbles	small spherical balls of ceramic tritium breeder made from a homogeneous mixture of lithium orthosilicate Li_4SiO_4 and 30 vol.% lithium metatitanate Li_2TiO_3
pre-corrosion	exposure of material to a corrosive environment before conducting mechanical tests (i.e. fatigue tests) to assess the combined effect of corrosion and loading on the material's mechanical properties
purge gas	a mixture of He + 0.1 vol.% H_2 gases which will be used to facilitate tritium release from the ceramic breeder and transport it from the blanket to the tritium plant of a nuclear fusion reactor

Abbreviations

ASME	American Society of Mechanical Engineers
ASTM	American Society for Testing and Materials
BSE	Back-Scattered Electron
CB	Ceramic Breeder
CGHE	Carrier Gas Hot Extraction
CTE	Coefficient of Thermal Expansion
DEMO	DEMOnstration Fusion Power Plant
DBTT	Ductile-to-Brittle Transition Temperature
EDS	Energy Dispersive X-ray Spectroscopy
EELS	Electron Energy Loss Spectroscopy
FIB	Focused Ion Beam
HAADF	High-Angle Annular Dark-Field
HCPB	Helium-Cooled Pebble Bed
HRTEM	High-Resolution Transmission Electron Microscopy
ICSD	Inorganic Crystal Structure Database
ITER	International Thermonuclear Experimental Reactor
KALOS	Karlsruhe Lithium Orthosilicate

KIT	Karlsruhe Institute of Technology
LCF	Low Cycle Fatigue
PDF	Powder Diffraction File
RAFM	Reduced Activation Ferritic/Martensitic Steels
SAED	Selected Area Electron Diffraction
SEM	Scanning Electron Microscopy
TEM	Transmission Electron Microscopy
USE	Upper Shelf Energy
WCLL	water-cooled lithium lead
WP	Work Package
XRD	X-Ray Diffraction analysis

Symbols

a ..... crack depth

$c(t)$ ..... corrosion thickness or mass per unit area

da/dN ..... fatigue crack growth rate

D ..... initial diameter of specimen

D_a ..... diffusion coefficient

F_n ..... geometric factor

K ..... stress intensity factor

N ..... number of cycles

N_d ..... number of cycles until the formation of a fatigue crack

N_f ..... number of cycles to failure

t ..... exposure duration

α ..... coefficient of thermal expansion

$\Delta\varepsilon_{tot}$ ..... total strain range

$\Delta\varepsilon_{in}/2$ ..... inelasitc strain amplitude

$\Delta\sigma$ ..... stress range

ε ..... strain

ε'_f ..... fatigue ductility coefficient

Θ ..... angle of inclination of the sample in X-ray diffraction

1 Introduction

The DEMOnstration Fusion power plant (DEMO) like most other tokamaks, will operate on the deuterium-tritium fusion reaction due to its high energy yield at the minimum required temperature [1]. While deuterium can be obtained relatively easily from sea water, tritium is a radioactive element with a half-life of 12.32 years and is found in nature only in very small quantities. The majority of tritium available on the world market is produced in heavy water nuclear reactors, such as Canada Deuterium Uranium, in quantities of only several kilograms per year. However, the DEMO reactor requires at least 112 kg of tritium per year for operation with a fusion power of 2 GW. Therefore, the DEMO reactor must produce its own tritium as fuel in the breeder blanket [2–5]. Currently, there are two main types of breeder blankets under designs development for EU DEMO: the Water-Cooled Lithium Lead (WCLL) and the Helium-Cooled Pebble Bed (HCPB).

WCLL is a breeder blanket design that uses liquid Pb-15.8Li as a neutron multiplier and as a tritium breeding material together [4]. The blanket is composed of a series of water-cooled steel tubes submerged in the flowing liquid lead-lithium, which can reach temperatures of up to 550°C (Fig. 1.1). Water serves as a coolant to extract the heat produced by the fusion reactions and carry it away from the blanket. The WCLL breeder blanket concept is considered to be one of the most promising designs for a fusion reactor, as it is highly efficient and compatible with existing water-cooled nuclear power plant technology. However, the design also presents some challenges, such as severe steel corrosion issues, tritium retention, and magneto-hydrodynamics issues. Studies have shown that EUROFER97 steel, which is used for tubes with high-pressure water inside, experiences severe corrosion when in contact with Pb-Li liquid. This could lead to serious accidents in the blanket and the entire reactor. Currently, various concepts are being developed to protect steel from corrosion by liquid lead and from tritium permeation [6].

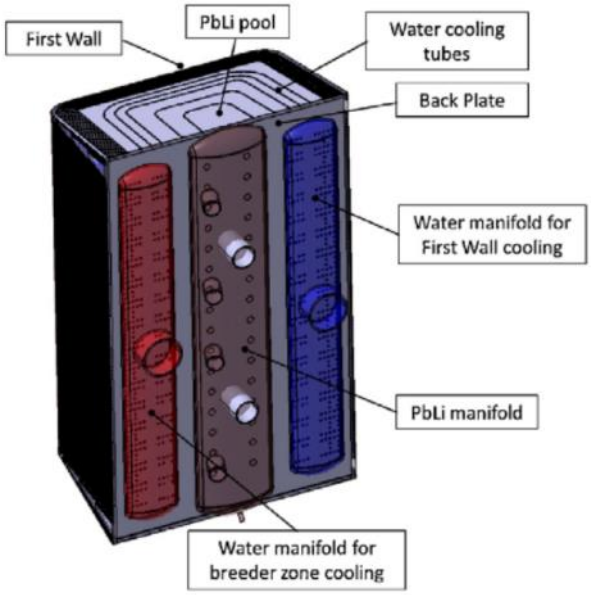

Fig. 1.1. The water-cooled lithium-lead blanket module with Pb-Li/water manifolds [4]

The second blanket concept, HCPB, is considered to be a more rational and safer option as it uses only solid materials, which eliminates the risk of rapid liquid metal corrosion. In this design, a bed of lithium-ceramics pebbles acts as the breeder material, while beryllide blocks act as the neutron multiplier material (Fig. 1.2) [5]. Helium gas is used as coolant due to its high heat capacity and good heat transfer properties. The pebbles are filled in the pins inside the blanket and undergo a transmutation process upon reaction with the neutrons produced by the fusion reaction. The transmutation process produces tritium which is extracted from the pebbles and used as fuel for the fusion reaction. Since helium gas cannot be activated during neutron irradiation, it is an ideal coolant to effectively remove the heat generated by the fusion reaction. The Li-ceramics are designed as small pebbles to facilitate the release of tritium, which will be purged using a mixture of helium and 0.1 vol. % hydrogen gas. In Figs. 1.2c and 1.2d, the lithium-ceramics pebbles are denoted as KALOS CB, meaning a ceramic breeder made by the KALOS method (Karlsruhe Lithium OrthoSilicate) [5,7].

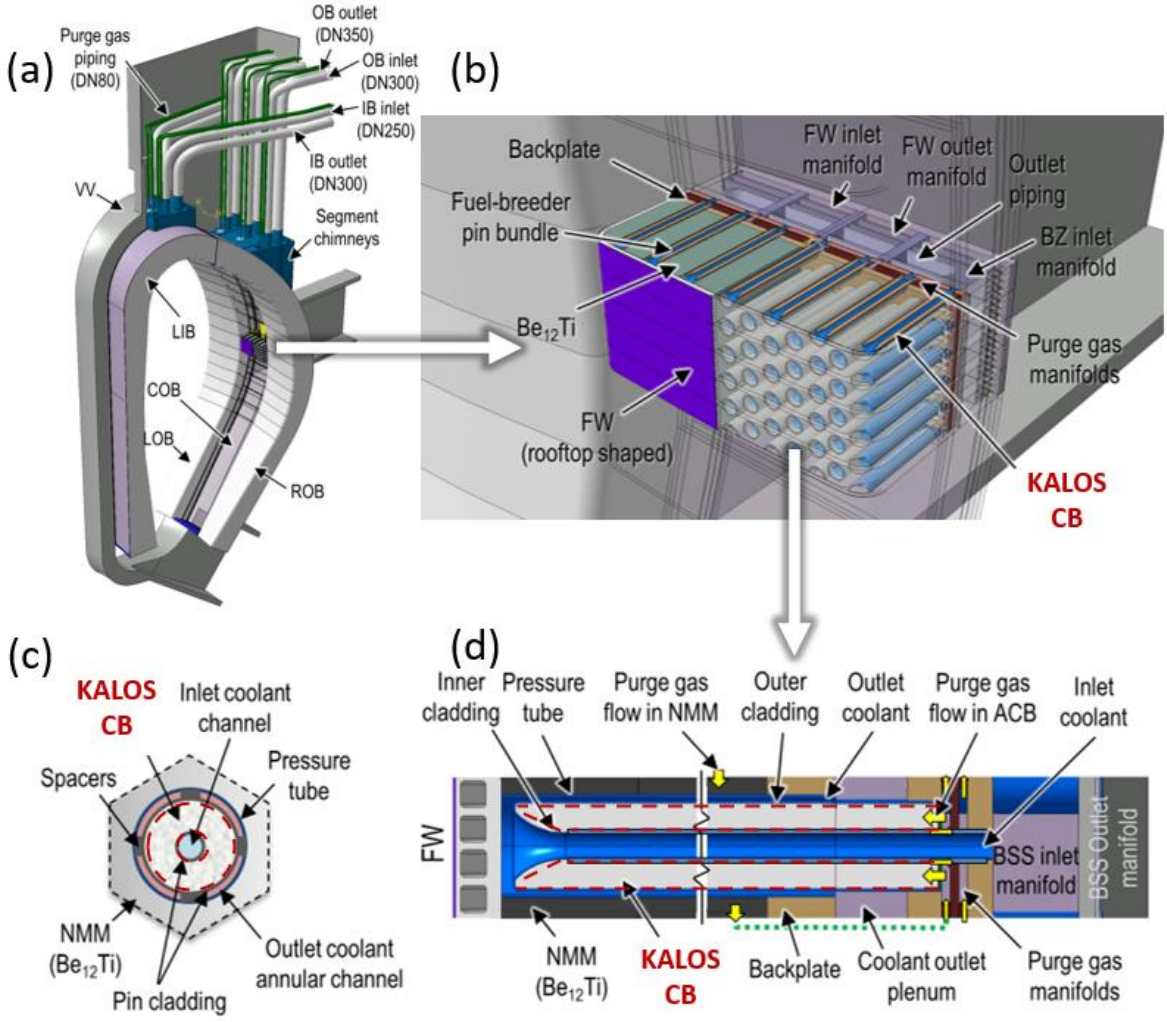

Fig. 1.2. (a) The sector of a DEMO reactor with a (b) the Helium-Cooled Pebble Bed design blanket module. The module is illustrated in a cross section (c) and a longitudinal section (d) of one of the fuel pins, containing Li-ceramics pebbles (denoted as KALOS CB) and EUROFER97 steel components [5]. The red dashed lines indicate the regions where the EUROFER97 steel components come into contact with the Li-ceramics pebbles.

In the HCPB design, the lithium-ceramics pebbles are situated within the EUROFER97 pins, occupying the space between the tubes with outer diameters of 28 mm and 64 mm. During reactor operation, the pebbles become heated and require cooling by a flow of helium through the pins (Fig. 1.3). At the end of the DEMO heating cycle, the temperature of the pebbles reaches 940°C (Fig. 1.3a), whereas the EUROFER97 temperature should not exceed 550°C. The contact points between the lithium-ceramics pebbles and the inner surface of the EUROFER97 pin are denoted by a dashed red line in the Figs. 1.2c and 1.2d. These contact points warrant special attention due to the complex working conditions of the EUROFER97 components. Besides the possible chemical impact of the pebbles on EUROFER97, these components experience alternating tension-compression due to the cyclic operation of the DEMO reactor. Additionally, the EUROFER97 components are subjected to helium flows from the outside and purged by He+0.1H_2 flow from the inside, which can contain impurities and lead to corrosion. All of these factors must be taken into consideration under conditions of high temperatures up to 550°C and a strong flux of high-energy neutrons (up to 14 MeV).

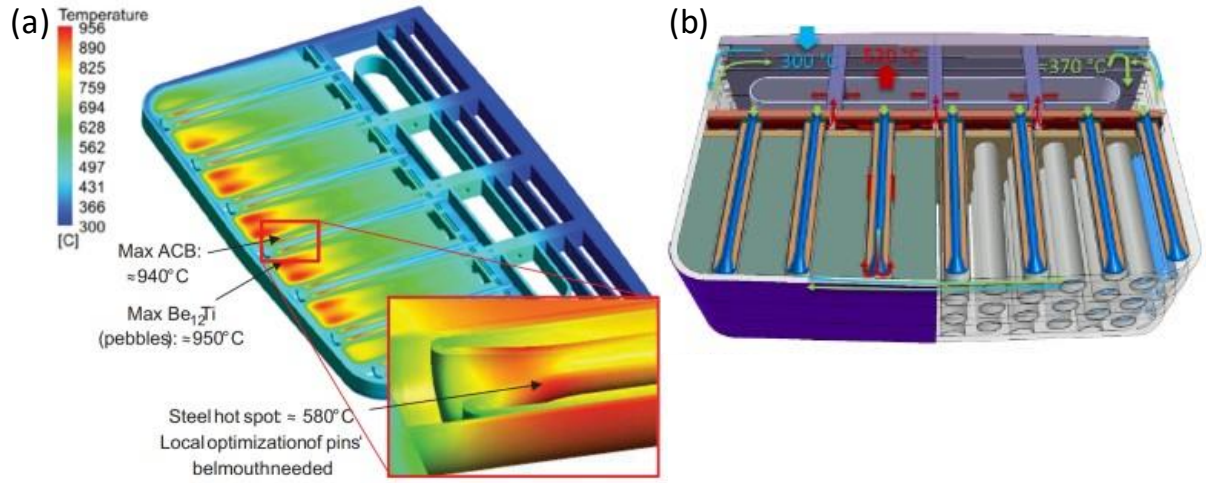

Fig. 1.3. Cross-section of an HCPB blanket module showing (a) the temperature distribution and (b) the structure of EUROFER97 pins filled with lithium-ceramics pebbles [5]

The interaction between lithium-ceramics pebbles and EUROFER97 components under tension-compression loads, possible corrosion from gases, high temperatures, and neutron irradiation is a significant and poorly understood issue. In the event of pin failure, radioactive tritium from purge gas can enter the helium cooling system, causing safety issues. In this work, an experiment is carried out partially simulating severe conditions described above. The primary objective is to investigate the effect of this simulated conditions on the low cycle fatigue properties of EUROFER97, taking into account the alternating thermomechanical loads to which the components will be subjected. Additionally, the study aims in providing a detailed understanding of the evolution of the microstructure of EUROFER97 during such an experiment. This information can be utilized to design more robust and reliable solutions to prevent possible corrosion and deterioration of mechanical properties in future nuclear fusion reactors.

2 State of research

2.1 Compatibility of EUROFER97 with lithium-ceramics pebbles

The compatibility of pebbles of lithium-containing ceramics and structural steel began to be studied with the emergence of blanket concepts where these materials could be placed in contact. The following section will provide a chronological overview of the research conducted on the problem of this compatibility. It will also discuss the current state of the problem and the existing challenges that need to be addressed in future research.

Already in the 1980s, it was found that Li-ceramics compositions such as Li_4SiO_4, Li_2TiO_3, and Li_2ZrO_3 had a lower free enthalpy of formation compared to other lithium-based ceramics like oxides or lithium aluminates. As a result, the direct interaction of these materials with steel is thermodynamically unfavorable. However, the presence of absorbed water in ceramics can still lead to some corrosion of ferrite-martensitic and austenitic steels [8]. Therefore, extensive research has been carried out to improve the compatibility between these ceramics and steel. Several approaches have been proposed, such as the addition of a protective coating layer or using alternative structural materials. Further studies of lithium-containing ceramics were focused on the abovementioned compositions.

The literature has shown that the diffusion of elements between the lithium-ceramics breeder and EUROFER97 can significantly affect the performance of the blanket. In the early 2000s in [9], the authors conducted a comparative analysis of lithium orthosilicate and metatitanate pebbles after long-term exposure (50–2000 h at 600°C) in contact with EUROFER97 in a purge gas atmosphere. The study revealed that iron and alloying elements from EUROFER97 can diffuse into Li_4SiO_4 pebbles, but do not diffuse into Li_2TiO_3. Conversely, lithium and other elements from lithium-ceramics pebbles can diffuse into EUROFER97, indicating a complex interaction between the breeder material and structural material. In a separate study [10], it was discovered that Li_4SiO_4 can undergo significant interaction with almost all materials examined, including EUROFER97, AISI 321, Inconel 718, and 15-15 Ti steel (with the exception of platinum), in a purge gas atmosphere at temperatures ranging from 200 to 1000°C. Conversely, Li_2TiO_3 exhibited limited interaction with EUROFER97 at 500°C. These findings emphasized the need for further research to better understand the effects on the corrosion of the structural material of the blanket in the DEMO reactor.

In contrast, Abou-Sena et al [11] did not observe significant interaction between Li_4SiO_4 pebbles and EUROFER97 during a standard heat treatment of EUROFER97 (austenitization at 980°C and tempering at 750°C). It is worth noting, however, that the experiment was conducted under vacuum conditions, intended to simulate the heat treatment of EUROFER97 after welding during blanket assembly. The surface of EUROFER97 underwent slight oxidation, resulting in a change in color. Hernandez et al [12] similarly exposed EUROFER97 to Li_4SiO_4 pebbles under vacuum and observed a corrosion layer less than 1 µm thick after exposure for 120 days at 550°C. X-ray diffraction analysis detected the presence of lithium-containing spinel ($(Li_2O)(Fe_2O_3)_4(Cr_2O_3)$) at the contact site. In continuation of this work, the authors

determined that this corrosion layer has an outer layer with an acicular morphology and a brittle amorphous inner layer [13]. The main cause of steel oxidation is considered to be oxygen or OH^- group from pebbles. Thus, it has been shown that if the contact of lithium-ceramics pebbles occurs in a vacuum, then the corrosion of the steel is negligible.

Further thorough studies [14] have been conducted on the interaction of lithium-ceramics pellets with EUROFER97 in a purge gas atmosphere at 550°C, revealing that a corrosion layer forms in the first few hours of corrosion. Already after the first week, the thickness of the corrosion layer reaches 18 µm. Interestingly, the thickness of the corrosion layer remains relatively constant after 28 and 56 days of corrosion, at approximately 25 µm. When recalculated to the specific area, the authors plotted an increasing corrosion kinetic curve (Fig. 2.1). However, the plotted points suggest a possible slowdown or cessation of further corrosion with increased exposure duration. Surface XRD analysis revealed the presence of iron oxides Fe_2O_3 and Fe_3O_4, as well as spinel $(Fe_{0.6}Cr_{0.4})_2O_3$.

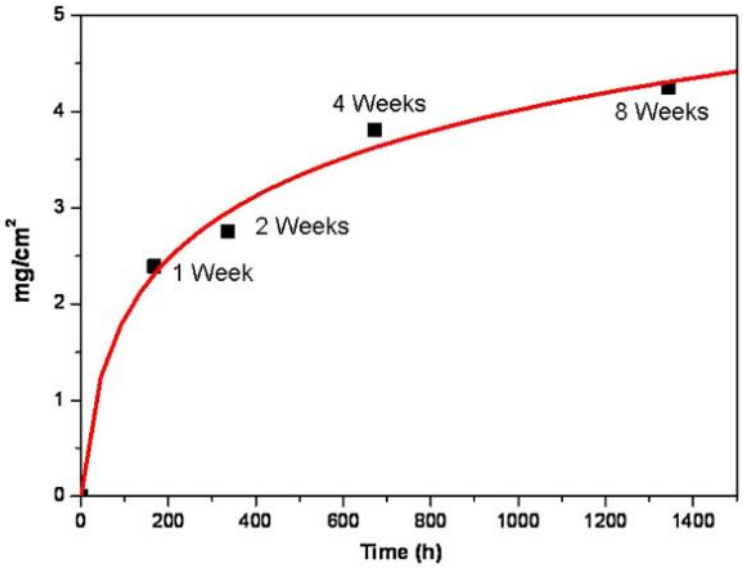

Fig. 2.1. Corrosion kinetics of EUROFER97 in contact with Li_4SiO_4 pebbles in a purge gas atmosphere [14]

An analogous corrosion phenomenon was also observed during the exposure of Indian RAFM steel to Li_2TiO_3 pellets in an argon atmosphere, lasting up to 38 days at 550°C [15]. The thickness of the corrosion layer increased from about 8 µm after 4 days to about 40 µm after 38 days (Fig. 2.2a), indicating an increase in corrosion with time. It should be noted that the corrosion atmosphere was only argon without hydrogen content. In this case, a two-layered corrosion film was formed on the steel surface, with magnetite as the outer layer and an inner, chromium-enriched corrosion layer (Fig. 2.2b).

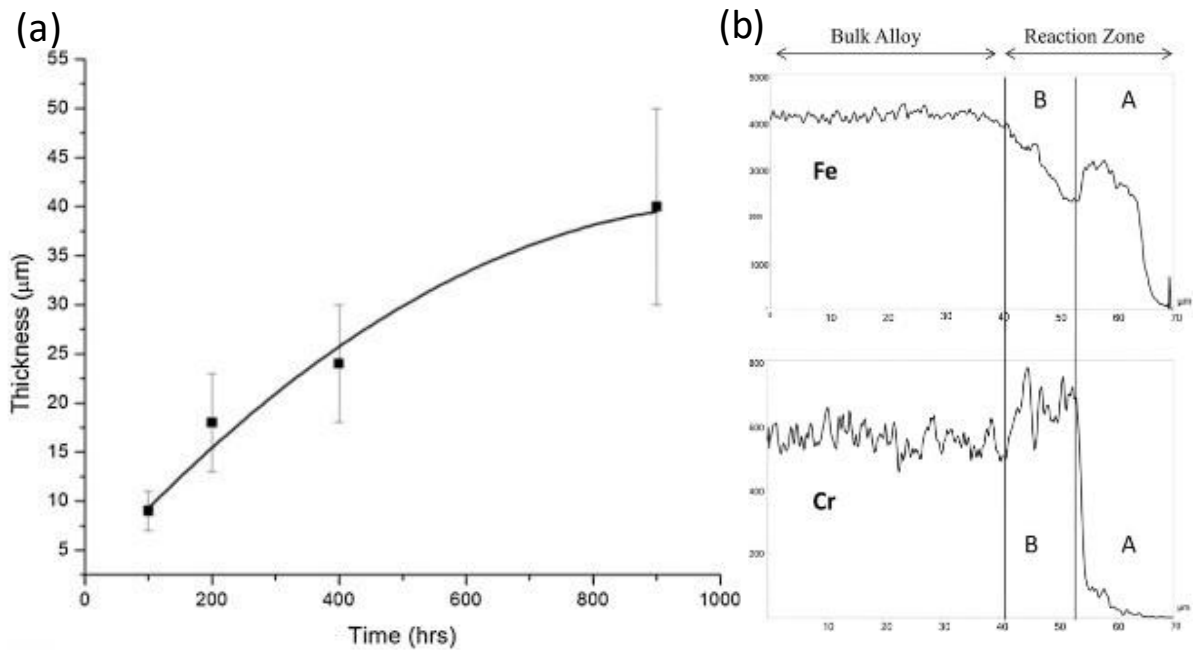

Fig. 2.2. (a) Corrosion kinetics of Indian RAFM steel in contact with Li_2TiO_3 pellets in an argon atmosphere and (b) corresponding EPMA profiles for Fe and Cr after corrosion for 8 days [15]

Mukai et al conducted a series of studies on the interaction tests between lithium-ceramics pellets and EUROFER97 in a purge gas atmosphere at temperatures of 350, 550, and 800°C. After 21 days of exposure, a corrosion layer with a thickness of 7.4 μm was observed on the EUROFER97 surface. The outer corrosion layer consisted of iron oxide and various lithium-containing oxides, while the inner corrosion layer was enriched with chromium Fig. 2.3 [16].

When an atmosphere containing water was used, the formation of a double oxide layer on EUROFER97 was increased, especially at elevated temperatures of 550 and 800°C. The results showed parabolic growth rates, yielding an effective diffusion coefficient of oxygen of $D_a = 4.5 \times 10^{-14}$ cm^2/s at 350°C. Additionally, the authors estimated thickness of the corrosion layer on EUROFER97 structural steel after two years of use as 17 μm [17].

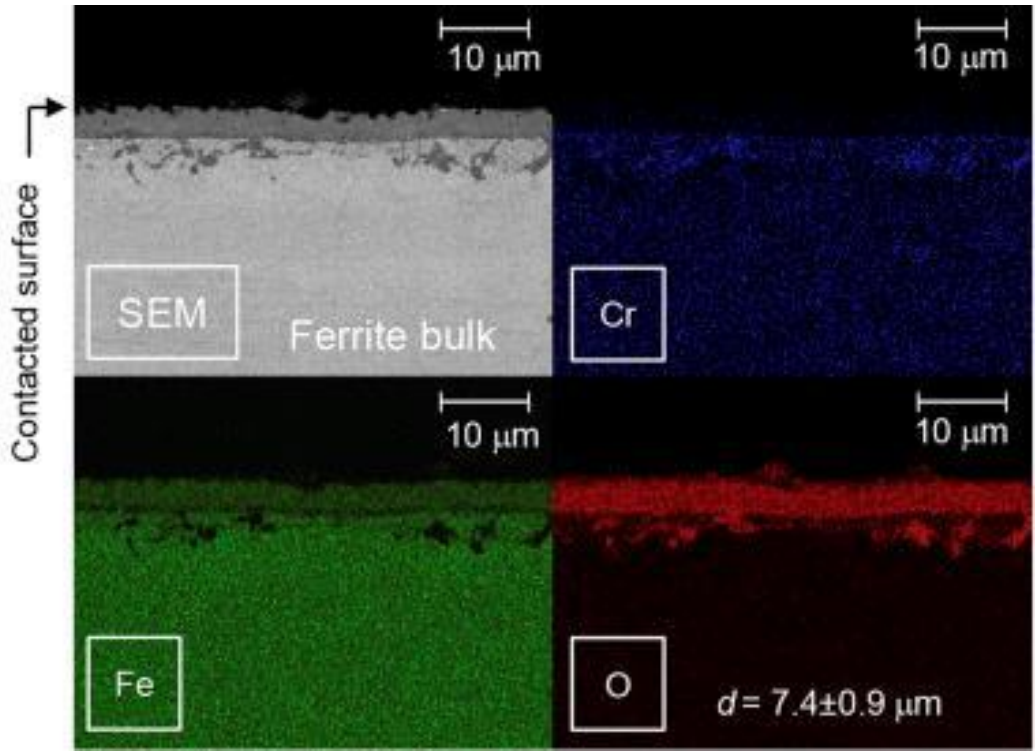

Fig. 2.3. Microstructure and corresponding elemental EDS maps of a surface of EUROFER97 sample exposed to Li-ceramics pellets in a purge gas atmosphere at 550°C for 21 days [16]

Mukai et al conducted another study [18] on the effect of exposure of EUROFER97 to Li_2TiO_3 pellets in a purge gas atmosphere, resulting in the formation of a double corrosion layer. The outer surface revealed grains of pure ferrite formed due to reduction of iron oxide with hydrogen, as depicted in Fig. 2.4. At 350°C EUROFER97 limitedly corroded with a thickness of less than 1 μm, even after 56 days. However, the growth rates at 550°C and 800°C followed a parabolic law until 14 and 21 days, respectively.

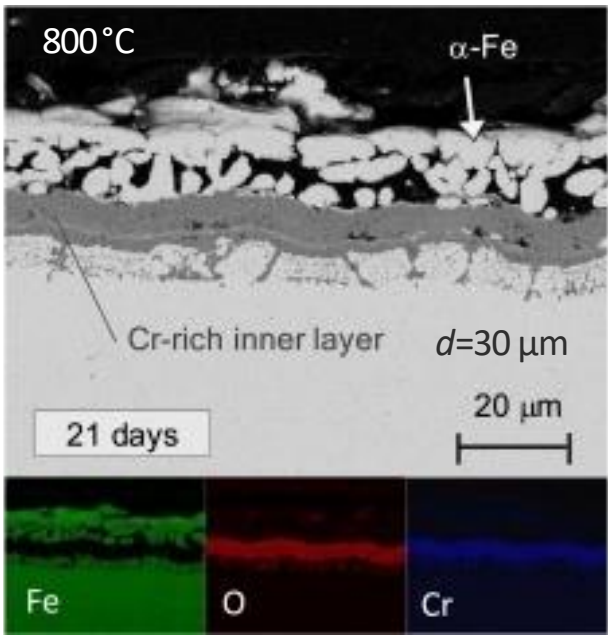

Fig. 2.4. Microstructure and corresponding elemental EDS maps of a surface of EUROFER97 sample exposed to Li_2TiO_3 pellets in a purge gas atmosphere at 800°C for 21 days [18]

In a study on the interaction of Korean ARAA steel with Li_2TiO_3 pellets at 550°C for up to 42 days, the authors investigated the effect of different gas environments, including pure helium and purge gas [19]. The thickness of the corrosion layer was greater in the case of a helium atmosphere, reaching about 50 µm after exposure for about 42 days, compared to about 12 µm in the case of purge gas atmosphere (Fig. 2.5). The presence of hydrogen in the purge gas had a noticeable impact on the oxide layer thickness, as it reduced the concentration of oxygen in the oxide layer and decreased the diffusion of oxygen at the interface of the bulk. This can be attributed to the reaction of hydrogen with oxygen, leading to a decrease in the concentration of oxygen in the oxide layer.

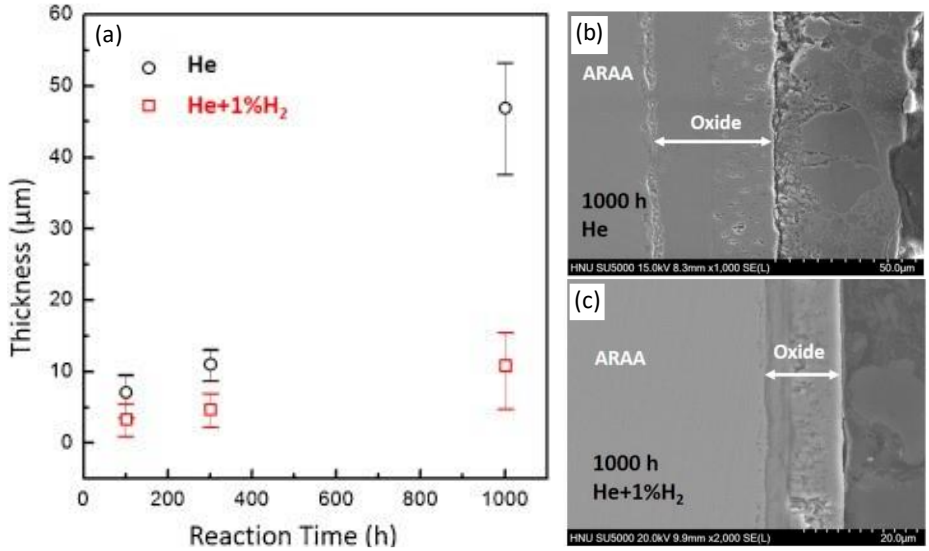

Fig. 2.5. (a) Thickness of the corrosion layer on the EUROFER97 surface after exposure to Li-ceramics in helium or purge gas atmosphere, (b-c) corresponding cross-sectional microstructures after such exposure for about 42 days [19]

To date, numerous studies have attempted to address the issue of compatibility between EUROFER97 and other RAFM steels with lithium ceramics. In nearly all cases, the interaction results in corrosion of the steel surface. The rate of corrosion is dependent on the interaction atmosphere, and interestingly, the use of an inert atmosphere can lead to more corrosion than a vacuum or purge gas atmosphere with a small fraction of hydrogen. However, despite the extensive research in this area, a comprehensive study of the phenomenon of corrosion is lacking, and the mechanisms and causes of such corrosion remain unexplained, which is critical for mitigating potential negative impacts. Furthermore, the effect of this corrosion on the mechanical properties, specifically the fatigue properties of the steel, remains largely unexplored, which is crucial from the perspective of possible application in a blanket.

2.2 Effect of corrosion on mechanical behavior

Corrosion is defined as the chemical or electrochemical reaction between a material, usually a metal, and its environment that produces a deterioration of the material and its properties [20]. Corrosion can lead to a range of structural damage. While severe thinning, general corrosion, and exfoliation reduce the cross-sectional area and can lead to reduced static load capacity; in less severe cases, corrosion may not affect

the load capacity but can still have a detrimental effect on its fatigue properties. This can happen in different ways, including when a material fractures prematurely due to simultaneous corrosion and cyclic loading (corrosion fatigue), when physical or chemical corrosion damage accelerates the formation of fatigue cracks (corrosion-nucleated fatigue), or when fatigue cracks encounter a previously corroded area (prior-corrosion fatigue or pre-corrosion fatigue) [21].

Under blanket operating conditions, both WCLL and HCPB, corrosion will occur simultaneously with alternating loads, i.e. corrosion fatigue. However, in order to simplify the testing process, researchers often separate corrosion and fatigue testing in favor of pre-corrosion fatigue experiments. It should be noted that such conditions are not equivalent, but due to its simplicity, pre-corrosion fatigue can act as a preliminary experiment before true corrosion fatigue.

Fig. 2.6 provides an example of the effect of corrosion fatigue on an aluminum alloy, where a decrease in the number of cycles to failure was observed depending on the test atmosphere. The diagram demonstrates that even seemingly insignificant factors, such as humidity, can significantly reduce fatigue life, even in cases where corrosion is not visibly present [22].

Fig. 2.7 demonstrates how prior-corrosion can affect the fatigue life of 316L austenitic stainless steel. Specimens for fatigue testing were exposed to hydrofluoric acid of varying concentrations for the same duration, resulting in differing corrosion rates as shown in Fig. 2.7. Even in cases where corrosion occurred in 10% acid concentration, fatigue life was reduced by more than 2 times compared to the as-received material [23].

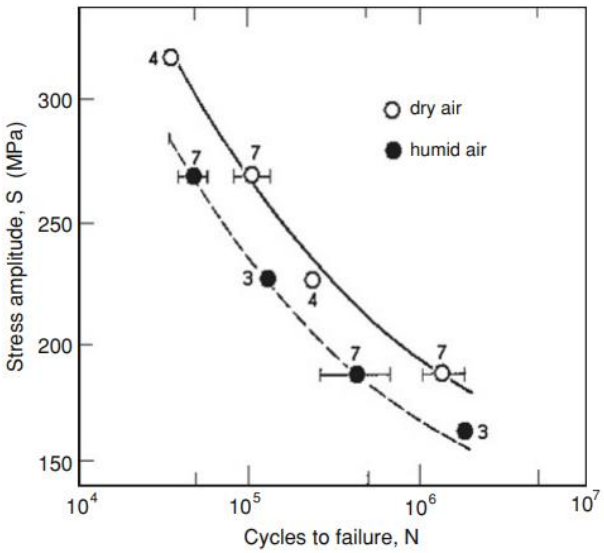

Fig. 2.6. S–N diagrams for 6060-T6 aluminum alloy showing the effect of corrosive atmosphere on fatigue life [22]

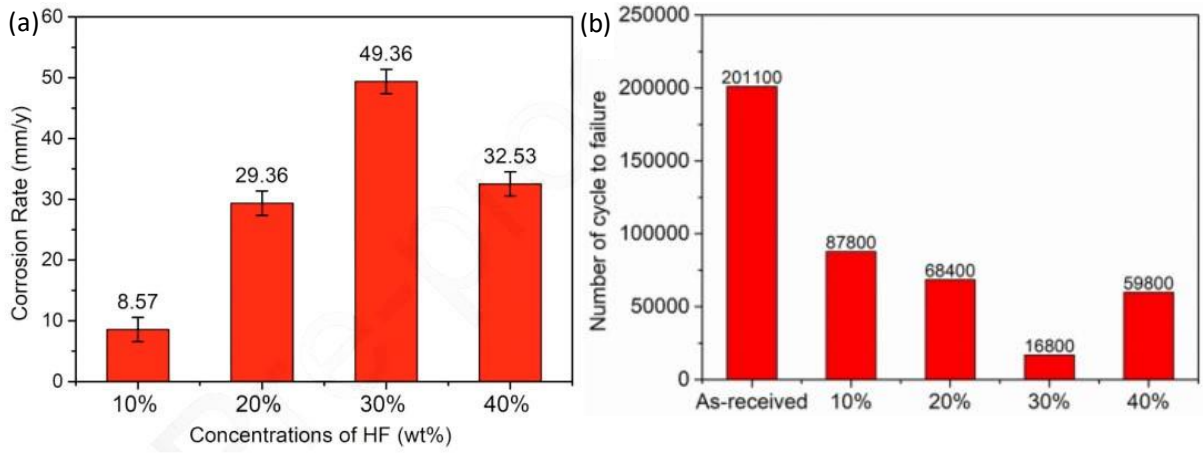

Fig. 2.7. (a) Corrosion rate of 316L austenitic stainless steel in hydrofluoric acid of different concentrations and (b) effect of this corrosion on fatigue life [23]

Reference [24] reports similar findings on high-strength 42CrMo steel specimens subjected to a saline environment for varying durations of 1, 2, and 4 days prior to fatigue testing. The salt exposure resulted in pitting corrosion with a maximum depth of 255 µm after 4 days. The fatigue tests revealed a significant reduction in fatigue life depending on the applied load (Table 2.1), indicating the detrimental effect of corrosion on the material's fatigue properties. This study highlights the importance of considering the effects of prior corrosion on fatigue behavior, particularly in applications where structures may be exposed to corrosive environments for extended periods.

Table 2.1. The fatigue testing results of 42CrMo steel specimens with different exposure times in the saline environment [24]

Pre-Corroded Time (h)	Depth of the maximum corrosion pit	Fatigue Life ($\times 10^5$ Cycles)		
		100 MPa	200 MPa	300 MPa
0	0	11.26	9.95	7.29
24	62	9.81	7.91	5.47
48	147	7.52	6.21	4.09
96	255	5.03	3.91	2.61

The effect of pre-corrosion on the fatigue behavior of high-strength steel 38CrMoAl was investigated in [25]. The specimens were corroded in a neutral salt spray environment before the fatigue tests. Under high fatigue loads, the fatigue lives of pre-corroded specimens were similar to those of specimens without corrosion, as the effects of the loads overrode those of corrosion. However, as fatigue loads decreased, the discrepancy in fatigue lives became more pronounced. For pre-corroded specimens under small loads, corrosion became the main factor leading to specimen fracture. Cracks in pre-corroded specimens initiated from corrosion pits on the specimen surface, resulting in earlier rupture compared to specimens without corrosion.

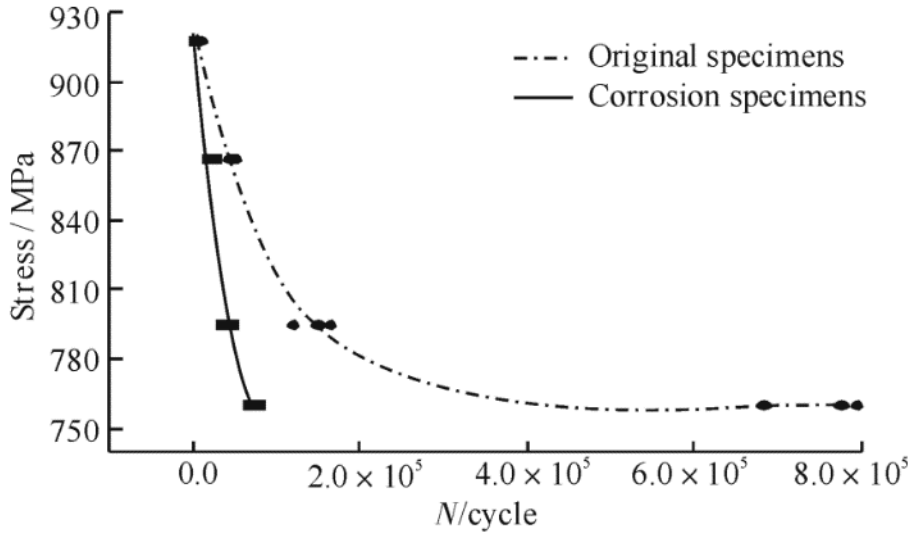

Fig. 2.8. Effect of corrosion on fatigue life of high-strength steel 38CrMoAl [25]

Thus, even minor corrosion can significantly reduce fatigue life, as it degrades the surface quality of the material, creating stress concentrators such as pits or cracks. In non-corroded specimens without surface defects, up to 90% of the number of cycles to failure may be spent in crack initiation, with only 10% in crack propagation. However, when corrosion and stress concentrators are present, crack nucleation may occur within 10% of the life, with the remaining 90% spent in crack propagation [24,26,27]. This results in a decrease in the total number of cycles to failure for corroded specimens. Pitting corrosion is particularly damaging, as it increases the crack-growth rate and further degrades the material's performance [22,24,28].

A number of studies have investigated the impact of corrosion on the mechanical properties of various metallic materials. However, there is a lack of research on the effect of such attacks on reduced activation ferritic martensitic (RAFM) steels like EUROFER97. Most studies have focused on the corrosion of steels in a Pb-17Li liquid mixture, which is relevant for blanket concepts similar to WCLL. For instance, in [29] the authors conducted a study on the effect of corrosion duration in such a liquid metals on the ultimate tensile strength, yield strength, and reduction of area. The results revealed that after 125 days of corrosion, the strength properties decreased by approximately 10% (Fig. 2.9). In another study [30], the effect of applied stress on the ductility of RAFM steel during long-term exposure in flowing Pb-17Li at temperatures ranging from 300 to 400°C was investigated using tensile tests. The results showed that the ductility of RAFM steels at a stress of 250 MPa decreased considerably after exposure to flowing Pb-17Li at 400°C for 1500 h, while only slight ductility loss occurred for the samples tested at 300°C, 350°C, and 400°C for 500 h.

The aforementioned studies investigated the impact of corrosion on static mechanical properties of EUROFER97 or other RAFM steels. However, these tests may not show a substantial deterioration in strength if there is no significant reduction in cross-sectional area owing to general corrosion. No research has been found on the effect of corrosion in liquid Pb-Li on the fatigue properties of steel. This knowledge gap is noteworthy as corrosion in this environment could lead to a significant decrease in the number of cycles to failure. Therefore, there is a clear need to investigate the fatigue behavior of steel under conditions

that accurately represent the service environment of fusion reactors, which includes exposure to liquid Pb-Li.

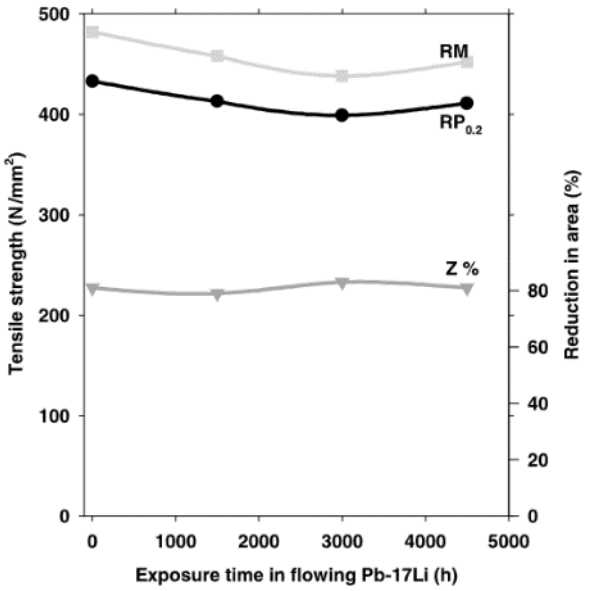

Fig. 2.9. Effect of exposure time in flowing Pb-17Li on tensile properties of EUROFER97 [29]

In [31], the effect of the test environment on the low-cycle fatigue (LCF) behavior of reduced activation martensitic steels F82H and EUROFER97 was investigated at 240°C. Two environments were used: air and water with a small amount of LiOH. The results showed that both alloys exhibited premature fracture in water compared to air (Fig. 2.10). The authors attributed the observed reduction in fatigue lifetime to an environment-induced decohesion mechanism, which was caused by the cathodic hydrogen supplied to the steel through water reduction.

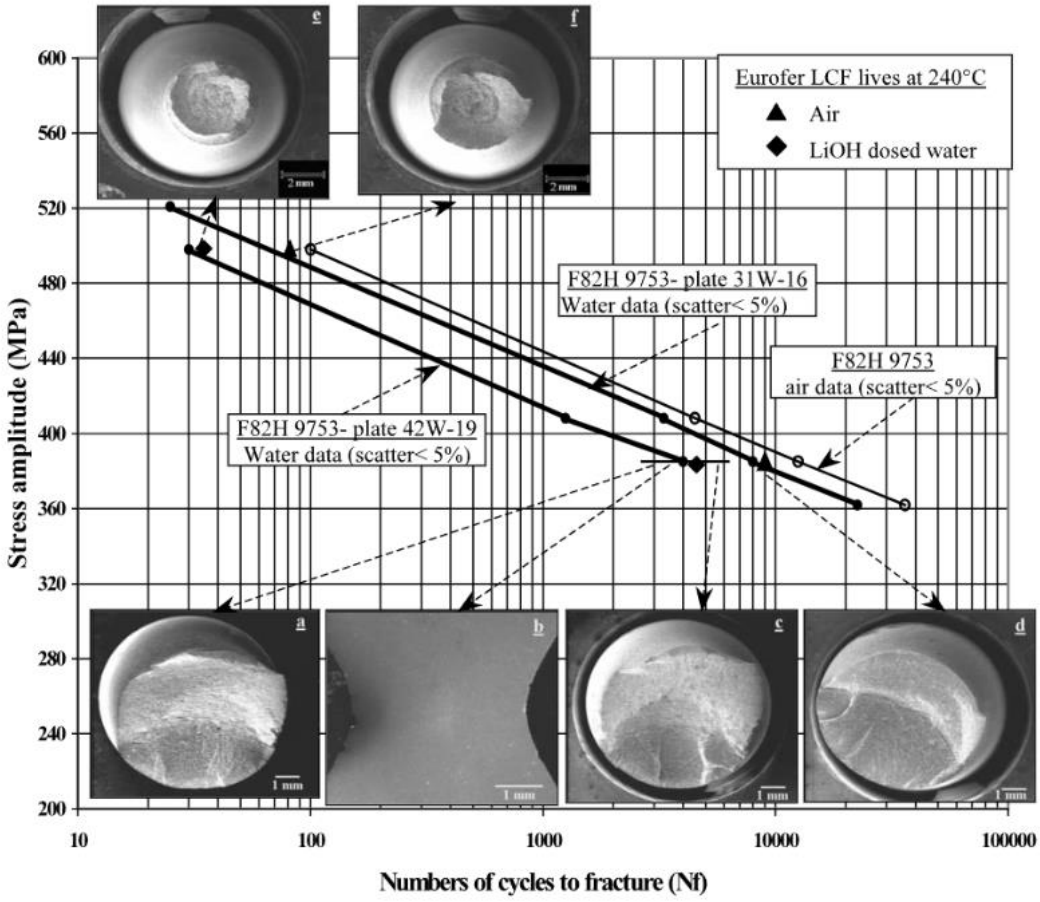

Fig. 2.10. Effect of testing environment at 240°C on number of cycles to failure of EUROFER97 and F82H steels with the corresponding fracture surfaces [31]

To date, only one study has investigated the effect of corrosion of EUROFER97 steel in contact with lithium-ceramics pebbles on mechanical properties, which is the work of Abou-Sena et al. [11] mentioned earlier. In this study, the authors examined the impact of various heat treatments of EUROFER97 in contact with lithium-ceramics pebbles on its tensile properties, with the heat treatment taking place in a vacuum. The heat treatment did not result in significant corrosion, and the tensile properties were found to be only slightly lower than that of the standard EUROFER97 (Fig. 2.11). The study found that the presence of lithium-ceramics pebbles did not affect the strength of EUROFER97, as the heat treatment with and without pebbles resulted in similar strength values.

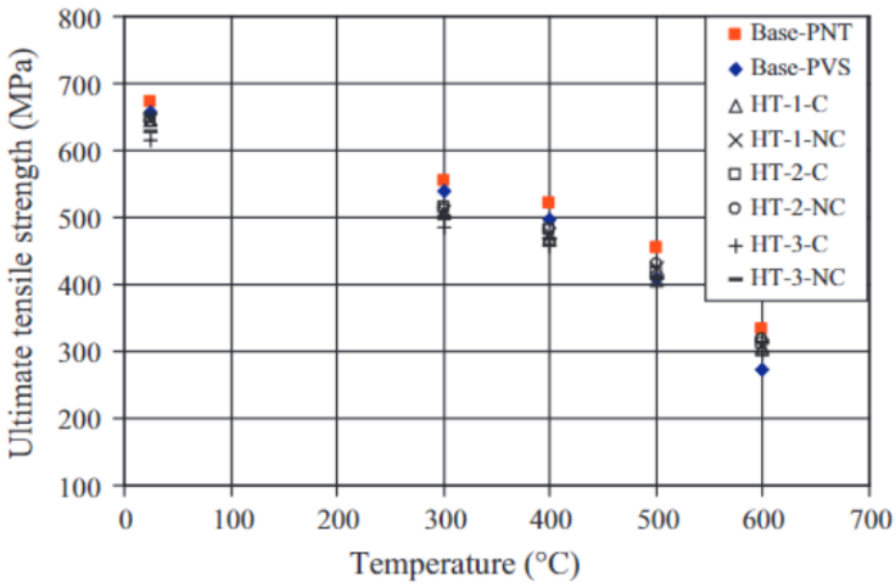

Fig. 2.11. Effect of different heat treatments (HT1-3) in contact with Li-ceramics pebbles (marked with "C" for contact and "NC" for no contact) on the ultimate tensile strength of EUROFER97 [11]

After reviewing the available literature, it appears that only one paper above has examined the effect of exposure to lithium-ceramics pebbles on the mechanical properties of steel. This experiment was conducted in a vacuum, which did not result in any noticeable corrosion and had little impact on the static mechanical properties of the steel. However, the fatigue properties of the steel would be much more critical in this case. As mentioned earlier, minor corrosion may not have a significant impact on static mechanical properties such as those obtained from tensile testing. However, fatigue properties, especially fatigue life, can be dramatically reduced. Furthermore, the components inside a fusion reactor are subjected to periodic tension and compression due to the reactor's operating cycles, making the fatigue properties the most important aspect. Therefore, it is crucial to conduct comprehensive fatigue testing of EUROFER97 specimens in contact with lithium-ceramics pebbles to address this serious problem.

3 Approach, materials, and methods

As follows from the literature review, EUROFER97 components in the HCPB breeder blanket design of DEMO will be subjected to a complex combination of stresses, temperatures, and exposures that can affect their mechanical properties. Specifically, tensile-compressive stresses from reactor cycled operation, high temperatures up to 550°C, mechanical and chemical exposure to lithium-ceramics pebbles, helium cooling or purge gas exposure, and neutron irradiation with high-energy neutrons of about 14 MeV can all influence the material's ability to perform as requested. Given that cyclic tension-compression will be experienced by the blanket components, it is the fatigue properties of EUROFER97 that are particularly critical, determining the ability of the material to work in such conditions. On the other hand, exposure of lithium-ceramics pebbles at high temperatures and purge gas atmospheres could lead to corrosion, which has been shown in the literature to significantly reduce fatigue life (while the effect on static mechanical properties may be insignificant). Since it is currently not feasible to reproduce all operating conditions of EUROFER97 components in a single experiment (especially irradiation with high-energy neutrons), it was decided to simulate such conditions by using a long pre-corrosion test and subsequent fatigue testing, as is customary in the literature. As a pre-corrosion test, a long-term exposure of EUROFER97 to lithium-ceramics pebbles in a purge gas at 550°C was chosen. Here and below, for simplicity, such conditions will be denoted by the term ceramic breeder environment. Low cycle fatigue was chosen as the most relevant fatigue test, taking into account the loads and deformations that occur in the blanket over a relatively small number of cycles (<10000 cycles).

The main objective of this study is to investigate the effect of exposure to the ceramic breeder environment on the low-cycle fatigue of EUROFER97. The objectives of the work should be achieved within the following work packages (WP) as shown in Fig. 3.1.

WP 1. Exposure of EUROFER97 samples to the ceramic breeder environment

The purpose of the exposure is to conduct a pre-corrosion treatment that simulates corrosion during corrosion fatigue in the breeder blanket. To ensure that diffusion-controlled processes are properly captured, the duration of the exposures should be doubled each time. The exposure duration should be long enough (days and months) to be representative for the blanket's lifetime (2 years). To obtain a clear and observable effect, the temperature of the EUROFER97 samples should be set to 550°C as highest operating temperature.

WP 2. Effect of the ceramic breeder environment on the microstructure of EUROFER97

The objective of this WP is to investigate the potential impact of exposure to the ceramic breeder environment on the microstructure of EUROFER97 samples obtained in WP 1. The microstructure of materials can significantly affect their mechanical properties, and exposure to the ceramic breeder environment could potentially alter the microstructure of EUROFER97 and hence its mechanical properties. This study aims to examine the surface and cross-section microstructure of EUROFER97 samples using scanning electron

microscopy and X-ray diffraction analysis to determine their phase composition. Since the conventional SEM methods cannot be used to determine the lithium content, transmission electron microscopy will be used to examine the lamellas extracted from the regions of interest using a focused ion beam.

WP 3. Effect of the ceramic breeder environment on the low-cycle fatigue of EUROFER97

This WP is the main focus of the work. It is planned to investigate the effect of exposure to the ceramic breeder environment on the low-cycle fatigue behavior of EUROFER97. The study will involve a series of experiments, including low cycle fatigue tests on a large number of sub-sized samples (around 100) to determine the extent to which the fatigue properties of EUROFER97 are affected. The findings will be verified by conducting tests on standard samples. The tests will be conducted at EUROFER97's maximum operating temperature of 550°C and at various total strain ranges to determine the maximum effects. The test results of the original samples and those exposed to the ceramic breeder environment will be compared to assess the impact of the environment on the fatigue properties of EUROFER97.

WP 4. Investigation of the factors causing corrosion on EUROFER97

This work package focuses on investigating the causes of corrosion on the surface of EUROFER97 after exposure to the ceramic breeder environment in WP 3. The exposure conditions will be divided into two parts: exposure to lithium-ceramics pebbles in a vacuum and exposure to a purge gas atmosphere without lithium-ceramics pebbles. Microstructural studies and low cycle fatigue tests will be subsequently conducted to evaluate the extent of corrosion and its impact on the fatigue properties of EUROFER97. The findings of this work package will provide insights into the behavior of EUROFER97 under specific environmental conditions and help in developing strategies to mitigate corrosion in the ceramic breeder environment.

WP 5. Investigation of factors causing the deterioration of the fatigue properties of EUROFER97 specimens exposed to the ceramic breeder environment

This WP aims to identify the reasons for the potential deterioration of the fatigue properties of EUROFER97 due to exposure to the ceramic breeder environment studied in WP 4. One of the plausible causes could be the presence of hydrogen in the purge gas (He + 0.1 vol.% H_2), which could lead to hydrogen embrittlement. Therefore, Charpy impact tests will be conducted, and the amount of hydrogen in EUROFER97 samples will be measured using carrier gas hot extraction. In order to gain a better understanding of the initiation and development of fatigue cracks, detailed studies of the surface of the specimens and cracks before, during, and after testing will be conducted. This will include longitudinal sections and fractography to provide more insight into the crack initiation process and its propagation. This WP will also investigate potential differences in the behavior of sub-sized and standard samples during low-cycle fatigue testing.

WP 6. Evaluation of fatigue life of breeder blanket components made of EUROFER97 and design recommendations

This WP will evaluate the fatigue life of breeder blanket components made of EUROFER97 based on the research results obtained from the previous WPs. Recommendations for designers will be provided to improve the design of the breeder blanket and address potential issues related to fatigue and corrosion. By

addressing the potential issues related to fatigue and corrosion, the research will contribute to the development of more reliable and efficient blanket components, which are critical for the success of fusion energy systems.

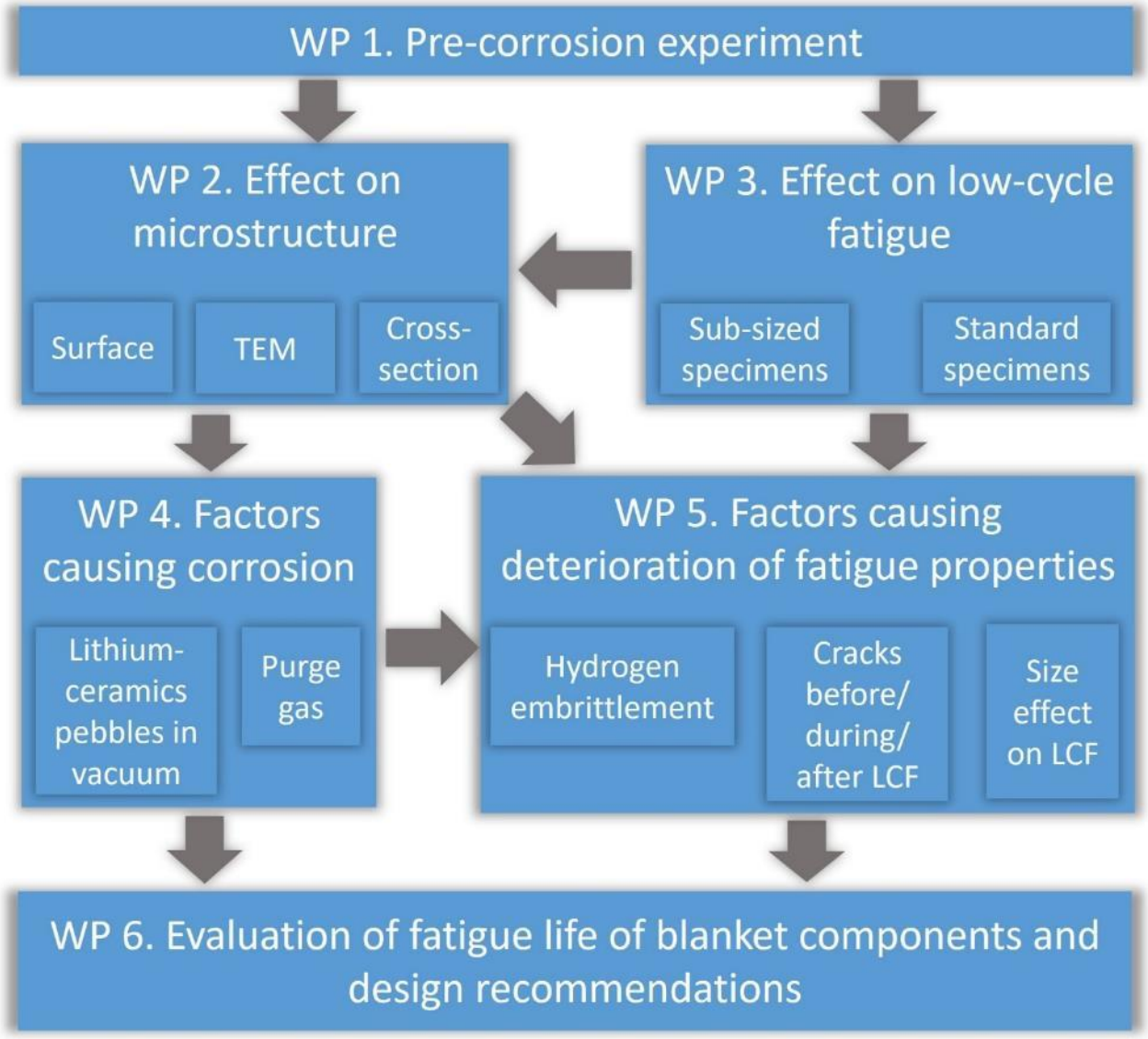

Fig. 3.1. Work plan divided into individual work packages

3.1 Materials

3.1.1 EUROFER97

The main material of interest is EUROFER97, a ferritic martensitic steel with good neutron irradiation resistance [32]. EUROFER97 was developed specifically for use in nuclear fusion reactors and is not yet a fully standardized quality. Only some batches have been produced by industry. Particularly, the batch number 2 of EUROFER97 was studied in this work. EUROFER97 steel is categorized as a reduced activation ferritic-martensitic (RAFM) steel, which was developed to reduce the cost and difficulties associated with

long-term safe storage of radioactive materials. EUROFER97 is composed of iron, chromium, and tungsten, as well as small amounts of other elements, see Table 3.1.

The as-received plate of EUROFER97 was heat-treated, which includes a high-temperature annealing at 960°C for 1.5 hours, followed by oil quenching and a tempering stage at 750°C for 4 hours with subsequent air cooling. The annealing stage allows for the dissolution of carbides, resulting in a homogeneous distribution of elements in the material. The quenching process rapidly cools the steel, preventing the formation of undesirable phases through diffusion, such as pearlite or bainite, and inducing a shear-assisted non-diffusional transformation from fcc to bcc. This generates a supersaturated tetragonal bcc structure rich in carbon, accompanied by significant accommodative deformation and increased dislocation density, ultimately resulting in enhanced hardness and strength. Finally, the tempering stage allows for the relaxation of residual stresses, the precipitation of finely dispersed carbides, and the adjustment of the material's mechanical properties [33,34]. It is worth noting that the recent heat treatment of EUROFER97 involves treatment at 980°C, followed by air quenching and tempering at 760°C [32]. However, these variations do not significantly impact the material's mechanical properties, as the temperatures deviate slightly and EUROFER97 can be effectively quenched in both air and oil.

As for EUROFER97's structure, following heat treatment, it primarily consists of a ferrite phase in a form of martensite packets and laths. The obtained by quenching tetragonal martensite, supersaturated with carbon, transforms into ferrite during the tempering stage. Additionally, carbon can precipitate in the form of particles (primarily $M_{23}C_6$), which develop along the boundaries of martensite laths and packets, and initial austenite grains.

Table 3.1. The specified chemical composition of EUROFER97 in wt.% [32,35]

	C%	S%	P%	Si%	Mn%	Ni%	Cr%	Mo%	W%
min	0.09	-	-	-	0.20	-	8.5	-	1.00
max	0.12	0.005	0.005	0.050	0.60	0.005	9.5	0.005	1.20
	Ta%	V%	Nb%	Cu%	B%	Al%	Co%	N_2%	Fe%-
min	0.10	0.15	-	-	-	-	-	0.015	Balance
max	0.14	0.25	0.001	0.005	0.001	0.01	0.005	0.045	Balance-

3.1.2 Lithium-ceramics pebbles

As a contact material for EUROFER97, lithium-ceramics pebbles were used, which were provided by the group of Dr. Knitter of KIT IAM-ESS. Ceramic pebbles are being developed as the EU reference tritium breeding material for ITER and DEMO and consist of a homogeneous mixture of lithium orthosilicate Li_4SiO_4 and 30% lithium metatitanate Li_2TiO_3 [7,36–38]. This material is considered one of the most promising candidates for tritium breeding due to its good chemical stability, low activation properties, and fast tritium diffusivity. The pebbles were manufactured using a liquid mixture, which was ejected through a small nozzle, resulting in a pebble size of 250–1250 µm [7].

Table 3.2. Calculated chemical composition (in wt.%) and major impurities (in ppm) in lithium-ceramics pebbles used for the pre-corrosion experiment [38]

wt.% (calculated)				ppm				
Li	O	Si	Ti	Al	Au	Ca	Cu	Co
20.2	50.67	16.83	12.29	18	25	11	1	<0.5
ppm								
Fe	K	Mg	Na	Nb	Pt	Rh	Zr	
2	<2	<2	<2	<3	30	9	5	

To ensure the purity of the pebbles, they were annealed at 300°C for an hour prior to use in order to remove any water vapor that may have been absorbed during storage. The pebbles were then placed in contact with the EUROFER97 specimens during the pre-corrosion process, simulating the conditions they would encounter in a fusion reactor.

3.2 Pre-corrosion experiments

As shown in the literature review, corrosion fatigue tests conducted in a corrosive environment are often replaced by pre-corrosion tests, where the samples are exposed to the corrosive environment for days or months, followed by fatigue tests of corroded samples. This is done to save time, as one fatigue test in a corrosive environment can take a long time, comparable to the lifetime of the corresponding component, i.e. according to the operating conditions of the blanket, the sample had to be loaded and unloaded relatively slowly while simultaneously undergoing the corrosion process. The study conducted three types of pre-corrosion tests, which will be discussed in detail below.

3.2.1 Exposure to the ceramic breeder environment

To replicate the operating conditions of EUROFER97 pressure tubes in the HCPB design of DEMO's breeding blanket, EUROFER97 specimens were subjected to unconstrained contact with lithium-ceramics pebbles at 550°C in a purge gas flow atmosphere (ceramic breeder environment). The experiment, designated as WP 1, serves as the foundational stage of the dissertation research (Fig. 3.1). The experiment was carried out on the setup of the group of Dr. Knitter at KIT IAM-ESS. The experimental setup, depicted in Fig. 3.2, consists of a furnace equipped with three ceramic tubes that can be heated simultaneously. Thermocouples were employed to monitor the temperature in each tube (Fig. 3.4). Each tube is linked to a gas supply system. The purge gas, consisting of He and 0.1 vol.% H_2, was maintained at a flow rate of 1200 ml/min at a pressure of 1200 mbar to maintain a slightly elevated pressure that prevents external air from infiltrating the system. The amount of gas impurities, particularly oxygen and water, was measured at the

inlet and outlet of each tube (Fig. 3.5 and Fig. 3.6). A more thorough description of the experimental setup can be found in [36].

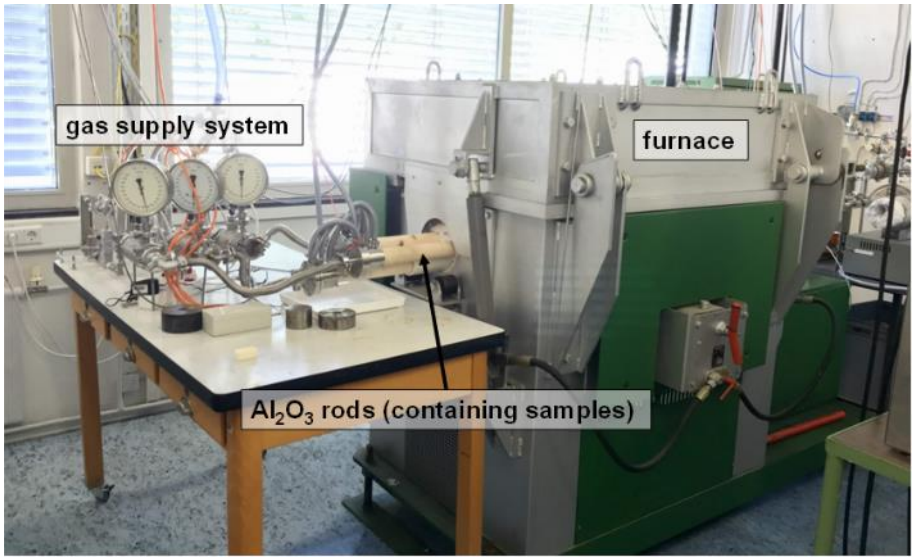

Fig. 3.2. Experimental setup used for pre-corrosion of EUROFER97 samples

Specimens for mechanical tests and samples for studying the microstructure of EUROFER97 were placed in ceramic containers and evenly covered with lithium-ceramics pebbles (Fig. 3.3). The containers were then placed in the tubes in a particular order to ensure that the samples to be exposed for the shortest time were installed last, thus enabling their removal from the furnace first when the required time was reached.

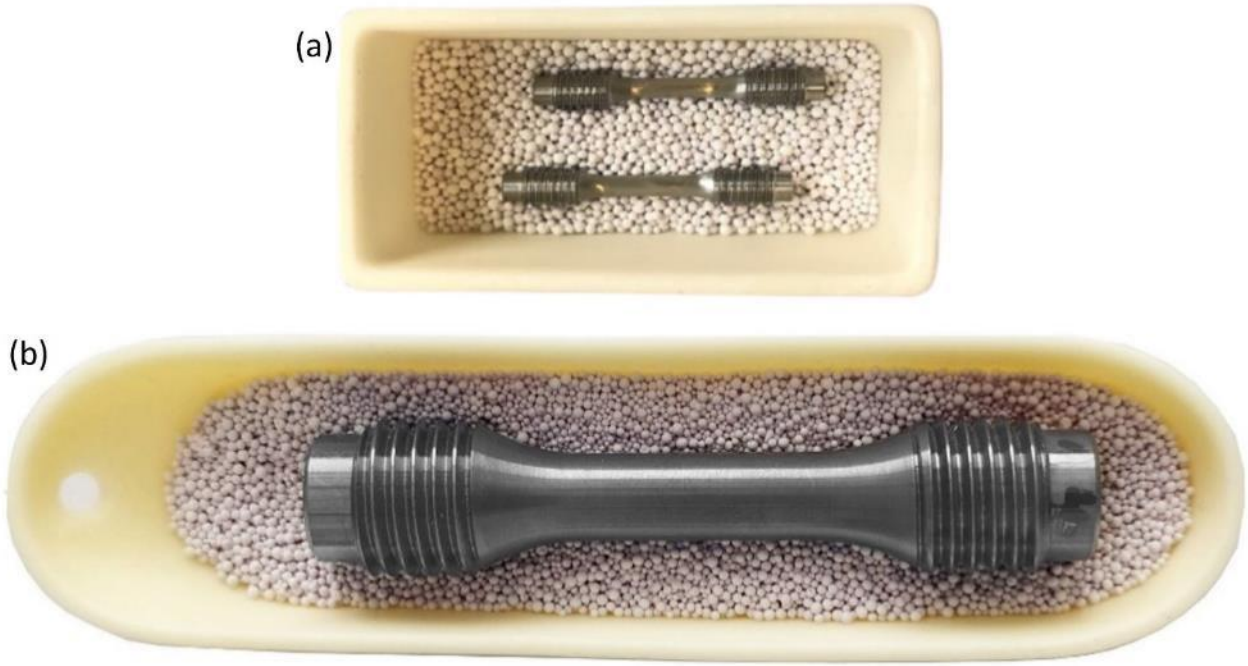

Fig. 3.3. Appearance of EUROFER97 specimens in containers prior to the final filling with lithium pebbles: (a) sub-sized, (b) standard specimens. Photographs are presented with the preservation of the original size ratio

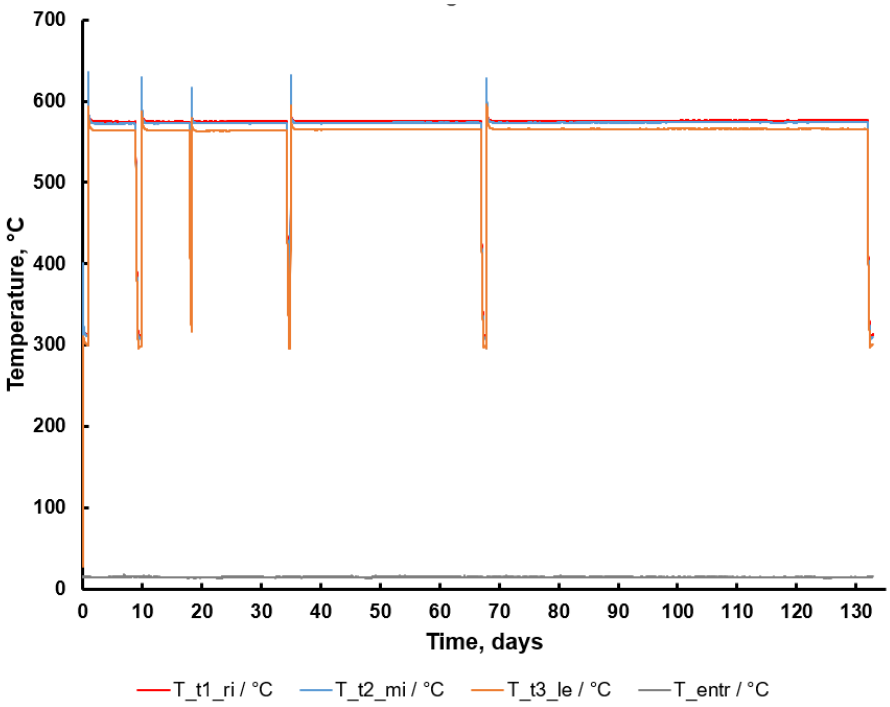

Fig. 3.4. Measured temperature during the exposure to the ceramic breeder environment inside one of the ceramic tubes for approximately 128 days [39]

After the placement of all three ceramic tubes, the entire setup was heated to 300°C while purging with gas to remove any impurities or water absorbed by the pebbles. After that, the temperature was increased to 550°C and the exposure to the ceramic breeder environment started. The sub-sized EUROFER97 specimens were exposed for 8, 16, 32, 64, and 128 days, while the standard specimens were exposed only for 64 days. Once the required exposure time was reached, the temperature was decreased to 300°C (as can be observed from the temperature jumps in Fig. 3.4), the purge gas flow was then stopped, and atmospheric air was introduced. The tube was then opened, and the next sample container was removed. The cooling rate of the samples from 550°C was about 32 K/h. During the opening of the tube, oxygen and water vapor detectors detected jumps in these gases due to the connection with the surrounding atmosphere (as can be seen from Fig. 3.5 and Fig. 3.6). The tube was subsequently sealed, purged with gas, and heated to 550°C again. During this process, the detected amount of impurity gases gradually decreased.

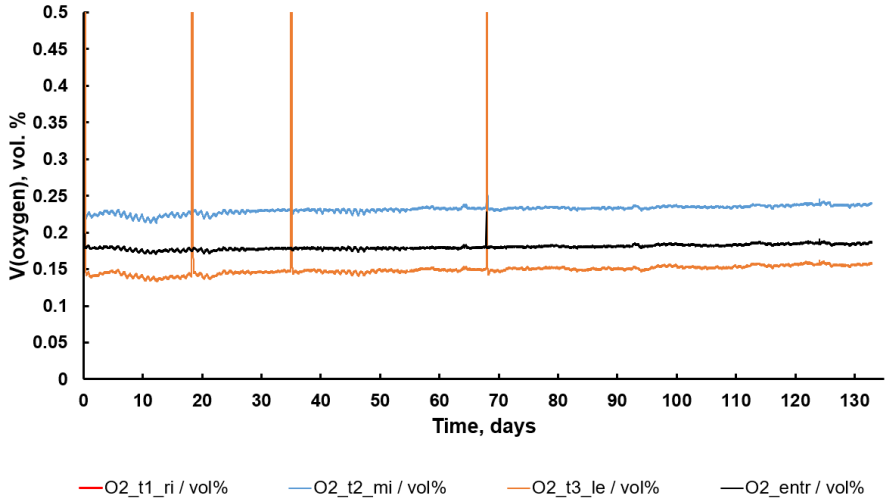

Fig. 3.5. Oxygen content in the atmosphere inside the furnace at the inlet (O2_entr) and outlet (O2_t1, t2, t3). The data was obtained from the group of Dr. Knitter, KIT IAM-ESS.

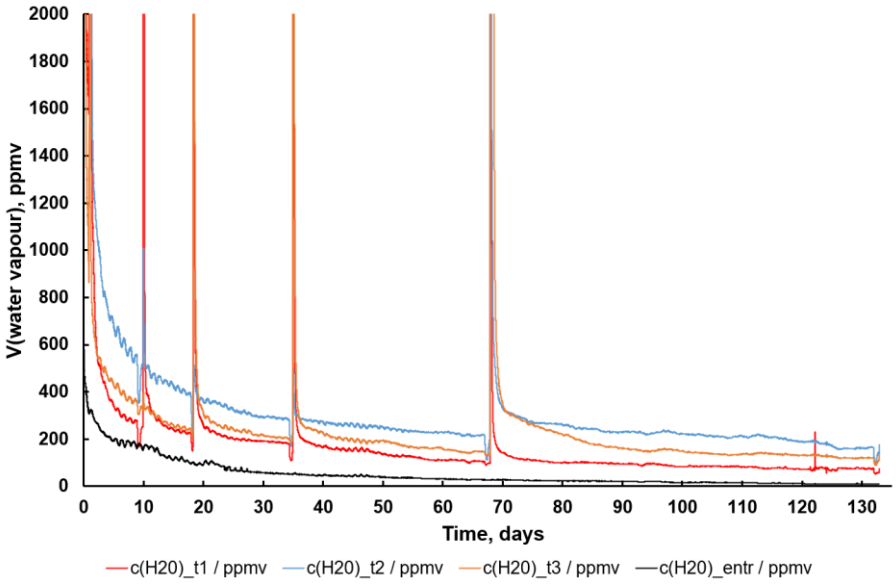

Fig. 3.6. Water vapor content in the atmosphere inside the furnace at the inlet (c(H2O)_entr) and outlet (c(H2O)_t1, t2, t3). The data was obtained from the group of Dr. Knitter, KIT IAM-ESS.

3.2.2 Exposure to Li-ceramics pebbles in vacuum

Part of sub-sized EUROFER97 specimens were also exposed to a vacuum environment in contact with lithium-ceramics pebbles. The specimens were placed in ceramic containers and covered evenly with the Li-ceramics pebbles, after which the containers were sealed in a quartz tube and the air was removed by vacuum pump until reaching ≈10^{-3} mbar. The tube was then placed in a furnace with three temperature control zones, and the exposure was initiated at 550°C, with a continuous high vacuum maintained throughout. The duration of the pre-corrosion was 64 days. After completion of the exposure, the quartz tube was removed from the furnace and opened only after the samples had completely cooled down.

Ten additional Charpy specimens were annealed in vacuum without Li-ceramics in order to evaluate the effect of long-term annealing at 550°C on the impact properties.

3.2.3 Exposure to a purge gas atmosphere

Another part of sub-sized EUROFER97 specimens was exposed to a purge gas atmosphere. Similarly, the samples were placed in ceramic containers, but without the presence of lithium-ceramics pebbles. The pre-corrosion experiment lasted for a period of 64 days, and all other exposure parameters remained consistent with those of the ceramic breeder environment exposure process.

3.3 Mechanical testing

3.3.1 LCF tests

In order to gain insight into the mechanical behavior under cyclic loading of EUROFER97 exposed to the ceramic breeder environment, low-cycle fatigue testing was conducted on both sub-sized (Fig. 3.7a) and full-size standard (Fig. 3.7b) specimens. These specimens were manufactured from a heat-treated EUROFER97 steel plate and prepared according to their specific dimensions. The sub-sized specimens had a nominal diameter of 2 mm and a gauge length of 7.6 mm, with an overall length of 27 mm (A.1). The design of the sub-sized specimens was developed at the Karlsruhe Institute of Technology (KIT), Germany, within the framework of an irradiation program. The miniature geometry was chosen to enable the maximum number of samples to be exposed and tested during the first stage of the experiment. This facilitated the identification of trends in properties based on exposure time in the ceramic breeder environment. The standard specimens had a nominal diameter of 8.8 mm and a gauge length of 23 mm, with an overall length of 77 mm (A.1). The specimens were fabricated using a turning process and were polished to remove turning marks, thereby minimizing the impact of surface quality on the test results. The only difference in the final polishing of the specimens was that the sub-sized specimens were polished axially to eliminate any possible influence of radial scratches, while the standard specimens were polished conventionally in the radial direction.

Fig. 3.7 Low-cycle fatigue specimens: (a) sub-sized, (b) standard. Photographs are presented with the preservation of the original size ratio

Low cycle fatigue tests were conducted on a computer-controlled MTS 810 servo-hydraulic testing machine, equipped with a radiative furnace from R-I Controls and a high-temperature extensometer from MAYTEC, model PMA-12/V7/1, using a gauge length of 7 mm (see Fig. 3.8). The specimens were first fixed on the

lower traverse of the machine, and the traverse was moved upwards to position the sample, ensuring that the compression force did not cause any damage. The application of a compressive load ensures a secure fixation of the sample without any gaps in both the lower and upper grips. A thermocouple was welded onto the specimen's bottom shoulder outside the gauge length using contact welding to accurately control the furnace temperature. The furnace was heated to a temperature of 550°C for about 30 min, and the specimens were soaked for an additional 20 min to stabilize the temperature. The tests were carried out in air applying a strain rate of 3×10^{-3} s^{-1}, using a fully-reversed triangular waveform (R=-1) and a total strain range of 0.6%, 1%, and 1.6%. Additionally, tests were performed at total strain ranges of 0.4%, 0.8%, 1.0%, and 1.2%. The tests concluded with a significant load drop, which did not always lead to complete specimen rupture. Upon completion of the test, the specimens were cooled with the furnace for approximately 1.5 hours, after which the thermocouple was removed, and the sample was dismantled for further structural analysis. After testing, the data obtained was analyzed according to ASTM 2714-13 [40].

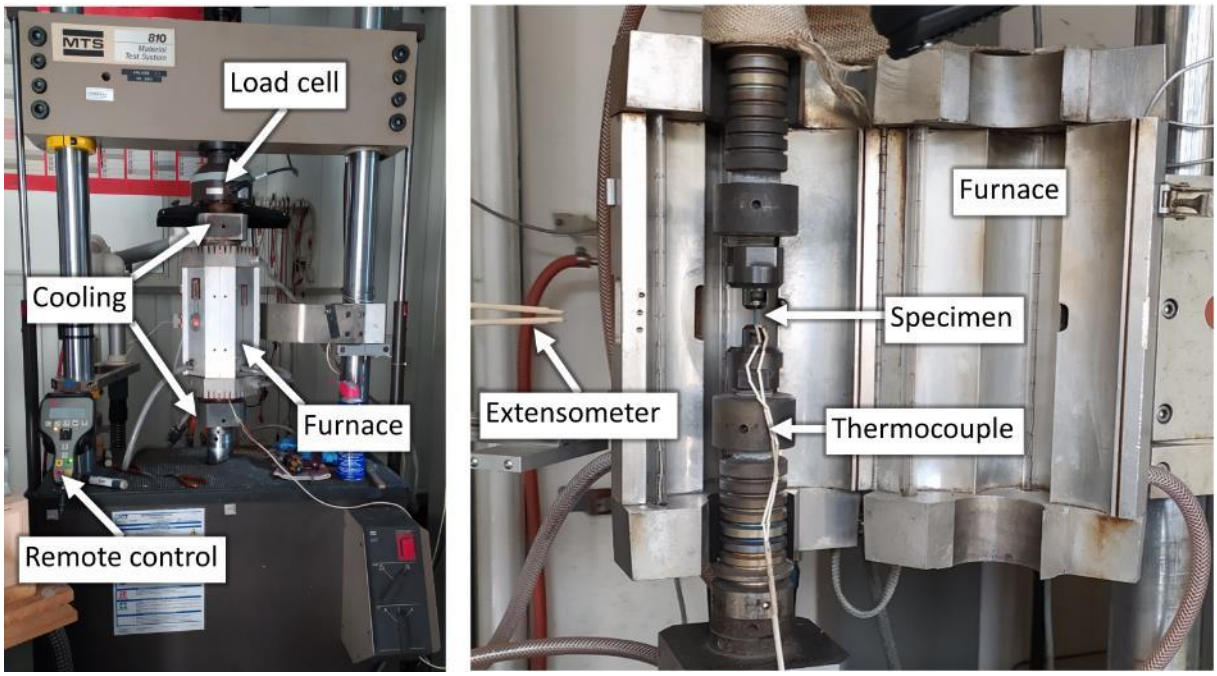

Fig. 3.8. MTS testing setup for low cycle fatigue investigations

3.3.2 Charpy impact tests

Charpy impact tests are an important method to determine the behavior of materials under impact loading, especially for metals that can be embrittled due to some reason. In this study, Charpy tests were carried out to investigate the possible effect of exposure to the ceramic breeder environment on the brittle-to-ductile transition temperature (DBTT) and impact energy of EUROFER97 steel. To perform these tests, KLST type sub-sized Charpy-V impact specimens were used (dimension: 27×4×3 mm^3) with a carefully prepared V-shaped notch in the middle (A.1).

The tests were conducted at various temperatures at -120, -115, -100, -80, -70, -60 and -50°C in air, and the specimens were cooled inside a cooling device before being transferred to an impact testing machine after a 10-minute soaking at a given temperature. After the test, the upper shelf energy (USE) and DBTT were

determined from the plotted diagram. These results were then compared to those obtained for as-received non-exposed specimens to determine the effect of exposure on the mechanical properties of the material.

3.4 Microstructural characterization

3.4.1 X-Ray Diffraction Analysis (XRD)

The phase composition of the EUROFER97 surface was analyzed using X-ray diffraction (XRD) with Cu-$K\alpha_{1/2}$ radiation on a Seifert PAD II diffractometer in both the as-received and pre-corroded conditions. The measurements were performed by Dr. Seemann, KIT IAM-AWP. Cubic samples, exposed to the same conditions as the specimens used for mechanical tests, exhibiting a size of approximately 10×10×10 mm³ were used for this studies. Prior to exposure, the surface of the samples was ground and polished to minimize surface defects. The measurements were taken at angles ranging from 2Θ=10–100° with a step of 0.01°. X-ray measurements were performed at a voltage of 40 kV and a current of 30 nA. To identify the various phases present in the samples, the following Powder Diffraction File (PDF) and Inorganic Crystal Structure Database (ICSD) numbers were used: α-Fe (PDF: 03-065-4899), FeO (PDF: 01-075-1550), Fe_3O_4 (PDF: 01-089-3854), $(Fe+Li)_3O_4$ (PDF: 00-037-1432), $FeCr_2O_4$ (PDF: 01-089-3855), $LiFeO_2$ (ICSD: 51207), $Li_2Fe_{3.2}Cr_{6.8}O_{16}$ or $(Li+Fe+Cr)_3O_4$ (ICSD: 21096).

3.4.2 Scanning electron microscopy (SEM)

In order to obtain a detailed understanding of the microstructure of the exposed to the ceramic breeder environment EUROFER97, comprehensive studies were conducted both on the surface and cross-sections of the material. To prepare the cross-sections, electrical discharge machining (EDM) was utilized to cut the samples, which were then either ground as is or embedded into an electroconductive resin. The grinding process involved a gradual reduction in grit size, starting with P120 and progressing to P240, P380, P500, P800, P1200, and finally P2000. The samples were then subjected to mechanical polishing using diamond suspensions of 9 µm, 6 µm, 3 µm, and 1 µm, and finally on a colloidal suspension of SiO_2 with 60 nm grains. Microstructural analysis was conducted using a Zeiss Evo and a Zeiss Merlin scanning electron microscope (SEM) in back-scattered electron (BSE) or secondary electron (SE) modes, providing high resolution images of the microstructure. Cross-sectional analysis was carried out using a voltage of 20 kV and a current of 10 nA, while surface features were studied at lower voltage and current settings of 5 kV and 2 nA, respectively. To obtain element distribution maps, energy-dispersive X-ray spectroscopy (EDS) was employed. The voltage and current were set to 15 kV and 6 nA, respectively, to maintain a dead time parameter within the range of 25–35%.

3.4.3 Focused Ion Beam (FIB)

Since the area of interest for the study in TEM was limited to the surface of samples and the corrosion layer, the conventional preparation of disc foils was not possible. Instead, a targeted lamellae preparation was

performed using a FEI Scios Focused Ion Beam (FIB) system. To do this, the samples were embedded into an electroconductive resin and the cross section was prepared by grinding and polishing. The lamellae with a size of about 20×10×2 μm^3 were lifted out from different corrosion layers and welded to copper grids. The final polishing of electro-transparent windows of about 8×8 μm^2 was carried out with a gradual decrease in voltage, namely, 30 kV, 16 kV, 10 kV and 5 kV. The work at the FIB was carried out under the guidance of Dr. Gaisin, KIT IAM-AWP.

In addition to lamellae preparation for TEM, FIB was used to determine the thickness of the corrosion layer for specimens for which cross-sectional preparation was not possible. To do this, a platinum coating about 1 µm thick was deposited onto the surface of the sample. Trenches of about 20×20 μm^2 in size were cut out with a gradual decrease in voltage.

3.4.4 Transmission electron microscopy (TEM)

The lamellae were examined using a Talos F200X transmission electron microscope (TEM) equipped with a Super X-EDS system for energy-dispersive X-ray spectroscopy, a Gatan Enfinium electron energy-loss spectrometer (EELS), and a scanning unit (STEM) with high-angle annular dark-field (HAADF) detector. The lamellae prepared by FIB were subjected to an extensive analytical TEM analysis including EDS and electron energy-loss spectroscopy (EELS) as well as imaging and diffraction methods to unravel the involved phases on the nanoscale. The TEM study was done by Dr. Dürrschnabel, KIT IAM-AWP [41].

TEM was employed to identify and study the distribution of lithium-containing phases in the corrosion layer across the outer, intermediate, and inner layers of the EUROFER97 sample. With its high-resolution imaging capabilities, TEM was used to detect nanoscale grains and particles, which are often not visible using other microscopy techniques such as SEM.

3.4.5 Carrier gas hot extraction (CGHE)

To measure the hydrogen content in the EUROFER97 material before and after exposure to the ceramic breeder environment, a carrier gas hot extraction method was used. The measurements were conducted by Dr. Bergfeldt, KIT IAM-AWP. First, a sample was cut into small pieces and placed in a quartz tube reactor. The reactor was then purged with argon gas to remove any air present. Next, the sample was heated to a high temperature under a flow of argon gas. During heating, the hydrogen in the sample was released and carried by the argon gas flow to a detection system where it was quantified using a thermal conductivity detector. This procedure was carried out both before and after exposure to the ceramic breeder environment to determine the effect of exposure on hydrogen content. The hydrogen content was calculated based on the known volume and flow rate of the carrier gas and quantified using a gas chromatography-mass spectrometry system.

4 Results and discussion

The research work for the dissertation followed the outlined work packages as depicted in Fig. 3.1, which provides an overview of the entire study. The division into work packages is somewhat arbitrary, the interconnections between different sections of the dissertation are more intricate. Section 4.1 discusses the progress of work packages WP 2 and WP 3, while Section 4.2 focuses on WP 4. Additionally, Section 4.3 explores the tasks of WP 5, concluding with the final results of WP 6, which completes the thesis.

4.1 Effect of ceramic breeder environment

4.1.1 Phase composition of the surface

The investigation was efficiently initiated with sub-sized specimens, which were designed at KIT as part of an irradiation program. The design featured miniature geometry to allow exposure and testing of maximum number of samples during the first stage of the experiment, thereby facilitating the identification of trends in material properties concerning the duration of exposure to the ceramic breeder environment. This strategic decision aimed to optimize resources and achieve a more efficient data collection process for the study.

Fig. 4.1 illustrates the visual appearance of sub-sized LCF specimens of EUROFER97 after exposure to 550°C in contact with Li-ceramics pebbles in a purge gas flow atmosphere (ceramic breeder environment) [42,43]. The surface color of the specimens has been altered as a result of exposure. After 8 days of interaction, black dots corresponding to the contact zones (imprints) of ceramic pebbles can be observed. With prolonged exposure for 16–64 days, imprints become more evident as black dots encircled by a brighter region. After exposure for 128 days, imprints are barely visible.

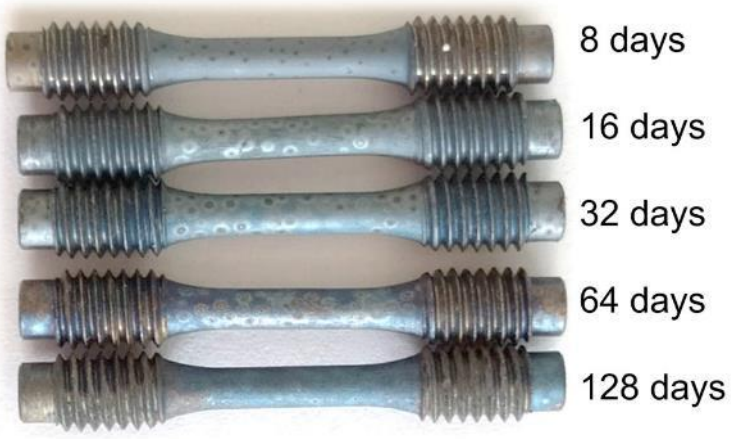

Fig. 4.1. Sub-sized low cycle fatigue specimens of EUROFER97 after exposure to the ceramic breeder environment for different durations [43]

Fig. 4.2 shows the typical microstructure of the surface of sub-sized EUROFER97 specimens used in LCF tests after exposure to the ceramic breeder environment for 64 days (Fig. 4.2a,b), as well as in the as-received state (Fig. 4.2c,d). The as-received state only shows marks from the final polishing stage along the length of the sample (Fig. 4.2c,d). After exposure, the main feature of the surface microstructure is the imprints of lithium-ceramics pebbles, which are distributed uniformly over the surface. The distance between neighboring imprints is essentially the sum of the radii of two neighboring lithium-ceramics pebbles, with pebble sizes ranging from 250 to 1250 µm [7]. The distance between imprints is measured to be similar, with an average range of 400–700 µm, while the imprint diameter is on average 100–200 µm. The imprints are generally circular, but may vary in shape depending on the shape of the lithium-ceramics pebble. Another characteristic of the surface is the presence of small protrusions (hillocks) on the entire surface of the sample, except for the area around the imprints. This feature will be discussed in more detail below.

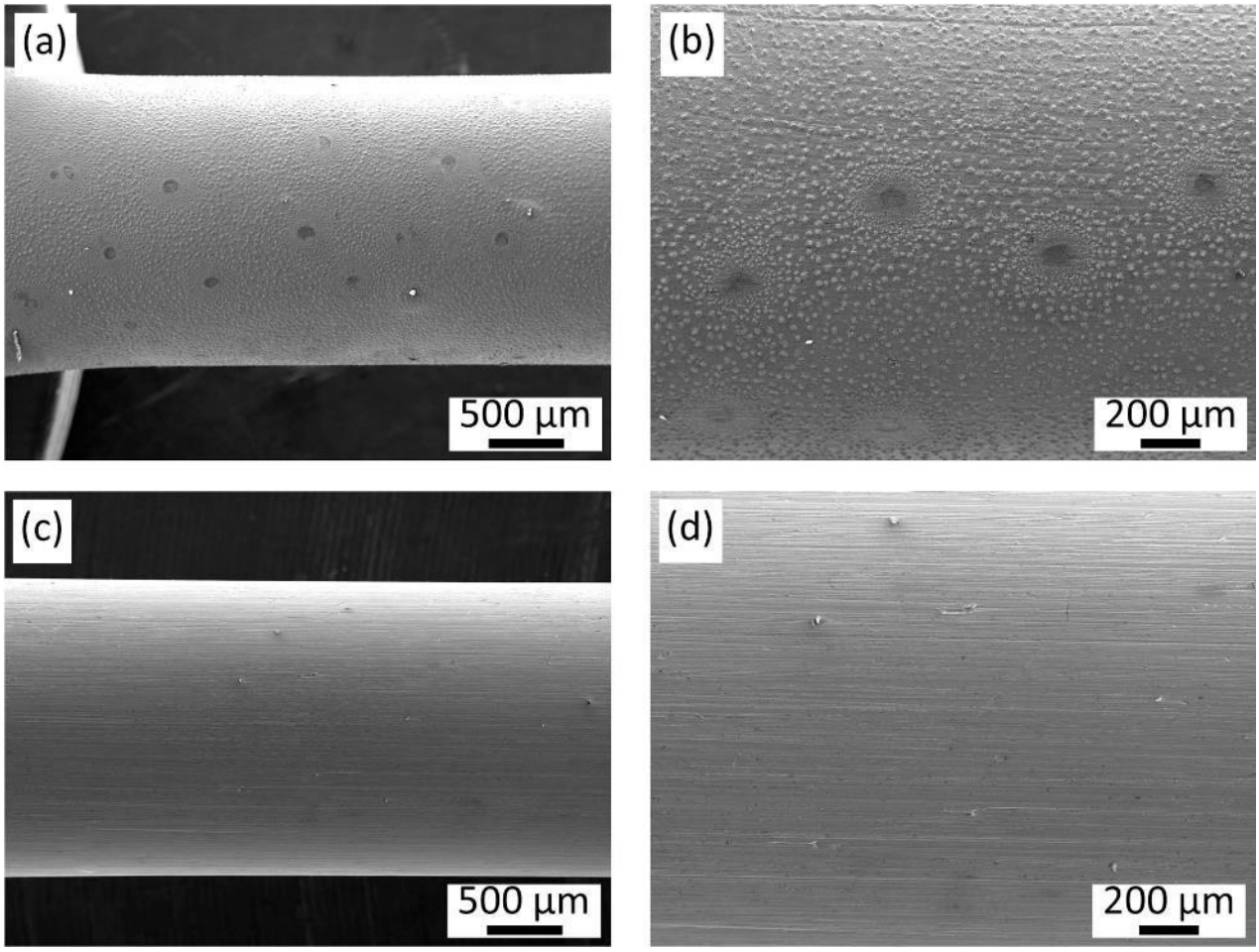

Fig. 4.2. SEM microstructure of the surface of EUROFER97 specimen: (a,b) after exposure to the ceramic breeder environment for 64 days, (c,d) as-received

X-ray diffraction analysis was conducted to investigate the phase composition change of EUROFER97 sample surfaces after exposure for different durations. Cubic samples were specifically prepared and exposed to the same conditions as those for LCF tests. The XRD patterns (Fig. 4.3) of the as-received EUROFER97 sample only displayed ferrite peaks (PDF: 03-065-4899). The slightly larger peak at approximately 44° than expected for ferrite may indicate some texture in the starting material, possibly due

to rolling. Moreover, all peaks shifted to the left by 0.15-0.2°, indicating an increase in interplanar distances due to solid solution doping. Notably, small peaks around 40° were observed in Fig. 4.3 and beyond. This was attributed to the X-ray used containing not only Cu-K_α radiation, but also a fraction of Cu-K_β, despite the presence of monochromators. The main highest peak of ferrite (110) in Cu-K_α radiation corresponds to about 44.7°, and in Cu-K_β – 40.1°. Hence, this peak at 40° is ignored and not noted hereinafter in the diffractograms.

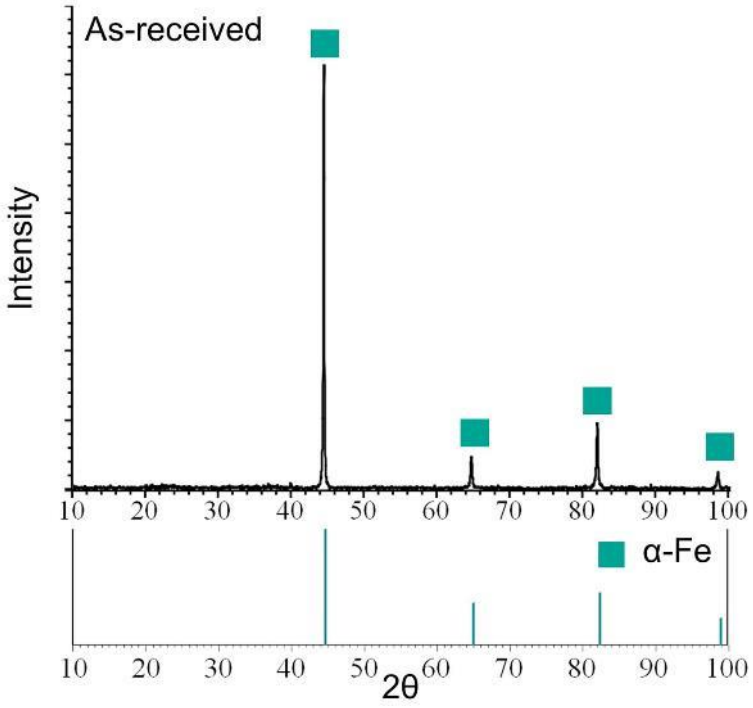

Fig. 4.3. X-ray diffraction pattern for as-received EUROFER97 sample. Below the diffraction pattern are the peaks for α-Fe used for the analysis.

After exposure for 8 days, a number of peaks corresponding to FeO (PDF: 01-075-1550) and Fe_3O_4 (PDF: 01-089-3854) are found along with the ferrite peaks (Fig. 4.4). It should be noted that the Fe_3O_4 peaks may also include peaks for Fe_2O_3, since Fe_3O_4 may contain the Fe_2O_3 phase especially in the presence of Li [44]. Thus, already after 8 days, a EUROFER97 sample placed in the ceramic breeder environment is covered with iron oxides. The source of oxygen for oxidation can be both lithium-ceramics pebbles and the atmosphere of purge gas, namely its impurities. Other possible oxides (chromium oxide) are not found in the XRD pattern, apparently due to the shallow penetration of X-rays.

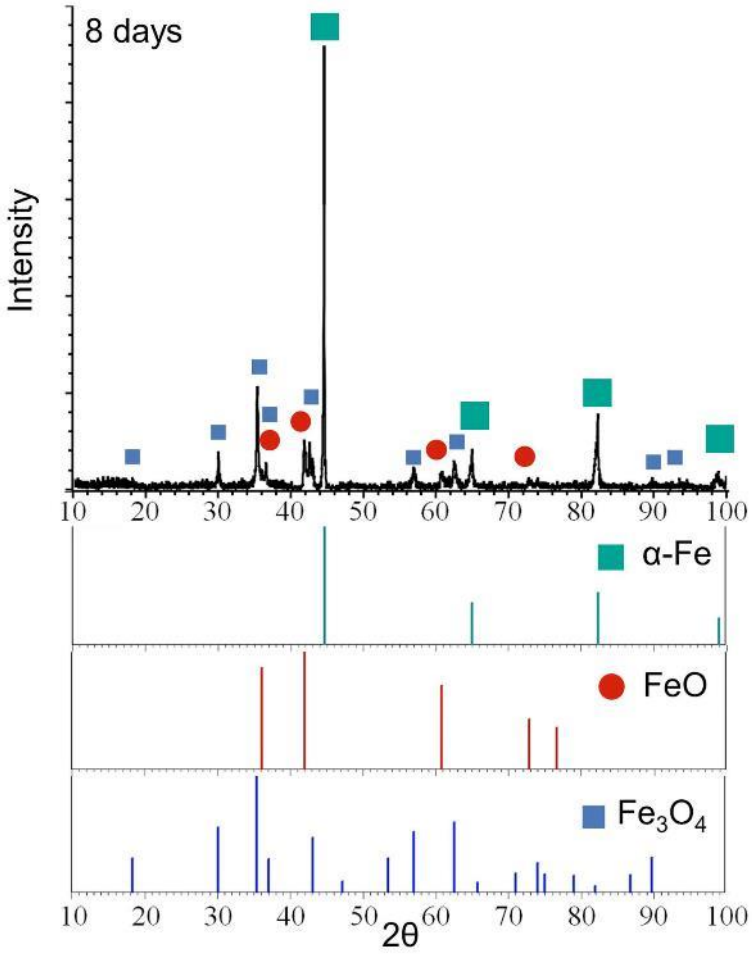

Fig. 4.4. X-ray diffraction pattern for EUROFER97 sample after exposure to the ceramic breeder environment for 8 days. Below the diffraction pattern are the peaks for α-Fe, FeO, and Fe_3O_4 used for the analysis.

After exposure for 16 days, the diffraction pattern in Fig. 4.5 shows very high peaks of iron oxides FeO and Fe_3O_4 (and Fe_2O_3), comparable in height to the ferrite peaks. Further exposure to a duration of 32 days led to the fact that the peaks corresponding to iron oxides sharply decreased in height (Fig. 4.6). In addition, the peaks corresponding to ferrite in this case are not shifted to the left (as in the case of as-received EUROFER97), but to the right by 0.05°. This may indicate that the surface of the sample does not contain EUROFER97, but unalloyed ferrite. The decrease in the amount of oxides and the appearance of pure iron can be associated with the reduction of iron oxides by hydrogen, which will be shown below. In the work [16], the appearance of shifted peaks of pure iron was also observed on the diffraction patterns.

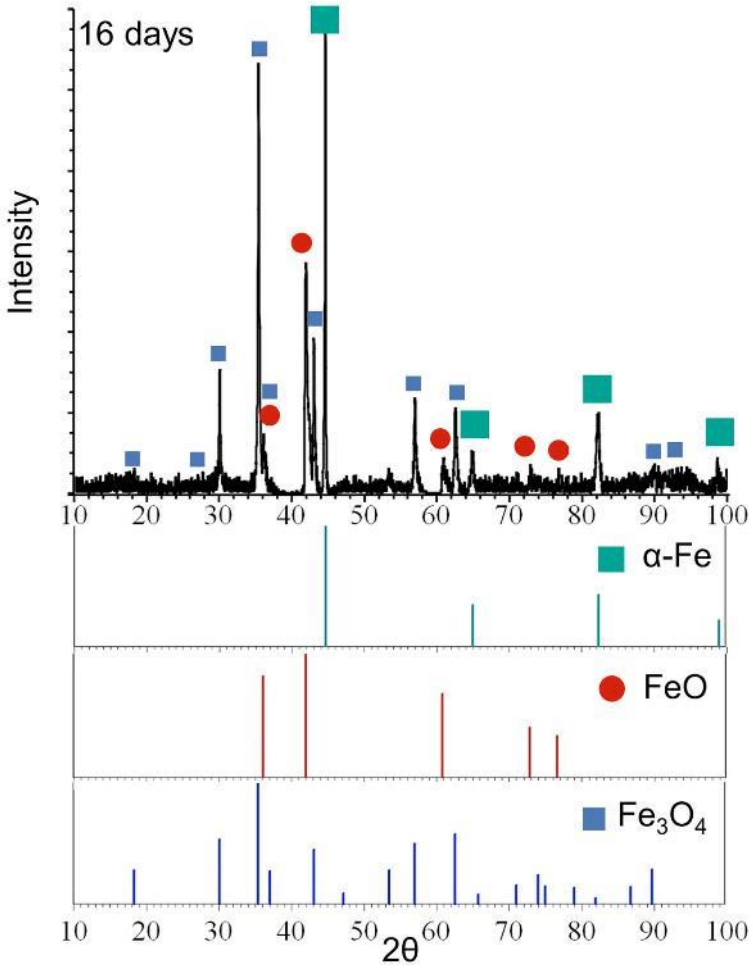

Fig. 4.5. X-ray diffraction pattern for EUROFER97 sample after exposure to the ceramic breeder environment for 16 days. Below the diffraction pattern are the peaks for α-Fe, FeO, and Fe_3O_4 used for the analysis.

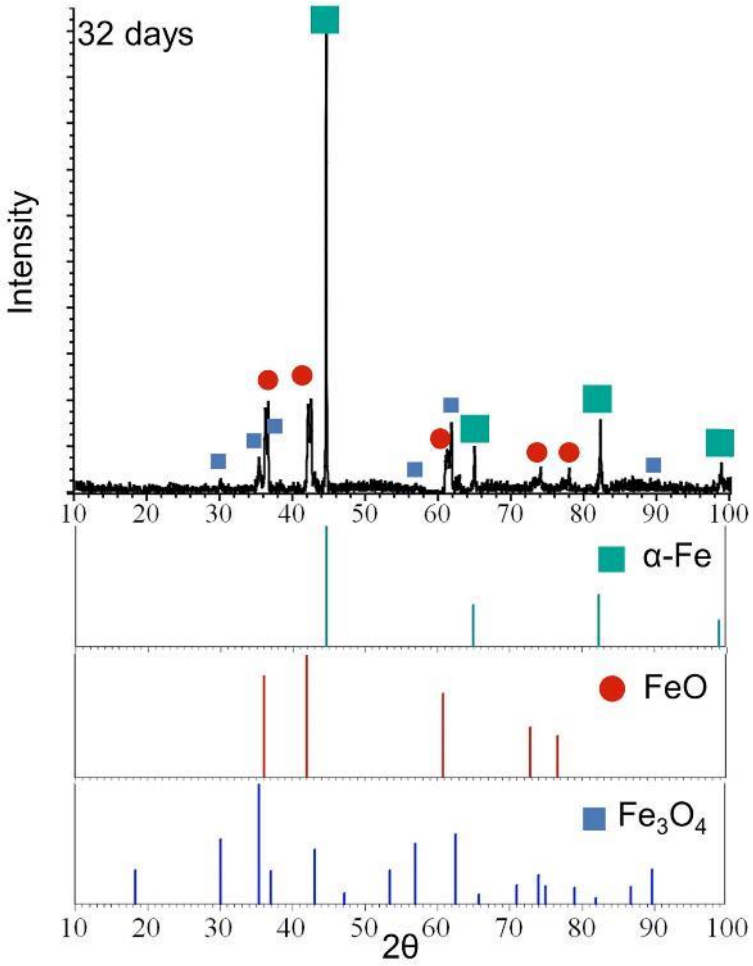

Fig. 4.6. X-ray diffraction pattern for EUROFER97 sample after exposure to the ceramic breeder environment for 32 days. Below the diffraction pattern are the peaks for α-Fe, FeO, and Fe_3O_4 used for the analysis.

Increasing the exposure time to 64 days leads to a further decrease in the height of iron oxide peaks (Fig. 4.7). In this case, iron oxide FeO is not found in the diffraction pattern. Compared to the peaks from ferrite, the height of the peaks from iron oxide Fe_3O_4 turned out to be negligible. The α-Fe peaks are shifted to the right of the table values, which indicates that an undoped ferrite phase (and not EUROFER97) is present on the sample surface as also shown in [16].

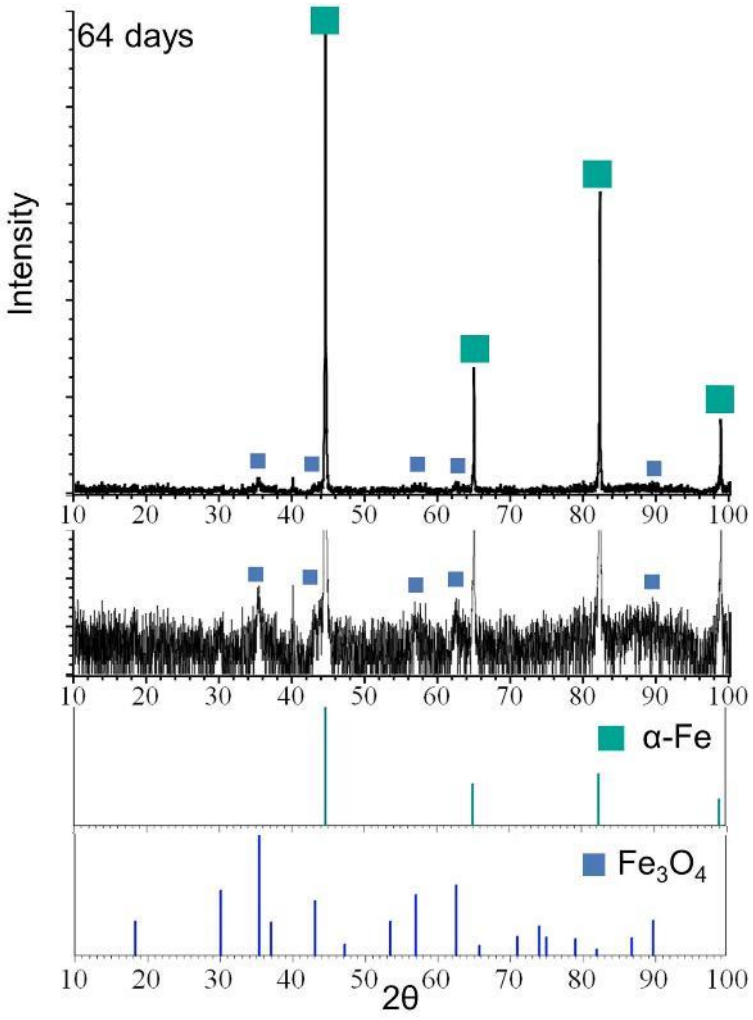

Fig. 4.7. X-ray diffraction pattern for EUROFER97 sample after exposure to the ceramic breeder environment for 64 days. Below the diffraction pattern is an enlarged image of the low peaks as well as the peaks for α-Fe and Fe_3O_4 used for analysis.

After exposure for 128 days, the XRD pattern did not change significantly (Fig. 4.8). There are also very high peaks corresponding to pure ferrite and low peaks for iron oxide Fe_3O_4. Automatic indexing identifies the phase $(Fe+Li)_3O_4$ (PDF: 00-037-1432) on the pattern. In fact, this phase is the iron oxide Fe_3O_4 phase, in which some of the iron atoms are replaced by lithium. The peaks of these two phases almost coincide, except that the $(Fe+Li)_3O_4$ peaks are shifted somewhat to the left (the radius of the lithium atom is larger than the radius of the iron atom). In addition, the relative height of the peaks of the $(Fe+Li)_3O_4$ phase at about 37°, 42°, and 62° is higher than for the Fe_3O_4 phase. All this helps to identify the presence of both oxide phases. Apparently, upon interaction for a long time, a sufficient amount of lithium diffuses from the lithium-ceramics into the EUROFER97 surface, so that its amount exceeds the detection limit of XRD. This is in agreement with other works, in which a lithium-containing oxide phases were also detected, but of different compositions, namely $Li_2Fe_3O_4$, $LiFe_5O_8$, $LiFeO_2$, and $LiCrO_2$ [16,18,45].

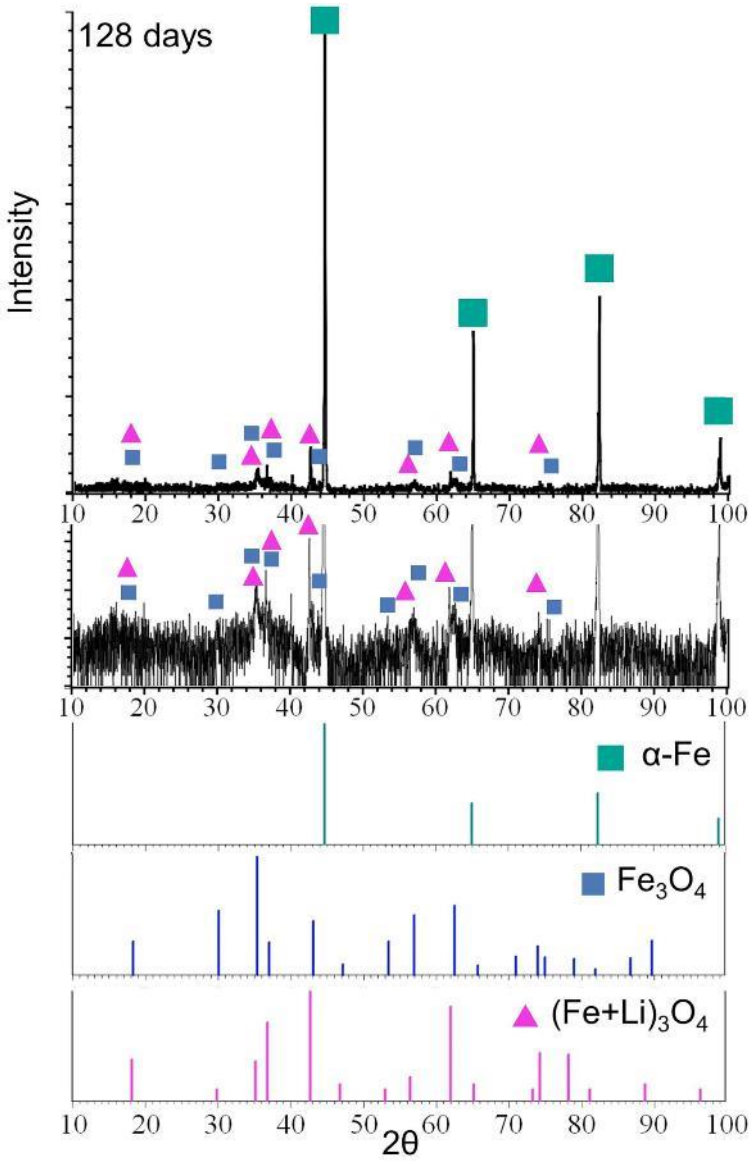

Fig. 4.8. X-ray diffraction pattern for EUROFER97 sample after exposure to the ceramic breeder environment for 128 days. Below the diffraction pattern is an enlarged image of the low peaks as well as the peaks for α-Fe, Fe_3O_4, and $(Fe+Li)_3O_4$ used for analysis.

Fig. 4.9 summarizes all obtained diffraction patterns and shows the evolution of phase composition on the surface of the EUROFER97 sample depending on the exposure duration in contact with lithium-ceramics pebbles in a purge gas atmosphere. Exposure for 8–16 days leads to an increase in the amount of iron oxides on the surface. After exposure for 32–64 days, the amount of oxides decreases, and peaks corresponding to the pure ferrite phase appear. Exposure for 64–128 days does not lead to a significant change in the diffraction pattern, except that an oxide phase containing lithium is found. It should be noted that XRD measurements shows the phase composition of the volume very close the surface; therefore, the cross sections are also needed to describe the entire corrosion layer.

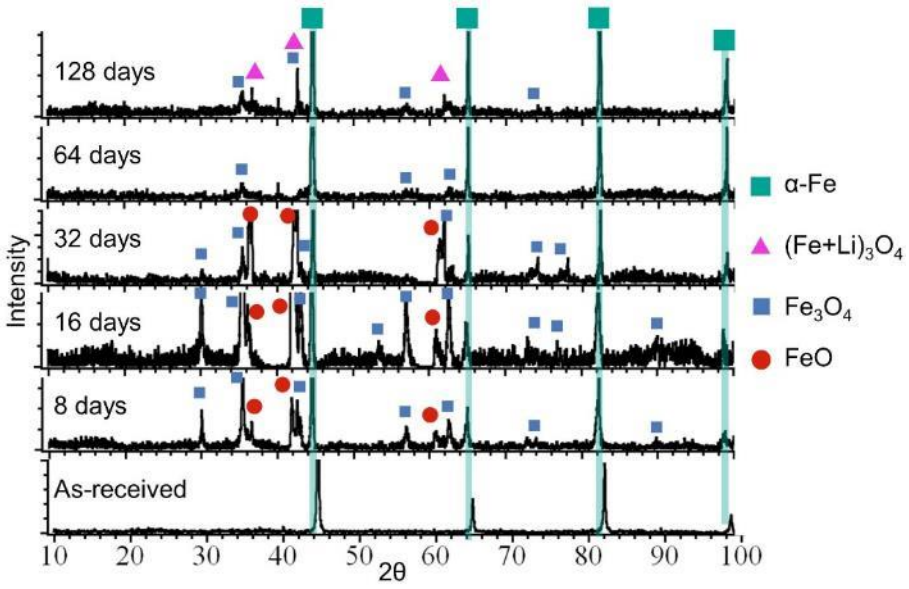

Fig. 4.9. Jointed X-ray diffraction patterns for as-received samples and after exposure to the ceramic breeder environment for different durations

Following X-ray diffraction analysis, SEM and EDS studies were performed to further examine the LCF specimens in the contact zones with lithium-ceramics pebbles, as well as in the surrounding areas. Fig. 4.10 presents the microstructure and corresponding EDS maps of an area adjacent to one of the imprints (left in the figure) of lithium-ceramics pebbles after exposure for 8 days. A high oxygen content is observed on the surface, although the exact amount cannot be determined using EDS. EDS analysis reveals that these contact zones after exposure consist of iron and chromium oxides. As previously noted, the primary sources of oxygen during exposure are the lithium-ceramics pebbles themselves and the purge gas, which contains impurities such as oxygen and water (Fig. 3.5–Fig. 3.6). The influence of the purge gas will be discussed in greater detail in Section 4.2.2. Iron oxide covers the majority of the surface around the imprint, while the contact zones (steel-pebble) are primarily comprised of chromium-rich oxide (it contains both Cr and Fe). Additionally, pure iron hillocks are observed around the imprints. Chromium-rich oxide is not detected on the diffraction pattern after exposure for 8 days (Fig. 4.4), possibly due to its low volume fraction on the surface. Previous research by Mukai and Takumi has associated the presence of pure iron on the surface with hydrogen-induced reduction of iron oxide [5, 7]. As for the chromium-rich oxide, this oxide also contains an increased amount of iron (Fig. 4.10b) and, apparently, can be denoted as spinel, for example, $(Fe_{0.6}Cr_{0.4})_2O_3$ as in [14] or lithium-containg spinel $(Li_2O)(Fe_2O_3)_4(Cr_2O_3)$ as in [13]. Since the EDS method in the SEM does not allow one to reliably determine the amount of oxygen, as well as to detect lithium, hereinafter this phase is denoted as chromium-rich oxide. However, section 4.1.3 will show the results of the TEM study of this phase.

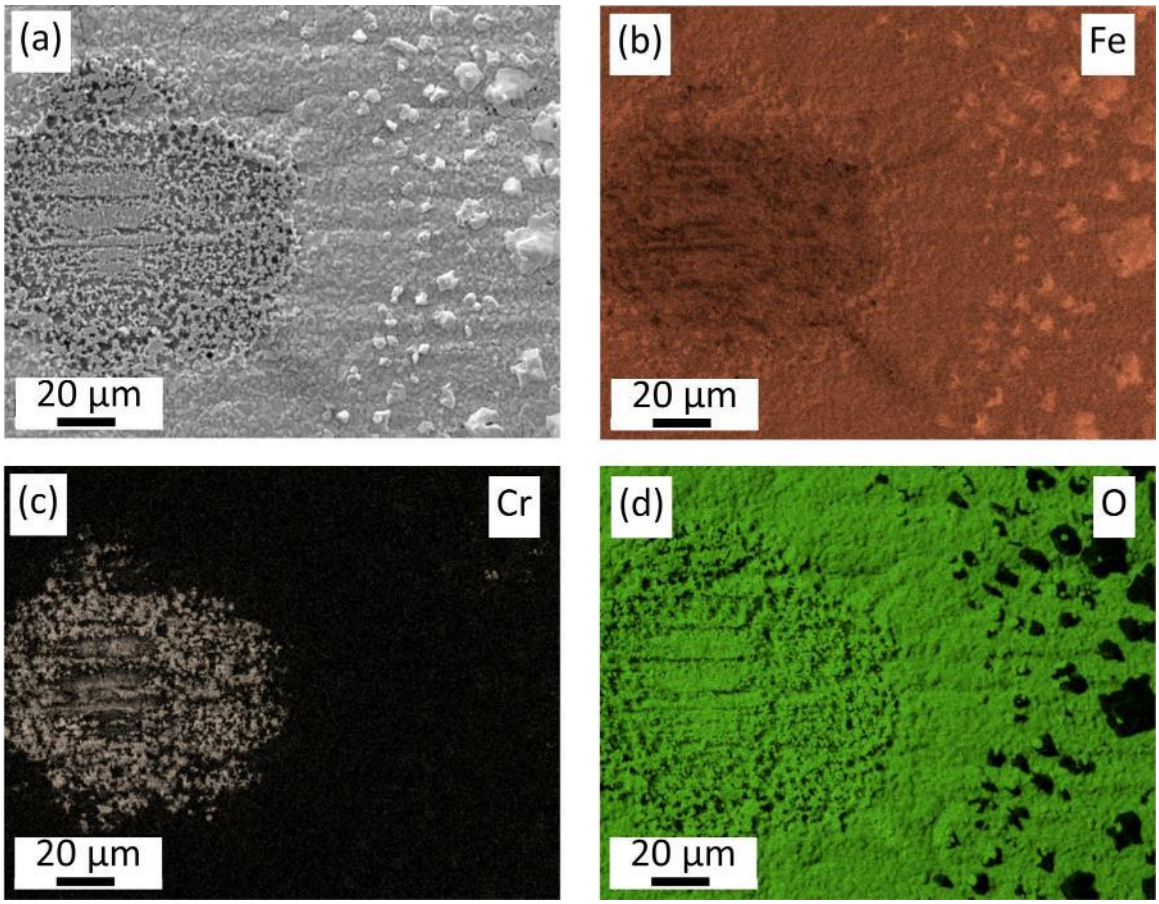

Fig. 4.10. (a) Microstructure and (b-d) corresponding elemental EDS maps of a surface of EUROFER97 sample exposed to the ceramic breeder environment for 8 days: (b) iron, (c) chromium, (d) oxygen

With an increase in the exposure time to 16 days, the number of iron hillocks formed on the surface increases (Fig. 4.11), while the rest surface is almost entirely covered in iron oxide. This is also consistent with the XRD analysis (Fig. 4.5). EDS analysis showed that the amount of chromium oxide decreases in the contact zone (Fig. 4.11c). In addition, a crack passes through the imprint, which also propagates up to a distance of 100 µm around the contact zone. An increased amount of chromium is observed along the crack line (Fig. 4.11c), which indicates that under the layer of iron oxide there could be a layer enriched in chromium. It should be noted that this is not the only crack on the surface, since, as will be discussed below, a number of imprints have cracks.

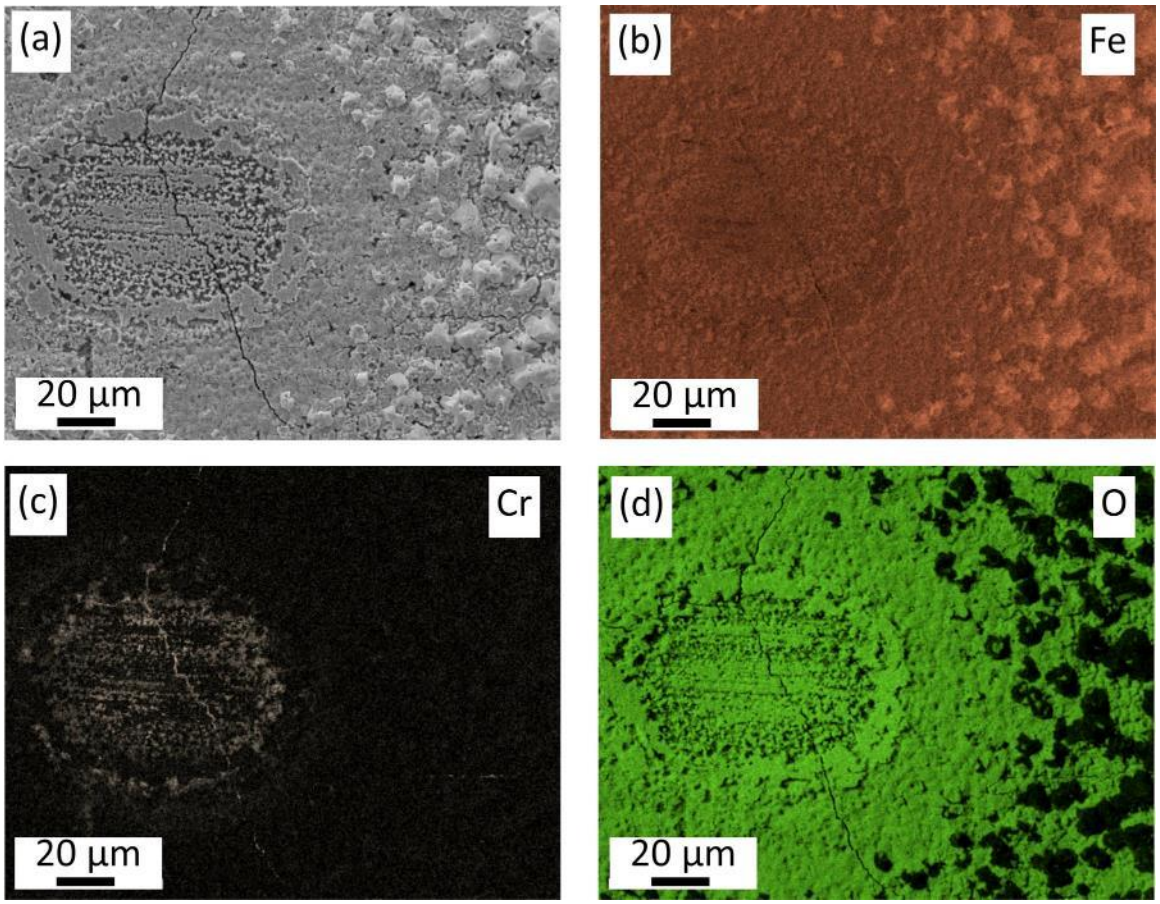

Fig. 4.11. (a) Microstructure and (b-d) corresponding elemental EDS maps of a surface of EUROFER97 sample exposed to the ceramic breeder environment for 16 days: (b) iron, (c) chromium, (d) oxygen

After exposure for 32 days, only single areas formed by chromium-rich oxide are observed on the surface. Chromium-rich oxide is no longer observed in the center of the imprint, apparently due to its coating with iron oxide. Approximately half of the observation surface is covered by iron oxide near the contact zone, and the other half is covered by merged hillocks of pure iron. There is a tendency of reduction of the amount of iron oxide on the surface, which is also confirmed by XRD analysis (Fig. 4.6).

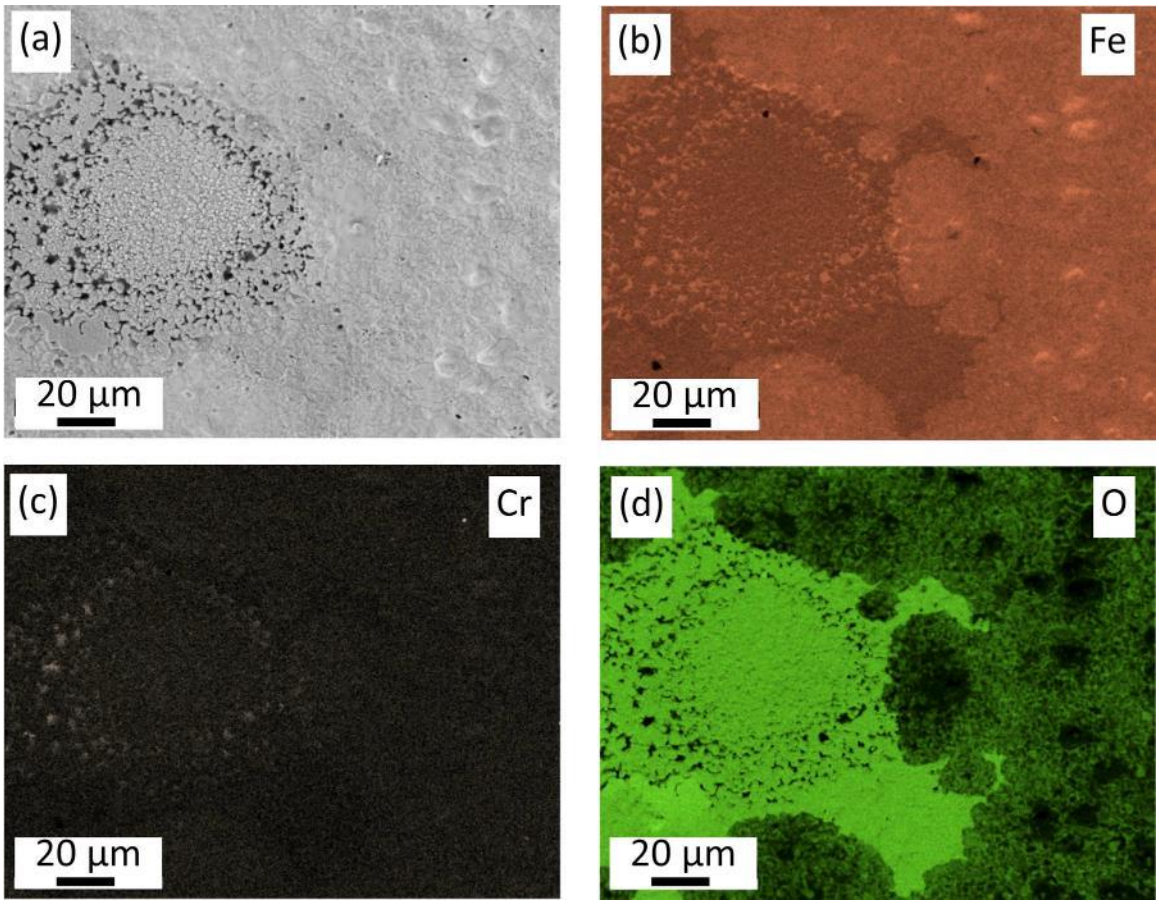

Fig. 4.12. (a) Microstructure and (b-d) corresponding elemental EDS maps of a surface of EUROFER97 sample exposed to the ceramic breeder environment for 32 days: (b) iron, (c) chromium, (d) oxygen

Fig. 4.13 shows the microstructure of EUROFER97 after exposure for 64 days. Almost the entire surface is covered with pure iron by merging individual hillocks into a single surface. At the same time, discontinuities and pores are observed at the junctions of the hillocks (black dots in Fig. 4.13a). Note that the XRD pattern (Fig. 4.7) is also dominated by peaks from pure iron. Accordingly, as already reported in other works, the reduction of iron oxide by hydrogen strongly increases with increasing interaction duration [5,7]. On the EDS map, chromium is not observed in the contact zone. Iron oxide is preserved only in the contact zones of EUROFER97 with lithium-ceramics pebbles.

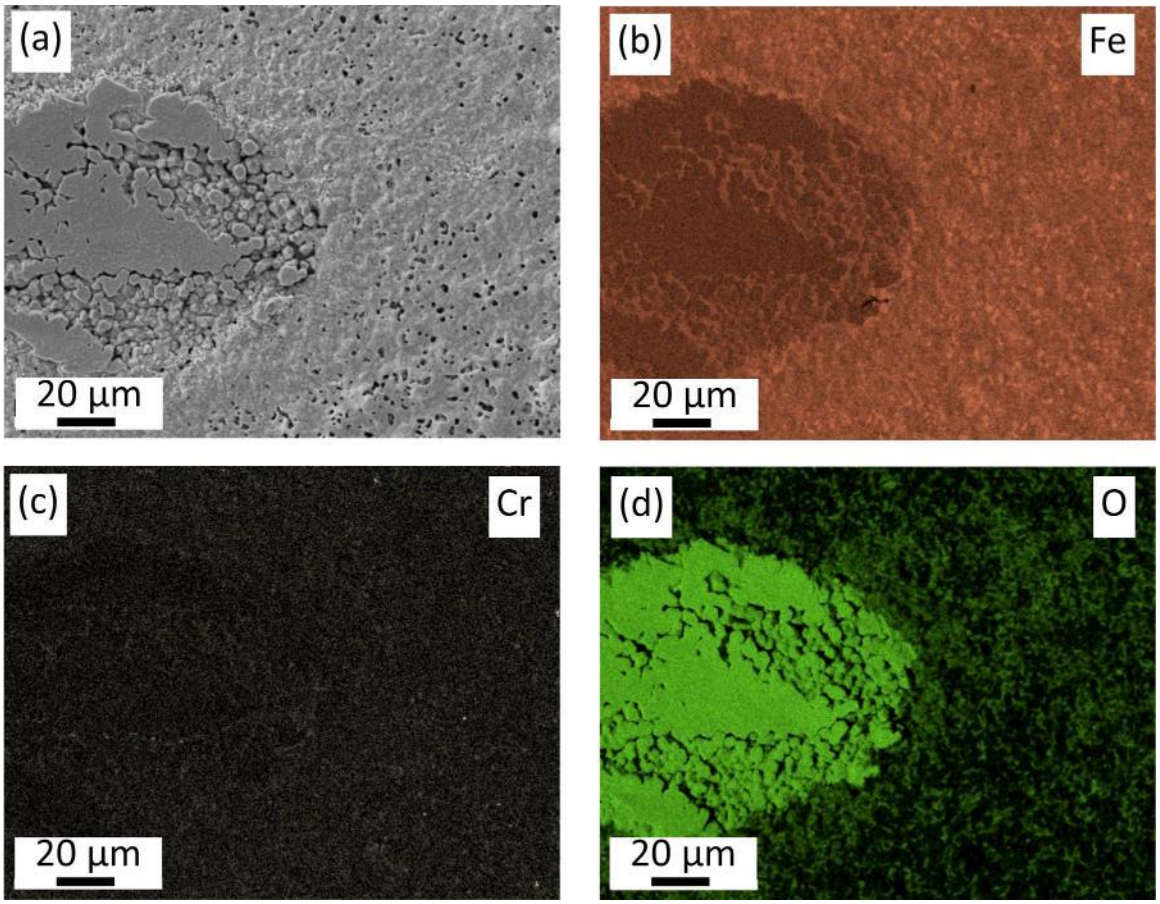

Fig. 4.13. (a) Microstructure and (b-d) corresponding elemental EDS maps of a surface of EUROFER97 sample exposed to the ceramic breeder environment for 64 days: (b) iron, (c) chromium, (d) oxygen

After exposure for 128 days, the microstructure changed insignificantly (Fig. 4.14). Almost the entire surface is covered with pure iron. Chromium oxide is practically not observed. Only in a few places of discontinuities of pure iron is an underlying layer with a high content of chromium found. EDS maps show the maximum oxygen content in the center of the contact zone, as well as in some areas of iron hillocks (Fig. 4.14d). X-ray diffraction studies indicate the presence of lithium-containing oxide Fe_3O_4. Unfortunately, the EDS cannot detect lithium, because the resulting characteristic X-rays are absorbed by the material itself. Auger spectroscopy also did not allow reliable detection of lithium, since peaks from lithium and iron overlap.

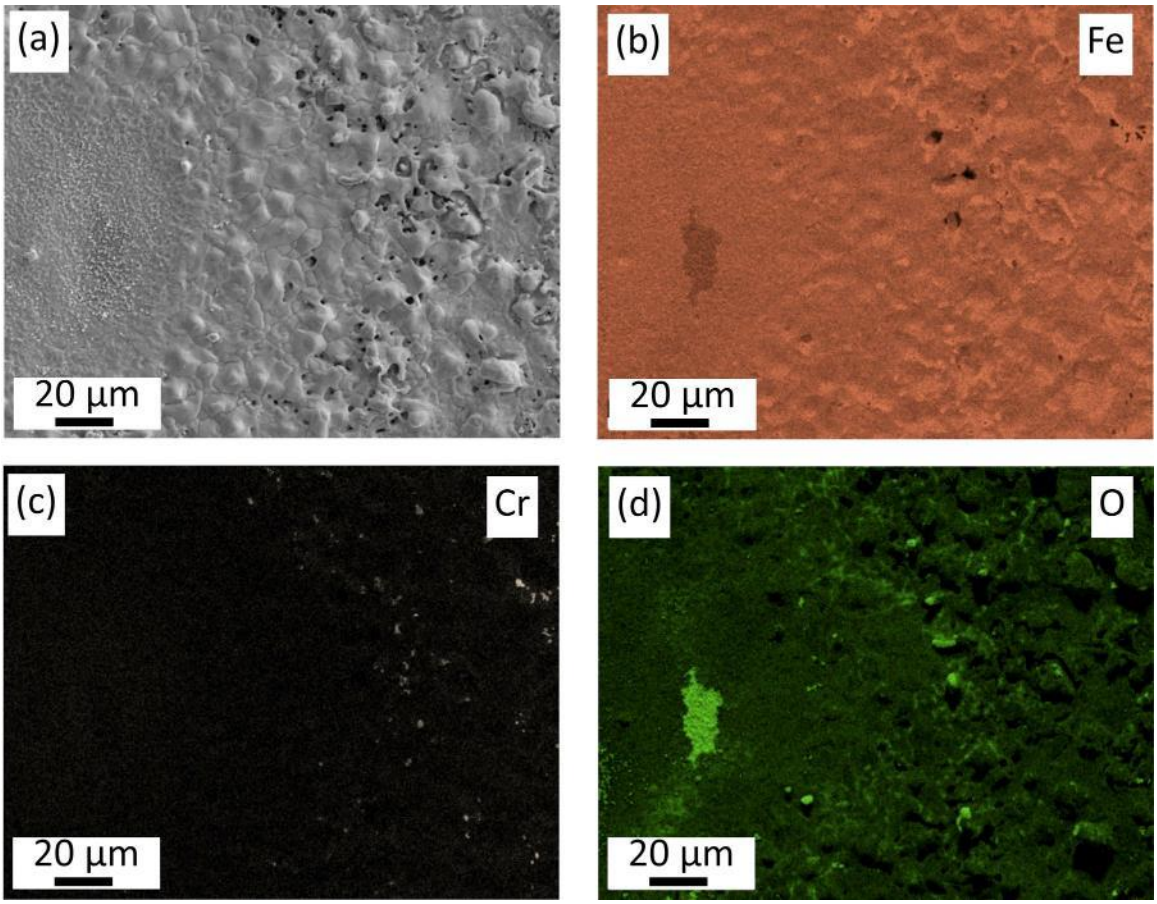

Fig. 4.14. (a) Microstructure and (b-d) corresponding elemental EDS maps of a surface of EUROFER97 sample exposed to the ceramic breeder environment for 128 days: (b) iron, (c) chromium, (d) oxygen

Fig. 4.15 shows the evolution of the surface microstructure of a EUROFER97 sample depending on the exposure time in contact with lithium-ceramics pebbles in a purge gas atmosphere [43]. The bottom row in the Fig. 4.15 shows the generalized results of the EDS, in which the phase with a high oxygen content (iron and chromium-rich oxides) is colored green, and the phase with a high iron content and low oxygen (pure iron) is colored orange. In general, as the exposure time increases, the amount of the oxide phase decreases and the amount of the ferrite phase increases. Overall, the XRD and EDS results are consistent in detecting that the amount of oxides on the surface decreases with increasing exposure duration for more than 16 days. At the same time, the peaks of chromium-rich oxide were not detected on XRD patterns, apparently due to their small volume fraction on the surface, and Li-containing iron oxide cannot be distinguished by EDS.

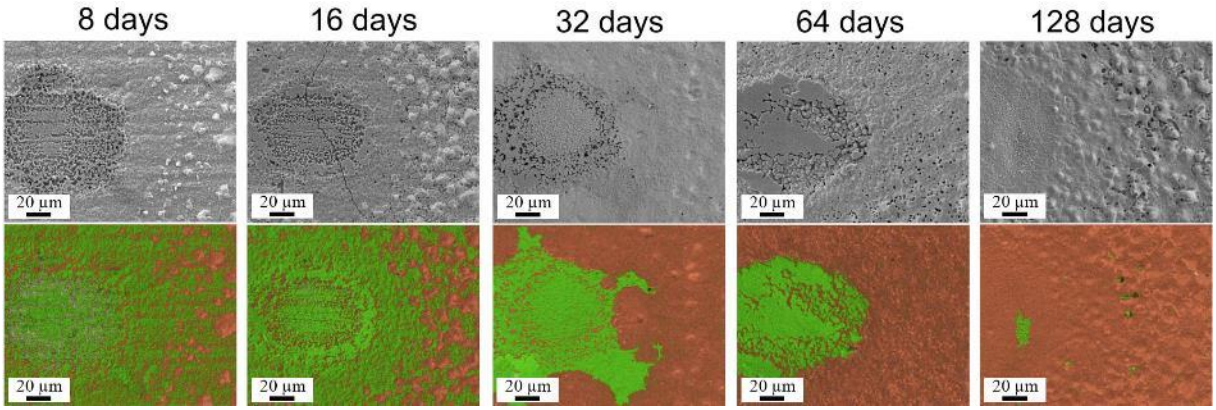

Fig. 4.15. Results of surface analyses of EUROFER97 samples after exposure to the ceramic breeder environment for different durations [43]. SEM micrographs are presented in the top row and corresponding EDS maps are in the bottom row. On the EDS maps, oxides are highlighted in green and ferrite is highlighted in brown.

One of the samples for LCF tests, exposed for 32 days, had an area far from the gage part, where the corrosion layer was chipped. Fig. 4.16 shows the microstructure and corresponding EDS maps of such a spallation zone. The imprint due to contact with lithium-ceramics pebbles is located at the top right. Due to partial spallation of the surface, internal corrosion layers were exposed. The red letters in the SEM photograph show the different structural elements on the EUROFER97 surface.

The letter A in Fig. 4.16a denotes the pure iron hillocks at some distance from the imprint. Fig. 4.17a shows the area containing the hillocks at higher magnification. Hillocks are usually 5–20 µm in diameter. A characteristic feature of hillocks is a smooth surface with marks of crystal growth planes. Note, that pure iron does not contain chromium, which once again testifies that ferrite phase on the surface is not EUROFER97 ferrite (Fig. 4.16c).

The letter B in Fig. 4.16a corresponds to iron oxide in the area close to the imprint, as also shown in Fig. 4.12. Iron oxide consists of crystals about 1–3 µm in size (Fig. 4.17b). The surface of the crystals is strongly faceted. The crystals themselves are often shaped as a rhombohedral dodecahedron.

The letter C in Fig. 4.16a corresponds to chromium-rich oxide, located directly under the layer of iron / iron oxide. The microstructure of chromium-rich oxide is not revealed by SEM, since the size of the structural components is apparently very small and reaches a maximum of up to 500 nm. (Fig. 4.17c). On the EDS map (Fig. 4.16c), this layer contains a large amount of chromium, but due to the surface relief (shading), the EDS could not detect oxygen just below the chromium-rich oxide layer, and therefore overestimated the content of chromium and iron accordingly.

The inner layer D in Fig. 4.16a consists mainly of iron and chromium, but also contains an increased amount of oxygen (Fig. 4.16d). The surface microstructure of this layer is tempered martensite (Fig. 4.17d) usual for EUROFER97 with well-defined boundaries containing oxides (to be shown below in cross section).

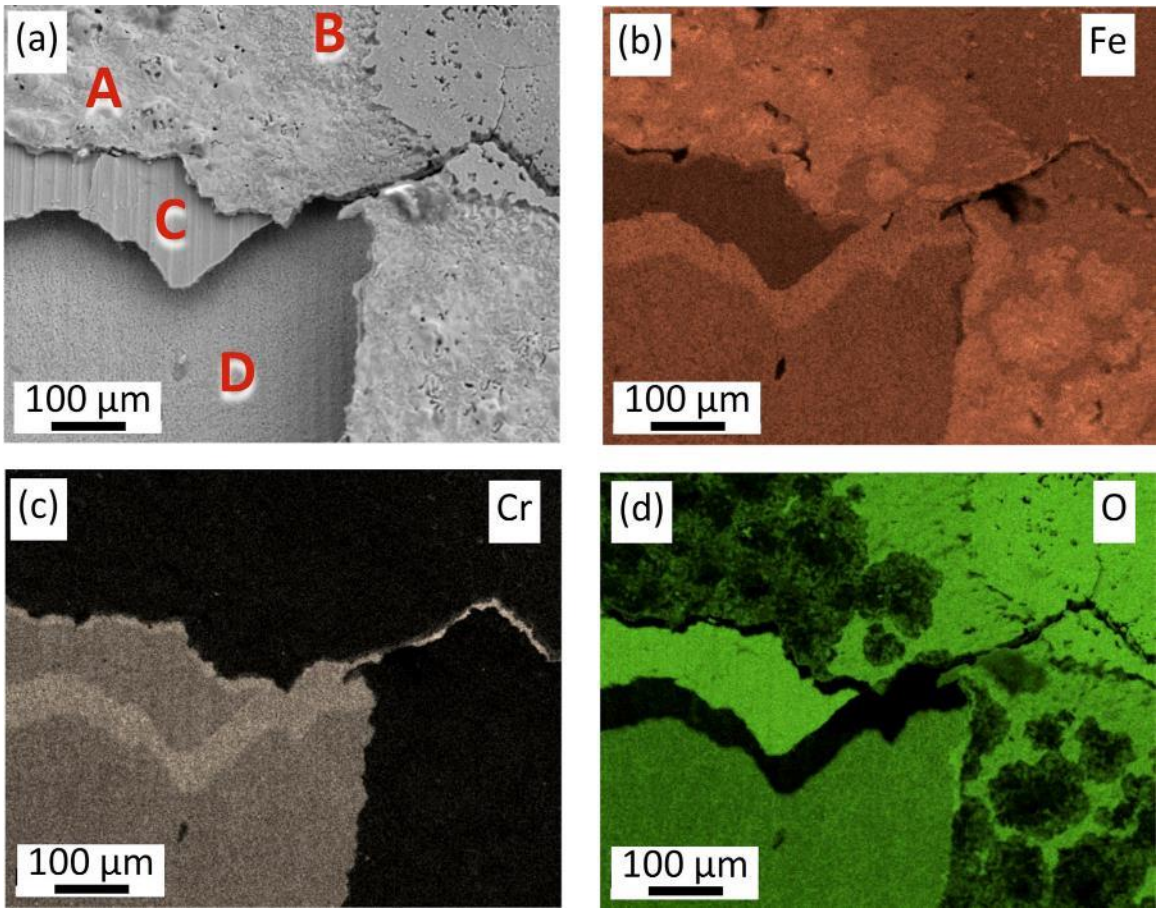

Fig. 4.16. (a) Microstructure and (b-d) corresponding elemental EDS maps revealing corrosion layers of EUROFER97 sample exposed to the ceramic breeder environment for 32 days: (b) iron, (c) chromium, (d) oxygen. Letters A-D designate 4 characteristic structural components of the surface.

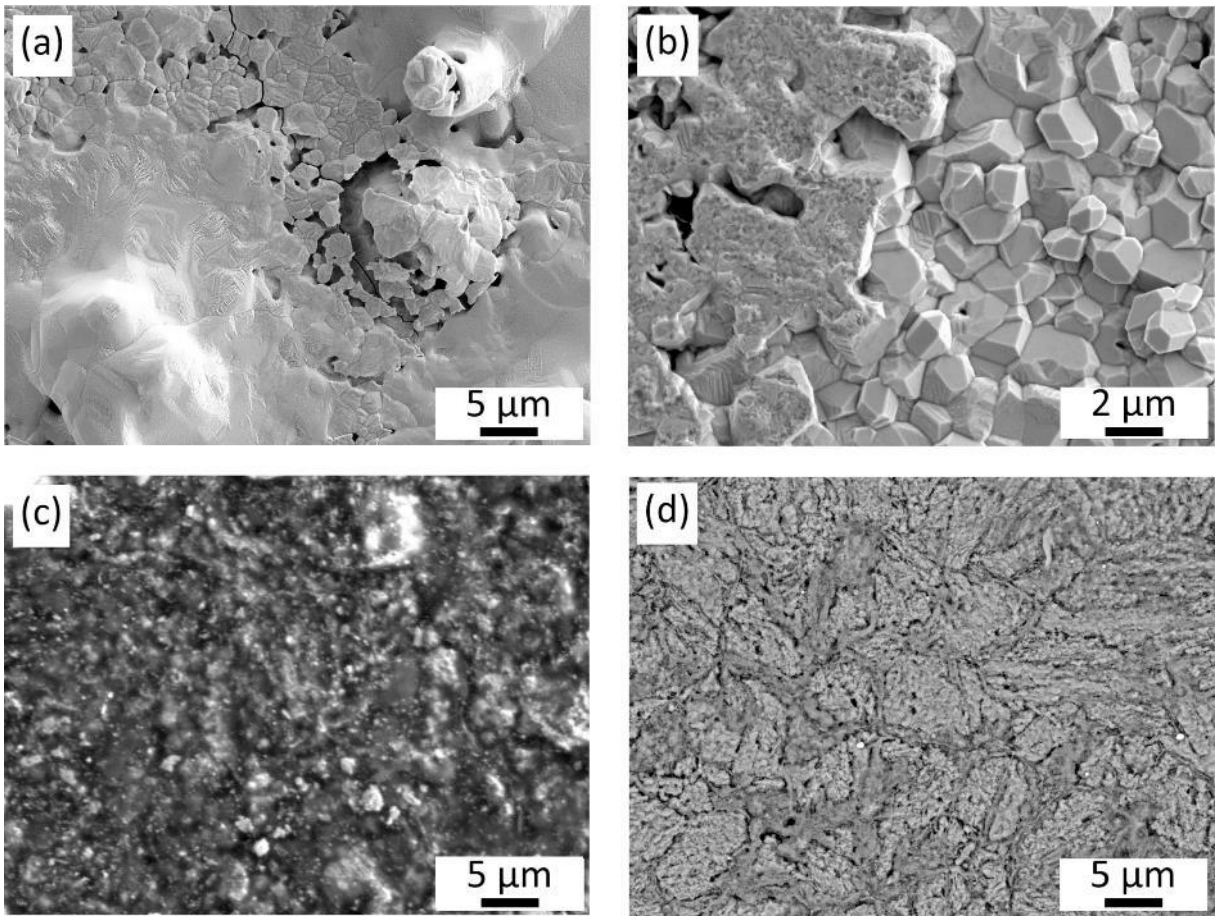

Fig. 4.17. Characteristic surface structural constituents A-D from Fig. 4.16:(a) pure iron hillocks, (b) iron oxide, (c) chromium-rich oxide, and (d) EUROFER97 adjacent to the corrosion layer.

4.1.2 Cross section of corrosion layer

Specially prepared cubic witness samples were studied to analyze the cross-section of the EUROFER97 specimens, exposed to the same conditions as the LCF specimens. The surface of one of these cubic samples, which was exposed to lithium-ceramics pebbles in a purge gas atmosphere for 32 days, is shown in Fig. 4.18. The surface structure observed is similar to that of the LCF specimens shown in Fig. 4.2. The surface is characterized by imprints, which are traces of contact with lithium-ceramics pebbles. Some lithium-ceramics pebbles were found adhering to the surface of the sample (Fig. 4.18a-c). These pebbles cover the surface of the samples fairly evenly, resulting in the distance between the imprints being the average size of the pebbles. The pebbles themselves have defects such as pores, discontinuities, and cracks (Fig. 4.18a-c). Another characteristic feature of the surface structure is the hillocks of ferrite. Some hillocks are formed as whiskers extending from the surface of the EUROFER97 specimen towards the pebble (Fig. 4.18c). Some of these whiskers were broken, revealing their internal microstructure (Fig. 4.18d). It was found that some whiskers can be formed only by ferrite, while others are covered with ferrite on the outside and contain iron oxide with characteristic crystals with a faceted surface on the inside. Discontinuities and porosity are also observed in the surface in the region of ferritic hillocks (Fig. 4.18d).

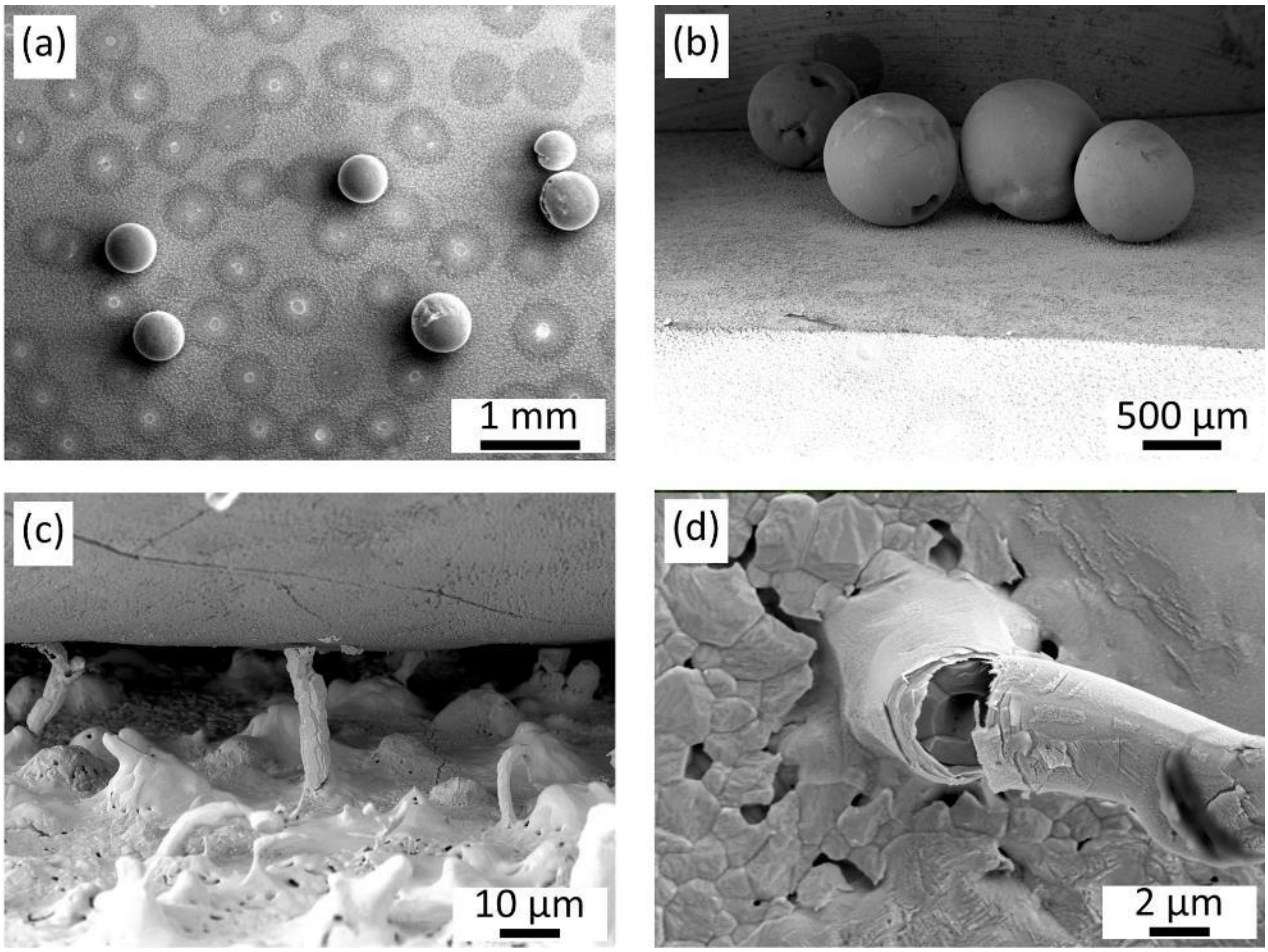

Fig. 4.18. Microstructure of the surface of a cubic witness sample exposed to the ceramic breeder environment for 32 days: (a) imprints together with adherent pebbles [46], (b) adherent pebbles at an angle of view of 45°, (c) growth of hillocks and whiskers near the pebbles, (d) internal structure of one of the whiskers [46]

After exposure to the ceramic breeder environment, the samples were cut in half and embedded in an electroconductive resin to avoid spallation and loss of the corrosion layer. Fig. 4.19 shows the microstructure of the cross section depending the exposure duration in contact with lithium-ceramics pebbles in a purge gas atmosphere. Already after two days of exposure, a corrosion layer of up to 2 µm in thickness was formed (Fig. 4.19a). The thickness of the corrosion layer varies from site to site. The entire thickness of the corrosion layer was taken into account as will be shown below. The minimum thickness of the corrosion layer after exposure for 2 days was measured to be 0.5 µm, and the average thickness after about 30 measurements was 1.4 µm. With increasing the exposure time, the thickness of the corrosion layer increases sharply with maximum thickness up to 12.5 µm after exposure for 8 days, up to 14 µm after exposure for 16 days, and 16.5 µm after exposure for 32 days (Fig. 4.19c,d,e). With an increase in the exposure time from 32 to 128 days, the maximum thickness of the corrosion layer does not change significantly and is about 18–19 µm (Fig. 4.19e,f,g). It should be noted once again that the thickness of the corrosion layer varies within the range of up to ±2.5 µm, especially in the case of protruding hillocks in the cross section. Therefore, for example, the total thickness of the corrosion layer after exposure for 64 days was measured to be about 13–18 µm.

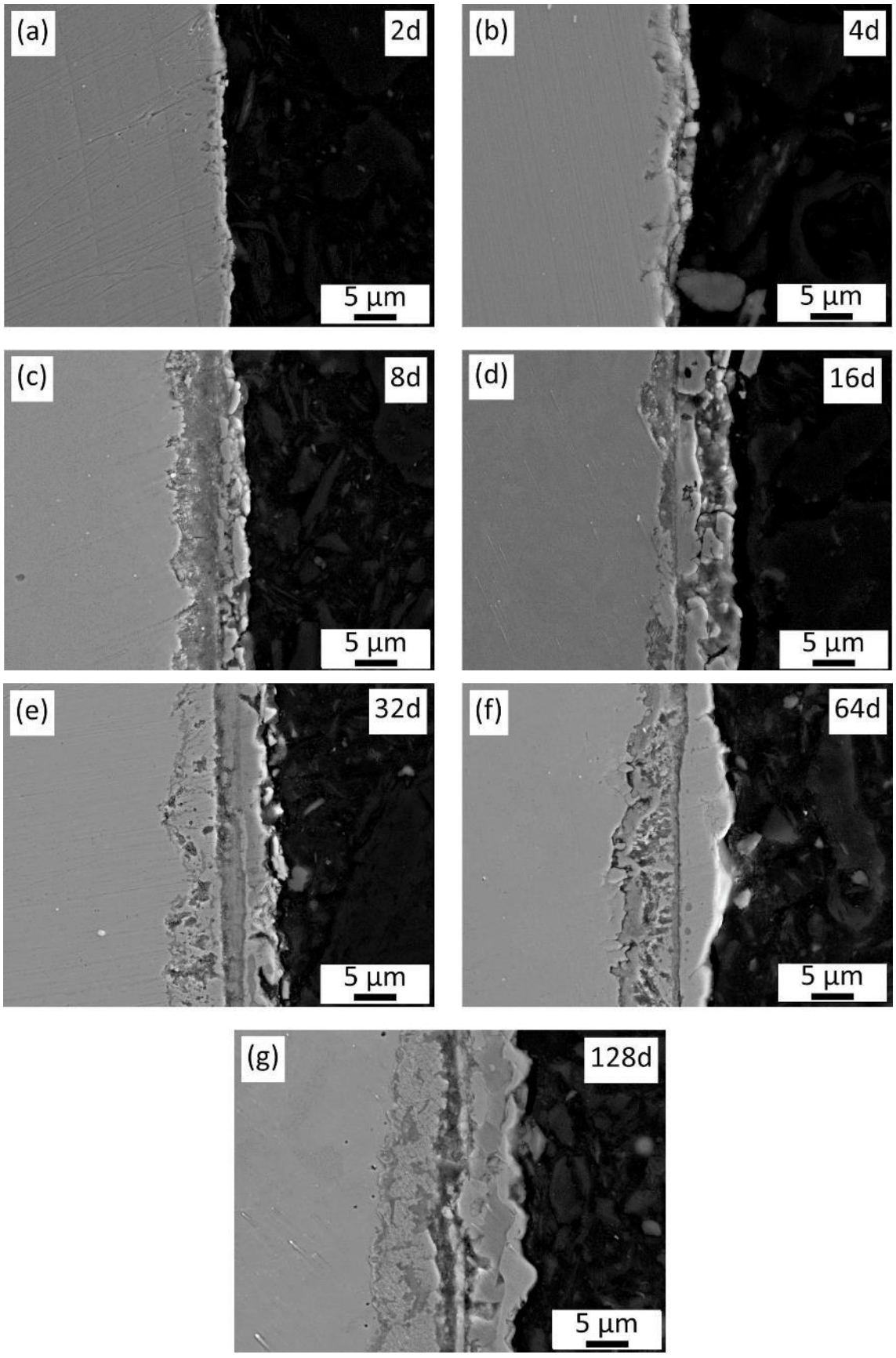

Fig. 4.19. Cross section of EUROFER97 samples after exposure to the ceramic breeder environment: (a) 2 days, (b) 4 days, (c) 8 days, (d) 16 days, (e) 32 days, (f) 64 days, (g) 128 days

Fig. 4.20 presents the total thickness of corrosion layer of EUROFER97 versus exposure duration in the ceramic breeder environment. The diagram clearly shows that the thickness of the corrosion layer grows especially rapidly up to an exposure duration of about 16 days, and after more than 64 days it reaches saturation with an average value of 16.5–17 µm. It should be noted that the resulting dependence is not typical for steel corrosion, in which the corrosion layer always continues to grow [47]. Therefore, a description of the resulting corrosion curve cannot be represented by the commonly used for the description of corrosion Pourbaix equation:

$$c(t) = A \cdot t^B + C \quad (1)$$

where $c(t)$ is corrosion thickness or mass per unit area, A, B, and C are empirical constants, t is corrosion duration [47].

This equation is usually valid for systems that are controlled by only one process of diffusion of oxygen. In the case of corrosion of EUROFER97 samples in contact with lithium-ceramics pebbles in a purge gas atmosphere, in addition to the oxidation process, the reduction of iron oxide by hydrogen occurs simultaneously. Therefore, fitting the curve according to the Pourbaix equation (1) does not lead to a satisfactory result (Fig. 4.21). The competing processes of oxidation and reduction seem to level off at about 64 days, which leads to the saturation of the curve. The resulting diagram can be described rather by the following exponential law:

$$c(t) = A \cdot e^{\wedge}(B \cdot t) + C \quad (2)$$

where $c(t)$ is corrosion thickness or mass per unit area, A, B, and C are empirical constants, t is corrosion duration. This is a modified expression from [47] for an exponential decay without a linear relationship part.

As a result of fitting the curve according to dependence (2), the following values of the coefficients were obtained for (2):

$$c(t) = -9.84 \cdot e^{\wedge}(-5.59 \cdot 10^{-7}\, t) + 16.76 \quad (3)$$

where c(t) is thickness in µm, t is corrosion duration in s. The resulting exponential dependence (3) also saturates (somewhat earlier than for the measured curve) reaching a value of about 16.8 µm with an increase in the exposure time of more than 64 days. It should be noted that similar corrosion behavior can be observed, for example, for aluminum alloys at low temperature, in which the alumina layer practically prevents further corrosion [47].

As shown in the literature review in [14], a similar dependence of the corrosion layer thickness on the corrosion time was plotted. In this case, despite the obvious slowing down of corrosion, as in this work, the authors fitted the curve according to the Pourbaix equation (Fig. 2.1). On the contrary, if the exposure atmosphere did not contain hydrogen, then corrosion reached 40 µm after 38 days of exposure to Li-ceramics pellets in argon [15]. In reference [19], the study demonstrated that after 42 days of exposure, the thickness of the corrosion layer under purge gas atmosphere was approximately 12 µm, whereas in the absence of hydrogen and only in helium environment, the thickness measured around 50 µm. This once

again proves that it is the presence of hydrogen that leads to the cessation of rapid corrosion after reaching a certain thickness of layer.

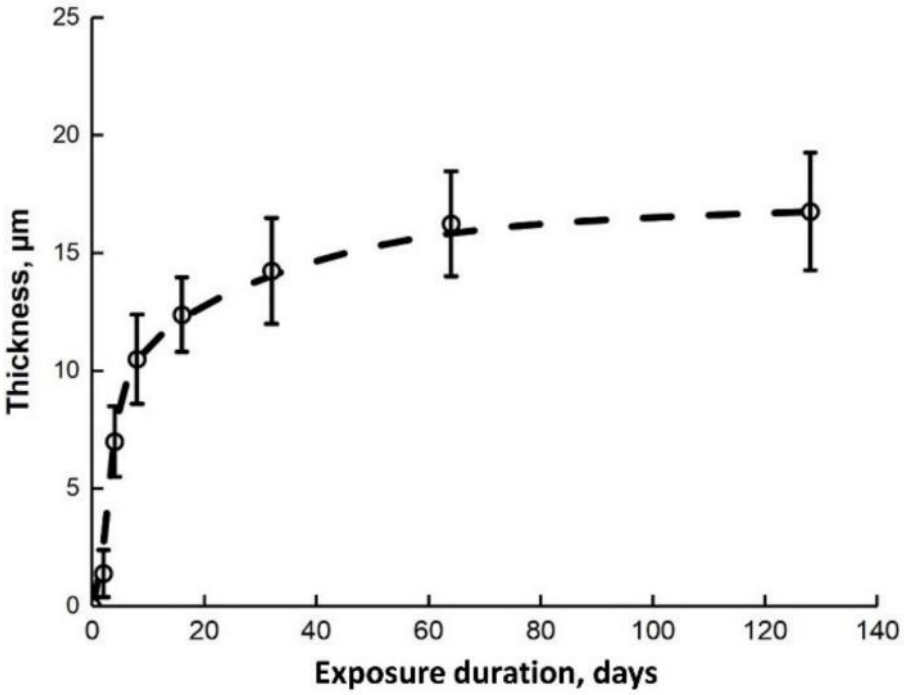

Fig. 4.20. The total corrosion thickness of EUROFER97 depending on the duration of exposure to the ceramic breeder environment [43]

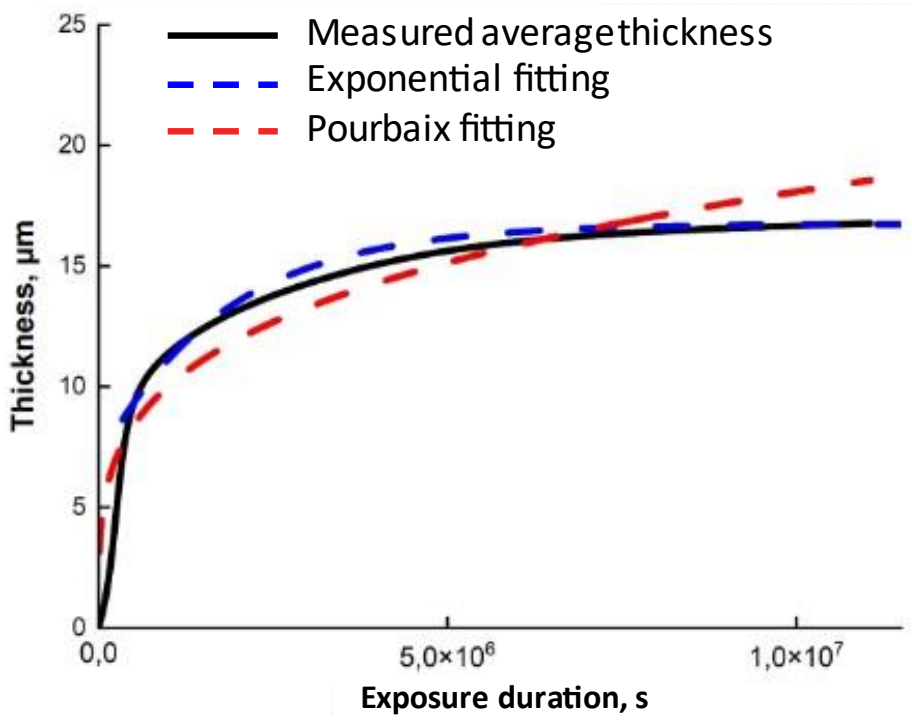

Fig. 4.21. Fitting according to the exponential law and according to the Pourbaix equation of the function of the measured average thickness of the corrosion layer on the exposure duration to the ceramic breeder environment

By following the approach of Mukai et al. [16], an investigation was conducted to assess the diffusion rate of oxygen atoms. A plot was generated to illustrate the relationship between the squared thickness of the corrosion layer and the duration of exposure (Fig. 4.22). The plot exhibited a decreasing slope after 16 days of exposure, indicating possible inhibiting processes like the reduction of iron with hydrogen that impede further oxidation. Consequently, fitting was performed considering the period of 2–16 days when the sample surface was not yet covered with ferrite. Utilizing the plot, the oxygen diffusion coefficient (D_a) was determined as $D_a=c^2/t$, where c represents the thickness of the corrosion layer and t denotes the duration of exposure. The fitting process yielded a diffusion coefficient of $D_a=1.2\times10^{-12}$ cm^2/s. Notably, this value was approximately 2.8 times larger than the value reported in the referenced work [16], potentially due to measurement errors and variations in corrosion conditions.

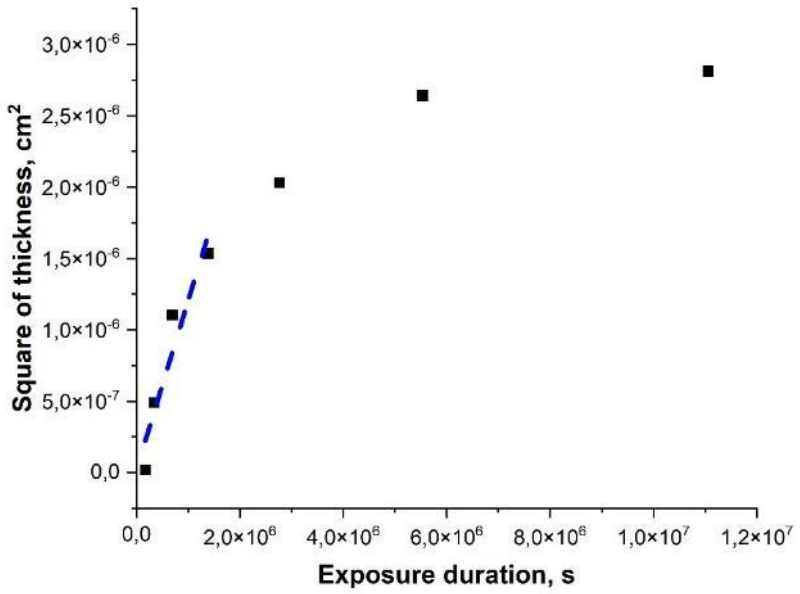

Fig. 4.22. Square of oxidized layer thickness on the surfaces of the EUROFER97 samples as a function of exposure duration. The blue dotted line represents the result of fitting for the first four points (2–16 days).

The microstructure of the cross section can be presented in more detail on the example of a sample exposed for 64 days to lithium-ceramics pebbles in a purge gas atmosphere. A cross-sectional SEM micrograph and elemental EDS mappings are shown in Fig. 4.23. Three different corrosion layers can be distinguished. The outer corrosion layer with a higher Fe content (A in Fig. 4.23a and Fig. 4.24) consists of two phases. The bright phase in the SEM micrograph (Fig. 4.23a) was identified as pure iron and the gray phase as Fe-rich oxide. The thickness of this outer corrosion layer is about 5–7 µm for 64 days of exposure. Pure iron has pores and voids and Fe-rich oxide is often cracked (Fig. 4.24). Note that iron oxide was also found inside the pure iron hillocks on the surface (Fig. 4.18d). Pores and voids can form due to the difference in density between iron oxide and ferrite. When reducing ferrite with hydrogen from iron oxide, the denser ferrite occupies a smaller volume than the less dense iron oxide, forming pores in the residual volume.

The intermediate layer with a higher Cr content (B in Fig. 4.23a and Fig. 4.24) consists of Cr-rich oxides. This is consistent with the study of the chipped corrosion layer in Fig. 4.16. The structure of chromium oxide in cross section is also not resolved in the SEM microscope. Chromium-rich oxide often cracks and also falls out the outer layer with iron oxide or ferrite (Fig. 4.19g, Fig. 4.23a, Fig. 4.24). This phenomenon will be discussed in more detail in Section 4.3.2. Note that this layer also contains some iron. In works [14,48], this layer is denoted by Fe-Cr spinel. The thickness of intermediate corrosion layer is about 1–2.5 μm for 64 days of exposure.

The inner corrosion layer (C in Fig. 4.23a and Fig. 4.24) is adjacent to the EUROFER97 and contains Cr-rich oxides, formed at the laths boundaries of EUROFER97. The formation of oxides mainly along the boundaries in EUROFER97 can be associated with accelerated grain boundary diffusion, forming diffusion channels of both chromium and oxygen. The morphology of these particles is apparently acicular or elongated, since in cross section, the particles look like short and elongated particles. The particles reach 10–15 μm in length and about 500 nm in cross section. The thickness of inner corrosion layer is about 7–10 μm for 64 days of exposure. A similar structure of the inner corrosion layer was observed in works [14,16,48]. Note that in the EUROFER97 layer adjacent to the internal corrosion layer there is a zone depleted of chromium-rich carbides ($M_{23}C_6$) common for EUROFER97, which can be seen on the left in Fig. 4.23c.

Cross-sectional microstructural studies show the complexity of the corrosion layer formed during exposure to the ceramic breeder environment of EUROFER97. The results are consistent with other works performed on EUROFER97 [16,18], F82H [45], and other RAFM steels [15]. Detailed corrosion studies of chrome-containing steel with gold markers left on the surface show that the corrosion layer with chromium oxide grows inward from the gold markers, and iron oxide grows towards outside of the former surface of the steel [49]. Thus, iron atoms diffuse through the chromium oxide layer to the surface where they form iron oxide.

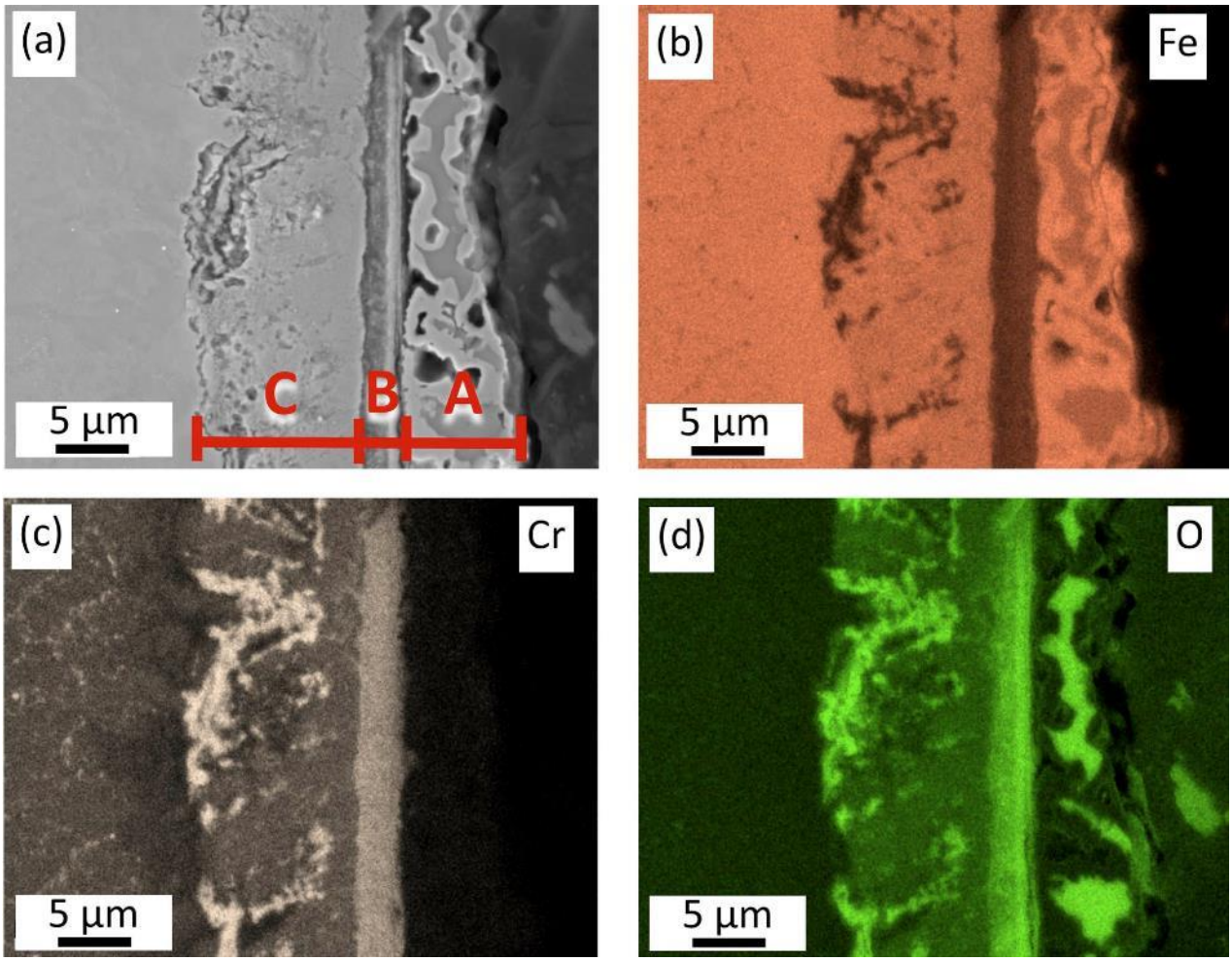

Fig. 4.23. (a) Microstructure and (b-d) corresponding elemental EDS maps of a cross section of EUROFER97 sample exposed to the ceramic breeder environment for 64 days: (b) iron, (c) chromium, (d) oxygen. In (a), three different corrosion layers can be distinguished: outer A with a higher Fe content, intermediate B with higher Cr content, and inner C adjacent to EUROFER97.

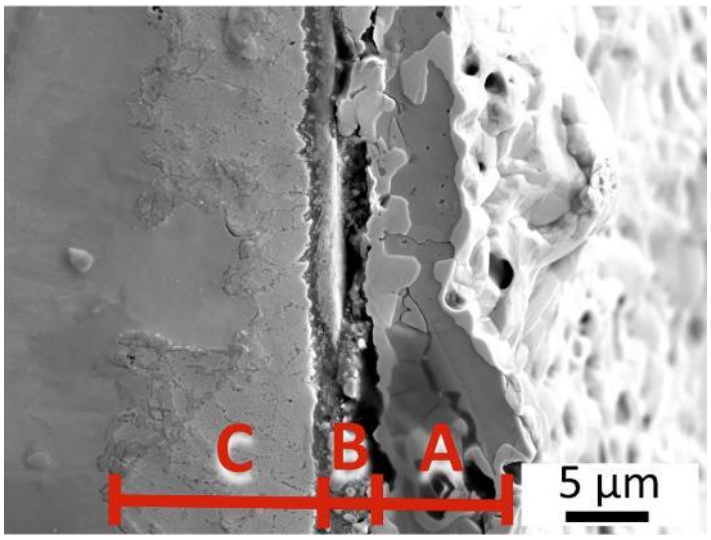

Fig. 4.24. SEM microstructure of a cross section of EUROFER97 sample exposed to the ceramic breeder environment for 64 days. Three different corrosion layers are denoted as in Fig. 4.23.

Based on the microstructural studies of the surface and cross section of the corrosion layer of EUROFER97 samples, the following sequence of the corrosion process can be assumed. First up to an exposure time of approximately 8 days (Fig. 4.24b), a chromium-rich oxide layer is formed, since chromium has a greater affinity for oxygen than iron [14]. The oxide layer is formed in the form of a relatively thin (up to about 1 μm) film on the surface. Apparently, a certain amount of oxygen penetrates through this oxide layer deeper into EUROFER97 along the grain and martensite laths boundaries, where diffusion occurs faster. In these places along the boundaries, oxygen meets chromium atoms and forms chromium-enriched oxides to a depth of about 5 μm (internal oxidation zone). At the same time, iron atoms diffuse outwards through the intermediate chromium-enriched layer to the surface of the sample, where they meet oxygen atoms and form an iron oxide layer. Islands of pure iron are formed on the iron oxide layer due to the reduction of iron oxide by hydrogen from the purge gas atmosphere. According to [50,51], hydrogen is adsorbed to the surface and react with oxygen from the iron oxide, forming water, which leads to the depletion of iron oxide in oxygen and the nucleation of pure iron grains. It is known that the rate of hydrogen adsorption on pure iron is much higher than on iron oxide [50]. Therefore, pure iron grows first in the form of hillocks, and not uniformly over the entire surface of the iron oxide. A similar morphology of elongated particles of pure iron was observed in [50].

Further for the exposure times ≈16–32 days, the pure iron hillocks continue to grow in width at the surface due to the reduction of iron oxide at the pure iron/iron oxide interface (Fig. 4.25c). This is due to the fact that the hydrogen adsorbed on pure iron interacts with oxygen on the surface of the iron oxide, and the formed water can be removed by desorption from the surface. The process is accompanied by pore formation to accommodate shrinkage of the volume (the volume of iron is about 40–50% less than the volume of iron oxide [50,51]).

Eventually, the entire surface is gradually covered with pure iron (Fig. 4.25d), which begins to grow deeper into the iron oxide. Inside the layer of pure iron, iron oxide can be found in the form of islands. In this case, the outward diffusion of oxygen atoms from iron oxide through the pure iron layer becomes the main limiting factor in the growth of the pure iron layer. Apparently, the kinetics of corrosion due to the influx of oxygen from the lithium-ceramics pebbles or the purge gas atmosphere and the kinetics of the iron oxide reduction due to the adsorption of hydrogen and the diffusion of oxygen atoms are equalized, which leads to the stage of saturation of the growth of the corrosion layer.

Another plausible explanation for passivation could be attributed to the potential evolution of the chromium-rich intermediate corrosion layer with prolonged exposure to the ceramic breeder environment. As exposure time increases, the diffusion of chromium atoms from EUROFER97 into this layer continues, gradually replacing iron atoms. Consequently, a corrosion layer enriched with chromium is formed, resulting in enhanced corrosion resistance. However, in-depth investigations exploring this aspect would necessitate labor-intensive studies extensively employing FIB and TEM, and these sophisticated analyses were beyond the scope of the study's goals and objectives.

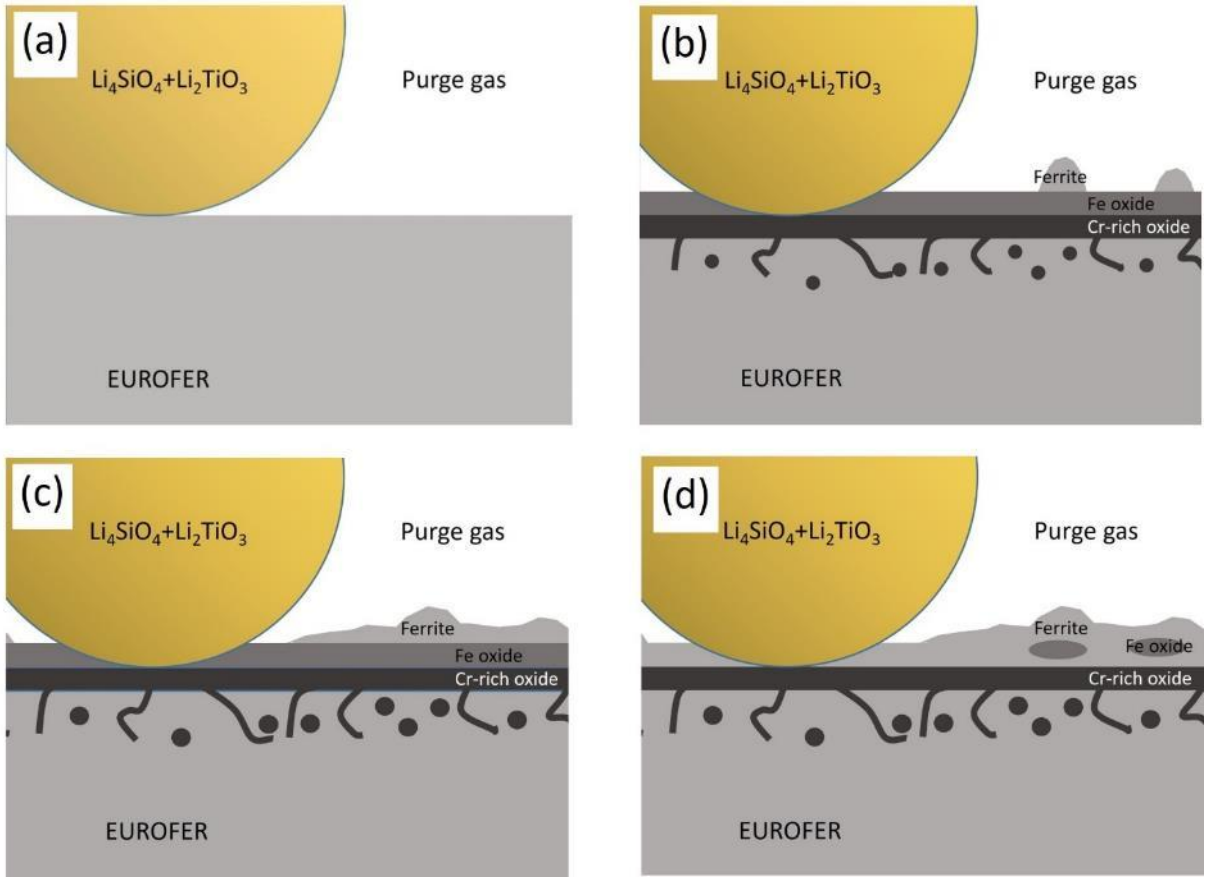

Fig. 4.25. Sketch of the sequence of processes occurring during exposure of EUROFER97 samples to the ceramic breeder environment: (a) start of exposure, (b) ≈2–8 days of exposure, (c) ≈8–32 days of exposure, (d) more than ≈64 days of exposure

4.1.3 TEM investigations

Studying the possible diffusion and penetration of lithium proved to be a challenging task. As previously mentioned, the detection of lithium atoms through EDS is not feasible due to the absorption of characteristic X-rays by the material itself, while Auger electron spectroscopy is hindered by peak overlap between lithium and iron. Nevertheless, it is critical to determine whether lithium atoms can diffuse inwards the corrosion layer and EUROFER97. If prolonged exposure to ceramic pebbles at elevated temperatures leads to the deep diffusion of lithium atoms into EUROFER97, these atoms could undergo transmutation during neutron irradiation within the fusion reactor, generating gases that may result in bubbles formation, swelling, and crack initiation. All this would strongly deteriorate the mechanical properties of the steel.

In order to study the possible lithium penetration, several lamellae from the different parts of corrosion layer were prepared by FIB for TEM study. For this purpose, a cross-section of a EUROFER97 sample was used after exposure to the ceramic breeder environment for 64 days. Two of these lamellae were lifted out from the outer corrosion layer parallel to the outer surface (Fig. 4.26a) and across the entire corrosion layer (Fig. 4.26b). The resulting lamellae are shown in Fig. 4.26c,d. In the case of a lamella lifted out from the outer corrosion layer (Fig. 4.26c), pores are found in the center that were not visible on the surface. The other lamella (Fig. 4.26d) has cracks, which were also observed earlier between the corrosion layers.

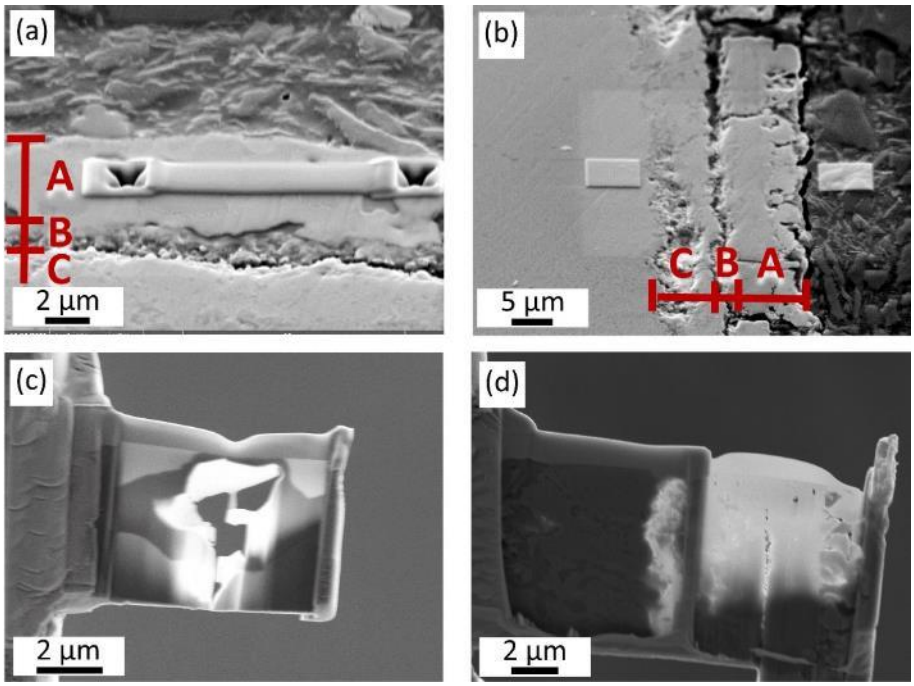

Fig. 4.26. (a, b) areas of EUROFER97 surface used for lifting out the lamellae (c, d): (a, c) outer corrosion layer, (b.d) across the entire corrosion layer. SEM

Fig. 4.27 shows a lamella that was lifted out from the outer corrosion layer (layer A in Fig. 4.24a). Ferrite and $LiFeO_2$ oxide were identified by diffraction analysis [41,43]. In the transparent window of the lamella, only a few crystals in cross section are found, reaching a size of about 6 µm. Pores were found in the ferrite phase. Lithium was not found in the ferrite phase using EELS, apparently due to its insolubility in iron [52]. As shown in [41], the $LiFeO_2$ phase has a rhombohedral structure (ICSD: 51207), which was confirmed by a series of diffraction patterns. At the same time, this phase differs from the lithium-containing phase $(Li+Fe)_3O_4$ detected by the X-ray method after 128 days of exposure (Fig. 4.8). This discrepancy can be explained by different exposure times, different regions used for analysis, X-ray measurement errors, and the locality of TEM. Nevertheless, the main point is that lithium atoms from lithium-ceramics pebbles can be found in the composition of iron oxides in the outer corrosion layer.

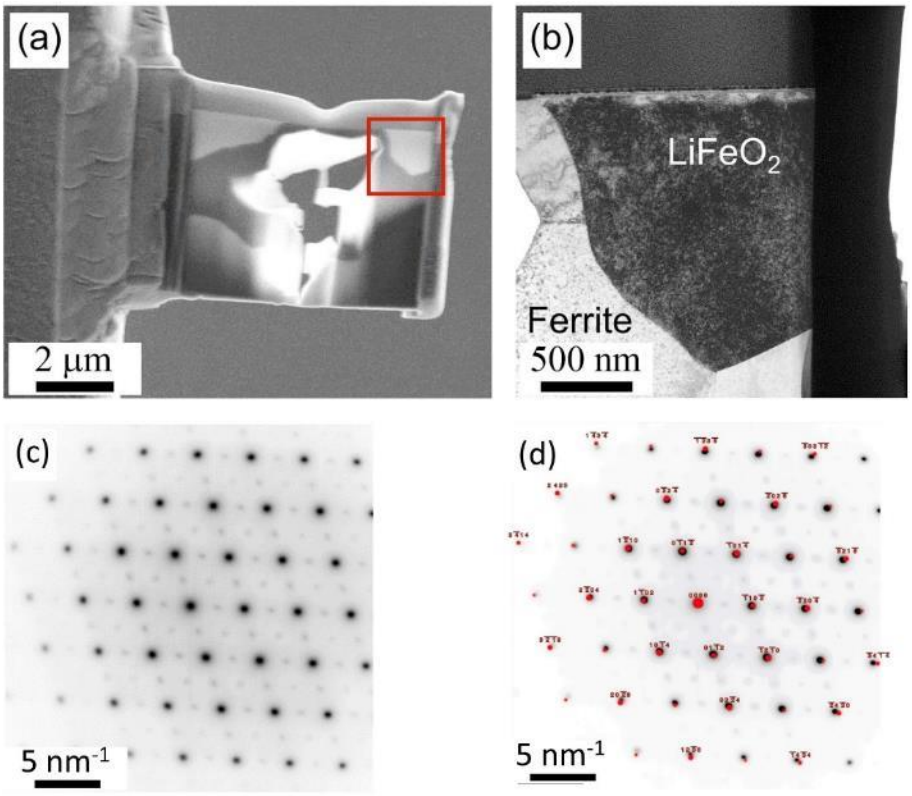

Fig. 4.27. (a) General view of the TEM lamella lifted out from outer corrosion layer of EUROFER97 exposed to the ceramic breeder environment for 64 days [43], (b) TEM image of the area indicated by the red square in (a) [43], (c) selected area diffraction pattern corresponding to $LiFeO_2$ from (b), (d) superposition of reflections from $LiFeO_2$ on (c) [41]

Another lamella was lifted out across the entire corrosion layer (Fig. 4.28a, Fig. 4.26b,d). This lamella represents all three corrosion layers that have been identified in Fig. 4.28a in analogy to Fig. 4.24. As in the first lamella, the outer corrosion layer consists of ferrite and iron oxide crystals up to 2 μm in size. Thanks to TEM, the structure of the intermediate layer, consisting of fine-grained particles, was studied in more details (Fig. 4.28b). This layer consists of fine grains 50–250 nm in size. A crack was found at the boundary between the intermediate and inner corrosion layers, which is also often observed on metallographic cross-sections by SEM. Due to the small grain size in the intermediate layer, the diffraction analysis was made not from one crystal, but from the polycrystalline region (red circle in Fig. 4.28b). The TEM diffraction analysis determined its crystal structure as of $Li_2Fe_{3.2}Cr_{6.8}O_{16}$ type (Fig. 4.28c,d). If the amount of all metals in this compound is summed up and compared with the oxygen content, then the composition can also be represented as $(Li+Fe+Cr)_3O_4$. It turned out that crystal structures of non-lithium containing oxides cannot fully match the diffraction pattern [41]. Thus, the TEM study revealed the diffusion of lithium not only into the outer corrosion layer, but also into the intermediate one of EUROFER97 after exposure to the ceramic breeder environment.

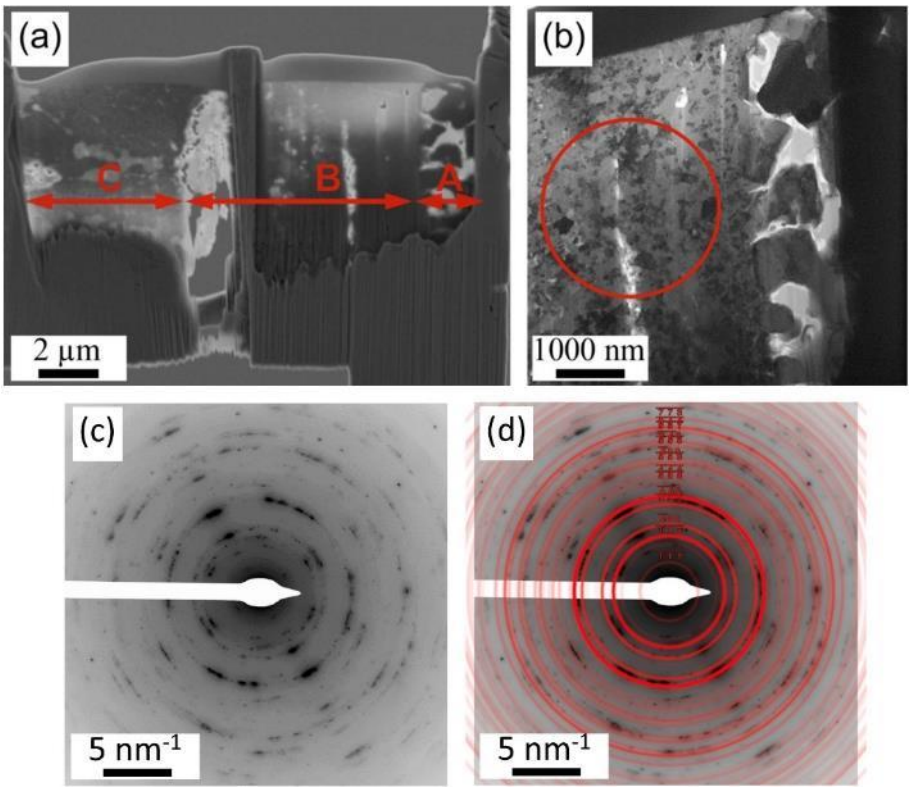

Fig. 4.28. (a) General view of the TEM lamella lifted out across three different corrosion layers (A, B, and C) of EUROFER97 exposed to the ceramic breeder environment for 64 days, (b) TEM image of the right window in (a), (c) selected area diffraction pattern corresponding to $Li_2Fe_{3.2}Cr_{6.8}O_{16}$ from a red circle area on (b), (d) superposition of reflections from $Li_2Fe_{3.2}Cr_{6.8}O_{16}$ on (c) [41]

The inner corrosion layer was studied from the left window of the lamella in Fig. 4.28a. Fig. 4.29 represents the high-angle annular dark-field (HAADF) image of the microstructure and the corresponding EDS maps. The iron distribution map (Fig. 4.29f) shows that the structure consists of a matrix with high iron content (ferrite in EUROFER97) with embedded various particles. In addition to relatively large particles of Cr-containing oxides up to 1500 µm × 500 µm in size, there is a number of small particles 30–200 nm in size, also containing an increased amount of chromium and oxygen (Fig. 4.29c,e). Comprehensive analyzes including selected area electron diffraction (SAED), EDX and high-resolution transmission electron microscopy (HRTEM) in [41] confirmed that the composition of these particles corresponds to $Li_2Fe_{3.2}Cr_{6.8}O_{16}$, while such oxides as Fe_3O_4 and $FeCr_2O_4$ lack some of the necessary reflections. In addition to $Li_2Fe_{3.2}Cr_{6.8}O_{16}$, smaller particles of about 30 nm in size with a high content of vanadium and nitrogen are present in the microstructure (Fig. 4.29b,d). These particles are MX-type precipitates abundant in EUROFER97 [53–55].

Higher resolution TEM analysis showed that some rectangular-shaped oxides have an MX-type carbonitride core (Fig. 4.30). The shell is formed by oxide containing a high amount of chromium and some iron, while the core contains vanadium and nitrogen. This indicates that the nucleation of chromium-iron oxides (apparently of the same composition as the oxides in Fig. 4.29) is facilitated in case of the presence of MX-type precipitates.

The TEM studies showed the presence of lithium atoms in the outer (in $LiFeO_2$ grains), intermediate (in $Li_2Fe_{3.2}Cr_{6.8}O_{16}$ grains) and inner (in separate particles of $Li_2Fe_{3.2}Cr_{6.8}O_{16}$) corrosion layers. Due to the low solubility in iron, lithium, apparently, cannot diffuse in pure iron in the outer corrosion layer and in EUROFER97. Thus, the presence of oxides facilitates the diffusion of lithium atoms inwards the material. As already noted, during the operation of the breeding blanket with a strong neutron flux, lithium atoms will be able to interact with neutrons to form tritium and helium atoms. This will create internal stresses and possibly form bubbles inside these oxide particles in all corrosion layers. In its turn, this can cause partial spallation of the outer and intermediate corrosion layers and further corrosion of EUROFER97. Particularly dangerous can be the formation of gas bubbles in oxides in the inner corrosion layer, which, under cyclic loads, can become an additional factor for facilitated cracking and, consequently, deterioration of fatigue properties. The products of the corrosion reaction after spallation will most likely remain between EUROFER97 and lithium ceramics, which can isolate the resulting corrosion layer from further diffusion of lithium atoms if the pebbles do not slide against the EUROFER97 surface during the heating and cooling cycles of the fusion reactor. Thus, the problem of lithium diffusion into EUROFER97 during prolonged contact with lithium-ceramics pebbles should be addressed to designers, as this may lead to serious deterioration of properties of EUROFER97 steel under the operating conditions of the breeding blanket.

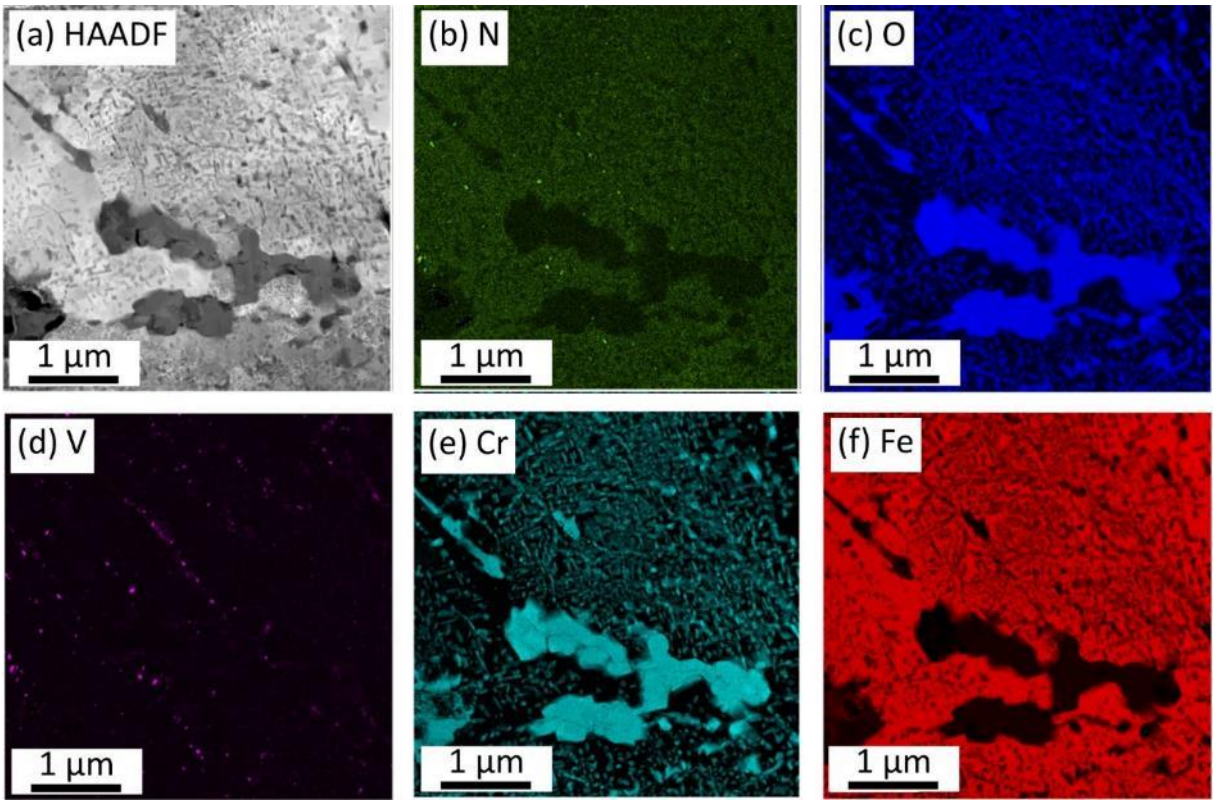

Fig. 4.29. (a) HAADF image and (b-f) corresponding EDSASME elemental maps of inner corrosion layer: (b) nitrogen, (c) oxygen, (d) vanadium, (e) chromium, (f) iron [41]

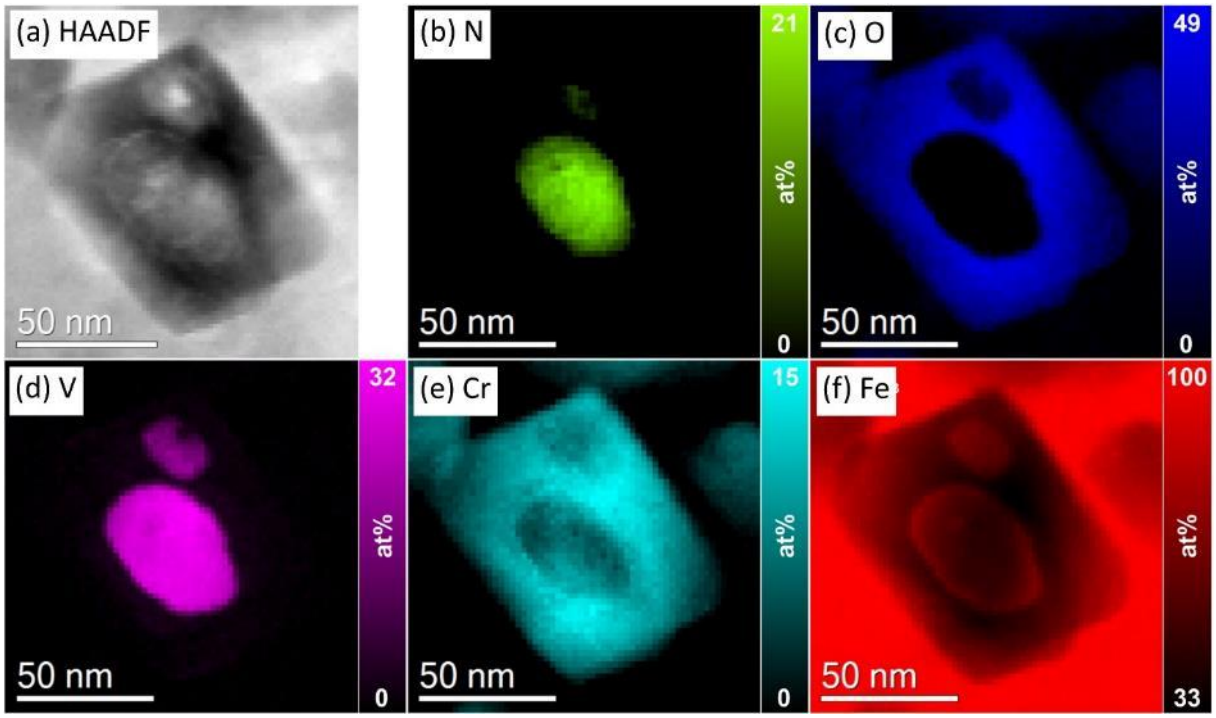

Fig. 4.30. (a) HAADF image and (b-f) corresponding STEM-EELS elemental maps of an oxide particle in inner corrosion layer: (b) nitrogen, (c) oxygen, (d) vanadium, (e) chromium, (f) iron [41]

4.1.4 LCF behavior of sub-size specimens

The primary focus of this study is the strain controlled low-cycle fatigue testing of EUROFER97 specimens as a part of WP 3. As per the literature review, the EUROFER97 components will be exposed to a range of challenging conditions, such as tensile-compressive stresses, high-temperature environments reaching up to 550°C, cooling through purge gas and He flow, and neutron irradiation while in contact with lithium-ceramics pebbles. To obtain a preliminary understanding of how these factors may impact the fatigue characteristics of the tube-shaped structures, low-cycle fatigue tests were performed on EUROFER97 specimens after their exposure to the ceramic breeder environment. As shown in the literature review, it is the fatigue properties that are of greatest interest, while, for example, the tensile strength may not change due to corrosion [11].

It should be noted that the specific tension and compression loading parameters that EUROFER97 tubes will experience are yet to be fully determined by the blanket designers. Therefore, to characterize the LCF of EUROFER97, three different strain ranges were selected for the tests, specifically 0.6%, 1.0%, and 1.6%. In general, higher strain amplitudes result in more rapid material degradation and shorter fatigue lives. The selected strain ranges are commonly used in low cycle fatigue testing, since these strain amplitudes are high enough to produce rapid material degradation, but not so high as to cause premature specimen failure or produce unrealistic loading conditions. As for the atmosphere inside the furnace during testing, it would be ideal to use a purge gas atmosphere to simulate the operation of EUROFER97 in the breeding blanket. However, the current equipment does not yet have the capability to achieve these conditions, so the tests were conducted in air instead. Despite this limitation, the effect of exposure to the ceramic breeder

environment should still be evident in the LCF tests, regardless of the atmosphere within the furnace during the testing. Finally, the test temperature was set to 550°C, which is the highest operating temperature specified for EUROFER97. This was done to ensure that any possible effects of the ceramic breeder environment are as noticeable as possible.

Firstly, sub-sized specimens were subjected to LCF fatigue tests at 550°C in air, with total strain ranges mentioned above. The small size of these samples was specifically designed to allow for a large number of samples with minimum volume, for example, for neutron irradiation. The samples were exposed to lithium-ceramics pebbles in an atmosphere of purge gas at 550°C for 8, 16, 32, 64, and 128 days. The microstructure of these samples is shown earlier in Sections 4.1.1-3. For comparison, the EUROFER97 specimens were also tested in as-received state.

Fig. 4.31 – Fig. 4.33 shows the hysteresis curves of the typical LCF test results for the first cycle, half-life cycle $N_f/2$, and for the fatigue life-time cycle N_f. The curves are shown for the specimen exposed for 64 days, but the revealed patterns are also preserved for other specimens. Typically, the first cycle involves tension with a small plastic deformation followed by a compression phase with higher plastic deformation. During the subsequent tension phase, a similar value of plastic deformation occurs as during compression. This leads to the appearance of a stress-strain hysteresis loop, where the sample experiences non-zero stresses at zero strain. The resulting stresses increase with the degree of deformation, reaching 350, 390, and 410 MPa for a total strain range of 0.6%, 1%, and 1.6%, respectively. As the number of cycles increases, the peak stresses decrease due to the so-called cyclic softening. At half-life, the peak stresses decrease to 270–290 MPa for all total strain ranges, and when the fatigue life cycle is reached, the peak stresses decrease to 190–240 MPa. Toward the end of the fatigue test, the fatigue crack formed opens and the deformation begins to localize, resulting in lower peak tensile stresses and slightly higher peak compression stresses due to the closure of the fatigue crack (red curves in Fig. 4.31-4.33).

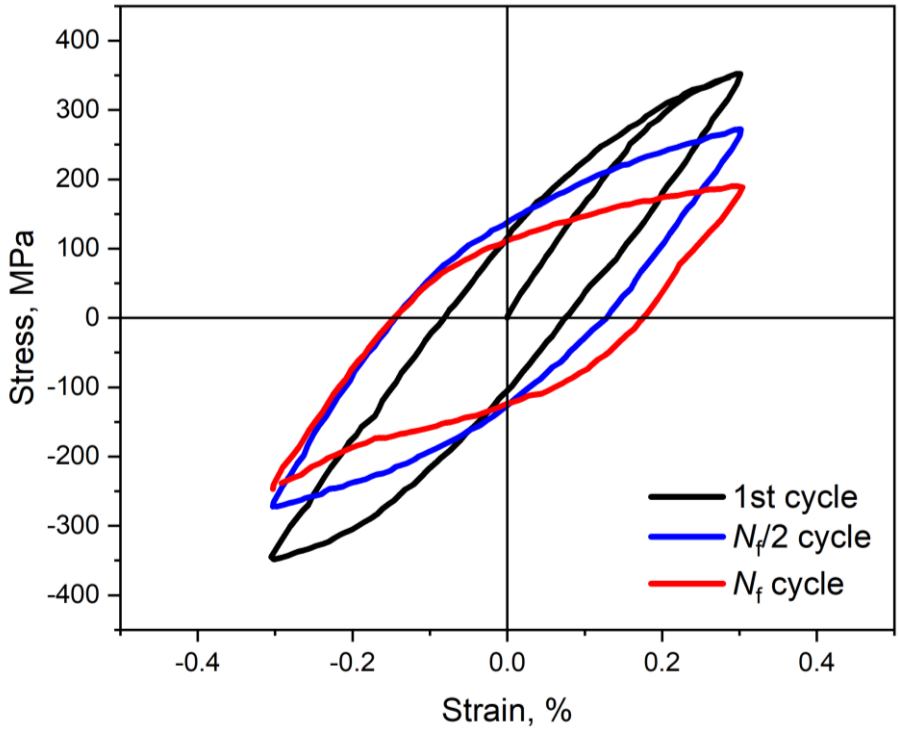

Fig. 4.31. Typical hysteresis loops at first cycle, half-life (N_f/2) cycle, and at N_f cycle for a total strain range of 0.6% (sub-sized specimen exposed to the ceramic breeder environment for 64 days)

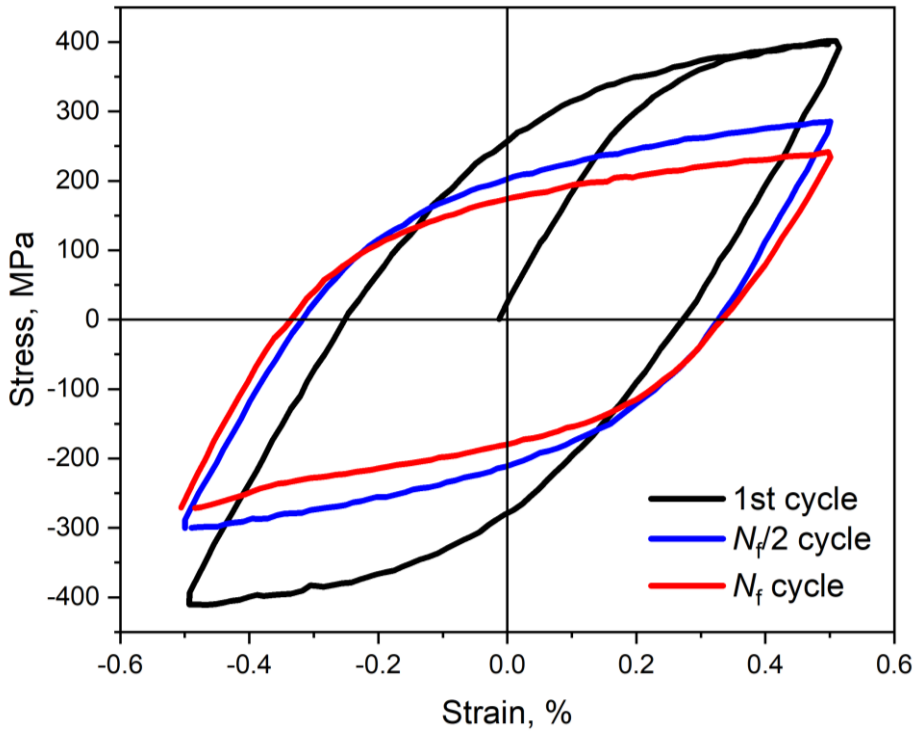

Fig. 4.32. Typical hysteresis loops at first cycle, half-life (N_f/2) cycle, and at N_f cycle for a total strain range of 1% (sub-sized specimen exposed to the ceramic breeder environment for 64 days)

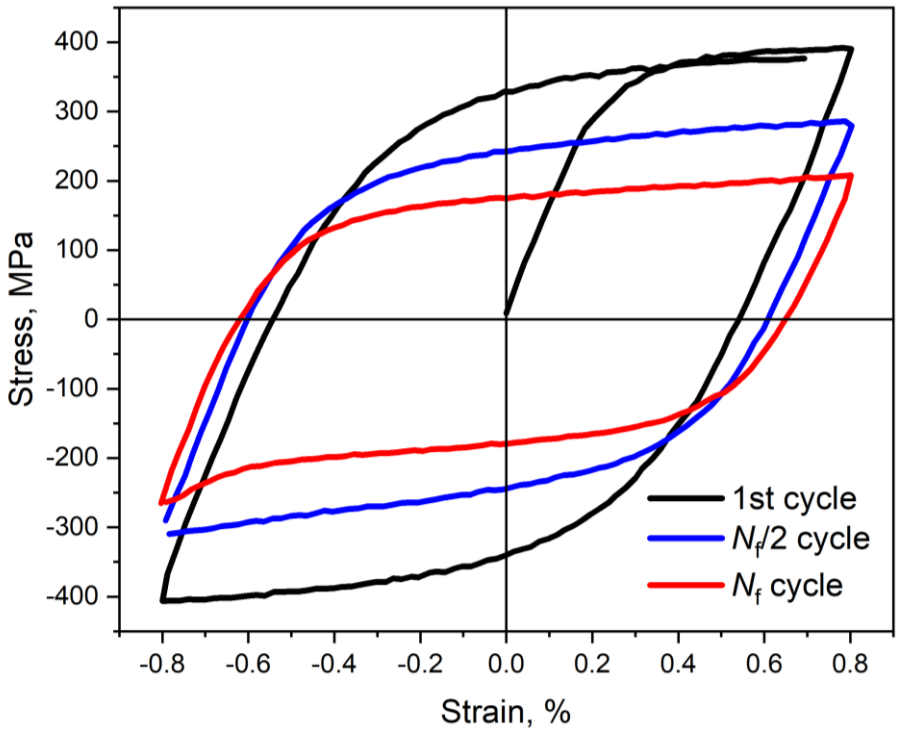

Fig. 4.33. Typical hysteresis loops at first cycle, half-life (N_f/2) cycle, and at N_f cycle for a total strain range of 1.6% (sub-sized specimen exposed to the ceramic breeder environment for 64 days)

Based on the initial fatigue test data (hysteresis loops), diagrams of peak tensile stresses as a function of the number of cycles were plotted (Fig. 4.34 – Fig. 4.36). It should be noted that the presented curves are typical, although, as is usual for fatigue tests, there is always a scatter in the fatigue life data. The diagram of peak compressive stresses versus the number of cycles is nearly symmetrical about the abscissa axis, with differences appearing only towards the end of the tests (as discussed above) and therefore is not shown.

As usual for EUROFER97, the reduction of peak stresses occurs in three stages. As noted in the literature review, during the first stage, peak stresses decrease relatively rapidly due to reorganization and a decrease in the density of existing dislocations. The second stage, which lasts the longest, is characterized by a linear, gradual decrease in peak stresses (near-steady state) resulting from the equalization of the rates of formation of new and disappearance of existing dislocations from the crystal lattice for various reasons [56]. During the third stage, peak stresses drop rapidly due to the accelerated growth of a fatigue crack, which leads to sample failure.

The diagrams as depicted in Fig. 4.34 – Fig. 4.36 were utilized to determine the number of cycles to failure, N_f. This is a critical parameter that indicates the number of times a material can undergo cyclic loading before failing under given testing conditions. The value of N_f can be determined using ASTM E2714-13 [40] as the number of cycles corresponding to a peak stress of 90% of the peak stress at the beginning of the third stage (i.e., the deviation from the linear stage). As the total strain range increases, not only do the peak stresses slightly increase, but the number of cycles to failure also decreases significantly. For as-received EUROFER97, the number of cycles to failure decreases from approximately 2600 to 700 and to 350 with an increase in total strain range from 0.6% to 1% and 1.6%, respectively.

In the case of samples exposed to the ceramic breeder environment, the first stage of fatigue softening practically coincides with that of the as-received EUROFER97, but the second stage is usually shorter. This leads to the pre-corroded specimens fracturing earlier than the specimens in the as-received state. Moreover, an increase in the exposure time results in even earlier specimen failure (i.e., 8 days – 2320 cycles, 16 days – 2100 cycles, 32 days – 1230 cycles, 64 days – 1155 cycles, 128 days – 1020 cycles). At a total strain range of 0.6%, it is evident that samples exposed for 32–128 days withstand only half as many cycles as the as-received EUROFER97. At larger total strain ranges, the peak stress diagrams for different exposure times can coincide and overlap. However, the number of cycles to failure for these curves is also usually shorter than for the as-received EUROFER97. This overlap of data for exposed samples can generally be explained by the relatively smaller number of cycles to failure and, consequently, the larger relative scatter of data at larger total strain ranges. As shown in literature review, the fatigue behavior of 38CrMoAl steel exhibited similar trends between as-received specimens and those exposed to corrosion [25]. At high loads there were no significant differences, however, noticeable distinctions were observed at low loads, indicating the influence of corrosion on the fatigue performance (Fig. 2.8).

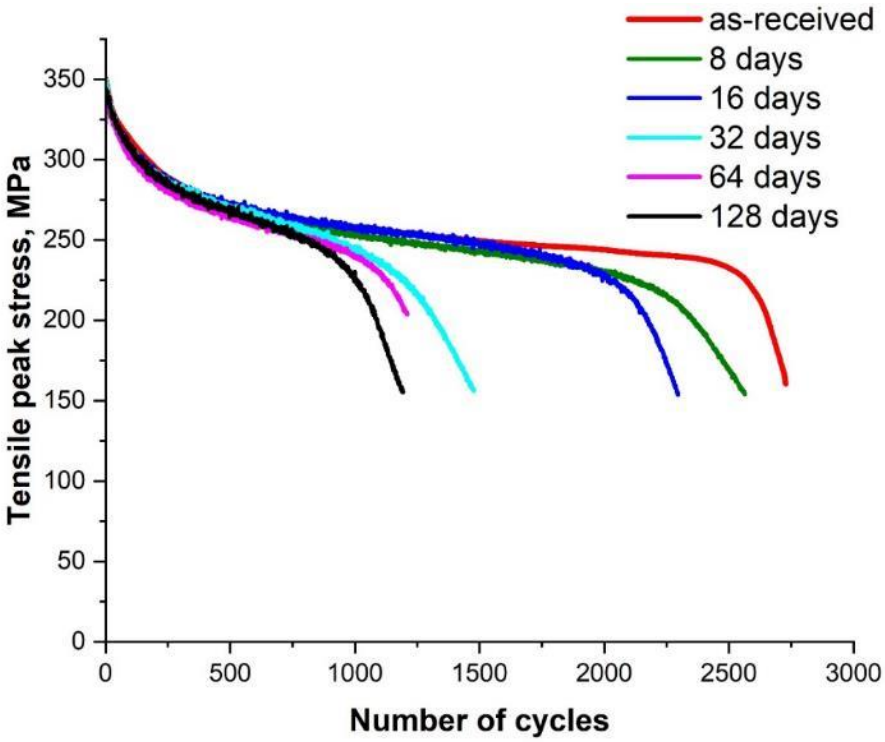

Fig. 4.34. Typical tensile peak stress versus the number of cycles tested at a total strain range of 0.6%

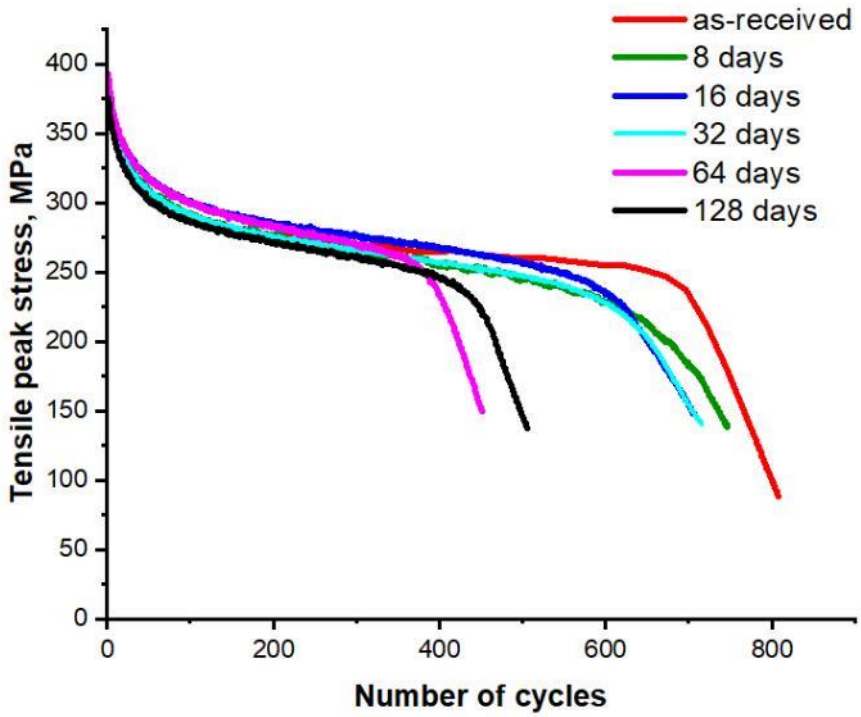

Fig. 4.35. Typical tensile peak stress versus the number of cycles tested at a total strain range of 1%

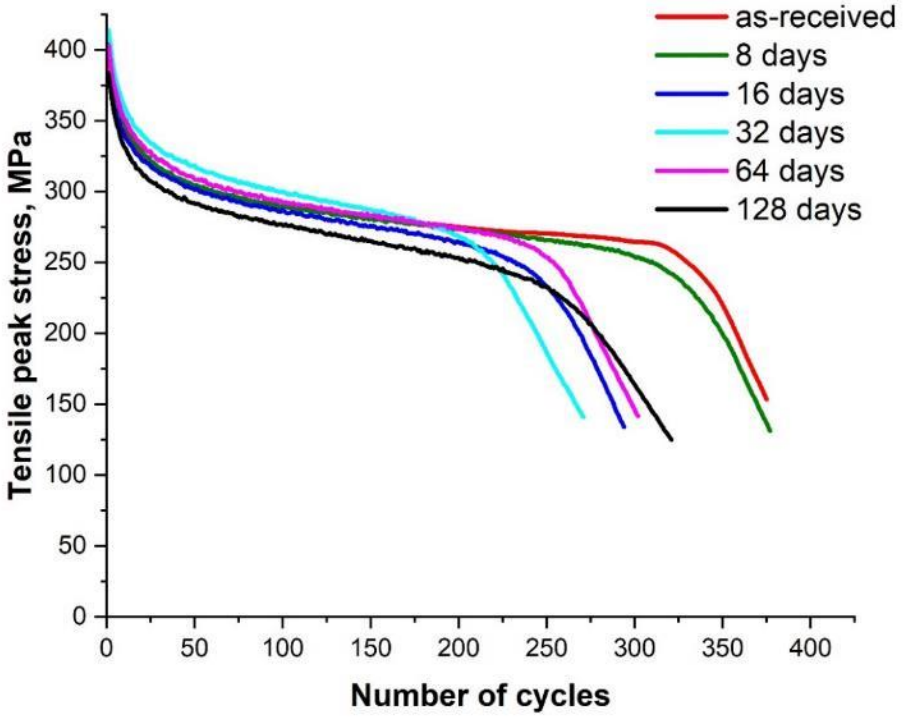

Fig. 4.36. Typical tensile peak stress versus the number of cycles tested at a total strain range of 1.6%

Based on the results of approximately 100 fatigue tests presented, the Wöhler diagram for the as-received and pre-corroded specimens was plotted and is shown in Fig. 4.37 [43]. The diagram reveals a significant

reduction in fatigue lifetime with increasing exposure duration, particularly at total strain ranges of 0.6% and 1%. At the total strain range of 0.6%, the reduction in the lifetime is approximately 60% for an exposure duration of 32–128 days. However, some values fall outside this trend at a strain range of 1.6%, such as the average lifetime of specimens exposed for 8 days, which was longer than that of the as-received specimen (Fig. 4.37). In this case, the results of testing of exposed specimens overlap partially with the data for the as-received specimens in terms of the scatter of the lifetime values. At a strain range of 1%, a clear decrease in the lifetime to failure is observed for exposed within 32–128 days specimens compared to the specimen in the delivery state.

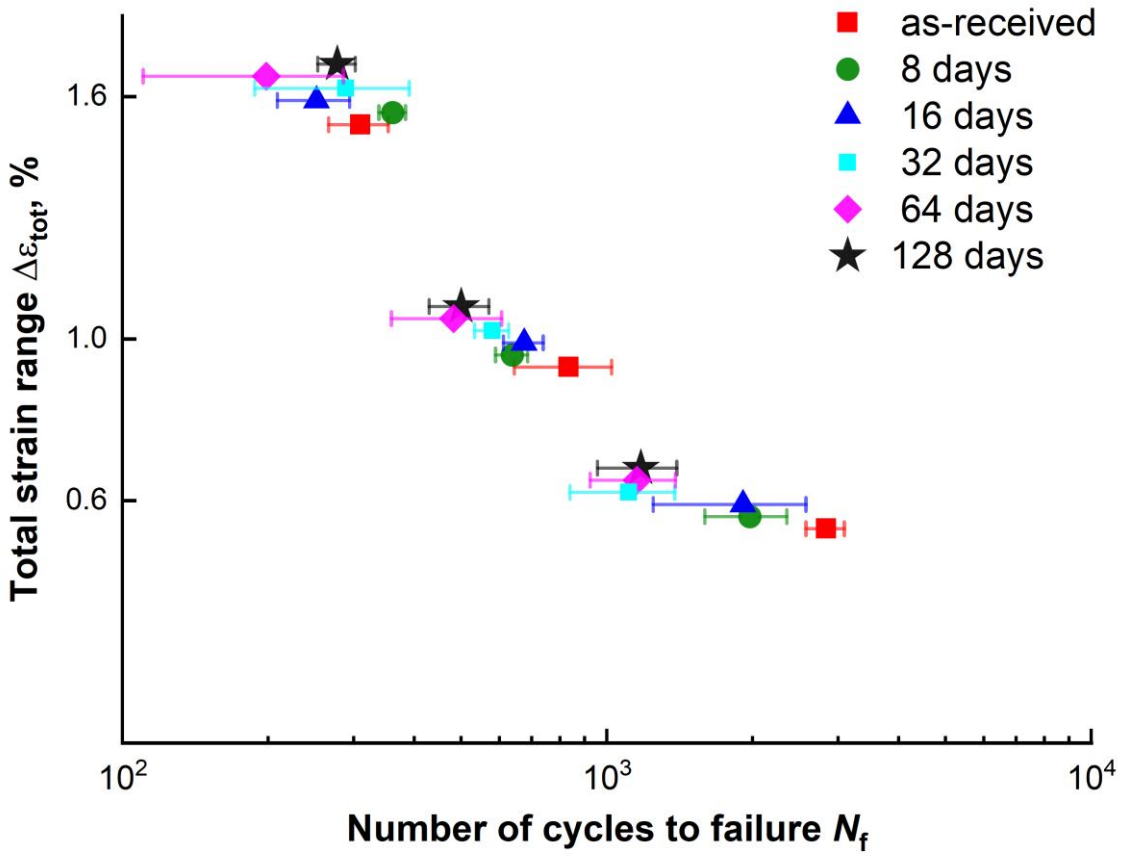

Fig. 4.37. Results of the LCF tests of EUROFER97 specimens exposed to the ceramic breeder environment for different durations [43]. The specimens were tested at 550°C at three different total strain ranges of 0.6, 1, and 1.6%. Vertical offset within a strain range is used to avoid data overlap.

When plotting the number of cycles to failure versus exposure duration (Fig. 4.38), it is evident that the most significant decrease in lifetime occurs for samples exposed up to 32 days. However, further increase in the exposure duration does not have a substantial additional effect on the fatigue life. At larger total strain ranges, the fatigue life ceases to decrease when the exposure time is increased to more than about 64 days. Taking into account the results depicted in Fig. 4.20, the LCF tests clearly show that reaching a certain thickness of the oxide layer leads to a passivation of the steel surface and, therefore, to a stop of the materials degradation. Consequently, the decrease in lifetime is also limited – but to a fairly low level, especially for low cyclic loads. It is important to note that in order to determine the maximum harmful effect of exposure to

the ceramic breeder environment, it is sufficient to limit the exposure to 64 days. There is no benefit to carrying out even longer exposures, as the thickness of the corrosion layer is not expected to increase and further deterioration of the LCF properties also cannot be expected. Therefore, the data suggests that the effect of exposure duration on LCF properties reaches a saturation point after about 64 days.

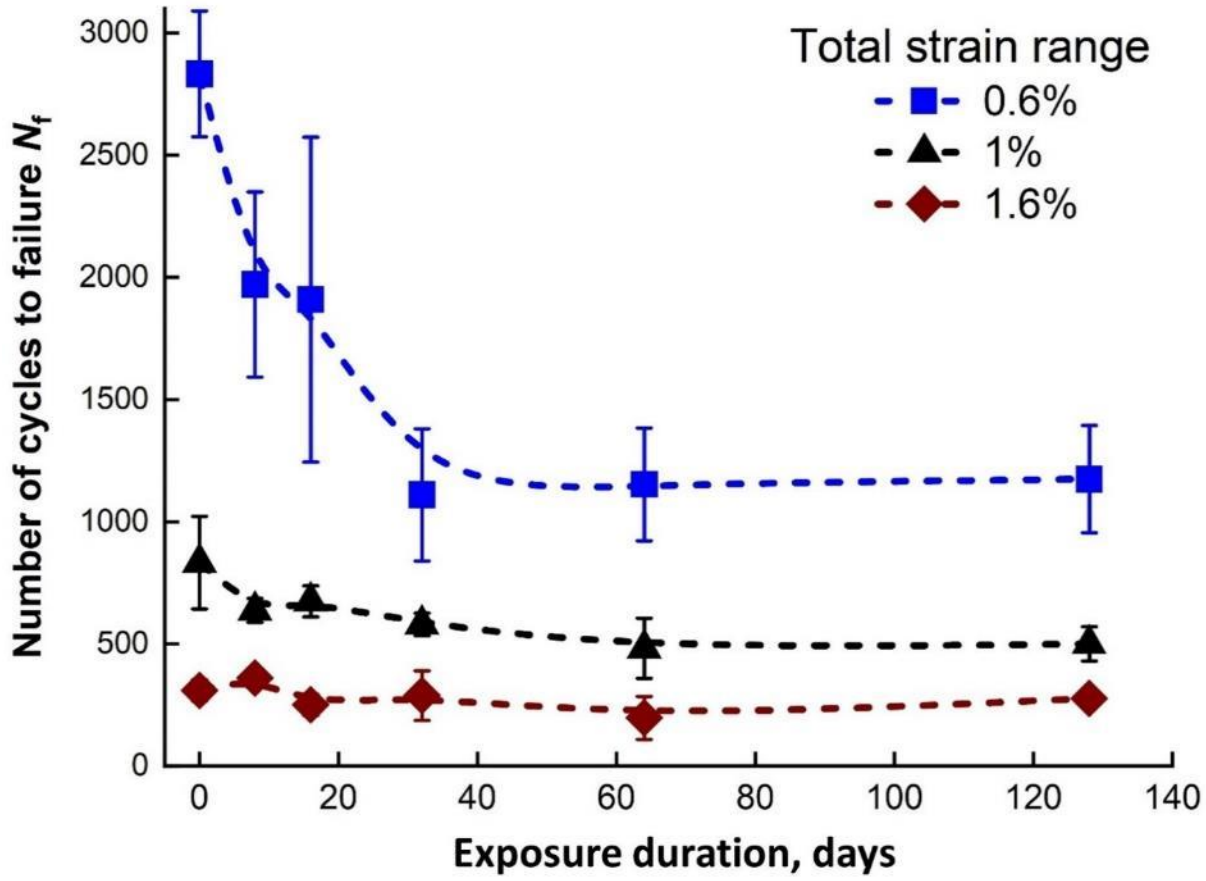

Fig. 4.38. Number of cycles to failure plotted versus exposure duration for three different total strain ranges of 0.6, 1, and 1.6% [43]

Based on this phenomenon, a plot was generated (Fig. 4.39) showing the relationship between inelastic strain amplitude $\Delta\varepsilon_{in}/2$ (for the half-life hysteresis loop as shown in Fig. 4.43-Fig. 4.45) and the number of reversals to failure $2N_f$. This relationship can be fitted using the Manson-Coffin equation [57,58]:

$$\Delta\varepsilon_{in}/2 = \varepsilon'_f (2N_f)^c, \quad (4)$$

where ε'_f is the fatigue ductility coefficient and c is the fatigue ductility exponent. The fitted parameters are also displayed in Fig. 4.39. The obtained values of fatigue ductility exponent were found to be typical for most metals (-0.8…-0.5). Evidently, the specimens pre-corroded for 64 days have a lower magnitude of fatigue ductility exponent than the samples in the as-received state (-0.72 and -0.59, respectively). This implies that at low degrees of inelastic deformation, the detrimental impact of exposure on the number of cycles to failure can be more significant compared to higher values of inelastic deformation.

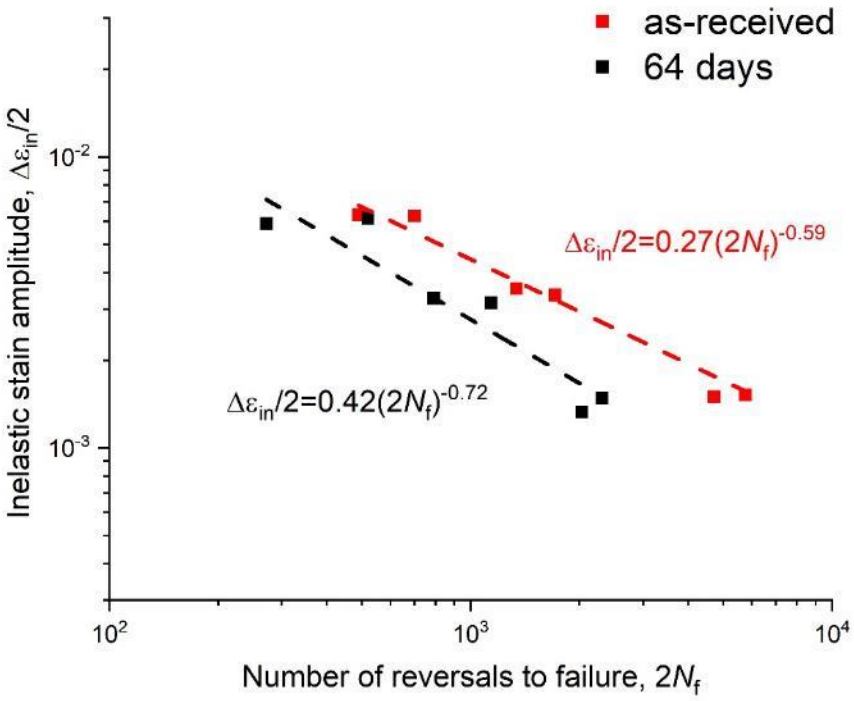

Fig. 4.39. Inelastic strain amplitude as a function of the number of reversals to failure for sub-sized specimens in as-received state and after exposure to the ceramic breeder environment for 64 days

4.1.5 LCF behavior of standard specimens

As previously mentioned, sub-sized specimens with a diameter of 2 mm were initially used to investigate the effect of ceramic breeder environment on a large number of samples subjected to different exposure durations. The experiments conducted with these samples demonstrated that the duration of exposure can be limited to 64 days since longer exposure has a minimal effect on the thickness of the corrosion layer and fatigue lifetime in LCF tests. However, to obtain more reliable fatigue test results, they should also be repeated on standard specimens with a much larger diameter of approximately 8.8 mm. The exposure duration can still be limited to 64 days, as there is no further benefit from longer exposure duration (shown in Section 4.1.4). All other test conditions should remain unchanged.

Fig. 4.40 depicts the appearance of standard specimens used in LCF tests in their as-received state and after exposure to the ceramic breeder environment for 64 days [46]. It should be noted that the surface of the standard specimens at the final stage of polishing was carried out radially, while the sub-sized specimens were polished axially (Fig. 4.2d), since the quality of surface preparation in the case of small specimens is obviously more important from the point of view of fatigue properties. After the exposure, the specimens displayed a bluish surface color resembling that of the sub-sized specimens shown in Fig. 4.1. The contact zones with the lithium-ceramics pebbles are clearly visible to the naked eye, revealing a portion of the pebbles that adhered to the surface during exposure (Fig. 4.40). These pebbles are easily dislodged from

the surface and were manually removed before conducting the fatigue test without affecting the corrosion layer. Additionally, the distance between the contact zones again represents the average diameter of the pebbles. As the standard specimens are much larger in size, the number of imprints of lithium ceramics is proportionally higher than that of sub-sized specimens.

Fig. 4.40. Standard (Ø8.8 mm) LCF samples made of EUROFER97 in the as-received state (top) and after exposure to the ceramic breeder environment for 64 days (bottom) [46]

Fig. 4.41 presents the SEM surface microstructure and corresponding EDS maps of a EUROFER97 specimen after exposure for 64 days in the ceramic breeder environment [46]. Similar to the sub-sized specimens, the primary characteristic of the microstructure is the presence of lithium-ceramics imprints as evidence of contact with pebbles. Fig. 4.41b indicates that the imprints have a higher content of chromium and oxygen. Furthermore, it can be observed that the outer corrosion layer at the imprint with the pebble has peeled off, revealing the inner chromium-rich oxide. A layer of pure iron with hillocks surrounds the imprints on the surface. The surface pattern obtained in this study is consistent with previous results for sub-sized samples and microstructural studies, suggesting the reproducibility of the findings.

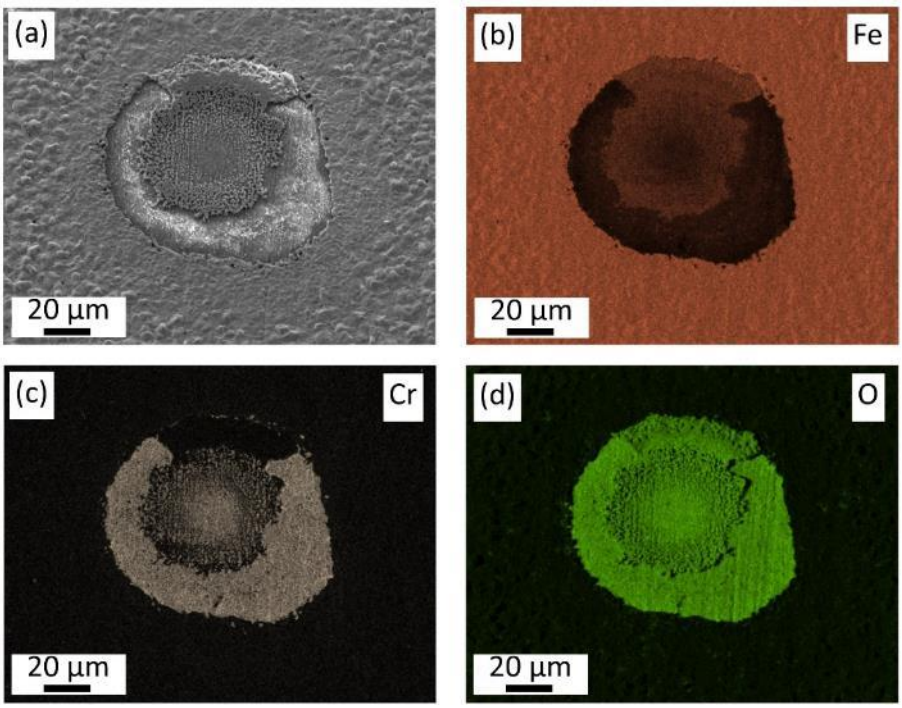

Fig. 4.41. (a) Microstructure and (b-d) corresponding elemental EDS maps of a surface of EUROFER97 sample exposed to the ceramic breeder environment for 64 days: (b) iron, (c) chromium, (d) oxygen [46]

In cross section (Fig. 4.42), the corrosion film formed on the standard specimens consists of the same layers as in the case of a sub-sized specimens [46]. The outer layer A consists of a pure iron phase (light phase) and an iron-rich oxide (dark phase). The intermediate layer B contains more chromium and oxygen. As shown in the TEM section (4.1.3) for the sub-sized specimen, this layer is formed by lithium containing spinel. The inner corrosion layer is a mixture of EUROFER97 and chromium-enriched oxides (spinel). The thickness of the corrosion layer of the standard specimen after exposure to the ceramic breeder environment for 64 days was 15–20 µm, with an average of 17 µm, which corresponds to the thickness of the corrosion layer in the case of a sub-sized specimen. Thus, exposure of a standard specimen to the ceramic breeder environment resulted in the formation of a corrosion layer similar in structure and thickness to that in the case of sub-sized specimens.

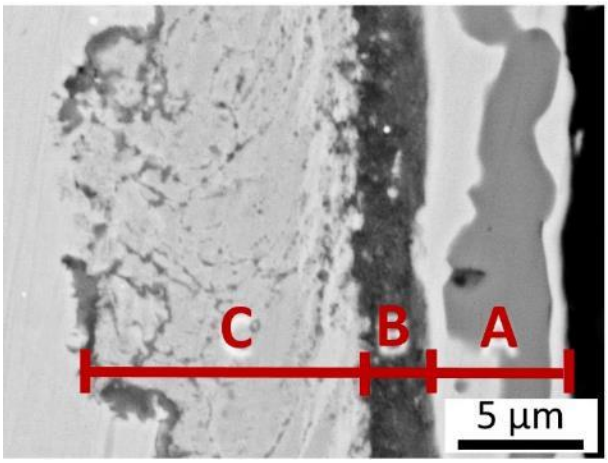

Fig. 4.42. SEM microstructure of a cross section of a standard EUROFER97 sample exposed to the ceramic breeder environment for 64 days [46]. Three different corrosion layers are denoted in analogy with Fig. 4.23

Low-cycle fatigue tests on standard specimens were conducted under the same conditions as the sub-sized specimens, which included a temperature of 550°C in air, a strain rate of $3 \cdot 10^{-3}$ s^{-1}, and total strain ranges of 0.6%, 1%, and 1.6%. Fig. 4.43–Fig. 4.45 display the hysteresis curves of typical LCF test results for the first cycle, half-life cycle $N_f/2$, and for the fatigue life-time cycle N_f. The curves are shown only for the specimens exposed for 64 days (the exposure duration of standard specimens was only 64 days), similar to the sub-sized specimens. The initial peak stresses observed for the standard specimens were found to be the same as those for the sub-sized specimens, reaching 350, 390, and 410 MPa for total strain ranges of 0.6%, 1%, and 1.6%, respectively. As the number of cycles increased, the peak stresses decreased, with the specimens enduring more cycles to failure than the sub-sized specimens. At half-life, the peak stresses decreased more to 250–270 MPa for all total strain ranges, and when the fatigue life was reached, the peak stresses decreased to 200–220 MPa. Although the initial peak stresses were the same as in the case of sub-sized specimens, due to the greater lifetimes of the standard specimens, the peak stresses logically decreased somewhat more towards the end of the test.

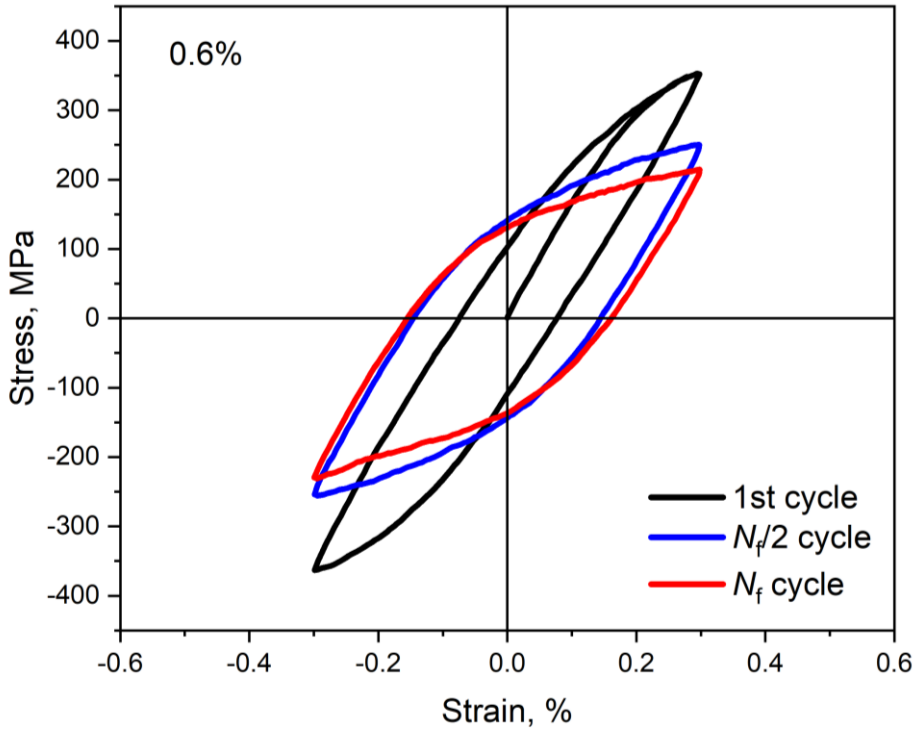

Fig. 4.43. Typical hysteresis at first cycle, half-life (N_f/2) cycle, and at N_f cycle for a total strain range of 0.6% (standard specimen exposed to the ceramic breeder environment for 64 days)

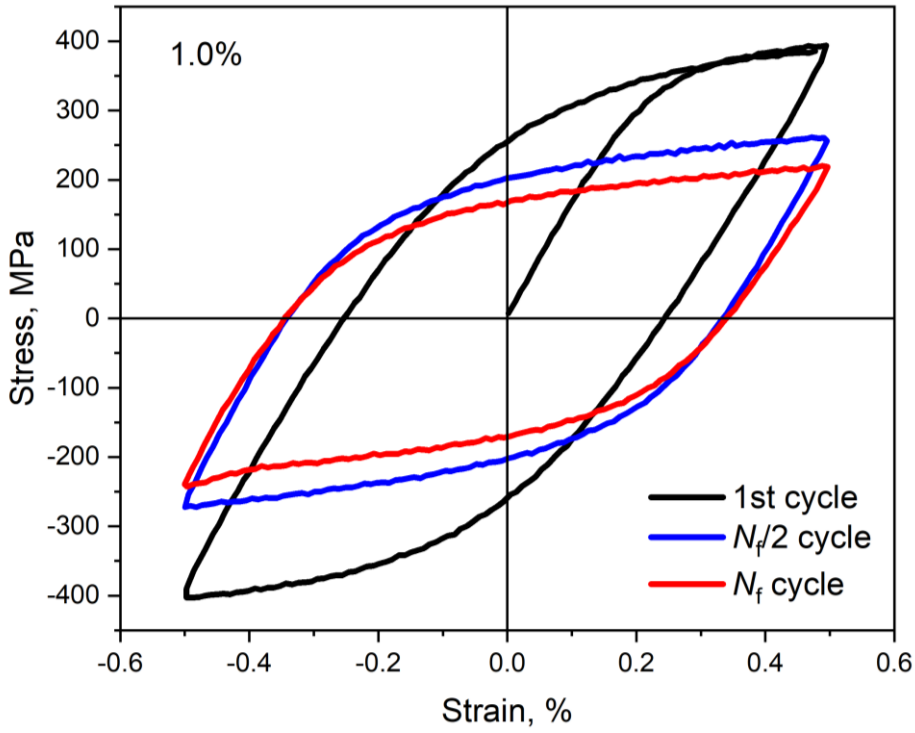

Fig. 4.44. Typical hysteresis at first cycle, half-life (N_f/2) cycle, and at N_f cycle for a total strain range of 1% (standard specimen exposed to the ceramic breeder environment for 64 days)

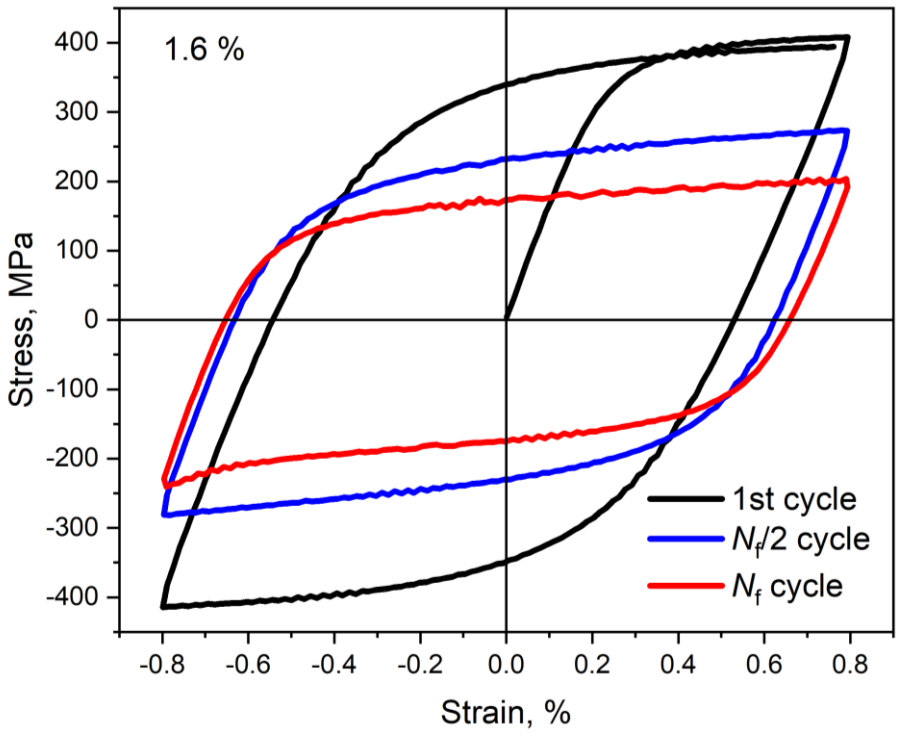

Fig. 4.45. Typical hysteresis at first cycle, half-life (N_f/2) cycle, and at N_f cycle for a total strain range of 1.6% (standard specimen exposed to the ceramic breeder environment for 64 days)

Fig. 4.46 compares typical hysteresis loops obtained for specimens exposed for 64 days sub-sized and standard specimens at a total strain range of 0.6%. The hysteresis loops for the first cycle are nearly identical. Hysteresis loops were also plotted for the 575th cycle, which corresponds to N_f/2 cycle for the sub-sized specimen. In this case, the hysteresis loops were also similar, indicating that the fatigue softening behaviour for both specimens occurs in a similar manner, with only slight differences in stress magnitudes.

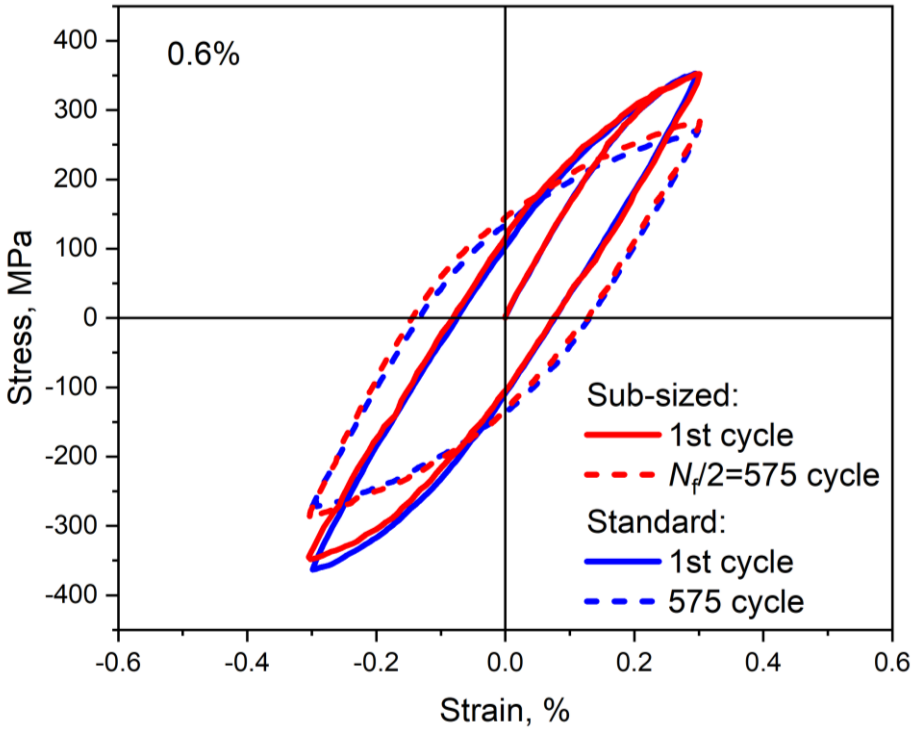

Fig. 4.46. Comparison of hysteresis for sub-sized (red lines) and standard specimens (blue lines) corresponding to the first cycle (solid lines) and the 575th cycle (dashed lines). The 575th cycle corresponds to $N_f/2$ for the sub-sized specimen. Total strain range is 0.6%. The specimens were exposed to the ceramic breeder environment for 64 days.

Fig. 4.47 represents similar hysteresis loops for a total strain range of 1%. In this case, the first cycle also closely matches. The hysteresis loops corresponding to the $N_f/2$ cycle for the sub-sized specimen exhibit minor differences. The maximum stresses are 285 MPa and 269 MPa for the sub-sized and standard specimens, respectively.

Fig. 4.48 presents hysteresis loops for a total strain range of 1.6%. In this case, the hysteresis loops for the first cycle and the cycle corresponding to $N_f/2$ for the sub-sized specimen show negligible differences between the sub-sized and standard specimens. Thus, the fatigue behavior of the sub-sized and standard specimens in the initial deformation cycle and the cycle corresponding to $N_f/2$ for the sub-sized specimen exhibit only minor differences for all three tested total strain ranges.

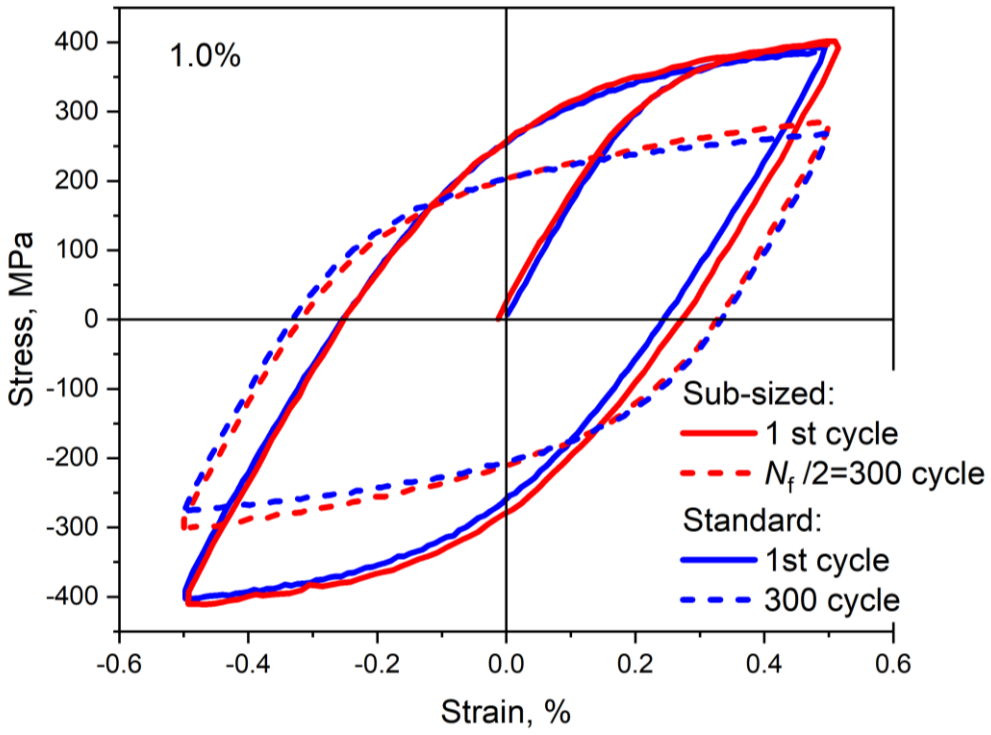

Fig. 4.47. Comparison of hysteresis for sub-sized (red lines) and standard specimens (blue lines) corresponding to the first cycle (solid lines) and the 300th cycle (dashed lines). The 300th cycle corresponds to $N_f/2$ for the sub-sized specimen. Total strain range is 1.0%. The specimens were exposed to the ceramic breeder environment for 64 days.

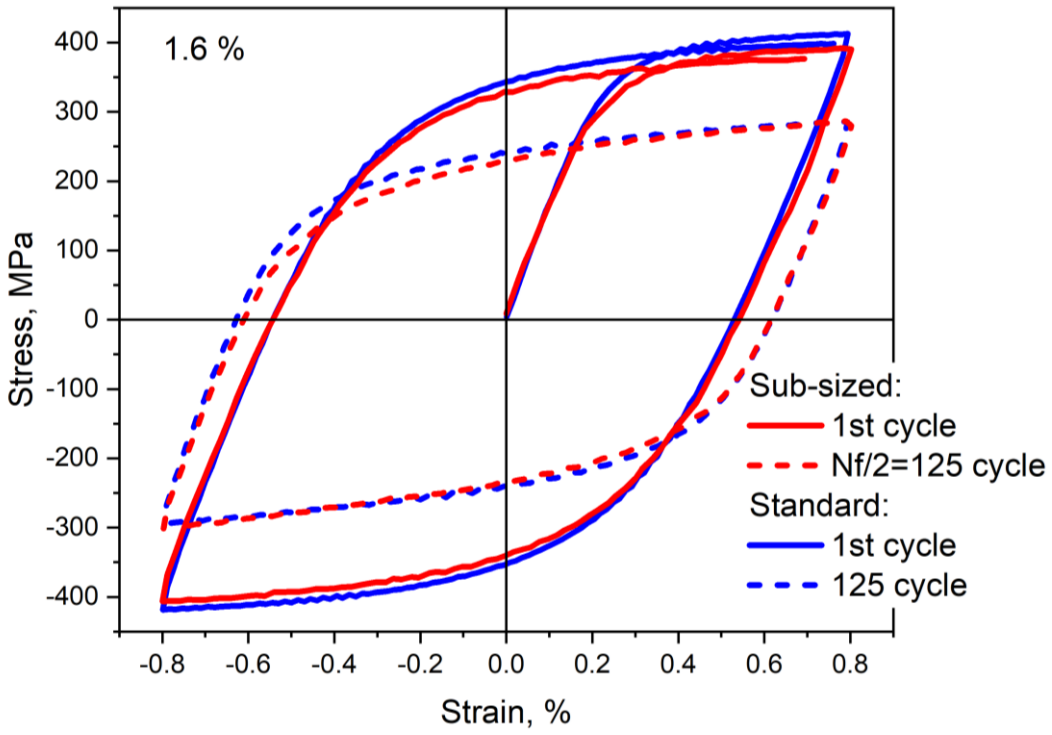

Fig. 4.48. Comparison of hysteresis for sub-sized (red lines) and standard specimens (blue lines) corresponding to the first cycle (solid lines) and the 125th cycle (dashed lines). The 125th cycle corresponds to $N_f/2$ for the sub-sized specimen. Total strain range is 1.6%. The specimens were exposed to the ceramic breeder environment for 64 days.

Fig. 4.49–Fig. 4.51 present diagrams of peak stress versus number of cycles for different total strain ranges, including two curves for both standard and sub-sized specimens in the initial state and after exposure to the ceramic breeder environment for 64 days [46]. The fatigue softening behavior of standard specimens was found to be similar to that of sub-sized specimens. The first stage for all four curves (at all total strain ranges) practically coincides, but the duration of the linear second stage differs due to the scale factor, resulting in the as-received standard specimen (blue curves, N_f=5100 cycles for $\Delta\varepsilon_{tot}$=0.6%) enduring a greater number of cycles to failure than the as-received sub-sized specimen (red curves, N_f=3100 cycles for $\Delta\varepsilon_{tot}$=0.6%) under the same test conditions.

The longer lifetime of the pre-corroded standard specimens (light blue curves, N_f=3250 cycles for $\Delta\varepsilon_{tot}$=0.6%) compared to the sub-sized specimens (pink lines, N_f=1150 cycles for $\Delta\varepsilon_{tot}$=0.6%) is also attributed to the scale factor, with the former even exhibiting a slightly longer lifetime than the as-received sub-sized specimen. However, the decrease in fatigue lifetime associated with exposure to the ceramic breeder environment, as shown in the previous section, is still observed for standard specimens. The observed effects persist for all total strain ranges tested, and the scatter in lifetime is larger for larger values of the total strain range.

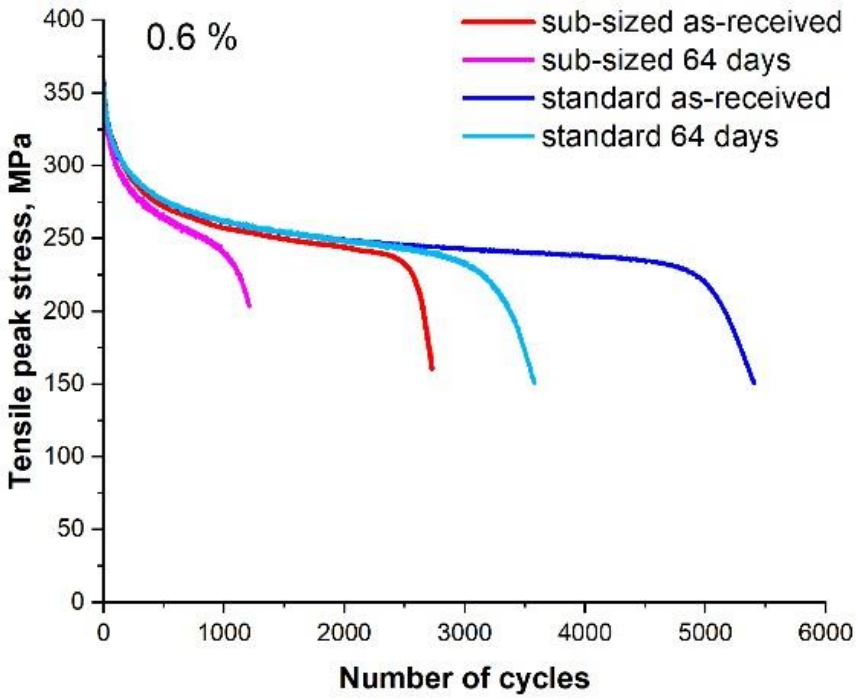

Fig. 4.49. Typical tensile peak stress versus the number of cycles tested at a total strain range of 0.6% for sub-sized and standard specimens [46]

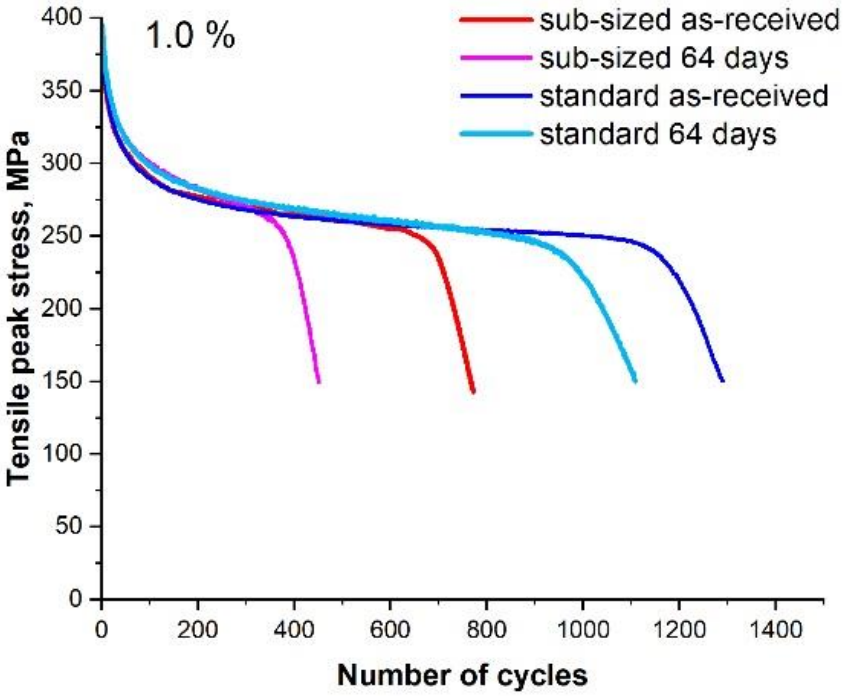

Fig. 4.50. Typical tensile peak stress versus the number of cycles tested at a total strain range of 1% for sub-sized and standard specimens [46]

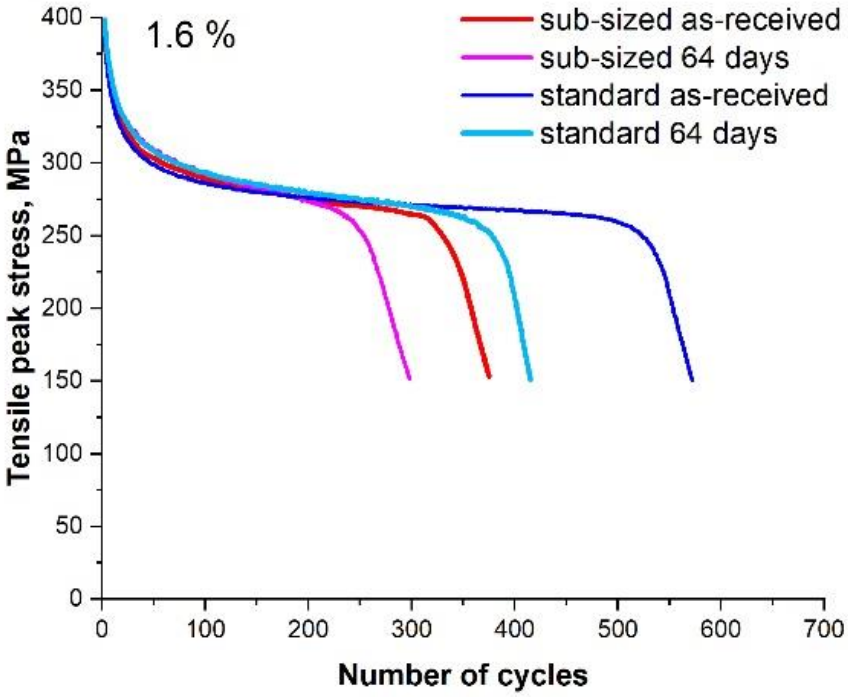

Fig. 4.51. Typical tensile peak stress versus the number of cycles tested at a total strain range of 1.6% for sub-sized and standard specimens [46]

The Wöhler diagram for the standard and sub-sized specimens in both as-received and pre-corroded conditions (64 days in the ceramic breeder environment) is presented in Fig. 4.52. Evidently, the standard specimens endured more cycles to failure compared to the corresponding sub-sized specimens. This can be attributed to the size factor, which is an already known phenomenon [59]. Additionally, exposure to the ceramic breeder environment for 64 days had a pronounced effect of deteriorating fatigue life. For sub-sized specimens, the degradation in fatigue life is 60%, 40%, and 35% for total strain ranges of 0.6%, 1%, and 1.6%, respectively. However, for standard specimens, the effect was less dramatic, with an average degradation of 35%, 10%, and 30% for the same total strain ranges. Section 4.3.3 will provide more detailed explanations for this phenomenon. The greatest deterioration effect was observed for the total strain range of 0.6% for both sub-sized and standard specimens. For higher strain range values, the effect of deterioration in fatigue properties was expressed to a lesser degree, possibly due to the greater scatter of data. As the tests for standard specimens were carried out in accordance with the ASTM standard [40], the fatigue life values obtained for them are more reliable. Therefore, the observed effect of deterioration in fatigue life due to exposure to the ceramic breeder environment can be considered as reliably established experimentally.

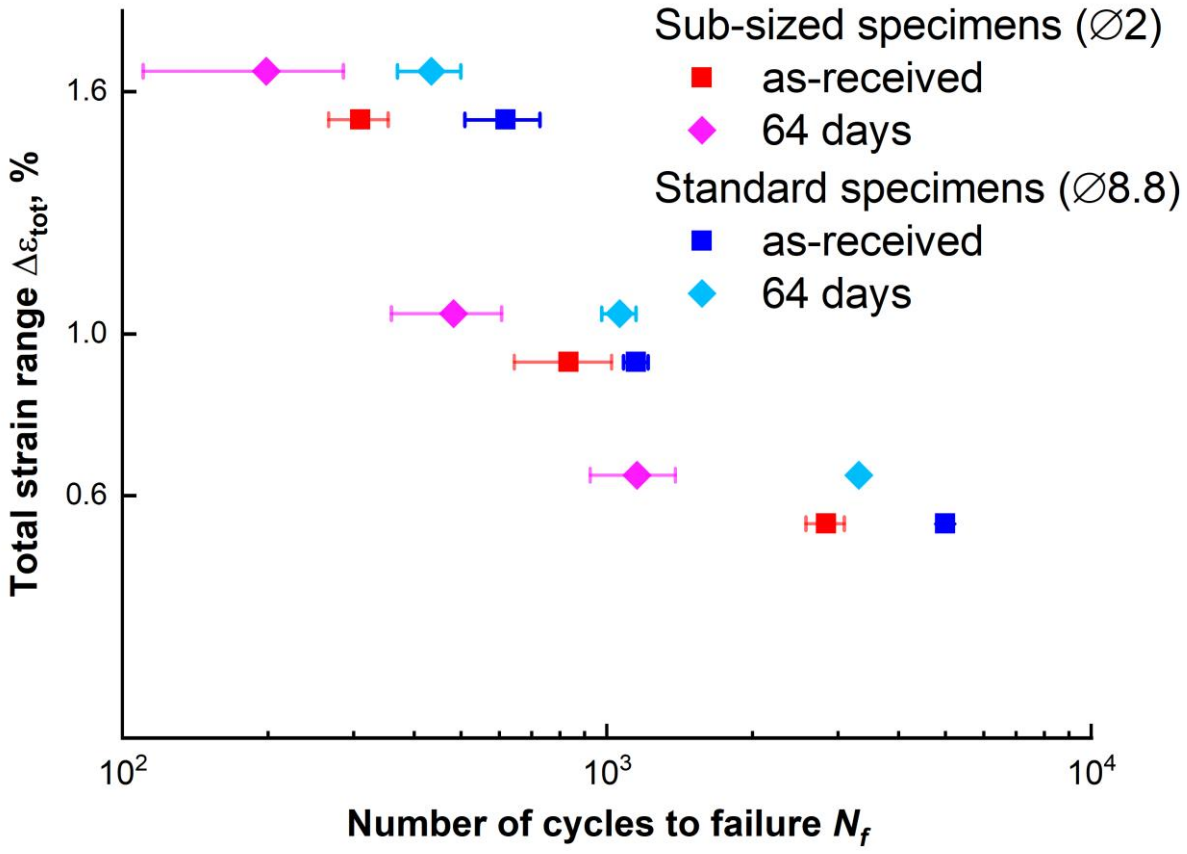

Fig. 4.52. Results of the LCF tests of EUROFER97 sub-sized and standard specimens in as-received condition and exposed to the ceramic breeder environment for 64 days condition. The specimens were tested at 550°C at three different total strain ranges of 0.6, 1, and 1.6%. Vertical offset within a strain range is used to avoid data overlap [46].

The fatigue behavior of the material was also characterized using inelastic strain amplitude $\Delta\varepsilon_{in}/2$ and the number of reversals to failure $2N_f$ for standard specimens in analogy as was done for sub-sized specimens. The fatigue ductility coefficient ε'_f and the fatigue ductility exponent *c* were determined by fitting the data on the graph (Fig. 4.53). The sub-sized specimens showed a more pronounced effect of exposure to the ceramic breeder environment, with exponent values of -0.59 and -0.72 for the as-received and pre-corroded specimens, respectively. Evidently, the effect of exposure for standard specimens was less distinct, with exponent values of -0.66 and -0.7 for the as-received and pre-corroded specimens, respectively. Overall, the results suggest that the pre-corrosion process had a greater impact on the fatigue behavior of sub-sized specimens than on standard specimens. The effect of exposure on the fatigue behavior for the standard specimens was still present, although less pronounced.

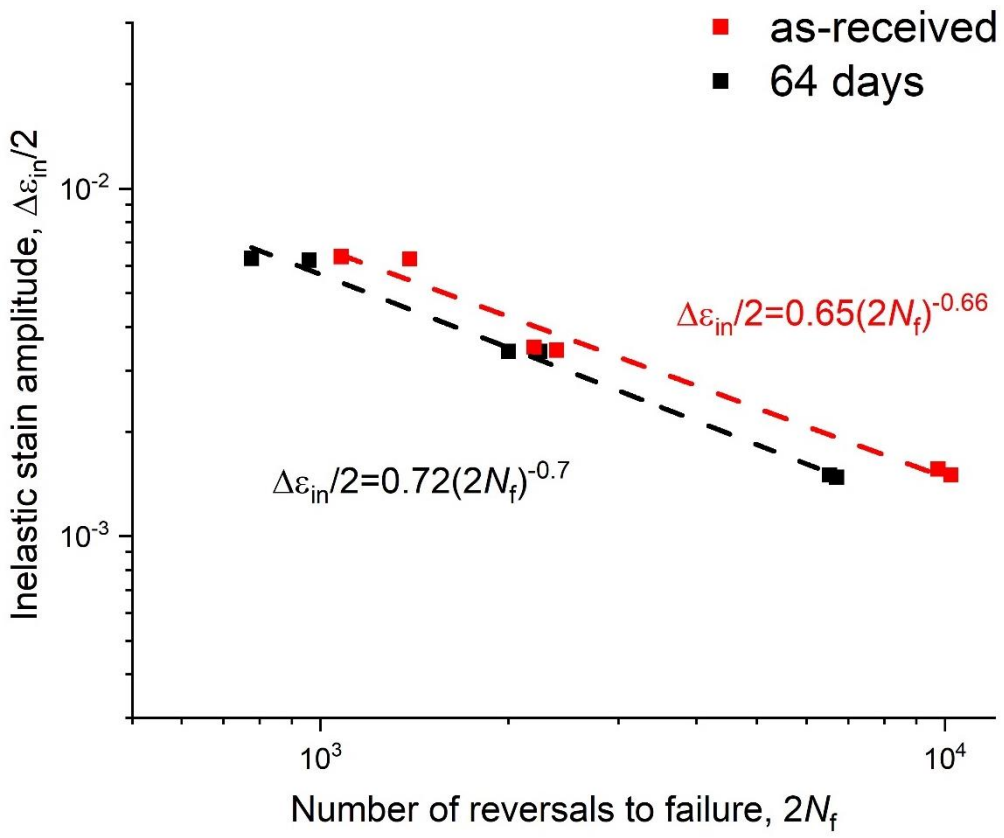

Fig. 4.53. Inelastic strain amplitude as a function of the number of reversals to failure for standard specimens in as-received state and after exposure to the ceramic breeder environment for 64 days

4.1.6 Summary and conclusions

The exposure of EUROFER97 samples to the ceramic breeder environment leads to significant surface corrosion. The imprints at the contact points of EUROFER97 with lithium-ceramics pebbles are the main visible characteristic. Iron oxide, chromium-rich oxide (in imprints), and pure iron hillocks were detected on the surface after exposure up to 8–16 days. As the corrosion time increased, the pure iron hillocks merged and almost completely covered the surface after exposure for more than 64 days. The three-layered corrosion film consisted of an outer layer 5–7 µm thick of iron oxide and pure ferrite, an intermediate layer

1–2.5 µm thick of fine-grained chromium-enriched oxide layer (Fe-Cr spinel), and an internal corrosion layer 7–10 µm thick containing Cr-rich oxide particles formed at the laths boundaries of EUROFER97. The total thickness of the corrosion layer of EUROFER97 increased rapidly up to an exposure duration of about 16 days and reached saturation after more than 64 days with an average value of 16.5–17 µm. The exponential dependence of the thickness on the exposition duration can be explained by the simultaneous oxidation of the surface and the reduction of iron oxide with hydrogen.

The TEM studies have revealed the presence of lithium atoms in the outer (in $LiFeO_2$ grains), intermediate (in $Li_2Fe_{3.2}Cr_{6.8}O_{16}$ grains), and inner (in separate particles of $Li_2Fe_{3.2}Cr_{6.8}O_{16}$) corrosion layers of EUROFER97 after exposure to the ceramic breeder environment. The low solubility of lithium in iron suggests that the presence of oxides is crucial for the diffusion of lithium atoms inwards the material.

The results of low-cycle fatigue tests on sub-sized specimens with a diameter of 2 mm demonstrated a significant decrease in the number of cycles to failure attributed to exposure to the ceramic breeder environment. The reduction in fatigue life became more pronounced with an increase in the duration of exposure to 32–64 days. However, further increase in the duration of exposure showed little effect on the number of cycles to failure. This is also consistent with microstructural studies that revealed saturation in the growth of the oxide layer after exposure for the same time. To conduct a more comprehensive investigation of this pre-corrosion effect, the duration of exposure was chosen to be 64 days, which corresponds to the maximum effect in the minimum time.

Standard specimens with a diameter of 8.8 mm subjected to LCF testing also showed a significant deterioration in fatigue life after exposure to the ceramic breeder environment. Despite the same testing conditions, the standard samples revealed a higher number of cycles to failure than the corresponding sub-sized samples. At 0.6% strain range, the negative impact of pre-corrosion on fatigue life was found to be about 60% and 35% for sub-sized and standard specimens, respectively.

4.2 Effect of exposure environment

As fatigue tests have shown, exposure of EUROFER97 specimens to lithium-ceramics pebbles in a purge gas atmosphere leads to a significant reduction in fatigue lifetime. In fact, such a prolonged exposure at 550°C essentially combines the chemical-mechanical action of lithium-ceramics pebbles and, importantly, the chemical impact of the atmosphere (purge gas + impurities) in which the exposure took place. To separate these two effects, two additional experiments were decided to be carried out. In the first experiment, EUROFER97 samples (including for microstructural studies) were exposed to lithium-ceramics pebbles in vacuum, in order to exclude the influence of the purge gas atmosphere. In the second additional experiment, on the other hand, EUROFER97 samples were exposed to a pure gas atmosphere without lithium-ceramics pebbles. The main purpose of this section of the dissertation is to determine the causes of corrosion of the EUROFER97 surface after exposure to the ceramic breeder environment in accordance with WP 4 (Fig. 3.1).

Fig. 4.54 illustrates the appearance of EUROFER97 specimens after additional exposure experiments. In the first experiment, the specimens were exposed to lithium-ceramics pebbles in vacuum for 64 days at 550°C [43]. Unlike the main experiment, the imprints of the lithium ceramics are barely visible and the sample has a brownish color (Fig. 4.54a). In the second experiment, the specimens were exposed to a purge gas atmosphere without the presence of ceramic pebbles at 550°C for 64 days. The specimen has a bluish color (Fig. 4.54b) that is similar to the specimens from the main experiment (Fig. 4.1).

Fig. 4.54. LCF specimens of EUROFER97 for additional experiments: (a) after exposure to Li-ceramics pebbles in vacuum for 64 days, (b) after exposure to a purge gas atmosphere for 64 days [43]

4.2.1 Exposure to lithium-ceramics pebbles in vacuum

The X-ray diffractogram in Fig. 4.55 displays the results of exposure of EUROFER97 sample to Li-ceramics pebbles in vacuum at 550°C for 64 days. The main peaks in the diffraction pattern are identified as ferrite, and small peaks of Fe_3O_4 and $Li_2Fe_{3.2}Cr_{6.8}O_{16}$ (ICSD: 21096) also present. The latter can also be represented as $(Li+Fe+Cr)_3O_4$. However, these peaks are only noticeable in the lower part of the diffraction pattern and require a close examination to be identified. The presence of a second lithium-containing phase (Li-

containing spinel) was previously confirmed using TEM analysis (4.1.3) in the intermediate and inner corrosion layers in the sample after exposure to the ceramic breeder environment for 64 days. Most likely, the detected peak at 18° is associated with $Li_2Fe_{3.2}Cr_{6.8}O_{16}$. However, in [16,17] this peak is identified as the $LiCrO_2$ phase, for which the peak at 18° is characterized by 100% intensity. In the present work, this is unlikely, since the chromium-containing phase also contains iron, as will be shown below. The peak observed at 40.1°, as mentioned earlier, should be ignored, since this peak corresponds to the reflection of the main ferrite peak in Cu-K_β radiation.

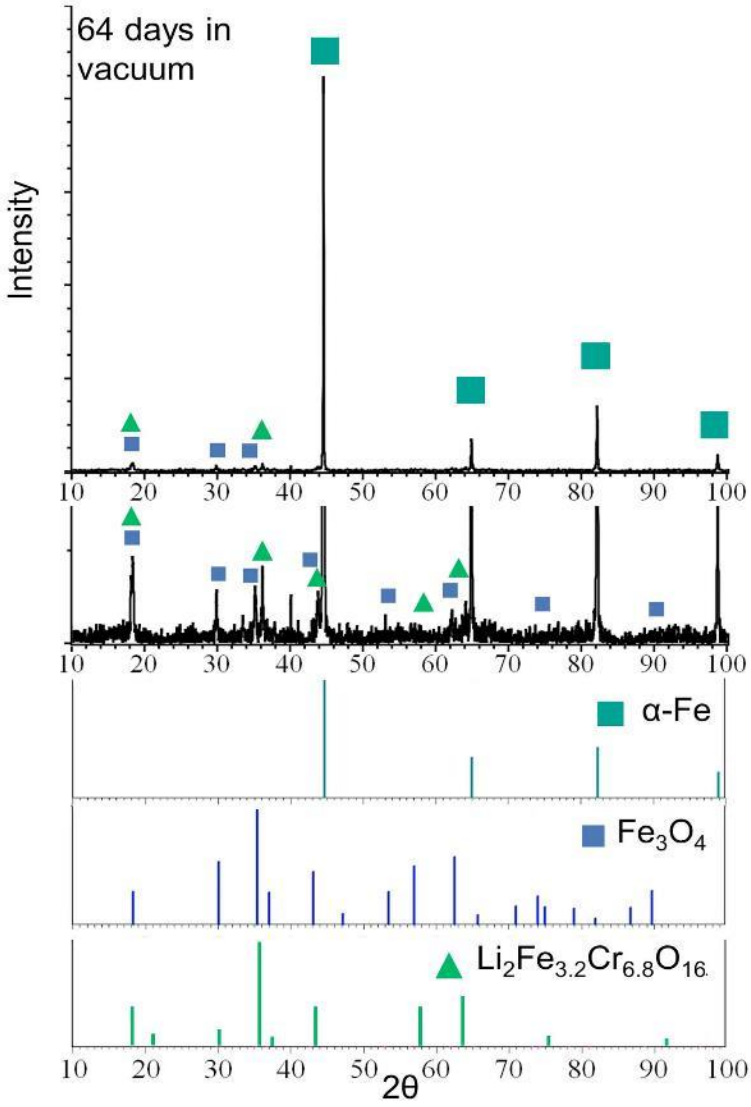

Fig. 4.55. X-ray diffraction pattern for EUROFER97 sample after exposure to Li-ceramics pebbles in vacuum for 64 days. Below the diffraction pattern is an enlarged image of the low peaks as well as the peaks for α-Fe, Fe_3O_4, and $Li_2Fe_{3.2}Cr_{6.8}O_{16}$ used for analysis.

Fig. 4.56 presents the microstructure of EUROFER97 specimens after exposure to Li-ceramics pebbles in vacuum at 550°C for 64 days. The imprint of ceramic pebbles is barely visible in SEM and the surface is covered by tiny needles of about 300–2000 nm in size of iron- and chromium-rich oxides, which was confirmed by EDS. By comparing the EDS and XRD data, the iron-rich oxide can be identified as Fe_3O_4, and the chromium-rich oxide as $Li_2Fe_{3.2}Cr_{6.8}O_{16}$, since this phase contains not only chromium, but also iron

(lithium cannot be detected using EDS). The imprint area has a slightly higher iron content and lower chromium and oxygen contents. This is likely due to the detachment of oxides along with lithium-ceramics pebbles from the sample surface. It is worth noting that the observed insignificant corrosion with the formation of iron- and chromium-rich oxides should be related to the presence of lithium-ceramics pebbles, as EUROFER97 samples exposed under the same conditions did not exhibit such a corrosive layer.

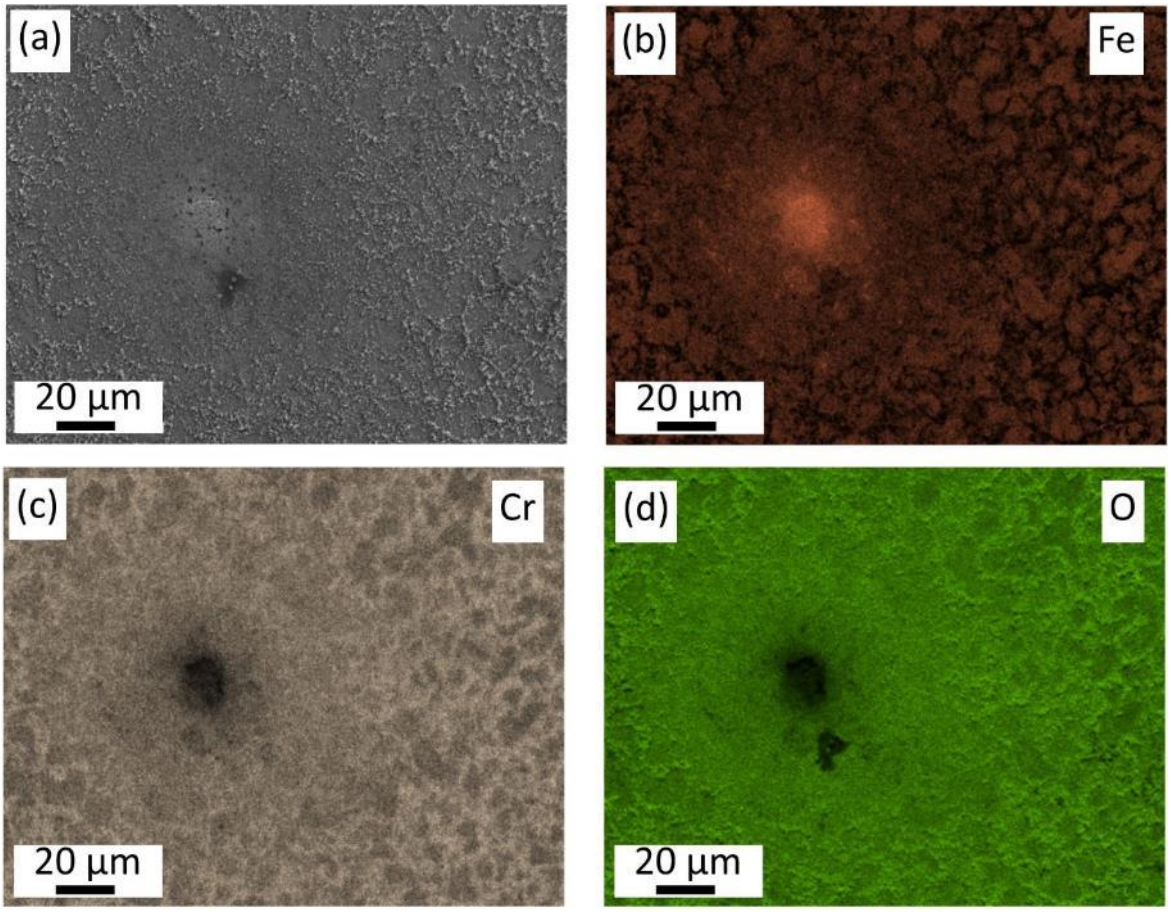

Fig. 4.56. (a) SEM microstructure [43] and (b-d) corresponding elemental EDS maps of a surface of EUROFER97 sample exposed to ceramic pebbles in vacuum for 64 days: (b) iron, (c) chromium, (d) oxygen

The thickness of the corrosion layer after exposure to vacuum turned out to be small so that the cross-sections were bared by FIB cutting (Fig. 4.57). The thickness is measured to be between 0.32 and 0.72 µm after exposure for 8 hours and between 0.45 and 0.85 µm after exposure for 64 days (Fig. 4.58). Therefore, the thickness of the corrosion layer does not change significantly with increased exposure time in vacuum. This thickness is significantly less than the thickness of layers on samples exposed to the ceramic breeder environment (13–18 µm). Based on this additional experiment, it can be conclusively stated that the impact of the lithium-ceramics pebbles on the corrosion behavior of the steel under breeder operating conditions is more or less negligible. Similar results were reported in [15]. It should be kept in mind that lithium may diffuse from lithium-ceramics pebbles into iron/chromium oxides, as previously demonstrated in section 4.1.3. Despite this, the diffusion of lithium inwards EUROFER97 through the oxide layer is improbable due to the extremely low solubility of lithium in ferrite [41].

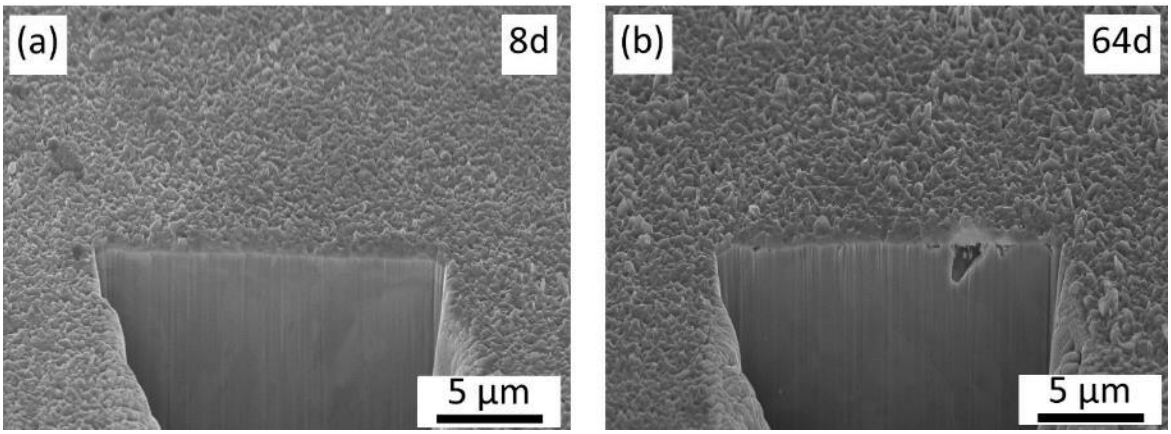

Fig. 4.57. Cross-sections on the EUROFER97 surface obtained with FIB, showing the thickness of the corrosion layer after exposure to the Li-ceramics pebbles in vacuum: (a) 8 days and (b) 64 days [43]

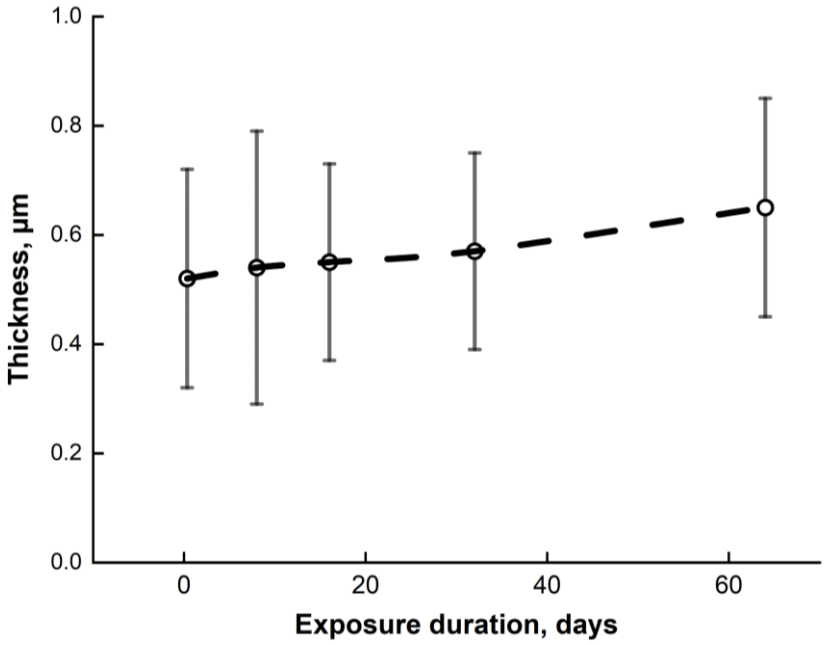

Fig. 4.58. The thickness of corrosion layer on EUROFER97 sample depending on the duration of exposure to Li-ceramics pebbles in vacuum

4.2.2 Exposure to a purge gas atmosphere

As previously noted, in the second additional experiment, the samples were exposed to a purge gas flow atmosphere without lithium-ceramics pebbles. It should be emphasized that the purge gas not only consists of He+0.1% vol. H_2, but also inevitably contains some impurities. Oxygen and water vapor contents were constantly monitored during the pre-corrosion tests and found to be present in small amounts. It appears that industrial gas purification methods are not able to completely eliminate these impurities. According to diagrams Fig. 3.5 and Fig. 3.6, the oxygen and water vapor content is approximately 0.14–0.24 vol.% and 0.01–0.03 vol.%, respectively. When the furnace is opened to remove samples, the level of these gases is temporarily increased, which could also contribute to corrosion.

The diffraction pattern of the EUROFER97 sample after exposure to a purge gas flow for 64 days (Fig. 4.59) is generally very similar to the diffraction pattern after the same exposure but in contact with lithium ceramics (Fig. 4.7). There are mostly peaks from pure ferrite (not EUROFER97), with small peaks corresponding to iron-containing oxide. These small peaks can be identified as both Fe_3O_4 and iron-chromium oxide $FeCr_2O_4$ (PDF: 01-089-3855) which have very similar peaks. As will be shown below, the oxide on the surface of the sample, in addition to iron, also contains a certain amount of chromium, therefore, most likely, this oxide phase can be iron oxide enriched in chromium, which does not lead to a shift of the peaks on the diffraction pattern.

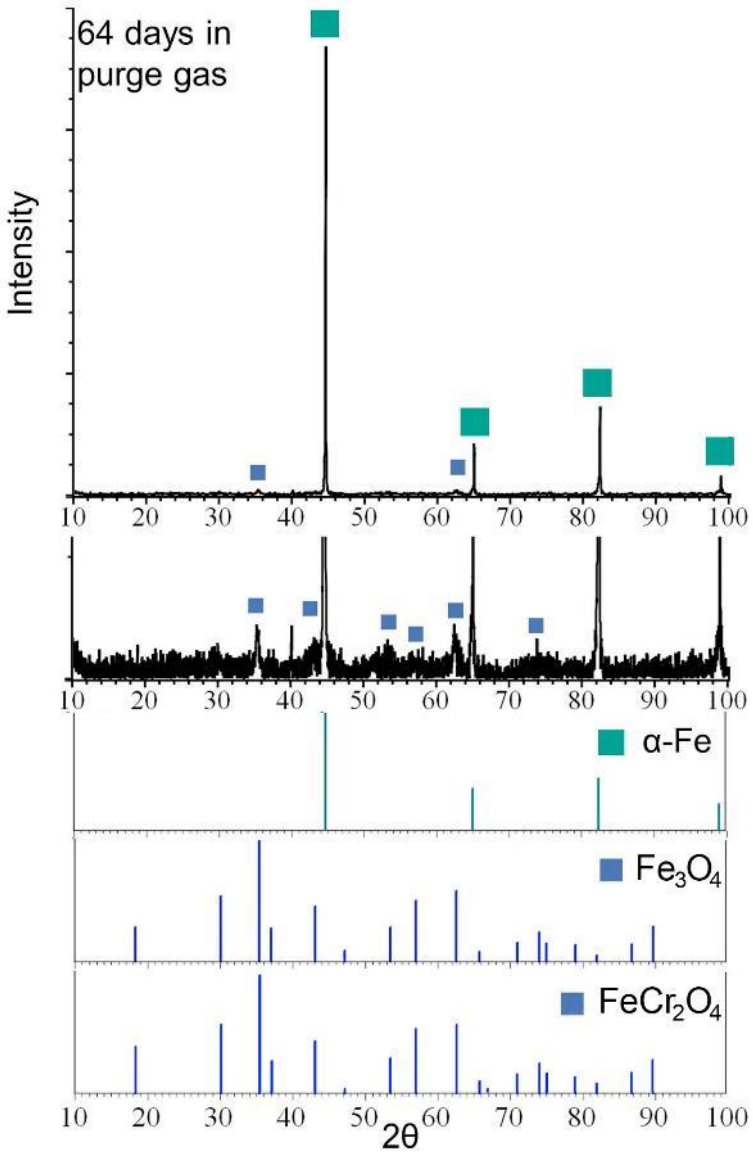

Fig. 4.59. X-ray diffraction pattern for EUROFER97 sample after exposure to purge gas flow (without Li-ceramics pebbles) for 64 days. Below the diffraction pattern is an enlarged image of the low peaks as well as the peaks for α-Fe, Fe_3O_4, and $FeCr_2O_4$ used for analysis.

Fig. 4.60 presents the results of surface analysis of an EUROFER97 specimen that has been exposed to a purge gas atmosphere at 550°C for 64 days. The sample's surface is covered with pure iron hillocks, with iron-chromium-rich oxides found in between. The corrosion layer is similar to the surface of the sample in

the main experiment in the periphery of contact zones with ceramic pebbles (Fig. 4.15), where hillocks of pure iron can be found. Note that there is no chromium in the ferrite phase (pure ferrite, not EUROFER97), and the oxide phase is enriched in both iron and chromium.

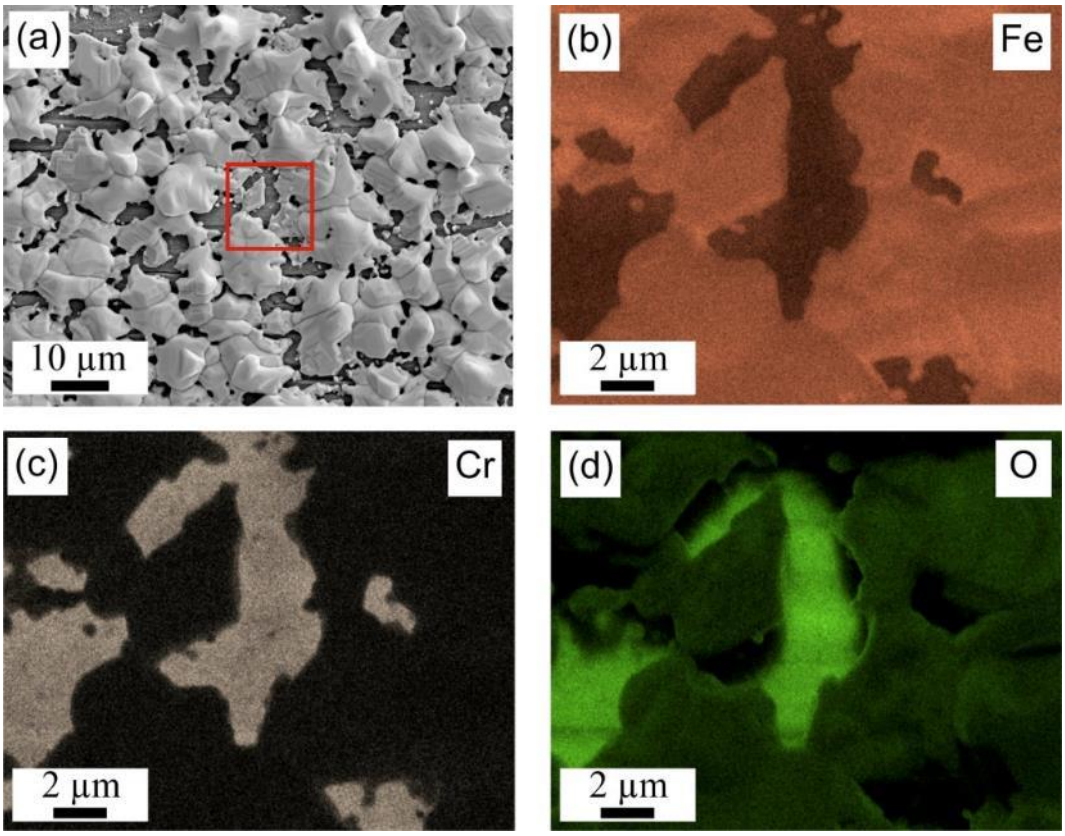

Fig. 4.60. (a) Results of surface analysis of EUROFER97 samples after exposure to a purge gas atmosphere for 64 days: (a) SEM micrographs and (b-c) elemental EDS maps: (b) iron, (c) chromium, (d) oxygen [43]. The EDS maps correspond to the indicated red square in (a).

Cross-sectional microstructural studies (Fig. 4.61) were used to measure the thickness of the corrosion layer, which was found to be 13–17 µm, similar to the thickness of layers from samples aged under breeder environment conditions. In cross-section, one can see pure iron hillocks on the outer corrosion layer (A on Fig. 4.61a). The intermediate corrosion layer (B on Fig. 4.61a) has increased chromium and iron contents and it is less distinct than in the main experiment. The inner oxide layer also contains particles with high chromium and oxygen content (C on Fig. 4.61a). The EUROFER97 adjacent to the inner corrosion layer is depleted of chromium, apparently due to chromium diffusion towards the corrosion layer.

Generally, the corrosion of EUROFER97 subjected to a breeder environment could be significantly reduced by removing purge gas impurities (water and oxygen). However, in the new design of the HCPB concept, it is proposed to use water vapor, since it better carries tritium [60]. This implies the development of protective coatings on EUROFER97 surface that not only solve the problem of corrosion and deterioration of mechanical properties, but also prevent tritium permeation and lithium penetration into the steel. Recently, several attractive protective coatings have been developed [45,61–63], but their compatibility with EUROFER97 during cyclic loading needs to be verified. In addition, the design of the HCPB blanket could be changed so that EUROFER97 does not exhibit a contact with ceramic pebbles as structural material.

In summary, the results of this additional experiment suggest that impurities present in the purge gas, such as water and oxygen (0.1–0.2 vol.% at the inlet of the furnace), are primarily responsible for the corrosion observed on the surface during the exposure to the ceramic breeder environment. The role of the pebbles themselves appears to be relatively minor, with the corrosion layer being less than 1 µm thick in vacuum.

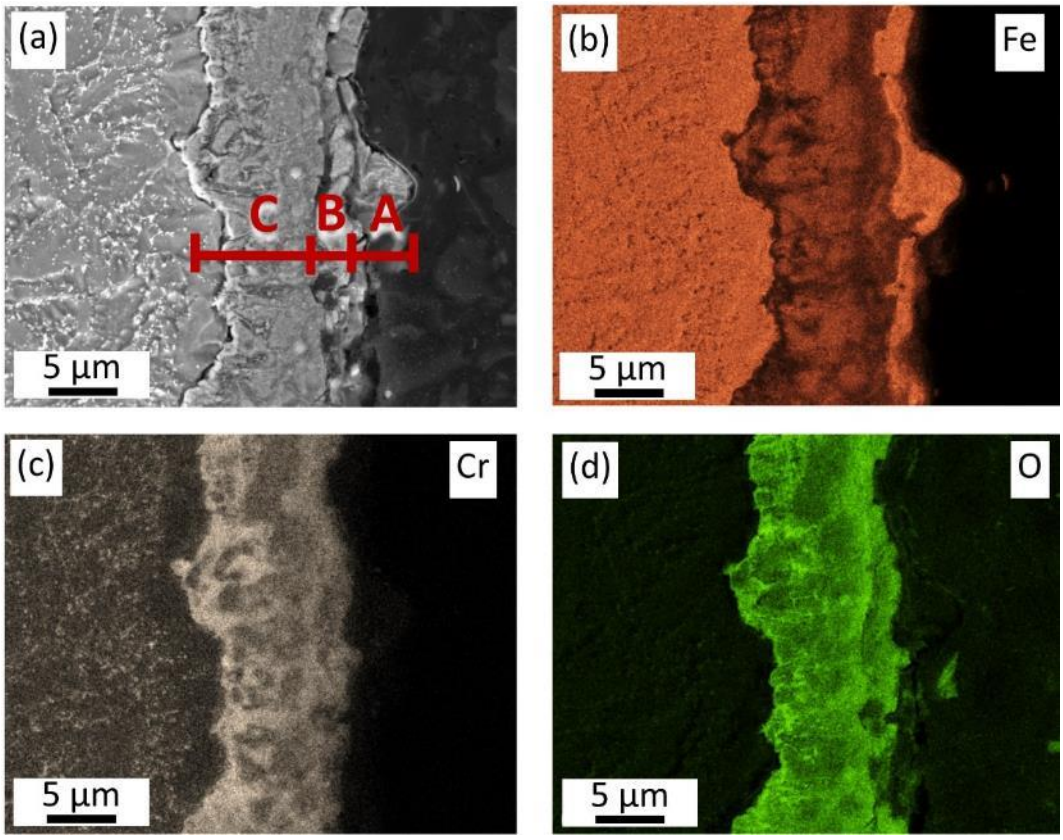

Fig. 4.61. (a) Microstructure and (b-d) corresponding elemental EDS maps of a cross section of EUROFER97 sample exposed to a purge gas atmosphere for 64 days: (b) iron, (c) chromium, (d) oxygen. In (a), three different corrosion layers can be distinguished: outer A with a higher Fe content, intermediate B with higher Cr content, and inner C adjacent to EUROFER97.

4.2.3 Effect of the exposure environment on LCF

This section examines the impact on (LCF properties by two distinct factors: the presence of lithium-ceramics pebbles (in vacuum) and the influence of the purge gas atmosphere (without pebbles). The experiments were conducted on sub-sized specimens using the same conditions as for the as-received specimens and specimens that underwent exposure to the ceramic breeder environment: 550°C in air, strain rate of 3×10^{-3} s^{-1}, and a total strain range of 0.6%, 1%, and 1.6%. The exposure duration of 64 days was chosen as optimal to reveal the effects, as discussed earlier in Section 4.1.4.

Despite the different exposure conditions, the peak stresses of all studied sub-sized samples were found to be similar (Fig. 4.62–Fig. 4.64). The peak load versus number of cycles curves showed similar fatigue behavior, with the rapid drop in peak stresses occurring at the first stage for all four presented states. The main difference among the specimens lies in the duration of the second linear stage. It was observed that exposure to vacuum in contact with lithium-ceramics pebbles has little effect on fatigue life, with the values

of fatigue life being close to those of the as-received specimens. For a total strain range of 0.6–1%, the fatigue life is slightly inferior compared to as-received state, while it slightly exceeds it for a total strain range of 1.6%.

In regards to the specimens exposed to the purge gas flow without pebbles, there is a noticeable decrease in the number of cycles to failure compared to the as-received specimens. However, despite the formation of a corrosion layer with a similar structure and thickness, the negative impact of exposure on fatigue life is not as severe as observed in the case of exposure to the ceramic breeder environment. For a total strain range of 0.6%, the peak stress load versus number of cycles curve was found to be intermediate between the curves for the as-received specimen and those exposed to the ceramic breeder environment. For larger total strain ranges, the impact of exposure to the purge gas is less significant.

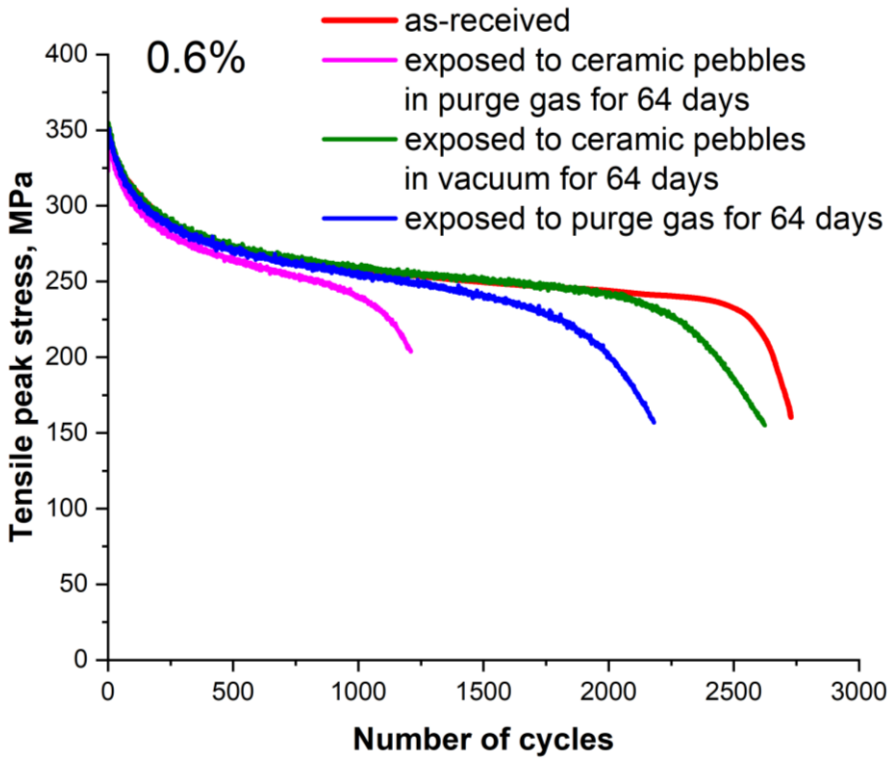

Fig. 4.62. Typical tensile peak stress versus the number of cycles tested at a total strain range of 0.6% for sub-sized specimens in the as-received state and after exposure to different environments for 64 days, including the ceramic breeder environment, vacuum in contact with Li-ceramics pebbles, and a purge gas

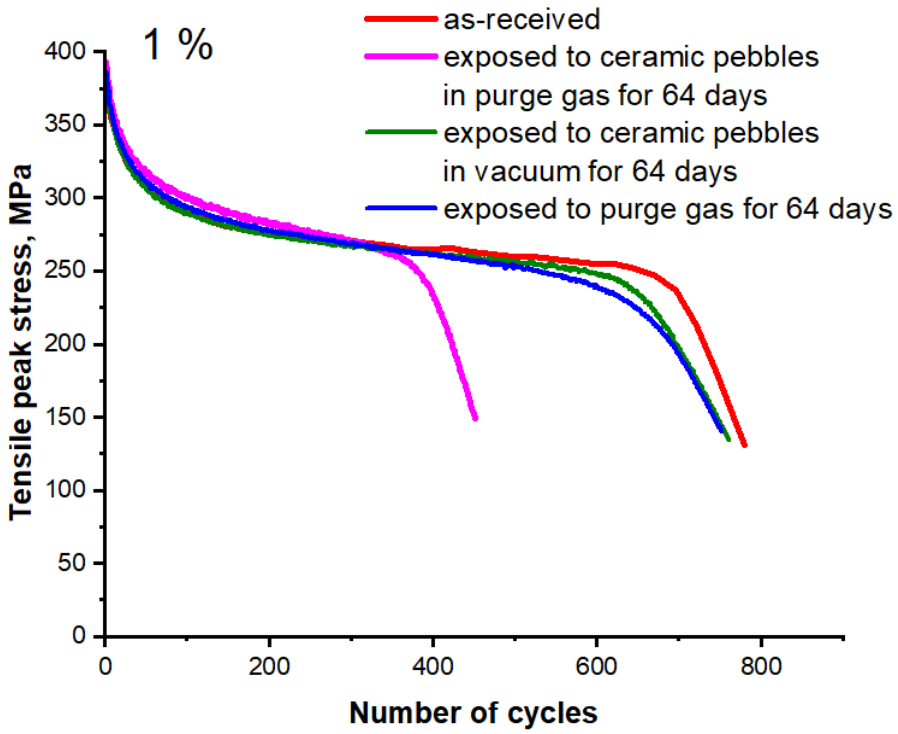

Fig. 4.63. Typical tensile peak stress versus the number of cycles tested at a total strain range of 1% for sub-sized specimens in the as-received state and after exposure to different environments for 64 days, including the ceramic breeder environment, vacuum in contact with Li-ceramics pebbles, and a purge gas

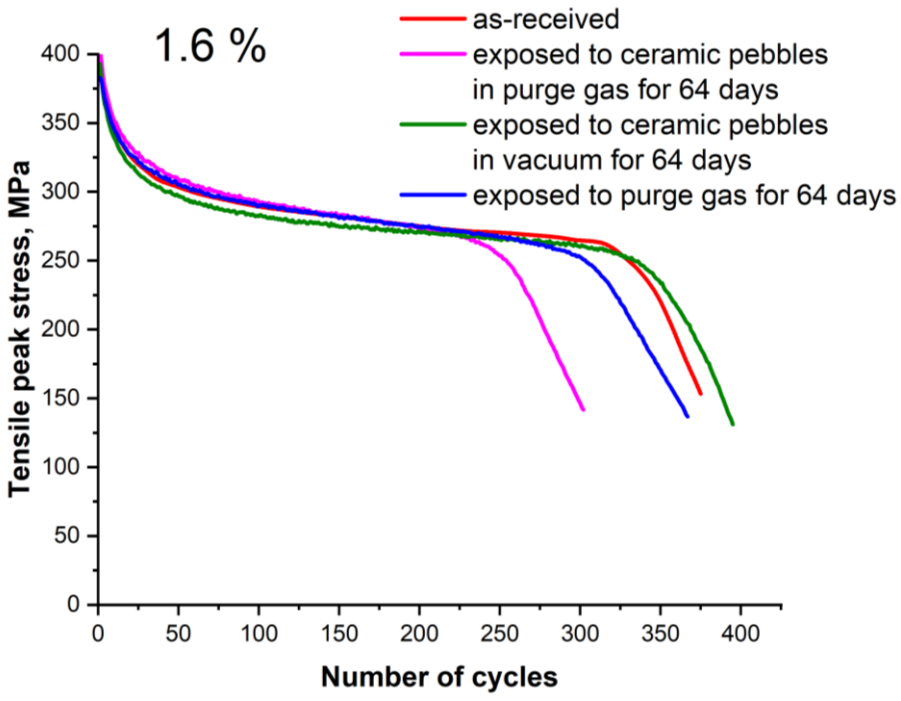

Fig. 4.64. Typical tensile peak stress versus the number of cycles tested at a total strain range of 1.6% for sub-sized specimens in the as-received state and after exposure to different environments for 64 days, including the ceramic breeder environment, vacuum in contact with Li-ceramics pebbles, and a purge gas

Fig. 4.65 presents a summary of the LCF test results obtained from the additional treated specimens, plotted alongside the results of tests on the as-received specimens and specimens exposed to the ceramic breeder

environment [43]. The diagram clearly illustrates that exposure to ceramic pebbles in vacuum has no significant effect on the LCF lifetime compared to the as-received state, as the error bars for these states overlap. In contrast, exposure to a purge gas flow reduces the LCF lifetime, at least for the total strain range of 0.6%, but not as much as exposure to both pebbles and purge gas atmosphere. This is likely due to the absence of imprints of Li-ceramics pebbles, which leads to a delayed formation of micro-cracks. The formation of a thin corrosion layer in the case of exposure to vacuum in contact with lithium-ceramics pebbles has no significant effect on the fatigue life, both because of the small thickness of the corrosion layer and the barely visible lithium-ceramics pebbles imprints. Therefore, the most pronounced effect on fatigue life degradation occurs only when both effects are combined – lithium-ceramics pebble attack and corrosion due to the purge gas atmosphere with impurities.

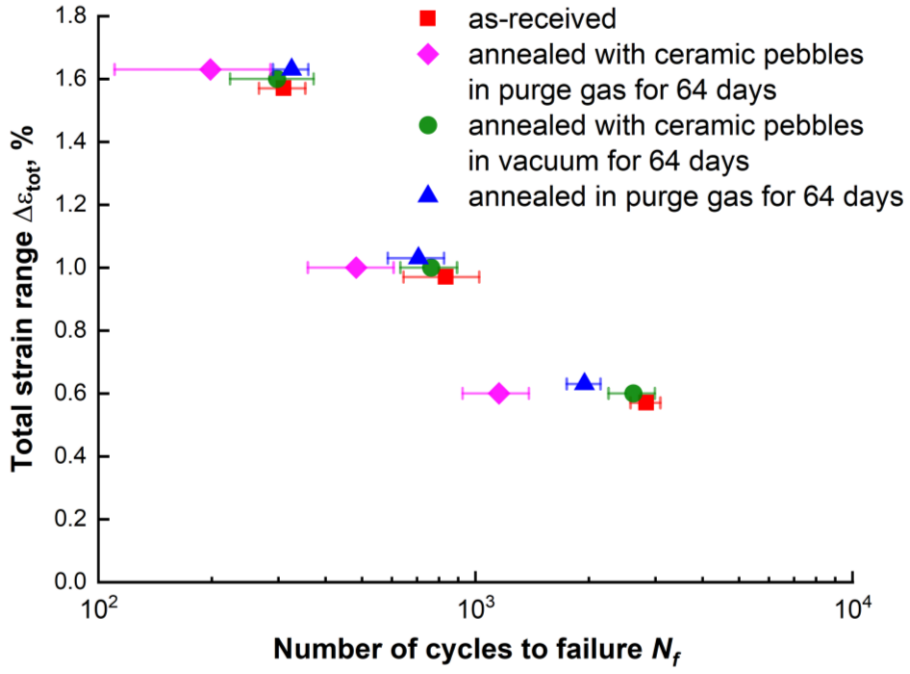

Fig. 4.65. (a) Results of the LCF tests of EUROFER97 specimens in as-received and exposed to various environments conditions [43]. The specimens were tested at 550°C at three different total strain ranges of 0.6, 1, and 1.6%. Vertical offset within a strain range is used to avoid data overlap.

4.2.4 Summary and conclusions

Additional experiments have revealed that impurities in the purge gas, specifically oxygen and water vapor, are the primary cause of corrosion on EUROFER97 steel surfaces when exposed to the ceramic breeder environment. Exposure of EUROFER97 specimens to lithium-ceramics pebbles in a vacuum does not result in noticeable corrosion, with corrosion layer thickness not exceeding 1 µm, regardless of the exposure time. Conversely, exposing EUROFER97 specimens to purge gas alone (without lithium-ceramics pebbles) results in corrosion of similar thickness to that observed in the ceramic breeder environment case.

After conducting LCF tests, it was found that exposure of EUROFER97 specimens to vacuum in contact with pebbles did not lead to significant changes in the number of cycles to failure. Exposure only to purge gas, without pebbles, resulted in a decrease in the number of cycles to failure, but not as significantly as in the

case of exposure to the ceramic breeder environment. Thus, it can be concluded that it is the combination of the purge gas atmosphere and contact with lithium-ceramics pebbles that leads to the most significant deterioration of fatigue properties in EUROFER97 steel.

4.3 Fatigue properties deterioration factors

In the preceding sections, it was demonstrated that a study aimed at simulating the operation of EUROFER97 tubes in contact with a tritium breeder in the blanket of the future DEMO fusion reactor resulted in the premature failure of the specimens. The primary cause of this failure is undoubtedly the prolonged exposure of the EUROFER97 samples to lithium-ceramics pebbles in a purge gas atmosphere at 550°C. This exposure caused corrosion, which was attributed to impurities present in the purge gas atmosphere. Conversely, when the same exposure was conducted under a vacuum, the corrosion layer formed was significantly thinner, and there was no noticeable decrease in the fatigue life of the specimens. Nevertheless, the exposure to a purge gas without the presence of lithium-ceramics pebbles resulted in a decrease in the fatigue life of the EUROFER97 specimens, albeit not to the same extent as in the main experiment. The factor responsible for this reduction in the number of cycles to failure during fatigue testing remains unclear, and obtaining this knowledge in accordance with WP 5 (Fig. 3.1) would be crucial in mitigating the consequences of this effect or reducing its impact.

To answer this question, one must consider the well-known fact that the structure of a material determines its properties. Therefore, one must investigate the structural characteristics of the material that may manifest themselves before, during, and after LCF tests. One crucial factor in this regard is the accumulation of hydrogen inside the metal in a hydrogen-containing environment, which can lead to hydrogen embrittlement and reduced fatigue life [64,65]. However, detecting hydrogen in small amounts within the structure using standard methods for studying the microstructure is practically impossible. In such cases, indirect methods for detecting the presence of hydrogen in the structure and its impact on ductility during Charpy impact tests can be utilized. These methods can provide crucial insights into the presence of hydrogen embrittlement, even when the hydrogen is present in small quantities. Therefore, identifying the presence of hydrogen and its impact on the material's properties may be crucial in understanding the reduced fatigue life of EUROFER97 specimens after exposure to the ceramic breeder environment.

Another additional factor that may contribute to the reduced fatigue life of EUROFER97 specimens after pre-corrosion test is the presence of micro-cracks on the Li-ceramics pebble imprints, as illustrated in Fig. 4.11 and Fig. 4.15. However, the root cause of these cracks remains unclear, including whether they propagate further during LCF testing or if they penetrate deeply into the specimen during testing.

Moreover, it is unclear why the effect of exposure to the ceramic breeder environment is more significant in sub-sized samples compared to standard samples. An analysis of the fractography of such samples is necessary to draw conclusions on the crack growth rate and identify how the scale factor impacts the theoretical number of cycles to failure.

In conclusion, this section aims to address the acceptable conditions for using EUROFER97 components in a breeder blanket, assuming that the factors leading to reduced fatigue life cannot be overcome or mitigated. Additionally, potential solutions to eliminate the detrimental factors contributing to reduced fatigue life will be discussed.

4.3.1 Hydrogen embrittlement

Since the atmosphere in which the EUROFER97 samples were exposed to lithium-ceramics pebbles was a purge gas consisting of helium and 0.1 vol.% hydrogen, it would be reasonable to assume that hydrogen could penetrate deeply into the material. As per prevailing theories, hydrogen can potentially accumulate in voids under high-pressure, impede the creation of dislocations during plastic deformation, or form hydrides. This results in so-called hydrogen embrittlement, with different materials reacting differently to an increased hydrogen content.

To determine the hydrogen content, carrier gas hot extraction (CGHE) investigations were conducted on EUROFER97 samples exposed to the ceramic breeder environment for 64 days. Results indicate that the as-received EUROFER97 exhibits hydrogen amounts lower than the precision of measurement (<0.23 ppm). However, a sample exposed to the ceramic breeder environment demonstrates a hydrogen content of 6.7±1.0 ppm. Removal of the entire corrosion layer through grinding reveals a significantly reduced hydrogen content of 2.6±0.3 ppm, thereby indicating that most of the hydrogen is concentrated in the corrosion layer close to the surface, with only a negligible amount diffusing into the material. Consequently, the analysis carried out confirms the presence of hydrogen after the exposure to the ceramic breeder environment, albeit in small quantities.

There are several works in the literature on the hydrogen embrittlement of EUROFER97 steel, but the impact of the concentration of dissolved hydrogen on the mechanical properties is still unclear. Some studies have shown that a concentration of already 2–4 ppm of hydrogen can significantly decrease fracture toughness of EUROFER97 [66,67], while others have found that 1.5 and 4 ppm of hydrogen have practically no effect on tensile properties [68]. In another study, samples loaded with 16.1 ppm of hydrogen did not experience changes in strength properties but did show a slight decrease in plasticity [69]. Given these mixed results, it is difficult to predict how exposure to the ceramic breeder environment may affect the mechanical properties of EUROFER97 steel.

The Charpy impact test is considered one of the most sensitive methods for detecting various types of material embrittlement. To this end, sub-sized Charpy specimens of EUROFER97 were exposed to lithium-ceramics pebbles in a purge gas atmosphere for 64 days (Fig. 4.66). For comparison, specimens in their original state were also tested, alongside specimens exposed to vacuum (without ceramic pebbles) for the same duration of 64 days. The experiments were performed at temperatures ranging from -120 to -50°C.

Fig. 4.66. Charpy impact test specimens (a) before and (b) after exposure to the ceramic breeder environment for 64 days

Fig. 4.67 depicts the results of the Charpy impact tests. Overall, the impact test outcomes for all specimens demonstrate a resemblance. The ductile-to-brittle transition temperature (DBTT) is -110°C, -97°C, and -113°C for the as-received, exposed to the ceramic breeder environment, and annealed in vacuum states, respectively. Notably, the slight differences observed in the curves are primarily attributable to variations in crack initiation. A comparison of the upper shelf energy (USE) of the pre-corroded samples with that of the as-received samples reveals no significant difference. Consequently, it can be inferred that the samples exposed to the ceramic breeder environment did not undergo considerable embrittlement.

The effect of hydrogen embrittlement on DBTT and USE was explored in structural steels other than EUROFER97. Results from [70] indicate that hydrogen concentrations of 1–1.29 ppm did not have a negative impact on steel API 5L X70. However, Fassina et al. observed an increase in DBTT and a decrease in USE for pipeline steels API 5L X65 and ASTM A 182 F22 with hydrogen content in the range 0.6–2 ppm [71]. Golisch et al. studied L415ME pipe steel, which had a hydrogen content of 3.43 ppm, and also observed a significant reduction in impact energy during Charpy tests [72]. These findings suggest that, at least in the case of pipeline steels, the effect of hydrogen embrittlement on Charpy properties was evident.

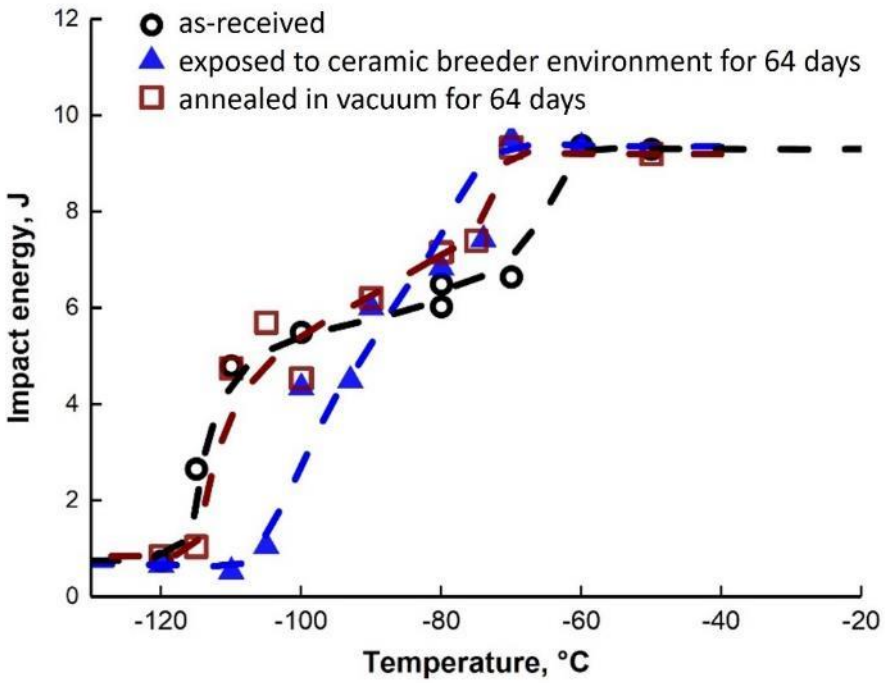

Fig. 4.67. Charpy impact energy versus test temperature curves for EUROFER97 in different conditions

Despite the presence of hydrogen in the sample composition of EUROFER97 exposed to the ceramic breeder environment using CGHE method, no noticeable embrittlement effect was observed. This lack of effect may be attributed to the low amount of hydrogen present in the EUROFER97 sample, which amounted to approximately 2.6 ppm, excluding the corrosion layer. It is possible that this amount of hydrogen was insufficient to produce an embrittlement effect that would have been detectable by the methods employed in this study. However, after 128 days of exposure, it would be expected that the EUROFER97 specimens would have accumulated a greater amount of hydrogen, resulting in a significant decrease in the number of cycles to failure during LCF tests as compared to tests conducted at 32 or 64 days (which is not the case). Nevertheless, it is unlikely that EUROFER97, being a ductile steel with relatively low strength, would be susceptible to hydrogen embrittlement, particularly at 550°C. Thus, the observed effect of a decrease in the fatigue life of EUROFER97 specimens during exposure to the ceramic breeder environment cannot be attributed to hydrogen embrittlement.

Maday et al. conducted LCF tests on EUROFER97 samples charged with hydrogen and found that the number of cycles to failure did not change when the hydrogen content was 2.2, 2.4 or 2.7 ppm, regardless of the total train range and frequency of testing [31,73,74]. However, at hydrogen concentrations of 6.6 and 7 ppm, a significant decrease in lifetime from 42 to 98% was observed at various loads and frequencies. Therefore, it can be inferred that a decrease in the lifetime of EUROFER97 samples after exposure to the ceramics breeder environment is not expected, based on the findings of Charpy impact tests and the LCF tests conducted in [73,74].

4.3.2 Cracks before and after LCF tests

One of the evident factors contributing to the premature failure of EUROFER97 specimens exposed to lithium-ceramics pebbles in a purge gas atmosphere is the presence of preexisting micro-cracks on the EUROFER97 surface even prior to LCF testing. As illustrated in Section 4.1.2, such exposure induces the formation of a complex corrosion layer, with a main surface feature as imprints representing traces of the impact of lithium-ceramics pebbles on the EUROFER97 sample surface.

Fig. 4.68 displays micro-cracks developed on imprints after exposure to the ceramic breeder environment for various durations. The results indicate that micro-cracks can be found even after 8 days of exposure. The micro-cracks propagate radially from the center of the imprint (where surface spallation occurs in the figure) along the iron oxide layer. After exposure for 16 days, the micro-cracks diverge by 100–150 µm from the center of the imprint, reaching the region of pure iron hillock growth (Fig. 4.68b). Such micro-cracks may also trigger surface spallation, exposing the internal layer of the specimen (Fig. 4.68c). This observation suggests that micro-cracks can penetrate through the thickness of the corrosion layer, reaching the internal ferritic phase (EUROFER97).

Observations of specimens exposed to lithium-ceramics pebbles in a purge gas atmosphere for 64 days reveal that micro-cracks propagate along the iron oxide layer and deviate in different directions depending on the crystals orientation (Fig. 4.68d). This suggests that the micro-cracks were formed after exposure, most likely during the cooling stage of the samples. If the micro-cracks were preexisting, the crystals could grow and heal the crack during exposure so that the micro-cracks would not be visible on the surface.

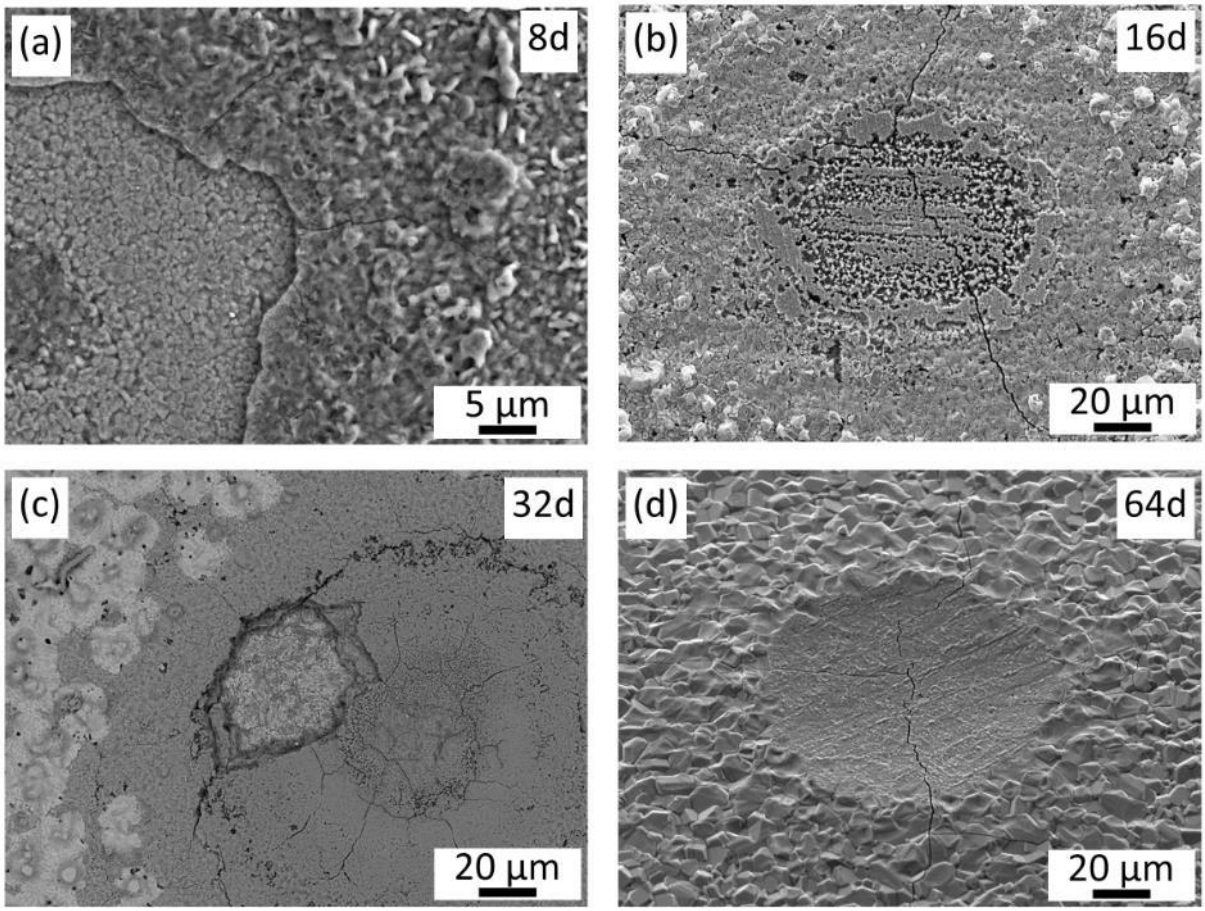

Fig. 4.68. EUROFER97 surface showing the formation of micro-cracks on the imprints of Li-ceramics pebbles after exposure to the ceramic breeder environment for different durations: (a) 8 days, (b) 16 days, (c) 32 days, (d) 64 days

After exposure, the specimens were cooled from 550°C to room temperature at a relatively slow rate of approximately 32 K/h (>100 K/h at the beginning of cooling in the 550-500°C temperature range). Despite this, it is evident that micro-cracks occurred during the cooling process. One plausible explanation for this phenomenon is that the corrosion layer, or a portion of it, experiences tensile stresses as a result of the difference in thermal expansion coefficients. Stresses arise due to the fact that a massive substrate in the form of EUROFER97 specimen shrinks when cooled, regardless of the presence of a thin corrosion film on the surface. In this case, the corrosion layer, being adhered to EUROFER97, will have to shrink by the same amount as the substrate. At the same time, by taking into account the values of the thermal expansion coefficients and the temperature difference, it is possible to estimate the stresses that a given corrosion layer will experience.

In general, the deformation of a film can be estimated based on the deformation of the film-substrate joint. In this case, the deformation of the substrate and film can be calculated as $\varepsilon_{EF}=\alpha_{EF}\cdot\Delta T$ and $\varepsilon_c=\alpha_c\cdot\Delta T$, respectively ($\alpha_{EF}$ and α_c are the coefficients of linear thermal expansion (CTE) for EUROFER97 and a corrosion layer, ΔT – the temperature difference). Therefore, the film will undergo deformation in the form of

$\varepsilon=(\alpha_c-\alpha_{EF})\cdot\Delta T$. In this scenario, a positive difference in deformations results in tension in the corrosion layer during cooling, whereas a negative deformation leads to compression.

Fig. 4.69 depicts a cross-sectional micrograph of a corrosion layer that consists of an outer layer of pure iron and iron-rich oxide, an intermediate layer of chromium-rich oxide, and an inner corrosion layer of EUROFER97 containing particles that are rich in chromium and oxygen. On the right to the photograph is a table that indicates the phase composition of the layers and the corresponding coefficients of thermal expansion (CTE) for these phases. With this information, it is possible to estimate the approximate deformation that different corrosion layers should undergo. As EUROFER97 is a massive body, the stresses that the corrosion layer can exert on it are negligible. The chromium-rich oxide layer will experience compressive stresses (the strain difference between Cr-rich oxide layer and EUROFER97 is approximately -0.17%). Such compressive stress is unlikely to cause the layer to crack or fracture. In contrast, the iron-rich oxide in the outer corrosion layer will experience tensile stresses (the strain difference between Fe-rich and Cr-rich oxide layers is on average 0.05%). This tensile stress is the primary cause of the cracking and partial spallation relative to the chromium-rich oxide (Fig. 4.69). Furthermore, the outer corrosion layer may have imprints with slightly thinner in places, which can create a stress concentrator that leads to local cracking in these areas. It should also be noted that lithium can diffuse from the Li-ceramics pebbles into the corrosion layer (as shown in section 4.1.3), which can further enhance cracking. All these factors may contribute to the observed radial micro-cracking in the imprint zone, as well as the occasional spallation of the outer corrosion layer.

Regarding the actual expected conditions of EUROFER97 application in the DEMO breeder blanket, it is highly likely that micro-cracks will also form under rapid heating and cooling cycles in accordance with the pulsed operation. These cycles involve even faster temperature changes, which can cause significant thermal stresses in the corrosion layer, leading to micro-crack formation, particularly in the iron-rich outer layer of the corrosion layer. Moreover, micro-cracks formed in the corrosion layer will be exacerbated by other environmental factors present in the breeding blanket. EUROFER97 tubes will experience substantial thermomechanical stresses that can generate additional stresses promoting crack formation. In addition, chemical attack from lithium-ceramics pebbles, impurities in the purge gas atmosphere, and neutron irradiation can all contribute to the propagation of micro-cracks in the corrosion layer. Thus, the actual operating conditions of the DEMO fusion reactor are likely to be much more severe, increasing the likelihood of micro-crack formation and propagation in the EUROFER97 corrosion layer.

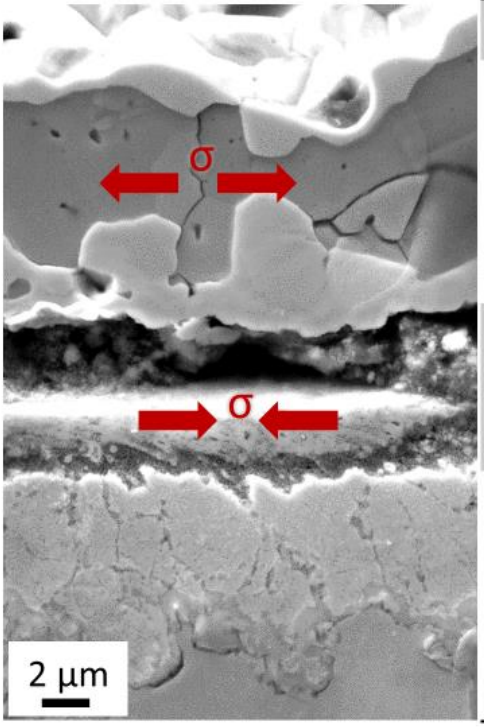

Phase	CTE, 10^{-6} K^{-1}
Fe	10–12
Fe-rich oxides	9–15
Cr-rich oxide	7–8.5
EUROFER	10–12

Fig. 4.69. Tensile and compressive stresses in the corrosion layer formed during EUROFER97 cooling from the exposure temperature, with the designation (on the right) of the phases in the corrosion layer and their corresponding thermal expansion coefficients

Imprints of lithium ceramics not only serve as sites of micro-crack initiation during cooling of samples after exposure, but what is more important, also during fatigue tests. These imprints, along with the pre-existing micro-cracks, act as significant stress concentrators during the tests. In areas near the micro-cracks and surface cleavages, there is a local increase in stresses, leading to the facilitated initiation and propagation of larger cracks. This is shown in Fig. 4.70, where stress concentrations are observed at the imprints. If we consider the tension axis passing through the three imprints in the figure, we can assume that small depressions from the imprints result in a relatively smooth increase in stresses, scaling of outer layer in the center of the imprints cause a rapid increase in stresses, and transverse micro-cracks with a small radius at the apex determine the maximum stress.

As highlighted in the literature review, point defects in the form of pits pose a greater risk for crack initiation compared to general corrosion, which spreads uniformly over the surface. These pits or micro-cracks concentrate stress and act as notches, making crack initiation more likely. Without corrosion, approximately 90% of the lifetime is dedicated to crack nucleation and 10% to crack growth on a polished surface, whereas with corrosion, crack nucleation time significantly decreases, and approximately 90% of the lifetime is allocated to crack growth [24,26,28]. As a result, the fatigue life of the sample is seriously reduced due to corrosion.

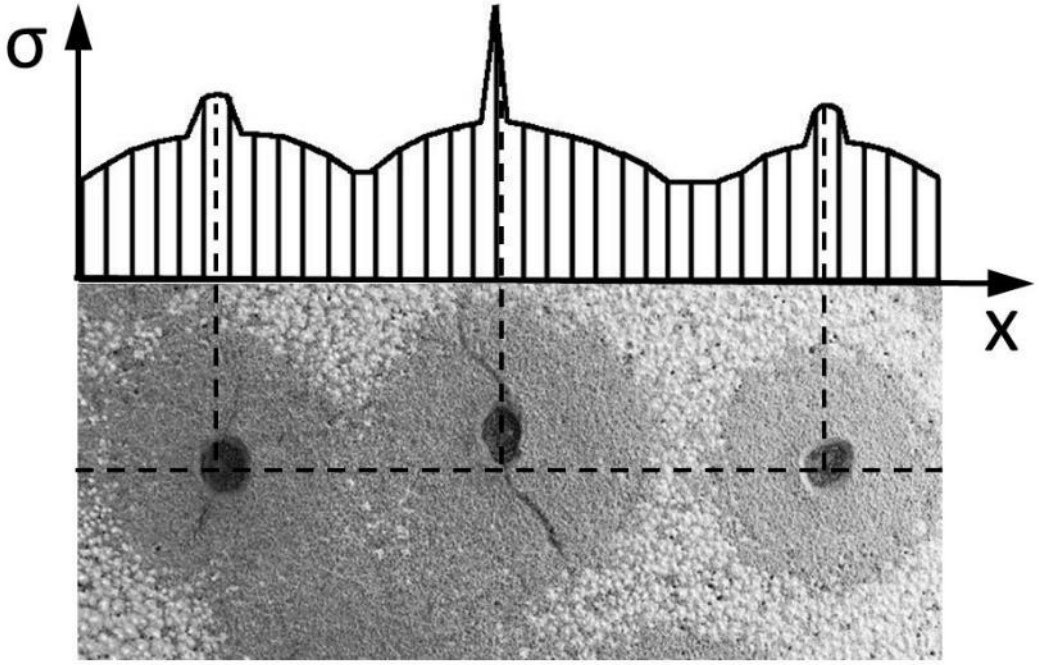

Fig. 4.70. Schematic diagram showing the distribution of stresses arising during tension of EUROFER97 samples with existing defects on the surface, in the form of imprints with micro-cracks or partial spallation of the surface layer

Fig. 4.71 shows typical EUROFER97 specimens after exposure to the ceramic breeder environment for 64 days and subsequent LCF tests. In the case of a sub-sized specimen with a 2 mm diameter, only a few imprints can be seen in the cross-section. It is evident that the fatigue crack runs along the diameter of the imprints. Additionally, the imprint, which is somewhat distant from the destruction zone, also cracked in diameter. On the other hand, in the case of a standard specimen with an 8.8 mm diameter, there are 4.2 times more imprints per cross-section in terms of geometry. In this case, it can be observed that the fatigue crack predominantly passes through imprints, but not as clearly as in the case of sub-sized specimens.

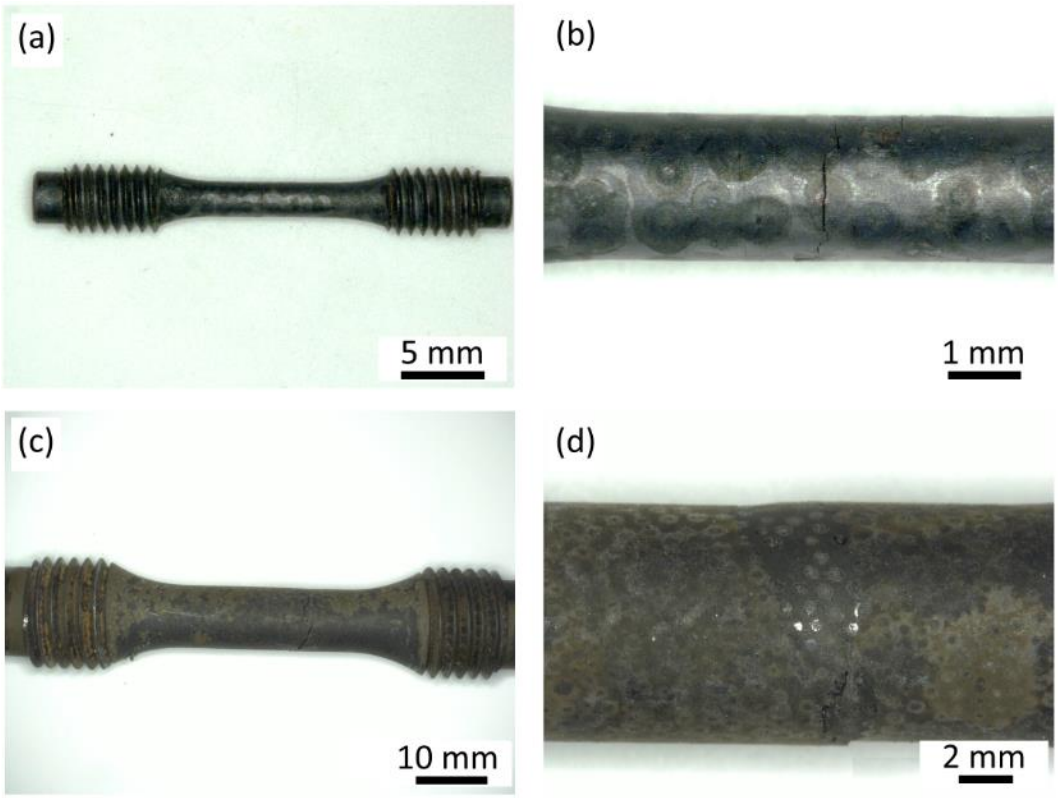

Fig. 4.71. Specimens of EUROFER97 after exposure to the ceramic breeder environment for 64 days followed by LCF testing: a-b) sub-size specimens, c-d) standard specimens. Optical metallography

Fig. 4.72 displays video macro shots of LCF testing performed on one of the EUROFER97 specimens following a 64-day exposure to the ceramic breeder environment with a total strain range of 1.6% [46]. During the initial cycles up to approximately 0.75N_f, the predominant behavior observed is the formation and propagation of small cracks (smaller than ≈1000 μm). It is only at around 300 cycles that visible larger cracks become apparent (as shown in Fig. 4.72b). The red circles in the figure indicate the specific imprints through which the crack propagates, while other imprints do not exhibit such cracking behavior. As testing progresses and reaches approximately 340 cycles, a fatigue crack develops along a part of the imprints previously indicated by red circles. Other cracks cease opening on the imprints due to the onset of strain localization (Fig. 4.72c). While the number of cycles to failure N_f for this particular specimen was calculated to be 388, the testing continued up to 410 cycles. At this point, the fatigue crack opened entirely, resulting in the destruction of the specimen (Fig. 4.72d). These observations indicate that the cracks present on the imprints after exposure represent pre-existing defects that can propagate further during fatigue testing, leading to the development of a fatigue crack in some cases.

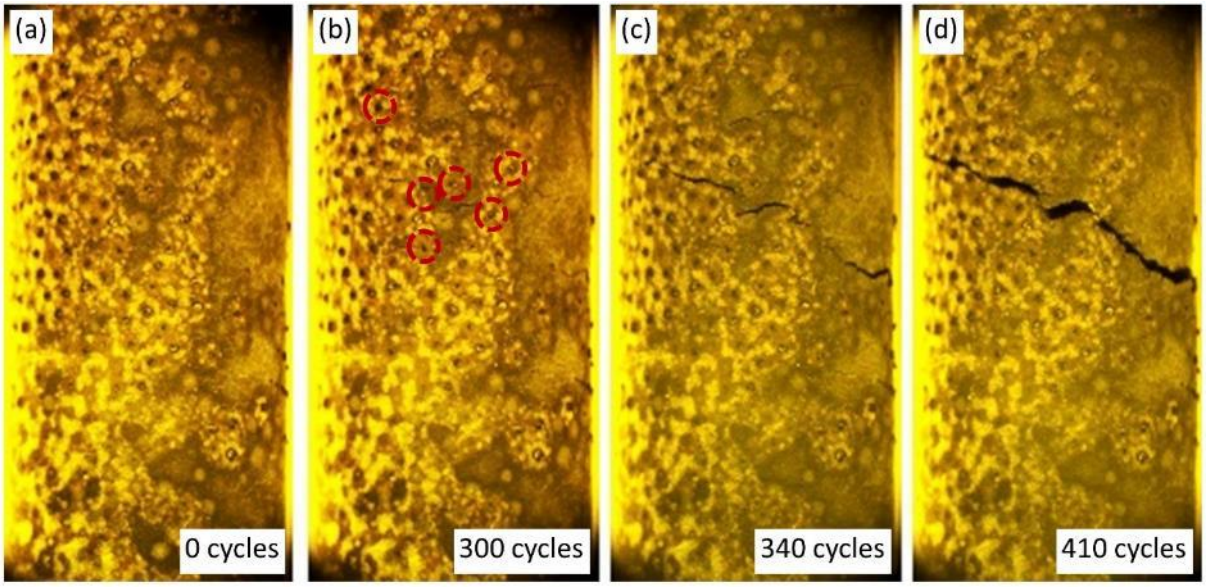

Fig. 4.72. Video macro shots of LCF test of a EUROFER97 sample exposed to the ceramic breeder environment for 64 days: (a) The beginning of the test, (b) After 300 cycles, (c) After 340 cycles, and (d) After 410 cycles. The total strain range was 1.6%, and the number of cycles to failure is 388 cycles. The diameter of the sample is 8.8 mm. In (b), the red circles indicate the imprints on which cracks opened during the tension. The videos were captured using a high-speed camera, and the images were extracted for analysis [46].

Fig. 4.73 illustrates the surface of a sub-sized specimen after the LCF test. The outer corrosion layer often undergoes shearing near the fracture zone, making it difficult to identify imprints. Nevertheless, imprints can be found by their characteristic round shape and the presence of former pure iron hillocks surrounding them. The red circles in the figure indicate the imprints that contributed to cracking during LCF testing. However, there are also imprints present in Fig. 4.73a, which did not cause visible cracking (indicated by blue circles). In general, most of the imprints exhibit small cracks approximately perpendicular to the direction of the load applied. If single small cracks are found far from the fracture site and stress localization (Fig. 4.73b), then closer to the fracture site, multiple cracks and surface chips can be observed on imprints (Fig. 4.73c-d). Overall, the photographs of the surface microstructure suggest that imprints with pre-existing micro-cracks on the surface of sub-sized specimens have a detrimental effect on fatigue life.

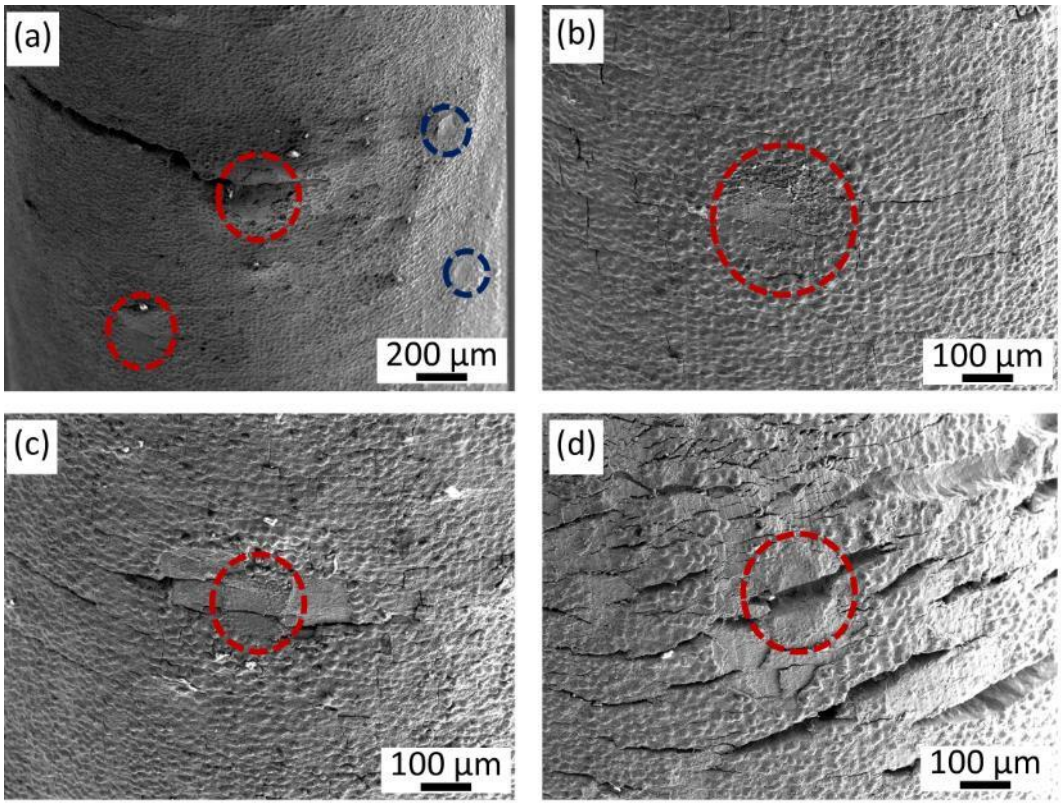

Fig. 4.73. Propagation of existing micro-cracks on imprints (indicated by red circles) after LCF testing of a sub-sized EUROFER97 sample exposed to the ceramic breeder environment for 64 days. The total strain range was 1.6%. Blue circles denote imprints without visible cracks. (a) General view of the sample [46], (b) Area away from the fatigue crack, (c) Area closer to the fatigue crack, and (d) In the fracture zone.

Fig. 4.74 depicts the surface of a standard specimen after LCF testing, showing a greater number of small cracks than that of a sub-sized specimen. The increased number of tension-compression cycles on the standard specimen's surface is thought to contribute to this observation. The surface small cracks are evident both near the fracture zone (Fig. 4.74a) and at a distance from it (Fig. 4.74b). Most of the imprints lead to the formation of small cracks, with red circles indicating only those imprints that generate relatively long cracks. In addition to the usual cracks for tension, which are located perpendicular to the direction of load, cracks propagating along the load direction are also observed, likely arising during compression (Fig. 4.74c). Similar to sub-sized specimens, the growth of macro-cracks and fatigue cracks seems to be facilitated at imprints with pre-existing micro-cracks on the surface of standard specimens (Fig. 4.74d).

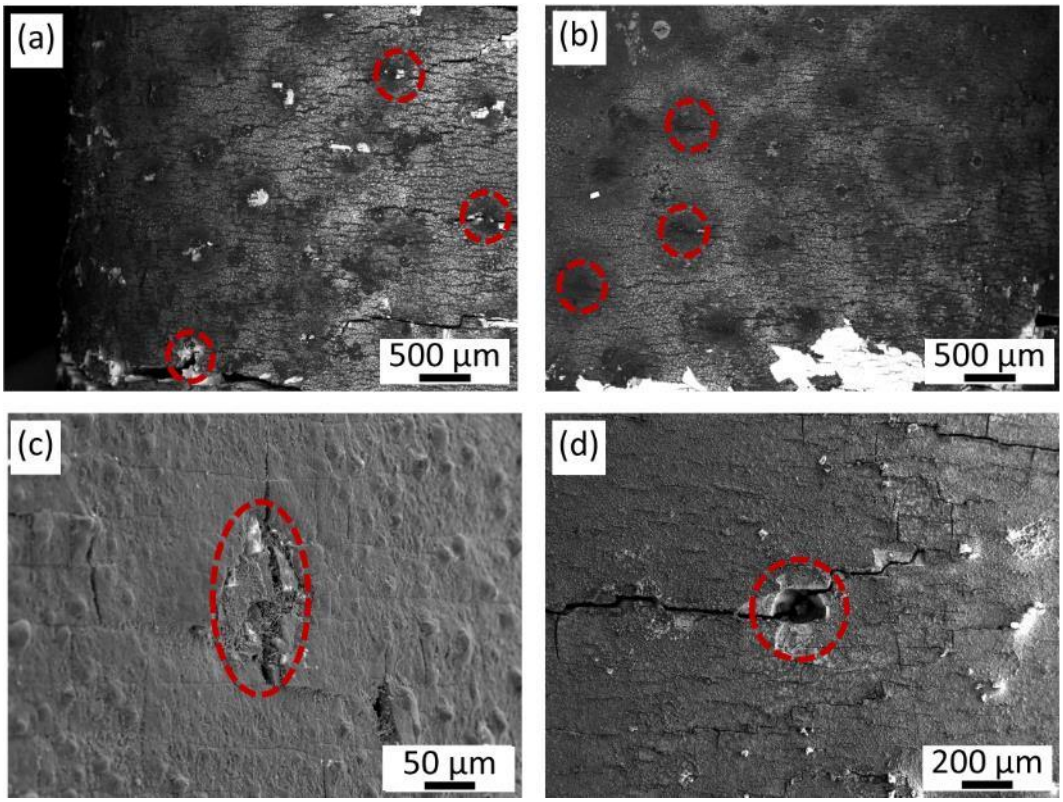

Fig. 4.74. Propagation of existing micro-cracks on imprints (indicated by red circles) after LCF testing of standard EUROFER97 specimen exposed to the ceramic breeder environment for 64 days. The total strain range was 1.6%. (a) Area close to fatigue crack [46], (b) Area away from the fatigue crack, (c) Crack propagating on the imprint along the strain axis, and (d) In the fracture zone.

Fig. 4.75 presents overview photographs of longitudinal sections of the initial and corroded standard specimens after LCF tests with total strain ranges of 0.6% and 1.6%. The photographs were taken at approximately equal distances from the fatigue crack. For the 0.6% total strain range, only a few cracks are observed in both specimens, whereas a higher number of small cracks propagate within the sample for the larger total strain range. The general longitudinal sections of the initial and exposed to the ceramic breeder environment specimens exhibit no significant differences, aligning with the overall fatigue behavior (stresses, fatigue softening) of the specimens. Apparently, the main reason for the difference in the number of cycles to failure can be attributed to the existence of micro-cracks on the imprints of the pre-corroded specimens, ultimately facilitating the initiation and development of the fatigue crack. However, towards the end of the testing, the final appearance of the specimens shows only negligible variation.

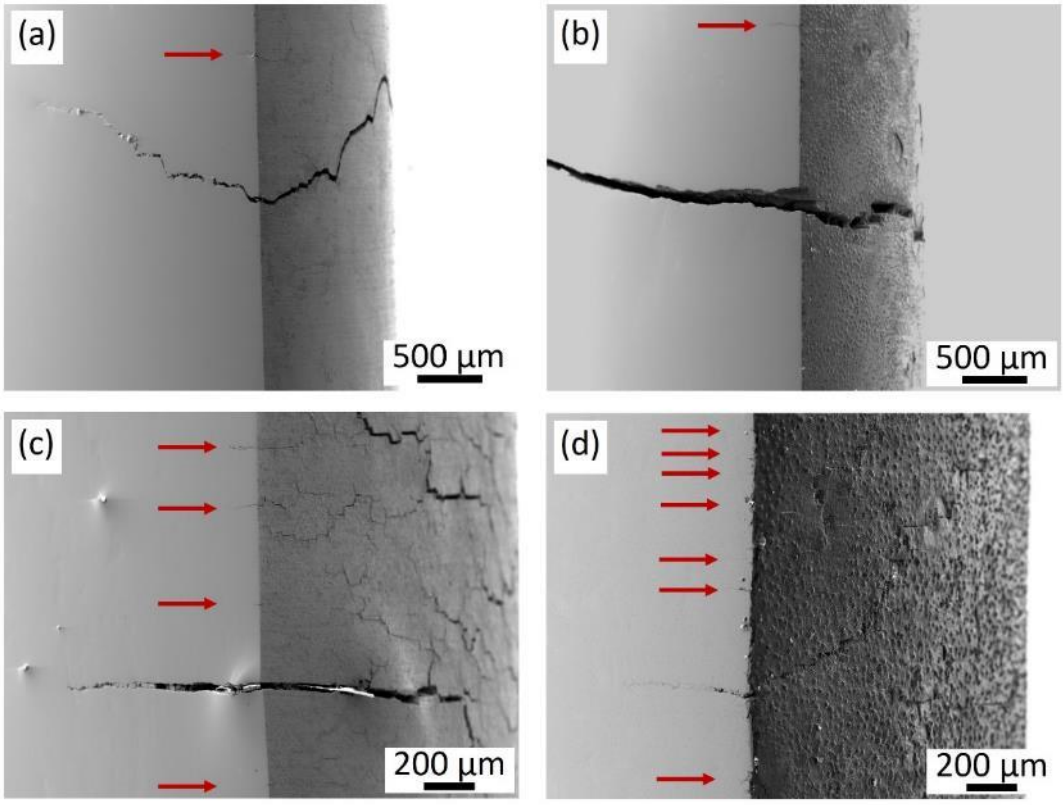

Fig. 4.75. Longitudinal section of standard EUROFER97 specimens after LCF testing with total strain range of: (a,b) 0.6%, (c,d) 1.6%. (a,c) as-received state, (b,d) after exposure to the ceramic breeder environment. Red arrows indicate small cracks propagating inside the specimen.

Fig. 4.76 shows specimens that have undergone LCF testing and were cut along their length to examine how deep cracks propagate from imprints. It is clear from the figures that cracks can penetrate deep into the specimen, sometimes several hundred microns, even far from the fracture zone (Fig. 4.76a-c) and sometimes without clearly visible crack propagation on the surface (e.g. Fig. 4.76b). In some cases, not only one but several cracks penetrate deep into the imprint (Fig. 4.76b-d). These observations suggest that the imprints serve as sites for fatigue crack initiation and that the cracks observed on the surface, passing through or starting with imprints, are not limited to surface cracks passing through a relatively brittle corrosion layer.

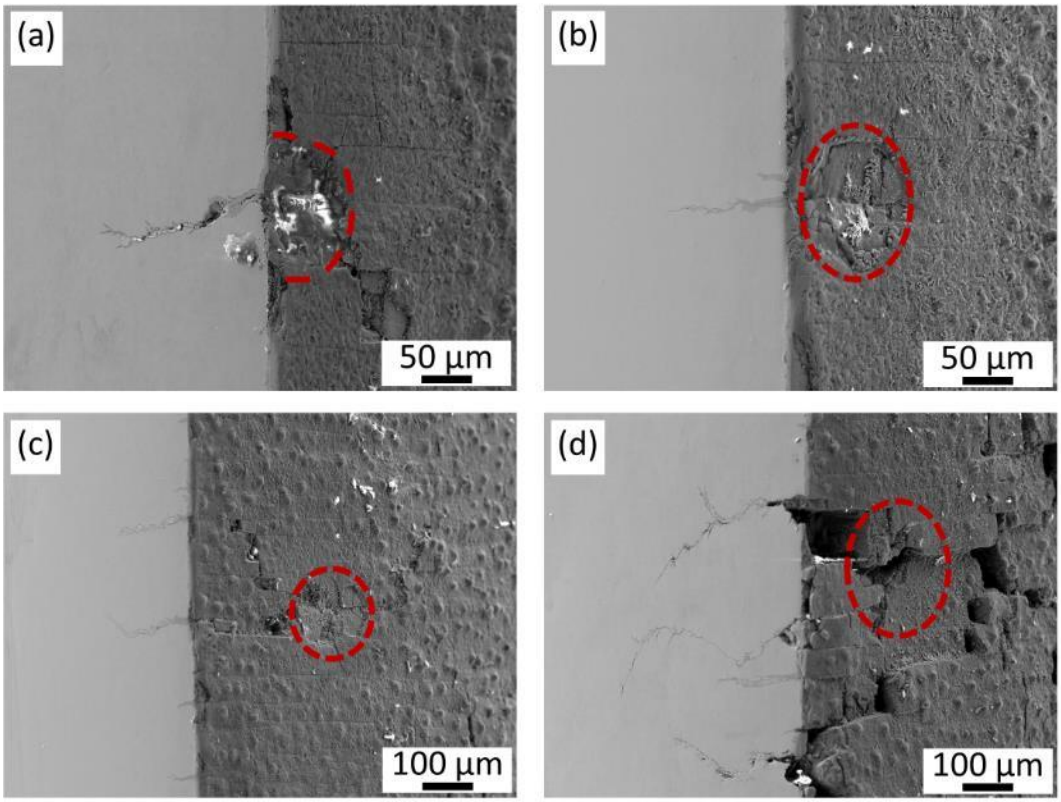

Fig. 4.76. Longitudinal section of standard EUROFER97 pre-corroded specimens after LCF testing, showing the propagation of existing cracks on the imprints (marked in red) deep into the specimen [46]: (a) Imprint on the longitudinal section, (b-e) Imprint near the longitudinal section. (a-c) Imprints away from the fatigue crack, and (d) In the fracture zone. The total strain range was 1.6%.

The study of EUROFER97 specimens after exposure to the ceramic breeder environment and LCF tests showed that the presence of pre-existing small cracks, which arise during cooling due to the difference in coefficient of thermal expansion, and imprints have a significant effect on fatigue life. These cracks on imprints serve as fatigue crack initiation sites and facilitate the growth of macro-cracks and fatigue crack. The number of cycles to failure for pre-corroded specimens decreases due to the presence of such cracks, since no time is required for the formation of surface damage in form of micro-cracks. Fatigue cracks were observed to grow predominantly along the pre-existing cracks. Additionally, testing of specimens exposed only to a purge gas atmosphere, which do not have imprints and cracks, also proves that pre-existing cracks worsen the fatigue life. In the case of exposure to a purge gas, the number of cycles to failure is greater than in the case of exposure to the ceramic breeder environment. The study emphasizes the importance of minimizing the corrosion of EUROFER97 in the presence of Li-ceramics pebbles causing the cracking before subjecting it to fatigue loading, as they significantly reduce the fatigue life of the material.

4.3.3 Size effects on LCF lifetime

Sections 4.1.4 and 4.1.5 detail the outcomes of a low-cycle fatigue assessment conducted on sub-sized and standard specimens in the as-received state and after being exposed to the ceramic breeder environment. The exposure conditions were the same, only the final polishing of the specimens differed. As already noted, the standard specimens were polished as usual radially, and the sub-sized specimens axially, because with

small specimen sizes, small grooves from radial polishing can have a significant effect on fatigue properties. The findings indicate that standard specimens exhibited greater fatigue life in comparison to sub-sized specimens under similar conditions. As already mentioned, this phenomenon was previously observed in standard and sub-sized EUROFER97 specimens in the as-received state [59]. Nonetheless, further investigation is required to elucidate the underlying reasons for the decrease in fatigue life observed in smaller samples, especially in cases where samples have been exposed to lithium-ceramics pebbles in a purge gas atmosphere. Such an inquiry would provide insights into the potential implications of reduced fatigue life on actual EUROFER97 components which will be used in a breeder blanket. The findings could help assess the criticality of such pre-corrosion effects and their impact on component performance.

As previously mentioned, small-sized specimens were purposely designed to ensure a maximum number of samples within a minimal volume, for instance, for neutron irradiation as part of the small specimen test technology program [75,76]. Specifically, sub-sized specimens for fatigue testing were developed at KIT. In [75], it was indicated that *S-N* results, along with cyclic stress-strain curves of these specimens, align well with data obtained from significantly larger standard specimens. In [77], Hirose et al. achieved similar outcomes using cylindrical specimens of RAFM steel F82H, with diameters of 6 mm and 1.25 mm. Additionally, Marmi et al. tested EUROFER97 specimens with a diameter of 2.6 mm, and their findings highlighted that room temperature fatigue properties were close to those observed in other RAFM steels like F82H or MANET [78]. In [79], fatigue test data from sub-sized specimens with a 2 mm diameter were compared with standard EUROFER97 specimens. Notably, the standard specimen endured approximately 3600 cycles at room temperature, while the sub-sized endured around 1000 cycles. However, the authors contend that the difference in the number of cycles to failure among various specimens is not larger than the natural scatter. Thus, the effect of specimen size on fatigue properties should still be considered ambiguous, and this deserves a separate study.

Given that the number of cycles required for fracture is affected by the nature of the fracture and the development of fatigue crack, it is reasonable to explore the fracture surfaces of sub-sized and standard specimens. It should be noted that for a total strain range of 1 and 0.6%, the striation lines on the fractography (after tests in air) merge and cannot be counted, so subsequent results were obtained only for a total strain range of 1.6%. Fig. 4.77 presents a photo of the fracture surface of a sub-sized specimen, as well as a panoramic photo of a standard specimen (owing to its significantly larger size) after LCF testing with a total strain range of 1.6%. Notably, the fractography exhibits clear evidence of crack propagation in each cycle, known as striation, despite surface oxidation (tests were conducted at 550 °C in air). Due to intense deformation on the fracture surface, the origin of fatigue crack growth cannot be evidently associated with surface features like imprints. Nonetheless, as demonstrated in Section 4.3.2, it is highly probable that fatigue cracking initiated on pre-existing cracks and imprints after exposure to the ceramic breeder environment. In this context, the distance that fatigue crack propagates in one cycle can be determined, particularly for the final cycles of the LCF test. The crack growth marks often coincide at the beginning of the test, likely due to small crack growth and surface oxidation.

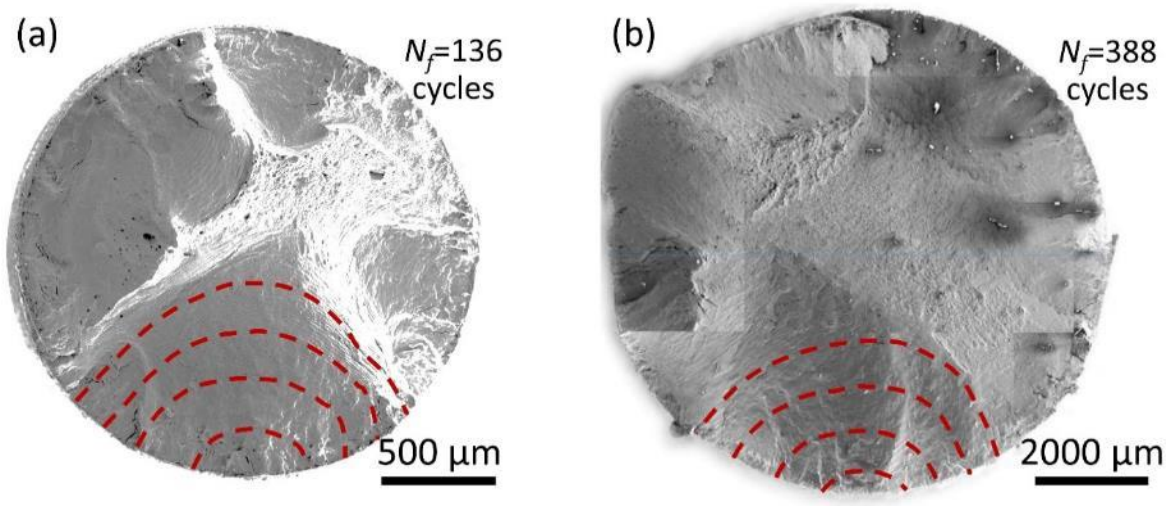

Fig. 4.77. The fracture surface of specimens after LCF test: (a) sub-sized specimen of Ø2 mm with N_f=136 cycles to failure, (b) standard specimen of Ø8.8 mm with N_f=388 cycles to failure [46]. Total strain range 1.6%. The red dotted lines indicate the propagation path of a fatigue crack.

To gain a deeper understanding of the fracture mechanical differences between standard and sub-sized specimens, the crack propagation rate was measured for specimens where possible. For each cycle, starting from the last one, the crack depth was measured as a distance from the initiation point (Fig. 4.78). Note that the last test cycle is not equivalent to the N_f cycle, i.e., the number of cycles to failure. The crack depth at the N_f cycle was measured as 503 µm (25.2% of diameter) and 2427 µm (27.6% of diameter) for the sub-sized and standard specimens, respectively. The fatigue crack depths for both standard and sub-sized specimens were approximately half the diameter 4.4 mm and 1 mm, respectively, before failure. At the end of the test, the crack depth increments were approximately 100 µm and 25 µm for the standard and sub-sized specimens, respectively. The measured portions of the crack depth vs. number of cycles chart are consistent with the appearance of standard ASTM crack depth growth curves [80,81]. In general, the crack growth pattern for standard and sub-sized specimens is similar, with rapid crack growth occurring for the standard specimen after approximately 300 cycles, and for the sub-sized specimen, after about 100 cycles. It should also be noted that visible crack growth occurs when reaching N_d, representing the number of cycles at which the linear second stage of fatigue testing transitions into the final nonlinear stage (Fig. 4.79). Typically, N_d is the number of cycles to the onset of visible crack growth also known as the crack initiation life. Fractography allowed the observation of striation lines from approximately this cycle count onwards both for sub-sized and standard specimens (Fig. 4.78). At lower cycle counts, corresponding to the area of propagation of small cracks, the striation lines practically merge. The depth of crack at N_d cycle was measured as 270 µm (13.5% of diameter) and 1380 µm (15.7% of diameter) for the sub-sized and standard specimens, respectively.

Under the assumption that the fracture initiates from a small crack with depth in the range of µm, the measured data can be fitted with curves to determine the crack depth a (in µm) as a function of the number of cycles N. For a sub-sized sample, the crack depth is given by $a=2.0\cdot10^{-4}\cdot N^{3.0}$, while for a standard sample, the crack depth can be fitted as $a=1.259\cdot10^{-7}\cdot N^{3.974}$. These dependencies can be differentiated to determine the fatigue crack growth rate, da/dN.

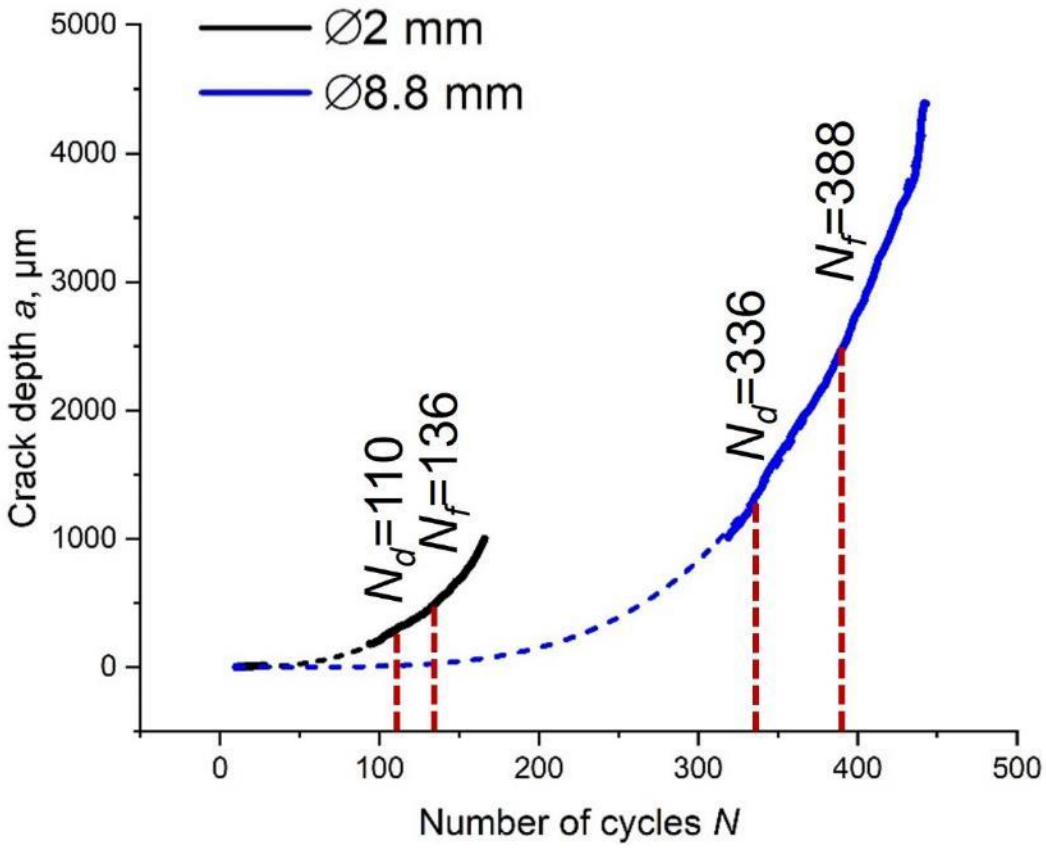

Fig. 4.78. The fatigue crack depth in the sub-sized and standard specimens as a function of the number of cycles during LCF testing. The measured crack depth based on fractography is indicated by solid lines, while the corresponding fitted curves are represented by dashed lines. Red dashed lines show the number of cycles until the formation of a fatigue crack N_d and the number of cycles to failure N_f.

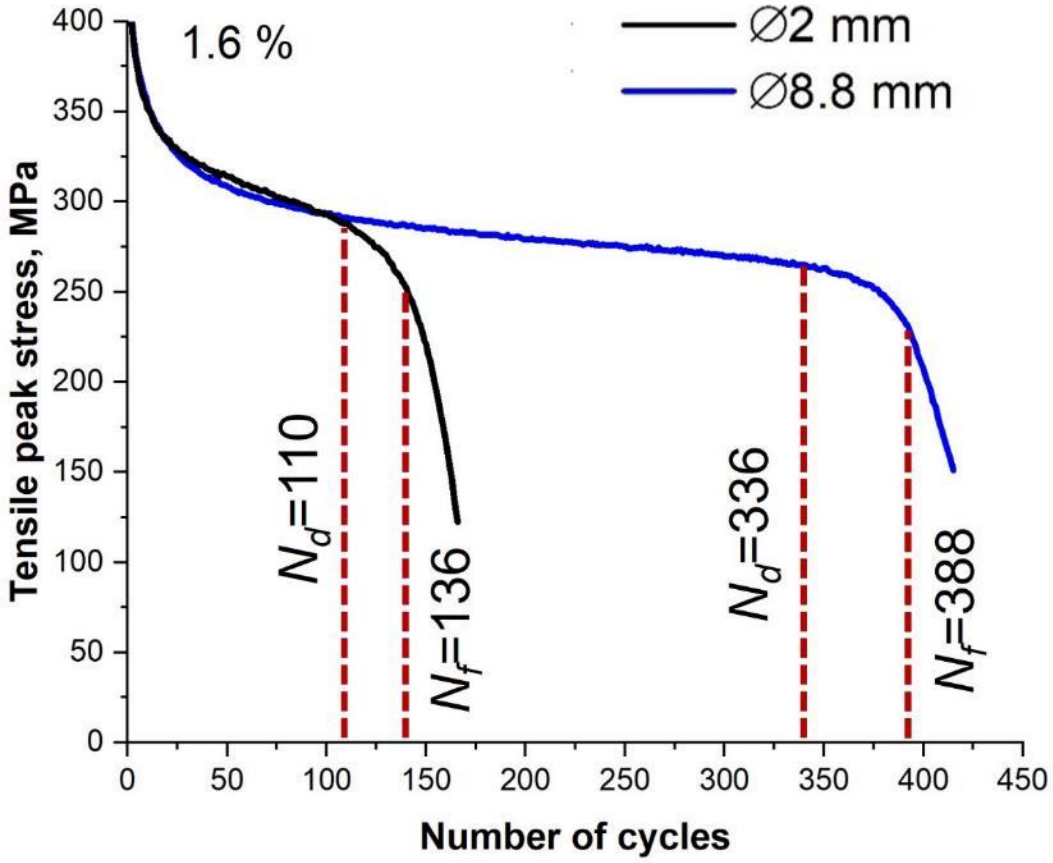

Fig. 4.79. Tensile peak stress versus the number of cycles tested at a total strain range of 1.6% for sub-sized and standard specimens from Fig. 4.77. Red dashed lines show the number of cycles until the formation of a fatigue crack N_d and the number of cycles to failure N_f.

It is well-known that low cycle fatigue life is commonly divided into three periods: micro-crack nucleation, micro-crack and small cracks growth, and finally formation of a macroscopic fatigue crack, initialising final failure [26,82]. The nucleation of micro-cracks predominantly occurs in the first stage characterised by strong softening. At the second stage, characterized by slight linear softening, the development of surface damage predominates in the form of both the growth of micro-cracks and an increase in the number of micro-cracks caused by the formation of additional micro-cracks. At a certain point, micro-cracks merge or a larger crack becomes dominant. As a result, at the beginning of the third stage, a macroscopic fatigue crack is formed, continuously growing deep inside the material with each cycle until the final failure occurs. Surface conditions affect the initiation period and micro-cracks can easily initiate on pits, surface defects, and inclusions. In the case of specimens exposed to the ceramic breeder environment, as shown in the previous section, the micro-cracks on imprints from lithium ceramic pebbles are already ready-made micro-cracks that begin to grow with the onset of loading. Video macro shots of both sub-sized and standard pre-corroded specimens confirmed that some small cracks begin to open almost immediately with the start of the test. Thus, the initiation period for both sub-sized and standard pre-corroded specimens is shortened compared to as-received specimens.

Generally, a fatigue test can also be divided into a cyclic mechanical test where the degradation of the material is caused by the evolution of damage (growth of micro-cracks and small cracks), and a cyclic

fracture mechanical test, where the crack growth behaviour is affected by varying loading conditions. The transition occurs with the formation of a fatigue crack and is represented by the value N_d. When analysing the results of tests performed on both sub-sized and standard specimens subjected to a ceramic breeder environment for 64 days it can be found, that the share of N_d related to N_f is varying from ≈79% up to ≈90% (see Table 4.1). Accordingly, the share of $N_f - N_d$ is varying from ≈10% up to ≈21%. On average, the share of N_d related to N_f is 82.5 % for small specimens while it is 87.8 for standard specimens. Accordingly, the share of $N_f - N_d$ related to N_f is on average 17.5% for small samples while it is 12.2% for standard specimens. So the effect of the fatigue crack growth behaviour on the lifetime is on average slightly higher for small samples compared to big samples, but generally much smaller than the effect of the evolution of damage for both type of samples. When now taking into account that the values of N_d of standard-sized specimens is on average 3.2 ($\Delta\varepsilon_t$ = 0.6 %), 2.4 ($\Delta\varepsilon_t$ = 1.0 %) and 2.2 ($\Delta\varepsilon_t$ = 1.6 %) times higher than the ones of sub-sized specimens it becomes clear, that the size effect is predominantly caused by an accelerated evolution of damage in the small samples.

As for the difference between the period of micro-cracks growth in sub-sized and standard specimens, from geometric point of view, an increase in the diameter of the specimen by 4.4 times, the number of imprints (and hence micro-cracks on them) for the cross section of the specimens (Ø2 mm×7.6 mm for sub-sized and Ø8.8 mm×23 mm for standard specimens) should increase by 4.4 times (ratio of circumference of gage parts of the specimens), while cross section itself increases by 19.36 times (ratio of cross sections of the specimens). Note that the imprint diameter and micro-crack parameters are similar for both types of specimens. Hence, the local stress within the remaining cross-sectional area of the sub-sized specimen (after subtracting the area occupied by microcracks) will still be higher compared to the standard specimen. This implies an accelerated development of damage within the material in case of the sub-sized specimen.

Further, with an increase in the number of cycles, some micro-cracks begin to grow deep into the material and continue to grow in the form of small cracks until they reach a certain size, which corresponds to the N_d cycle. Crack growth period starts when the crack growth resistance of the material is controlling the crack growth rate and obeys the stress intensity factor K [82]. In the example above, upon reaching 110 cycles with a crack depth of 270 µm for the sub-sized specimen and 336 cycles with a crack depth of 1380 µm for the standard specimen, the fatigue crack propagation period and non-linear stress reduction begins.

Table 4.1. The number of cycles until the formation of a fatigue crack N_d, the number of cycles to failure N_f, and the cycle count between them (N_d-N_f) for LCF tests of sub-sized and standard specimens exposed to the ceramic breeder environment for 64 days

Total strain range	Sub-sized specimens			Standard specimens		
	N_d / % of N_f	N_f-N_d, % of N_f	N_f	N_d / % of N_f	N_f-N_d, % of N_f	N_f
0.6%	839 / 82.7	176 / 17.3	1015	2854 / 85.1	501 / 14.9	3355
	955 / 82.7	200 / 17.3	1155	2816 / 86.2	452 / 13.8	3268
1.0%	448 / 78.6	122 / 21.4	570	1003 / 89.3	120 / 10.7	1123
	328 / 83	67 / 17	395	867 / 86.7	133 / 13.3	1000
1.6%	110 / 80.9	26 / 19.1	136	336 / 86.6	52 / 13.4	388
	227 / 87.3	33 / 12.7	260	418 / 87.1	62 / 12.9	480

Hence, considering the presence of pre-existing micro-cracks on the surface of pre-corroded specimens prior to testing, which begin to open with the onset of fatigue testing, the difference in the growth rate of small cracks, and then the fatigue crack, determines the difference in the number of cycles to failure between sub-sized and standard specimens. Future work will involve interrupted fatigue tests with measurements of crack length and depth using focused ion beam techniques, while the current study primarily focuses on fractography analysis. Furthermore, it is important to acknowledge that the growth of fatigue cracks in cylindrical specimens is affected by the orientation of the crack related to the position of the extensometer at strain-controlled conditions and that fatigue cracks do not necessarily propagate strictly perpendicular to the applied load. To obtain more precise measurements of crack depth, compact tension specimens (CT) would be required for specific testing in accordance with standards.

Although a strain controlled LCF experiment is not really suitable to determine the fatigue crack growth behaviour in a correct manner (the growth of a crack in cylindrical specimens is affected by its orientation towards the position of the extensometer, cracks do not necessarily propagate strictly perpendicular towards the load direction etc), the specimens shown in Fig. 4.77 were used to compare the fracture-mechanical behaviour of sub-sized and standard specimens.

Generally, the fatigue crack growth rate *da/dN* is dependent on the stress intensity factor range Δ*K*, following the Paris-Erdogan law:

$$\frac{da}{dN} = C \cdot \Delta K^m \tag{5}$$

where *C* and *m* are material constants, and Δ*K* is the stress intensity factor range. The stress intensity factor range in its turn can be calculated as:

$$\Delta K = F_n \cdot \Delta\sigma \cdot \sqrt{\pi \cdot a} \tag{6}$$

where F_n is a dimensionless geometric factor that is dependent on the geometry of the crack, Δσ is the applied stress range, and *a* is the crack depth.

The geometric factor is a critical component in the above equations as it takes into account the differing geometric dimensions of the sub-sized and standard samples. In the case of a crack in cylindrical specimens, the geometric factor can be calculated using the following equation [83–85].

$$F_n = 0.92 \cdot \frac{2}{\pi} \cdot sec\beta \cdot \sqrt{\frac{tan\beta}{\beta}} \cdot (0.752 + 1.286 \cdot \beta + 0.37 \cdot Y^3) \tag{7}$$

where $Y = 1 - sin\beta$ and $\beta = \frac{\pi}{2} \cdot \frac{a}{D}$. In the last equation, *D* is the diameter of the specimen, so the geometric factor depends on it in a complex way. The equation is derived for the highest value of stress concentration factor calculated at the crack front based on the boundary integral method for the aspect ratio of a fatigue crack (depth to half-length) equal to 1, which is close to the experimental aspect ratio measured for fatigue crack under tension-compression [83,86].

The dependence of the geometric factor F_n on the crack depth a, calculated using equation 7, is presented in Fig. 4.80. Notably, the geometric factor increases more gradually for the standard specimen compared to the sub-sized specimen. For example, for a crack depth of 0.5 mm, the geometric factor is 0.675 and 0.875 for the standard and sub-sized specimen, respectively. For a crack depth of 1 mm, the corresponding values are 0.711 and 1.655. Thus, it is evident that cracks of the same depth result in significantly different geometric factors for specimens of different sizes. In other words, a specimen with a larger diameter will experience a lower stress intensity factor and a crack will grow more slowly than in a specimen with a smaller diameter with a crack of the same size. The geometric factors corresponding to N_d and N_f turned out to be close for different specimens. For the sub-sized specimen, they are 0.737 and 0.879, and for the standard sample, 0.745 and 0.921, respectively. However, due to the difference in the crack depths, the stress intensity factors at these values are significantly different.

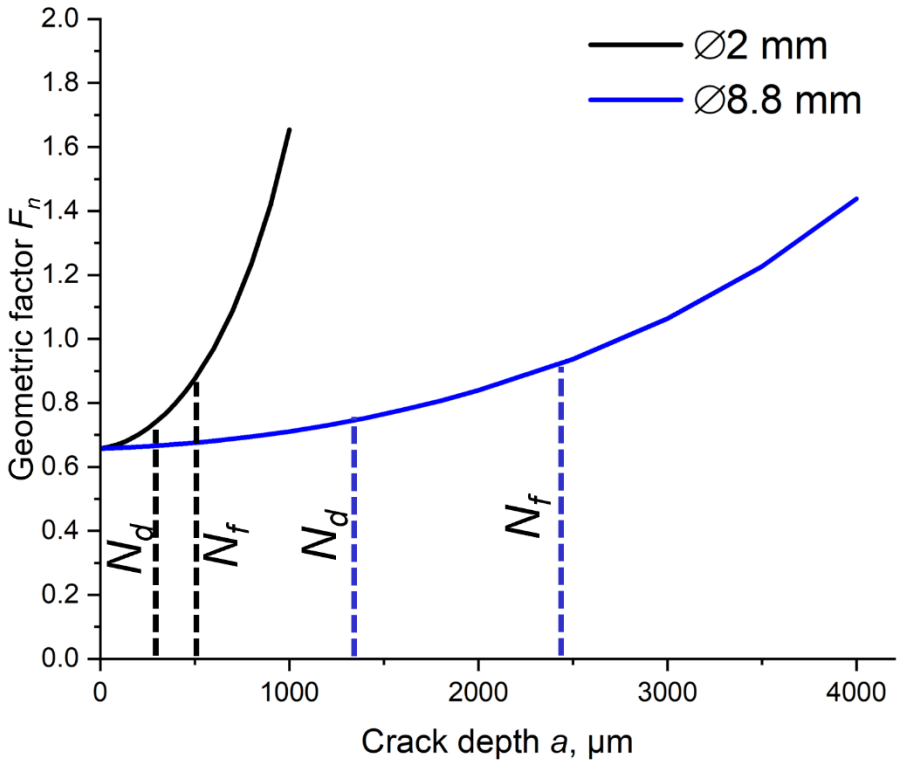

Fig. 4.80. The calculated value of the geometric factor depending on the depth of the crack in the sub-sized and standard specimens. Black and blue dashed lines show the number of cycles until the formation of a fatigue crack N_d and the number of cycles to failure N_f for the sub-sized and standard specimens, respectively.

It should also be noted that the fatigue stress ratio R can also indirectly affect the stress intensity factor range ΔK, and hence the crack propagation rate and the number of cycles to failure. Fig. 4.81 shows examples of the dependence of the ratio R on the number of cycles at a total strain range of 1.6% for sub-sized and standard specimens. In general, up to the first hundreds of cycles, the R values for all specimens are similar (except for one sub-sized specimen). With an increase in the number of cycles particularly beyond N_d, the ratio R for sub-sized specimens turns out to be slightly lower than for standard specimens. For the number of cycles N_d it is -1.095 to -1.077 and -1.036 to -1.035 for sub-sized and standard specimens, respectively. For the number of cycles N_f it is -1.16 to -1.14 and -1.086 to -1.081 for sub-sized and standard specimens,

respectively. However, these small variations in the ratio *R* are taken into account when calculating the stress intensity range factor Δ*K*, because slightly smaller values of *R* lead to smaller value of the stress range Δσ.

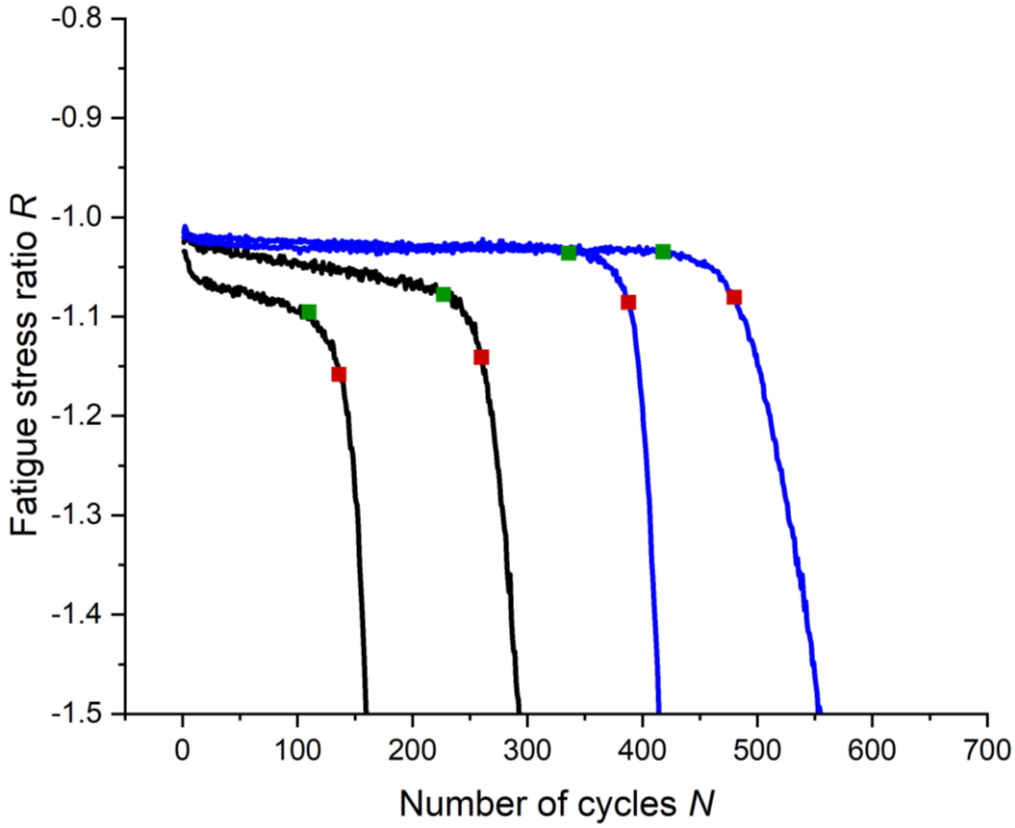

Fig. 4.81. Fatigue stress ratio R as a function of number of cycles N at a total strain range of 1.6% for the sub-sized and standard specimens. Green and red points correspond to the number of cycles until the formation of a fatigue crack N_d and the number of cycles to failure N_f, respectively.

The fatigue crack growth rate, *da/dN*, was determined by analyzing striation traces on the fracture surfaces, and the corresponding stress intensity ranges were determined from the peak stress diagrams for the same cycle number values as *da/dN*. The relationship between fatigue crack growth rate and stress intensity range is illustrated in Fig. 4.82. Although this graph is typically constructed using ASTM CT fatigue tests [80], the one shown here appears reasonable since it is based on experimental observations. Notably, only data points towards the end of the test, where the striation marks were visible on the fractography images, were used to generate the graph. This resulted in the exclusion of the first stage of crack growth, which occurs after the threshold stress intensity range, and only the second stage is visible. During the second stage, the fatigue crack growth rate is linearly proportional to the stress intensity range. Towards the end of the test (the samples fractured into 2 parts at the end of the test), the test conditions changed greatly, namely, the peak tensile stresses were significantly less than the peak compressive stresses, and bending moments could also appear. Therefore, the obtained values of the curves beyond N_f are apparently distorted, although an acceleration of the crack growth rate is observed. For sub-sized specimen from the example above, the critical stress intensity range at N_f is approximately 20 MPa·m$^{1/2}$, whereas for standard specimen, the critical stress intensity range at N_f is approximately 40 MPa·m$^{1/2}$. It should be noted that the dependence obtained is strictly speaking valid only for a couple of specimens tested at a total strain range of 1.6%, for which the

crack depth was measured from Fig. 4.77. Nevertheless, similar effects and trends should be preserved for other total strain ranges, for which, unfortunately, the striation lines are poorly distinguishable from each other on fractography

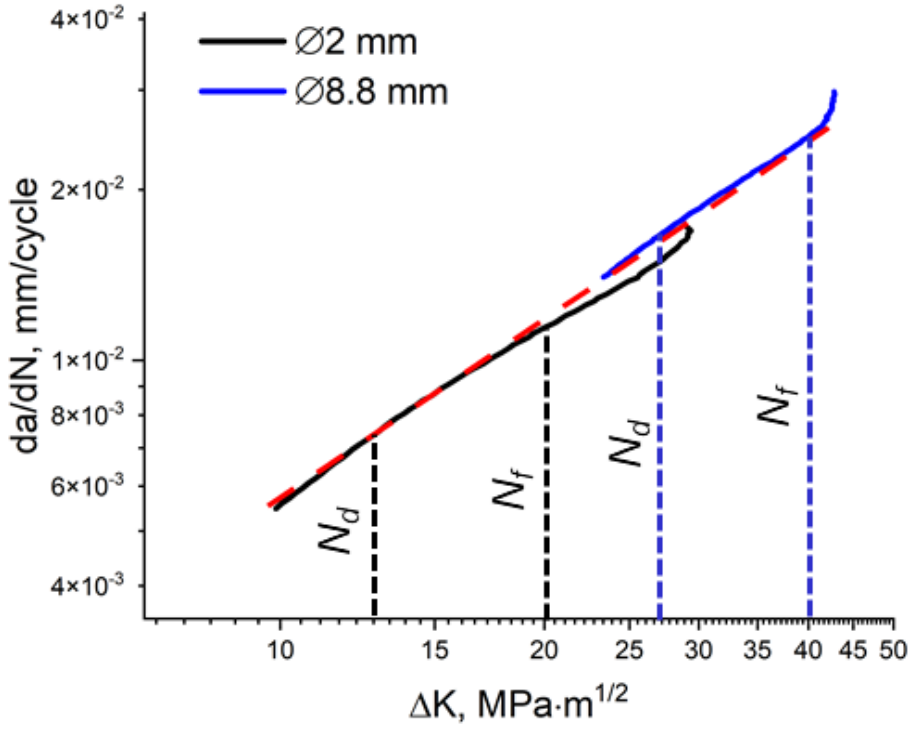

Fig. 4.82. Fatigue crack growth rate da/dN versus stress intensity factor range ΔK for sub-sized (Ø2 mm) and standard (Ø8.8 mm) specimens. Parameters m and C were calculated using the fitted red dashed line.

The linear section for both the sub-sizes and the standard sample turned out to be similar and can be fitted to one straight line. This indicates similar fatigue crack behavior, which is expected since the samples are made of the same material. Based on equation 5, the material parameters *m* and *C* were calculated for the fitted straight dashed line in Fig. 4.82. The value of the parameter *m* is 1.045, and the value of the parameter *C* is $5.17 \cdot 10^{-7}$ (for *da/dN* in m/cycle). However, these values differ substantially from those obtained according to ASTM E647-15e1 [80], where *m* ranges were 2.5 and *C* is approximately $2 \cdot 10^{-11}$ (for *da/dN* in m/cycle) [87]. This discrepancy can be attributed to differences in the test method, as well as higher test temperatures and less severe crack growth conditions than those employed in ASTM E647-15e1. In the case of CT specimen in the above standard, the plastic zone in front of the crack tip is negligible compared to the cylindrical specimens used in the work. Therefore, when testing CT samples, crack growth can be observed from values of *da/dN* about 10^{-8} m/cycle [87], while for the sub-sized and standard fatigue specimens, crack growth occurred at values of *da/dN* about 10^{-5} m/cycle.

The results of the calculations suggest why a standard specimen can withstand more cycles than the sub-sized specimen, despite both were made of the same material and subjected to the same pre-corrosion. This can be attributed to the difference in crack initiation due to the difference in stress concentration in the case of specimens of different diameters and different numbers of defects of the same size. Another factor is the larger geometric factor in a small sample, which generates a higher stress intensity range for the same crack size, which leads to accelerated fracture.

In order to assess the behavior of the real component in the DEMO breeder blanket, an analysis of the component's response is necessary. It is anticipated that the interstitial space between two EUROFER97 tubes will be filled with lithium-ceramics pebbles. The inner tube has a thickness of 2 mm and an outer diameter of 28 mm, while the outer tube has the same thickness with an inner diameter of 60 mm [88–90]. The importance of the inner tube lies in its contact with the lithium ceramic pebbles on the outside of it, since the larger diameter tube is in contact with the pebbles on the inside. According to [83], an external crack in a tube causes a larger stress intensity factor than an internal crack. Because of this, a crack would be expected to propagate more slowly in a 60 mm diameter tube from the inside than in a 28 mm diameter tube from the outside, so the smaller diameter tube was selected for further consideration.

To calculate the geometric factor of a tube with an external crack, such as nucleated on imprints of lithium-ceramics pebbles, the methodology outlined in references [85] was employed. The aspect ratio of the semi-elliptical crack (depth by half length) in the equation used appears to be chosen as 1, which is also consistent with the experimental data [83]. The calculated relationship between the geometric factor and the crack depth is shown in Fig. 4.83. In this particular case, the crack depth was limited to half the tube wall thickness, namely a depth of 1 mm. While the geometric factor of the tube is slightly lower than that of sub-size and standard specimens, the slope of the curve relating the geometric factor to crack depth is similar to that of the standard specimen, rather than the sub-size specimen. This suggests that using results obtained for standard specimens to evaluate the fatigue life of real components can be more relevant.

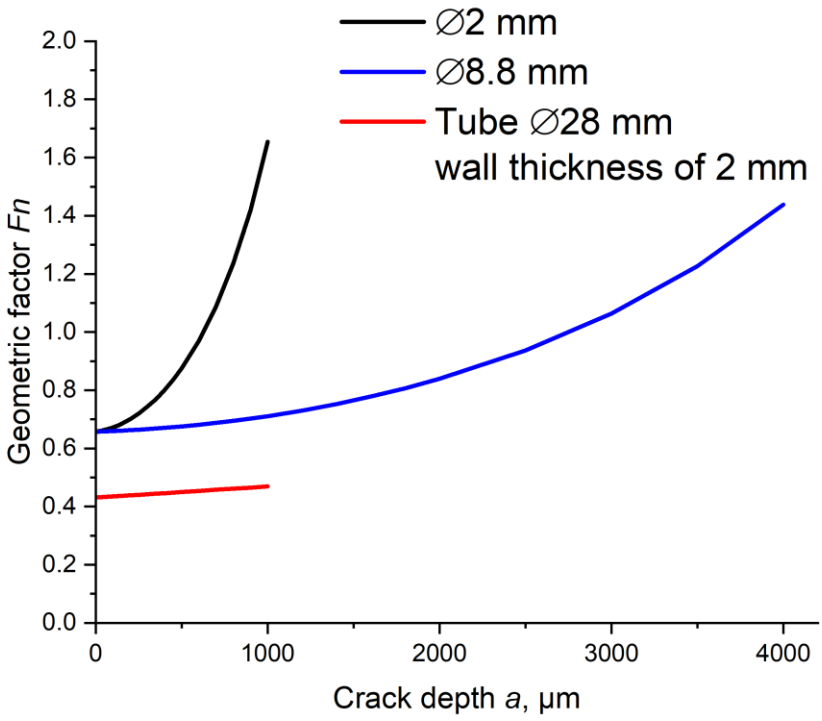

Fig. 4.83. The calculated value of the geometric factor depending on the depth of the crack in the tube Ø28 mm and wall thickness 2 mm in comparison with that in sub-sized and standard specimens

4.3.4 Impact on lifetime of components

The knowledge gained in the course of the work showed a considerable reduction in the fatigue life of EUROFER97 specimens exposed to the ceramic breeder environment for an extended period of time. However, it is important to acknowledge that the experiments only partially mimic the operational conditions of EUROFER97 tubes in the DEMO breeder blanket. Under intense irradiation with high-energy neutrons and a maximum dose of up to 20 dpa by the end of the first phase [2,3], it is probable that the fatigue properties will deteriorate even further. Furthermore, the interaction between EUROFER97 and Li-ceramics pebble bed in a purge gas atmosphere, under variable tension and compression, remains unclear, since corrosion fatigue will develop instead of pre-corrosion fatigue studied in the work. Another critical factor, which was not taken into account, is the creep of EUROFER97 tubes that can occur after a period of rapid heating during two hours of full power operation at high temperature. This, in turn, will exacerbate the decrease in fatigue life.

Nevertheless, to determine the permissible operating conditions of EUROFER97 components in contact with Li-ceramics pebbles in the breeder blanket, a fundamental approach was adopted in this study. The Wöhler diagram was used to demonstrate how many cycles to failure the specimen can withstand, depending on the total strain range experienced. As illustrated in section 4.1.5, Wöhler diagrams were created for only three values of the total strain range for standard and sub-sized specimens. However, only three data points are inadequate to form a curve and extrapolate it. Thus, additional tests were conducted on standard EUROFER97 specimens exposed to the ceramic breeder environment for 64 days, using total strain ranges of 0.4%, 0.8%, and 1.2%, to increase the number of data points.

Fig. 4.84 displays a Wöhler diagram including additional test results for other total strain ranges for standard as-received EUROFER97 specimens [46]. A curve was generated for six data points using automated fitting to minimize the sum of squared deviations. The total strain range follows the equation $\Delta\varepsilon_{tot} = 0.00382 + 3.74663 \cdot N_f^{-0.89846}$, where N_f represents the number of cycles to failure and the total strain range is presented as a fraction (not in percentage). The results from automated fitting differ slightly from previously acquired EUROFER97 data at 550°C [91], which can be attributed to the fact that the data was obtained for the EUROFER97 Batch 1 which generally showed lowers stress levels and higher lifetimes. Nevertheless, for further analysis, the results obtained in this study will be considered since the samples exposed to the ceramic breeder environment were initially in the same state as the as-received samples for which the data were fitted.

With the available data and the fitting curve, it is possible to estimate the allowable maximum total strain range for a known number of cycles that a component undergoes according to the WP 6 (Fig. 3.1). One of the approaches to achieve this is the use of ASME Code Case N-47, which provides guidelines for the evaluation of LCF in nuclear power plant components. This code case is specifically designed for metallic materials that experience a limited number of load cycles, typically less than 10000 cycles, at high loads or stresses. The code is applicable for materials used in fusion reactors such as EUROFER97 [91]. The design fatigue curves are derived from the fit curve by applying a factor of 2 on the strain range or a factor of 20 on cycles, depending on which is more conservative at each point. The purpose of these factors is to account

for various effects, such as environmental factors, scale differences between the material and test specimen, surface finish, and data scatter [91,92]. It should be noted that these factors are not intended to provide a safety coefficient in any case.

The obtained N_f-0.5Δε, and 0.05N_f-Δε curves are illustrated in Fig. 4.84 as red and black dotted lines, respectively. By using these two curves, the ASME design code curve was derived and is represented by the green line in the figure. It should be noted that the data points obtained for standard specimens exposed to the ceramic breeder environment exceed the ASME design code curve. This indicates that the approach taken in this study accounts for environmental factors and surface deterioration due to pre-corrosion experiment.

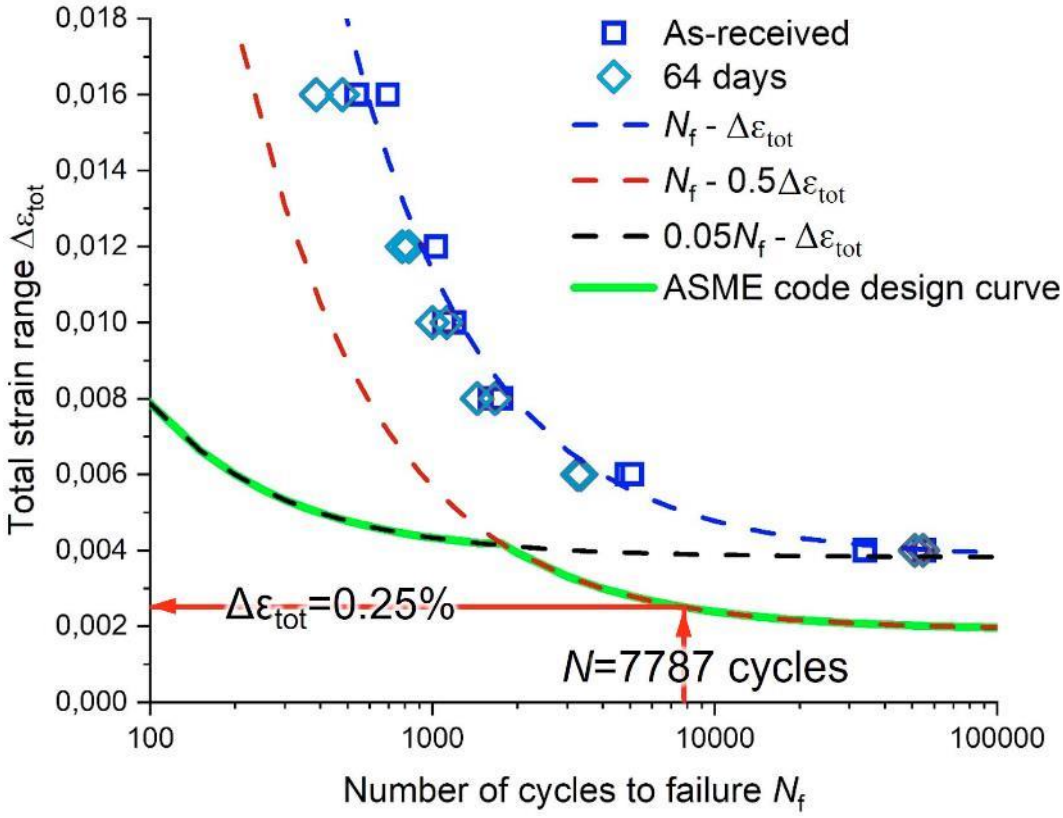

Fig. 4.84. Results of the LCF tests of EUROFER97 specimens in as-received and pre-corroded in the ceramic breeder environment conditions. The N_f-Δε, N_f-0.5Δε, and 0.05N_f-Δε curves are shown for the as-received specimens [46]. The design fatigue strain range curve was built according ASME code design. The red arrows show how the allowed total strain range was determined.

To determine the number of heating and cooling cycles with tension-compression that EUROFER97 tubes inside the DEMO blanket will be subjected to, it is necessary to consider the cyclic operation of the DEMO reactor. Each DEMO cycle consists of a ramp up in 150 s, 2 hours of full power operation, 150 s of ramp-down, and a 600 s dwell period (Fig. 4.85) [93]. Thus, a single DEMO cycle lasts for a total of 2.25 hours. It is known that the first blanket in the DEMO reactor will need to operate for a duration of 2 full power years. Therefore, the total number of cycles N can be calculated as $N = 2 \cdot 365 \cdot 24/2.25 = 7787$ cycles. As a result, EUROFER97 tubes will be subjected to a total of 7787 heating and cooling cycles during their operational lifespan.

It is important to note that the actual operating conditions would also include neutron irradiation and creep during the full power and dwell stages. However, for a conservative estimate of the allowable total strain range, 7787 cycles can be considered the minimum number of cycles before failure, as indicated by the red arrows in Fig. 4.84. The maximum allowable total strain range corresponding to 7787 cycles on the ASME code design curve was then calculated to be 0.25%. It should be emphasized that this value was determined without taking into account neutron irradiation and the effect of creep, which will most likely result in a further reduction of the resulting value of the total strain range.

The strain induced by heating or cooling of EUROFER97 tubes (without considering the effects of creep) can be estimated and compared to the allowable total strain range limit. The strain (ε) is calculated as $\varepsilon = \alpha \cdot \Delta T$, with α being $11.9 \cdot 10^{-6}$ K^{-1} (within the 300–550°C temperature range, the operational temperature for EUROFER97 tubes) and ΔT as 250 K in the same range. The calculated strain value is ε=0.2975%, slightly exceeding the allowable limit of 0.25%. Consequently, in the case of a perfectly rigid system in constrained conditions it is likely that the required number of cycles (7787 cycles within 2 years of operation) may not be endured by EUROFER97 tubes, even without considering the effects of strong neutron irradiation and creep. In real conditions it is impossible to assume a completely rigid system so that the ends of the EUROFER97 tubes do not move at all during operation. Tube deformation parameters require the use of a finite element method and have not yet been calculated by designers.

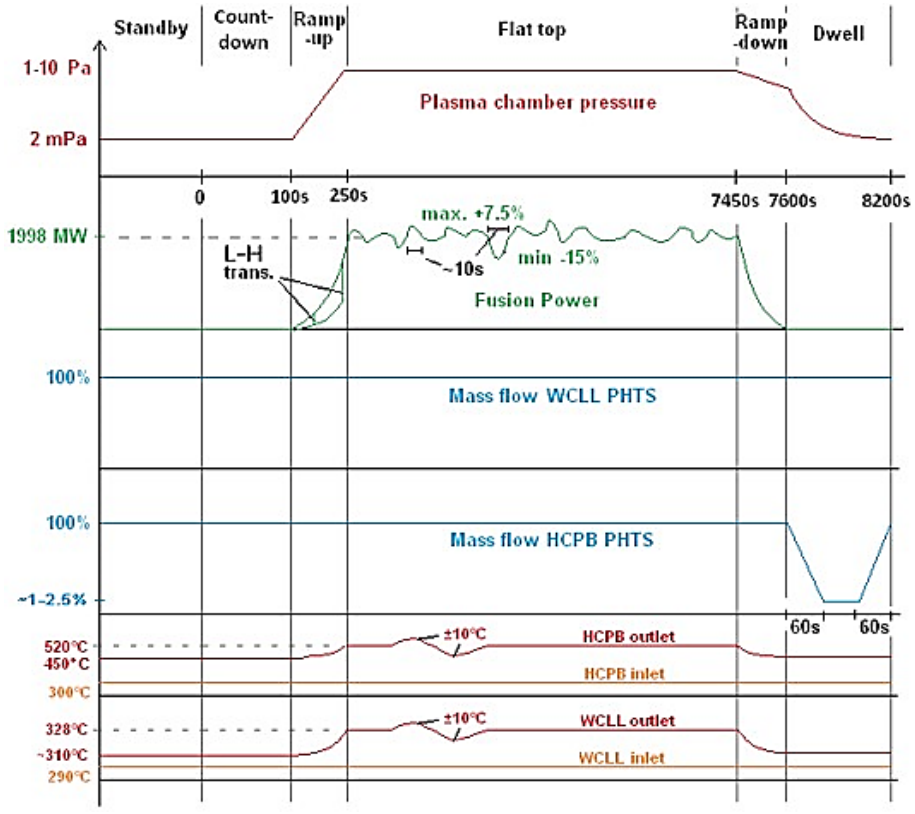

Fig. 4.85. DEMO pulsed operation parameters showing the duration of different stages [93]

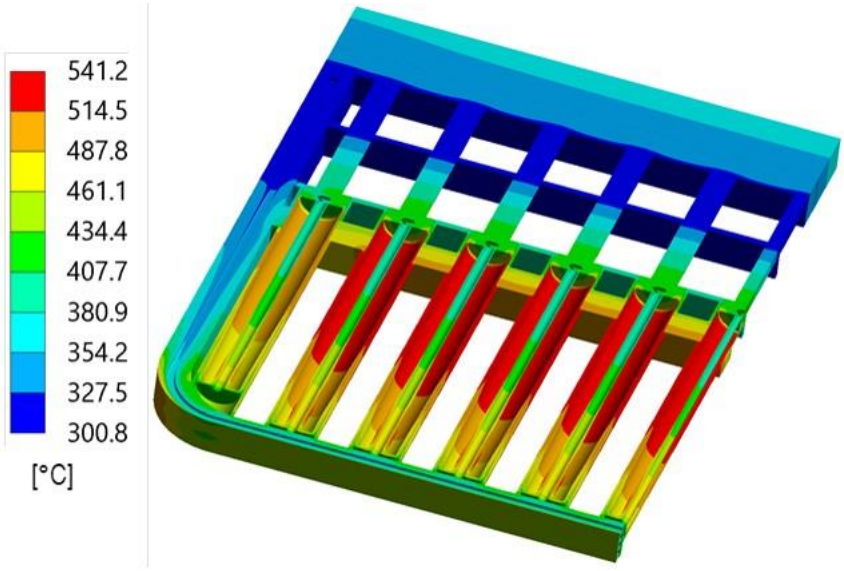

Fig. 4.86. Temperature field of EUROFER97 in the HCPB breeding blanket at central outboard [94]

Finally, various potential solutions have been explored to mitigate the harmful effects of the ceramic breeder environment on the fatigue life of EUROFER97:

1. Increasing the thickness of components

One approach that may seem straightforward is to increase the thickness of the tubes, since this could increase at first glance the number of cycles to failure, but if there are imprints on the surface with micro-cracks, they will eventually lead to accelerated evolution of damage. However, the obtained design curve already considers the data points corresponding to specimens of different sizes. Secondly, increasing the thickness of the EUROFER97 tubes beyond a reasonable limit may cause more neutrons to be consumed or slowed down and decrease in the tritium generation, which would ultimately result in a reduction in the tritium breeding ratio. Thus, this solution has been deemed unsatisfactory by designers, as the tubes must be of a reasonable thickness to maintain the desired tritium breeding ratio.

2. Surface coating of EUROFER97

The next logical way to mitigate the issue would be to apply protective coatings on EUROFER97 from some material that prevents severe corrosion and cracking of its surface during exposure to lithium-ceramics pebbles in a purge gas atmosphere. However, several obstacles exist that make this approach challenging. Firstly, there is currently no technology available to uniformly apply a coating layer to the internal cavities inside the tubes in blanket (after its assembly by welding). Additionally, stringent requirements must be met by the coating material, including non-activation by irradiation and being composed solely of elements highlighted in green and yellow as shown in Fig. 4.87. This is especially important, because after the work of the material in the DEMO, it should contain as low as possible amount of long-lived isotopes. The protective coating must also have a coefficient of thermal expansion similar to that of EUROFER97 to prevent thermal stress and peeling during heating-cooling cycles, and must effectively adhere to the substrate while protecting it from corrosion.

Table 4.2 provides an overview of various coatings applied to the surface of EUROFER97 and other RAFM steels to protect them from corrosion in the ceramic breeder environment. According to [62,63], aluminum oxide forms a dense layer, but lithium atoms can penetrate it easily. This can lead to their transmutation upon neutron irradiation and bubble formation, which can destroy the coating. Aluminum can also be activated by irradiation and form long-lived isotopes, limiting its content to 0.1% or even 0.01% [95,96]. Moreover, aluminum oxide has a lower coefficient of thermal expansion compared to EUROFER97, leading to thermal stresses during heating and cooling and damage to the protective layer.

The tungsten coating also turned out to be unstable and, when heated, peels off the surface, exposing unprotected EUROFER97 [62,63]. The CTE of tungsten is especially low compared to EUROFER97, which may have caused its peeling.

A thin 100 nm thick chromium oxide layer formed upon short-term corrosion of a RAFM steel in [45,97]. Although this layer can reduce hydrogen permeation, it is unstable and transforms into a three-layer structure when exposed to the ceramic breeder environment (similar to the structure shown in 4.1.2).

Table 4.2. A review of coatings studied for corrosion protection of RAFM steels in contact with Li-ceramics pebbles

Coating composition, thickness, reference	Features of the resulting layer	Coefficient of thermal expansion, $\times 10^{-6}$ K^{-1} / difference to EUROFER97*	Limits on the use from Fig. 4.87
Al_2O_3, 50 µm, [62]	Thick layer with rough surface but protects against corrosion	5.5–8.5 / 31–53%	Al: <0.1% / 0.01% O: unlimited
Al_2O_3, 5 µm, [62]	Coating fragmented on heating resulting in severe corrosion.		
Al_2O_3, 2 µm, [63]	Protects against corrosion, but forms $LiAlO_2$ allowing the penetration of Li into the coating.		
W nanostructured, 3.5 µm, [62]	The layer is not stable and peels off leaving the surface unprotected.	4–5 / 59–66%	W: <10%
W nanostructured, 3.5 µm, [63]	The layer peels off. Corrosion thickness is 20 µm after 10 days at 550°C.		
Cr_2O_3, 0.1 µm, [45,97]	The layer is not stable during corrosion. Reduces hydrogen permeation	6–8 / 35–49%	Cr: unlimited O: unlimited
Er_2O_3, 1µm, [45,98]	The layer can be damaged by corrosion. One of the best hydrogen penetration barriers.	6.5 / 44–47%	Er: <0.001% O: unlimited
SiC, 1.5 µm, [63]	SiC coating is stable material with low chemical reactivity with lithium. The coating has a good adhesion to the substrate	4–5 / 66–69%	Si: <1% C: unlimited
Al/Cr oxynitride, 2.5 µm, [62]	Peels off and doesn't protect the surface	10–12 / the same	Al: <0.1% / 0.01% Cr, O: unlimited N: <10% / 1%

* CTE of EUROFER97 at 330–550°C is 11.7–12.3·10^{-6} K^{-1}

Erbium oxide is considered one of the best barriers against tritium permeation, but its exposure to the ceramic breeder environment can damage the coating [45,98]. The compound also has a low CTE, and the difference with EUROFER97 is 44–47%. What is especially important, and what the researchers did not pay

attention to, is that erbium can be activated by irradiation, necessitating its content to be limited to less than 0.001% [95,96].

Silicon carbide forms a dense layer with good adhesion to steel, preventing the diffusion of lithium through the layer [63]. Nevertheless, it has a low CTE, and the difference with EUROFER97 reaches 66–69%.

Aluminum/chromium oxynitride coating was applied in [62], which has the same CTE as EUROFER97 but does not offer adequate protection against corrosion.

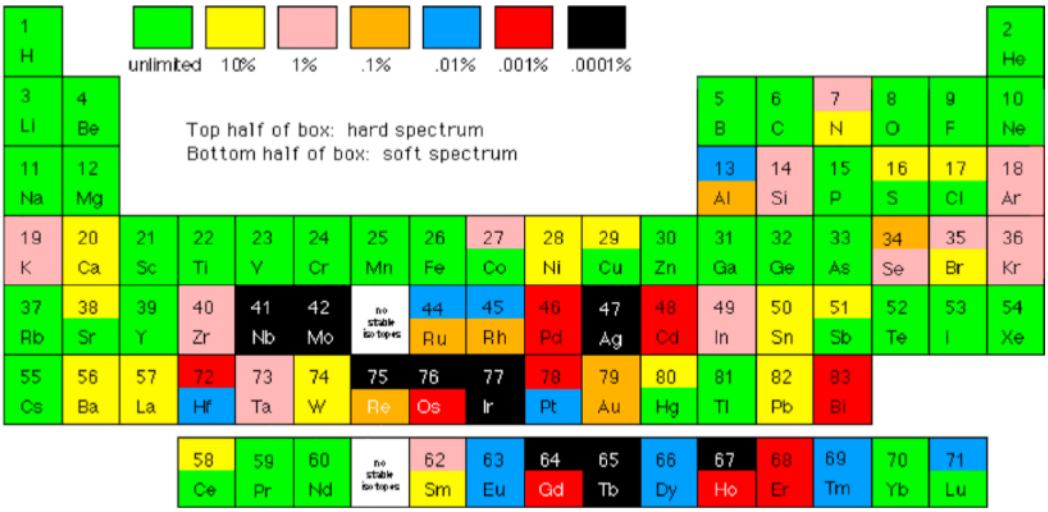

Fig. 4.87. Limits on the use of elements for near-surface burial after US methodology [95,96]

Thus, none of the studied coating compositions currently meets all the requirements for its use as EUROFER97 corrosion protection in the ceramic breeder environment. Unfortunately, it is also impossible to control the coating's thickness on all areas of EUROFER97 inside the blanket, making it difficult to ensure its efficacy. Furthermore, it is impossible to determine if the coating has collapsed during operation of the blanket. Given these challenges, it is unlikely that the use of coatings will be a viable option for protecting EUROFER97 from the harmful effects of the ceramic breeder environment.

It should be noted that any coating of lithium-ceramics pebbles will inevitably worsen the possibility of tritium desorption from them and decrease the tritium breeding ratio. In addition, the corrosion of EUROFER97 is mainly attributed to the impurities in the purge gas, and not solely to the interaction with lithium-ceramics pebbles.

3. Using high purity purge gas

Another potential approach to address the issue is to eliminate impurities, such as oxygen and water, from the purge gas. As shown in Section 4.2.2, it is the presence of impurities in the purge gas that leads to the formation of a complex corrosion layer, which in turn at least partly reduces the fatigue life of the EUROFER97 specimens. However, removing impurities from the large volumes of purge gas, avoiding any air leaks, is a complex task that may not be practical. Additionally, there are proposals to incorporate water vapor at concentrations of approximately 0.1–0.2 vol.% for improved transport and retention of tritium in the

form of HTO molecules [99], which may exacerbate the corrosion of EUROFER97 in contact with lithium-ceramics pebbles.

4. Further improvement of the blanket design

Addressing the problem of EUROFER97 degradation within the current design may not have a simple solution. One potential approach being considered by HCPB breeding blanket designers is to avoid direct contact between the lithium-ceramics pebbles and EUROFER97 by placing the pebbles within beryllide blocks or placing beryllide blocks between Li-ceramics pebbles and EUROFER97 components. Beryllide blocks serve as a functional neutron multiplication material that do not bear load and are not considered to be sensitive for fatigue life degradation. In the latest version of the HCPB design, titanium beryllide blocks are already placed inside EUROFER97 pins, as shown in Fig. 4.88, near the first wall where the highest temperatures between EUROFER97 and lithium-ceramics pebbles are expected (Fig. 1.3). Initial experimentation has already shown negligible interaction between beryllides and EUROFER97 or Li-ceramics pellets, even at temperatures as high as 900°C [100]. This approach has already been utilized in the Japanese DEMO concept, where lithium-ceramics pebbles are mixed with beryllide pebbles [101]. Ultimately, a solution to the problem will likely require further modification to the HCPB breeding blanket design.

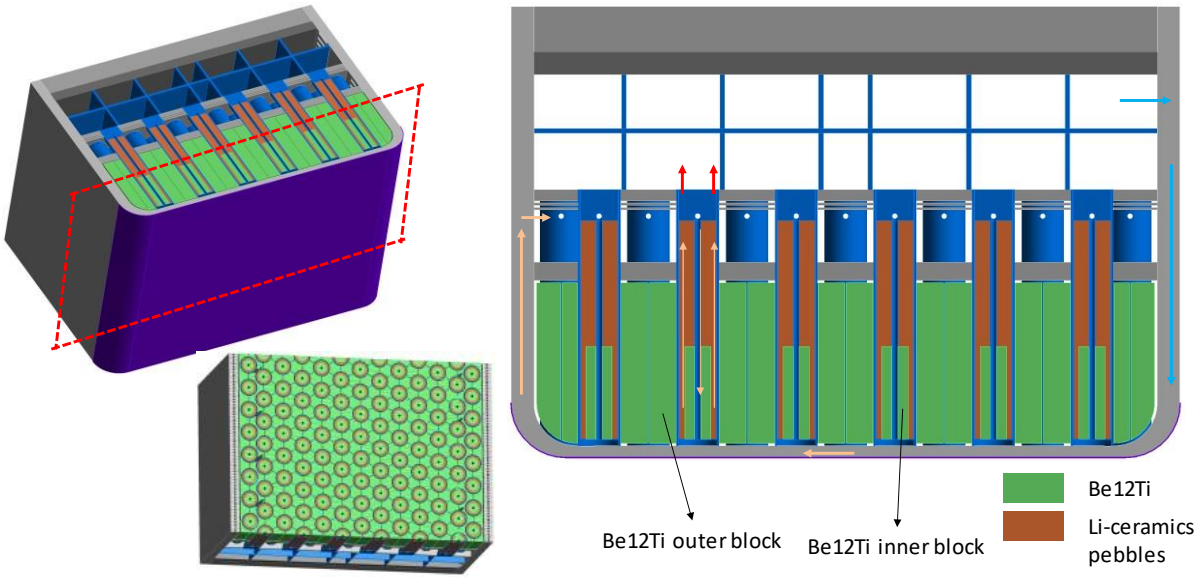

Fig. 4.88. Updated in 2023 design of the helium-cooled pebble bed blanket module with $TiBe_{12}$ blocks installed between the lithium-ceramics pebbles and EUROFER97 internal tube to prevent contact at maximum temperature [102]

In addition, blanket designers are exploring the use of lithium-ceramics blocks instead of pebbles. These blocks can be manufactured in the form of foams or solid blocks with channels, which increases the thermal conductivity of the lithium ceramics and minimizes or eliminates its interaction with the EUROFER97 blanket components [103–105]. If the contact between the lithium-ceramics blocks and EUROFER97 is excluded, or if it is replaced by contact along the plane rather than individual pebbles, it will likely be possible to avoid

stress concentration at the contact point and the resulting cracking on imprints. This would improve the material's durability and increase the number of cycles to failure.

4.3.5 Summary and conclusions

Summing up the issue of the premature failure of EUROFER97 specimens exposed to the ceramic breeder environment, several factors appear to be involved:

1) The hydrogen content of 2.6 ppm in the samples does not seem to have a detrimental effect on fatigue properties, as it was not found to significantly affect DBTT and USE in Charpy impact tests. Other studies also support this, suggesting that such low concentrations of hydrogen in EUROFER97 do not lead to a decrease in the number of cycles to failure.

2) Exposure to the ceramics breeder environment results in the formation of a rough, corroded surface on EUROFER97 samples, featuring imprints left by contact with lithium-ceramics pebbles. These imprints are notches and lead to the accelerated formation of surface micro-cracks, based on local stress concentrations. The cracks on imprints can appear even when the samples are cooled after exposure.

3) The cracks observed passing through the imprints before LCF tests are leading to an accelerated evolution of damage. This eliminates the time required for fatigue crack initiation, leading to a reduction in the total number of cycles to failure.

4) The relatively brittle corrosion layer on the surface can crack easily under stress. This also concerns to the internal corrosion layer consisting of EUROFER97 with elongated oxide particles along the boundaries of the martensite laths. The decrease in the plasticity of the outer layer of EUROFER97 will inevitably cause faster growth of micro-cracks and, accordingly, will as well shorten the lifetime.

The greater number of cycles to failure of the standard sample compared to the sub-sized sample was attributed to a differences in the evolution of damage. When considering testing and evaluation of blanket components, it is recommended to rely on results obtained from standard samples, which are tested under conditions more representative of real-world scenarios.

The ASME code design curve was used to estimate the maximum allowable total strain range for 2 full power years of operation in DEMO (7787 cycles), which is 0.25%. However, the calculated strain value for the EUROFER97 component is 0.2975%, slightly exceeding the allowable limit of 0.25%. Consequently, in the case of a perfectly rigid system in constrained conditions the required number of cycles may not be endured by EUROFER97 tubes, even without considering the effects of strong neutron irradiation and creep. In reality, the system will not be completely rigid. The value of deformation of tubes have not yet been determined by designers.

Several solutions have been explored to address the issue of EUROFER97's fatigue life degradation caused by the ceramic breeder environment. It appears that the key to resolving this problem lies in improving the blanket design to prevent direct contact between the lithium-ceramics pebbles and EUROFER97.

5 Conclusions

1. The ceramic breeder environment (exposure to the Li-ceramics pebbles in a purge gas atmosphere at 550°C for 8–128 days) caused significant corrosion of EUROFER97 forming imprints at the contact zones of lithium-ceramics pebbles, iron oxide particles, and pure iron hillocks on the surface. In the cross-section, the corrosion layer consists of iron oxide and pure ferrite in an outer layer, fine-grained chromium-rich oxide in an intermediate layer, and Cr-rich oxide particles in EUROFER97 in an internal corrosion layer. The thickness of the corrosion layer increased rapidly up to an exposure duration of about 16 days and reached saturation after more than 64 days with an average value of 16.5–17 µm. The TEM analysis has indicated the presence of various lithium-containing phases in the corrosion layers.

2. Additional experiments have revealed that impurities in the purge gas, specifically oxygen and water vapor, are the primary cause of corrosion on EUROFER97 steel surfaces when exposed to the ceramic breeder environment. Exposure of EUROFER97 specimens to lithium-ceramics pebbles in a vacuum does not result in noticeable corrosion, while exposing EUROFER97 specimens to purge gas results in corrosion of similar thickness to that observed in the exposure to the ceramic breeder environment.

3. The fatigue life of sub-sized EUROFER97 specimens with a diameter of 2 mm decreased significantly when exposed to the ceramic breeder environment. The reduction in fatigue life became more pronounced with an increase in the duration of exposure to 32–64 days. Further increase in the exposure duration showed little additional effect on the number of cycles to failure. At the total strain range of 0.6%, the reduction in the lifetime is approximately 60% for an exposure duration of 32–128 days.

Standard specimens with a diameter of 8.8 mm also showed a significant deterioration in fatigue life after exposure to the ceramic breeder environment. Despite the same testing conditions, the standard specimens demonstrated a higher number of cycles to failure than the corresponding sub-sized specimens. At 0.6% total strain range, the negative impact of exposure on fatigue life of standard specimens was 35%.

4. Exposure to vacuum in contact with Li-ceramics pebbles did not cause significant changes in the fatigue life of EUROFER97. Exposure to purge gas alone led to a decrease in the number of cycles to failure, but to a lesser extent than when in contact with pebbles. It is the combination of a purge gas environment and contact with lithium-ceramics pebbles that is responsible for the observed deterioration of the fatigue life of EUROFER97 steel.

5. A rough, corroded surface on EUROFER97 samples with imprints left by contact with lithium-ceramics pebbles could be regarded as notches and lead to the accelerated formation of surface micro-cracks, even when the samples are cooled slowly after exposure. These cracks can be considered as sites of fatigue crack initiation. Therefore, the reduction in the time required for fatigue crack initiation leads to a decrease in the total number of cycles to failure.

6. The maximum allowable total strain range of EUROFER97 components for 2 years of operation in DEMO (7787 cycles) was estimated using the ASME code design curve as 0.25%. However, the calculated strain value is 0.2975%, slightly exceeding the allowable limit of 0.25%. Consequently, in the case of a perfectly rigid system in constrained conditions the required number of cycles may not be endured by EUROFER97 tubes, even without considering the effects of strong neutron irradiation and creep. Apparently, the system will not be completely rigid, however the values of deformations of tubes have not yet been determined by designers. Several options to address the issue have been evaluated, leading to the conclusion that an enhanced blanket design is necessary to mitigate the problem effectively.

A. Appendix

A.1 Technical drawings

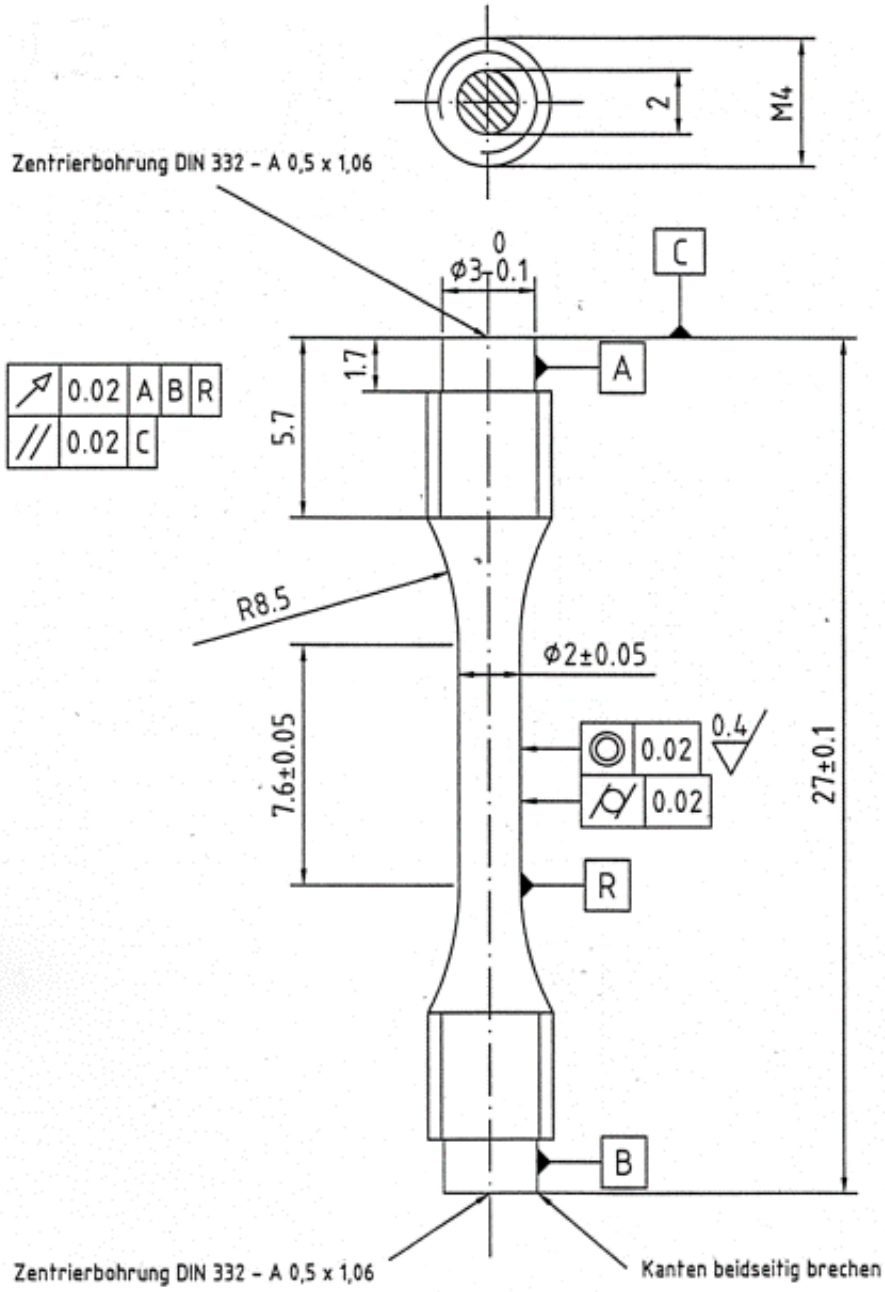

Fig. 5.1. Drawing of a sub-sized specimen for LCF testing

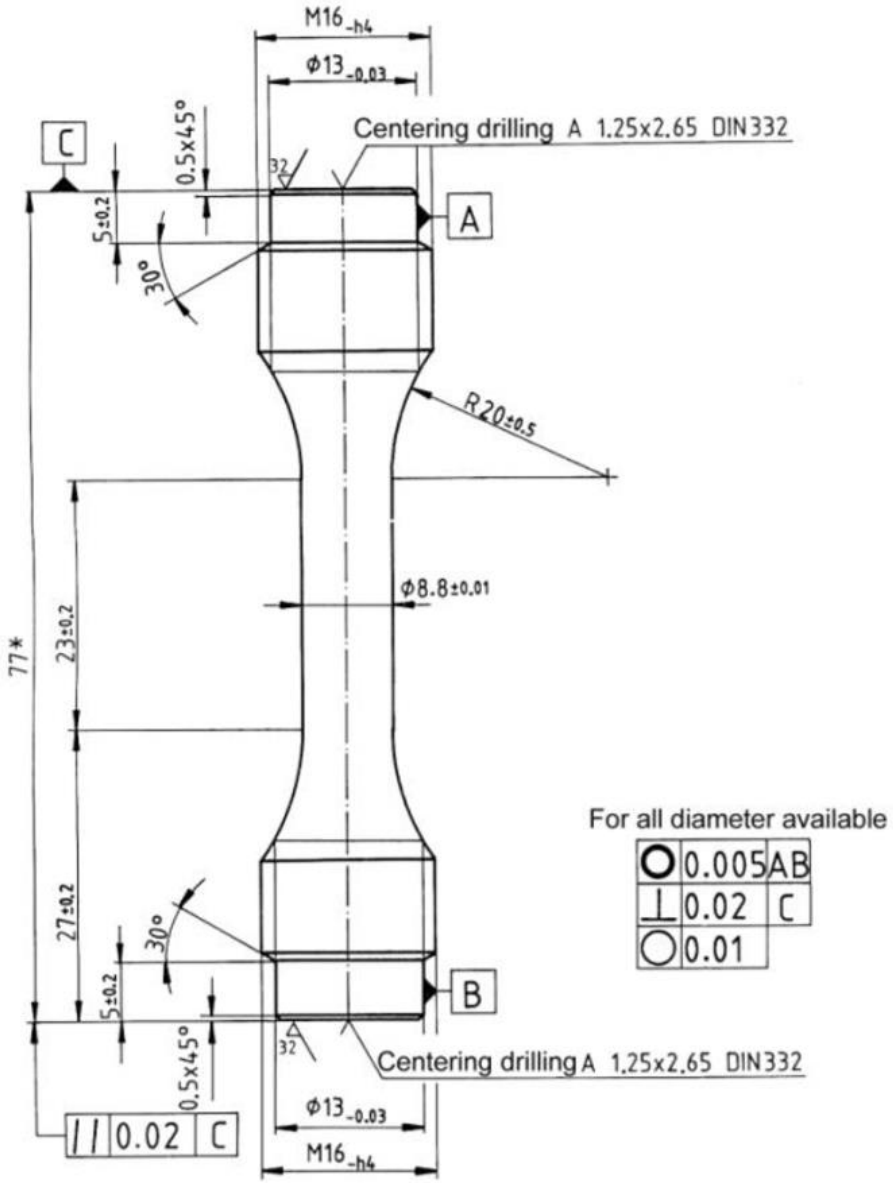

Fig. 5.2. Drawing of a standard specimen for LCF testing

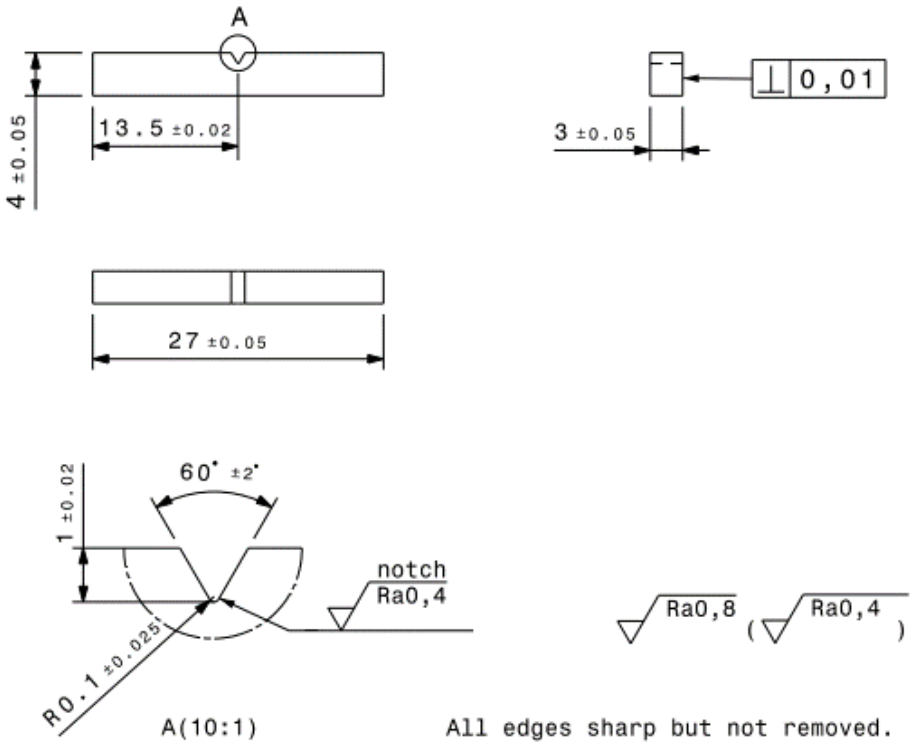

Fig. 5.3. Drawing of a KLST type sub-sized Charpy-V impact specimens

A.2 List of own publications

1) **E. Gaisina**, R. Gaisin, J. Leys, R. Knitter, J. Aktaa, M. Walter. Comparative analysis of low cycle fatigue behavior of pre-corroded standard and sub-sized EUROFER97 specimens exposed to ceramic breeder environment. Nuclear Materials and Energy 36 (2023) 101497. https://doi.org/10.1016/j.nme.2023.101497.

2) **E. Gaisina**, M. Duerrschnabel, J. Leys, R. Knitter, J. Aktaa, M. Walter, Recent studies to the impact of a ceramic breeder environment on the mechanical properties of EUROFER97 under operating conditions, Journal of Nuclear Materials 564 (2022) 153677. https://doi.org/10.1016/j.jnucmat.2022.153677.

3) M. Duerrschnabel, **E. Gaisina**, R. Gaisin, M. Walter, J. Aktaa, M. Rieth, Nanoscale insights into the corrosion of EUROFER by lithium ceramics, Corrosion Science 199 (2022) 110190. https://doi.org/10.1016/j.corsci.2022.110190.

4) J. Aktaa, M. Walter, **E. Gaisina**, M. Kolb, R. Knitter, Assessment of the chemical compatibility between EUROFER and ceramic breeder with respect to fatigue lifetime, Fusion Engineering and Design 157 (2020) 111732. https://doi.org/10.1016/j.fusengdes.2020.111732.

Publications not related to the dissertation topic

1) R. Gaisin, P. Pereslavtsev, S. Baumgaertner, K. Seemann, **E. Gaisina**, V. Chakin, S. Udartsev, P. Vladimirov, B. Gorr, Lanthanum plumbide as a new neutron multiplier material, Journal of Materials Research and Technology 24 (2023) 3399–3412. https://doi.org/10.1016/j.jmrt.2023.03.211.

2) V.M. Imayev, R.A. Gaisin, **E.R. Gaisina**, R.M. Imayev, Microstructure, processing and mechanical properties of a titanium alloy Ti-20Zr-6.5Al-3.3Mo-0.3Si-0.1B, Materials Science and Engineering: A 696 (2017) 137–145. https://doi.org/10.1016/j.msea.2017.04.056.

3) Gaisin R.A., Imayev V.M., **Gaisina E.R.**, Shaimardanov R.A., Imayev R.M. Structure and properties of cast composite materials based on high-temperature titanium alloys reinforced with TiB whiskers // Deformation and destruction of materials. 2017. №1. P. 18-23. [in Russian]

4) Gaisin R.A., Imayev V.M., **Gaisina E.R.**, Shaimardanov R.A., Imayev R.M. On an extraordinarily high strength of a two-phase VT8-based titanium alloy heavy alloyed with zirconium // Letters on materials. 2016. V. 6. I. 4. P. 327-332. [in Russian]

5) Gaisin R.A., Imayev V.M., Imayev R.M., **Gaisina E.R.** Microstructure and Mechanical Properties of Ti-TiB Based Short-Fiber Composite Materials Manufactured by Casting and Subjected to Deformation Processing // Russ Phys J. 2015. V. 58. I. 6. P. 848-583.

6) Gaisin R., Imayev V., Imayev R., **Gaisina E.** Effect of boron addition on recrystallization behavior of commercially pure titanium // Letters on materials. 2015. V. 5. I. 2. P. 124-128. [in Russian]

7) Gaisin R.A., Imayev V.M., Imayev R.M., **Gaisina E.R.** Microstructure and hot deformation behavior of two-phase boron-modified titanium alloy VT8 // Phys. Metals Metallogr. 2013. V. 114 I. 4. P. 339-347.

8) **Gaisina E.R.**, Gaisin R.A., Imayev V.M., Imayev R.M. Microstructure and mechanical characteristics of VT1-0-based composite material reinforced with titanium monoboride. Phys. Metals Metallogr. 2013. V. 114. I. 7. P. 623-629.

9) Gaisin R.A., Imayev V.M., Imayev R.M., **Gaisina E.R.** Microstructure and mechanical properties of a two-phase titanium alloy VT8 modified with boron // Perspective materials. 2013. №15. P. 49-53. [in Russian]

10) V. Imayev, R. Gaisin, **E. Gaisina**, R. Imayev, H.-J. Fecht, F. Pyczak, Effect of hot forging on microstructure and tensile properties of Ti–TiB based composites produced by casting, Materials Science and Engineering: A 609 (2014) 34–41. https://doi.org/10.1016/j.msea.2014.04.091.

6 Bibliography

[1] S. Atzeni, J. Meyer-ter-Vehn (Eds.), The Physics of Inertial Fusion: BeamPlasma Interaction, Hydrodynamics, Hot Dense Matter, Oxford University Press, Oxford, 2004.

[2] G. Federici, C. Bachmann, W. Biel, L. Boccaccini, F. Cismondi, S. Ciattaglia, M. Coleman, C. Day, E. Diegele, T. Franke, M. Grattarola, H. Hurzlmeier, A. Ibarra, A. Loving, F. Maviglia, B. Meszaros, C. Morlock, M. Rieth, M. Shannon, N. Taylor, M.Q. Tran, J.H. You, R. Wenninger, L. Zani, Overview of the design approach and prioritization of R&D activities towards an EU DEMO, Fusion Engineering and Design 109-111 (2016) 1464–1474. https://doi.org/10.1016/j.fusengdes.2015.11.050.

[3] G. Federici, C. Bachmann, L. Barucca, W. Biel, L. Boccaccini, R. Brown, C. Bustreo, S. Ciattaglia, F. Cismondi, M. Coleman, V. Corato, C. Day, E. Diegele, U. Fischer, T. Franke, C. Gliss, A. Ibarra, R. Kembleton, A. Loving, F. Maviglia, B. Meszaros, G. Pintsuk, N. Taylor, M.Q. Tran, C. Vorpahl, R. Wenninger, J.H. You, DEMO design activity in Europe: Progress and updates, Fusion Engineering and Design 136 (2018) 729–741. https://doi.org/10.1016/j.fusengdes.2018.04.001.

[4] U. Fischer, C. Bachmann, J.-C. Jaboulay, F. Moro, I. Palermo, P. Pereslavtsev, R. Villari, Neutronic performance issues of the breeding blanket options for the European DEMO fusion power plant, Fusion Engineering and Design 109-111 (2016) 1458–1463. https://doi.org/10.1016/j.fusengdes.2015.11.051.

[5] F.A. Hernández, P. Pereslavtsev, G. Zhou, B. Kiss, Q. Kang, H. Neuberger, V. Chakin, R. Gaisin, P. Vladimirov, L.V. Boccaccini, G.A. Spagnuolo, S. D'Amico, I. Moscato, Advancements in the Helium-Cooled Pebble Bed Breeding Blanket for the EU DEMO: Holistic Design Approach and Lessons Learned, Fusion Science and Technology 75 (2019) 352–364. https://doi.org/10.1080/15361055.2019.1607695.

[6] M. Utili, S. Bassini, S. Cataldo, F. Di Fonzo, M. Kordac, T. Hernandez, K. Kunzova, J. Lorenz, D. Martelli, B. Padino, A. Moroño, M. Tarantino, C. Schroer, G.A. Spagnuolo, L. Vala, M. Vanazzi, A. Venturini, Development of anti-permeation and corrosion barrier coatings for the WCLL breeding blanket of the European DEMO, Fusion Engineering and Design 170 (2021) 112453. https://doi.org/10.1016/j.fusengdes.2021.112453.

[7] O. Leys, J.M. Leys, R. Knitter, Current status and future perspectives of EU ceramic breeder development, Fusion Engineering and Design 164 (2021) 112171. https://doi.org/10.1016/j.fusengdes.2020.112171.

[8] P. Hofmann, W. Dienst, Chemical compatibility between lithium-based oxide ceramics and stainless steels, Journal of Nuclear Materials 141-143 (1986) 289–293. https://doi.org/10.1016/S0022-3115(86)80052-6.

[9] L. Alves, E. Alves, M. da Silva, A. Paúl, A. La Barbera, Li ceramic pebbles chemical compatibility with Eurofer samples in fusion relevant conditions, Journal of Nuclear Materials 329-333 (2004) 1295–1299. https://doi.org/10.1016/j.jnucmat.2004.04.227.

[10] J. Hegeman, E. van Essen, M. Jong, J.G. van der Laan, J. Reimann, Thermomechanical behaviour of ceramic breeder pebble stacks for HICU, Fusion Engineering and Design 69 (2003) 425–429. https://doi.org/10.1016/S0920-3796(03)00086-3.

[11] A. Abou-Sena, B. Löbbecke, A. von der Weth, R. Knitter, Effect of post welding heat treatment of the HCPB TBM on Eurofer and lithium orthosilicate pebbles, Fusion Engineering and Design 86 (2011) 2254–2257. https://doi.org/10.1016/j.fusengdes.2011.03.038.

[12] T. Hernández, P. Fernández, Corrosion susceptibility comparison of EUROFER steel in contact two lithium silicate breeders, Fusion Engineering and Design 89 (2014) 1436–1439. https://doi.org/10.1016/j.fusengdes.2013.12.043.

[13] T. Hernández, P. Fernández, R. Vila, Corrosion susceptibility of EUROFER97 in lithium ceramics breeders, Journal of Nuclear Materials 446 (2014) 117–123. https://doi.org/10.1016/j.jnucmat.2013.11.047.

[14] T. Hernández, P. Fernández, Effect of the environment on the corrosion of EUROFER97 by solid lithium breeders, Journal of Nuclear Materials 447 (2014) 160–165. https://doi.org/10.1016/j.jnucmat.2013.12.026.
[15] S. Sonak, U. Jain, R. Haldar, S. Kumar, Chemical compatibility study of lithium titanate with Indian reduced activation ferritic martensitic steel, Fusion Engineering and Design 100 (2015) 507–512. https://doi.org/10.1016/j.fusengdes.2015.07.026.
[16] K. Mukai, F. Sanchez, R. Knitter, Chemical compatibility study between ceramic breeder and EUROFER97 steel for HCPB-DEMO blanket, Journal of Nuclear Materials 488 (2017) 196–203. https://doi.org/10.1016/j.jnucmat.2017.03.018.
[17] K. Mukai, M. Gonzalez, R. Knitter, Effect of moisture in sweep gas on chemical compatibility between ceramic breeder and EUROFER97, Fusion Engineering and Design 125 (2017) 154–159. https://doi.org/10.1016/j.fusengdes.2017.10.001.
[18] K. Mukai, F. Sanchez, T. Hoshino, R. Knitter, Corrosion characteristics of reduced activation ferritic-martensitic steel EUROFER by Li2TiO3 with excess Li, Nuclear Materials and Energy 15 (2018) 190–194. https://doi.org/10.1016/j.nme.2018.04.010.
[19] S. Cho, Y.-H. Park, Y.-B. Chun, K.-M. Min, M.-Y. Ahn, S.C. Park, Y. Lee, Chemical compatibility between ARAA alloy and lithium meta-titanate breeder material, Fusion Engineering and Design 124 (2017) 1052–1058. https://doi.org/10.1016/j.fusengdes.2017.04.007.
[20] S.D. Cramer, Covino, Bernard S., Jr. (Eds.), Corrosion: Fundamentals, Testing, and Protection, ASM International, Russell Township, Geauga County, Ohio, 2003.
[21] C.L. Brooks, K.T. Honeycutt, T.B. Mills, Predictive Modeling of Structure Service Life, in: S.D. Cramer, Covino, Bernard S., Jr. (Eds.), Corrosion: Fundamentals, Testing, and Protection, ASM International, Russell Township, Geauga County, Ohio, 2003, p. 0.
[22] P.P. Milella (Ed.), Fatigue and Corrosion in Metals, Springer Milan, Milano, 2013.
[23] X. Chen, L. Yang, H. Dai, S. Shi, Exploring factors controlling pre-corrosion fatigue of 316L austenitic stainless steel in hydrofluoric acid, Engineering Failure Analysis 113 (2020) 104556. https://doi.org/10.1016/j.engfailanal.2020.104556.
[24] D. Liu, Y. Li, X. Xie, J. Zhao, Effect of Pre-Corrosion Pits on Residual Fatigue Life for 42CrMo Steel, Materials (Basel, Switzerland) 12 (2019). https://doi.org/10.3390/ma12132130.
[25] J. Liu, X. Hao, S. Li, M. Yu, Effect of pre-corrosion on fatigue life of high strength steel 38CrMoAl, Journal of Wuhan University of Technology-Mater. Sci. Ed. 26 (2011) 648–653. https://doi.org/10.1007/s11595-011-0284-3.
[26] J. Schijve, Four lectures on fatigue crack growth: I. Fatigue crack growth and fracture mechanics, Engineering Fracture Mechanics 11 (1979) 169–181. https://doi.org/10.1016/0013-7944(79)90039-0.
[27] A. Wildeis, H.-J. Christ, R. Brandt, Influence of Residual Stresses on the Crack Initiation and Short Crack Propagation in a Martensitic Spring Steel, Metals 12 (2022). https://doi.org/10.3390/met12071085.
[28] S. Xu, Y. Wang, Estimating the effects of corrosion pits on the fatigue life of steel plate based on the 3D profile, International Journal of Fatigue 72 (2015) 27–41. https://doi.org/10.1016/j.ijfatigue.2014.11.003.
[29] G. Benamati, C. Fazio, I. Ricapito, Mechanical and corrosion behaviour of EUROFER 97 steel exposed to Pb–17Li, Journal of Nuclear Materials 307-311 (2002) 1391–1395. https://doi.org/10.1016/S0022-3115(02)00990-X.
[30] Z. Sun, X. Zhang, Y. Zhao, H. Liao, L. Wang, H. Fu, J. Wang, X. Wang, X. Lv, P. Li, Effect of applied stress on the ductility of RAFM steel during long-term exposure in flowing Pb-17Li, Fusion Engineering and Design 192 (2023) 113640. https://doi.org/10.1016/j.fusengdes.2023.113640.
[31] M.-F. Maday, Comparison of the low cycle fatigue behaviour of F82H mod. and Eurofer 97 in water coolant, Fusion Engineering and Design 61-62 (2002) 665–670. https://doi.org/10.1016/S0920-3796(02)00257-0.
[32] EUROfusion, Material Property Handbook EUROFER97: Grant Deliverable MAT D25.15: MAT.D06.2 Materials Properties Handbook: 2nd formal release. Grant Agreement-633053-EUROfusion (2MKKGB v1.0) including also the AWP2016 and AWP2017, 2017.

[33] K.D. Clarke, 12.10 - Austenite Formation and Microstructural Control in Low-Alloy Steels, in: S. Hashmi, G.F. Batalha, C.J. van Tyne, B. Yilbas (Eds.), Comprehensive Materials Processing, Elsevier, Oxford, 2014, pp. 345–361.
[34] H.R. Bhadeshia H.K.D.H., Steels: Microstructure and Properties: 4th Edition, Butterworth-Heinemann, Oxford, 2017.
[35] R. Lindau, A. Möslang, M. Rieth, M. Klimiankou, E. Materna-Morris, A. Alamo, A.-A.F. Tavassoli, C. Cayron, A.-M. Lancha, P. Fernandez, N. Baluc, R. Schäublin, E. Diegele, G. Filacchioni, J.W. Rensman, B. Schaaf, E. Lucon, W. Dietz, Present development status of EUROFER and ODS-EUROFER for application in blanket concepts, Fusion Engineering and Design 75-79 (2005) 989–996. https://doi.org/10.1016/j.fusengdes.2005.06.186.
[36] J.M. Heuser, M. Kolb, T. Bergfeldt, R. Knitter, Long-term thermal stability of two-phased lithium orthosilicate/metatitanate ceramics, Journal of Nuclear Materials 507 (2018) 396–402. https://doi.org/10.1016/j.jnucmat.2018.05.010.
[37] R. Knitter, M. Kolb, U. Kaufmann, A.A. Goraieb, Fabrication of modified lithium orthosilicate pebbles by addition of titania, Journal of Nuclear Materials 442 (2013) S433-S436. https://doi.org/10.1016/j.jnucmat.2012.10.034.
[38] Julia M. Heuser, Oliver Leys, Regina Knitter, Material Property Handbook on Advanced Ceramic Breeder: WPBB-DEL-BB-1.3.1-T007-D008, Karlsruhe, 2019.
[39] R. Knitter, J. Leys, private communication, KIT IAM-ESS.
[40] A. E2714-13, Standard Test Method for Creep-Fatigue Testing, West Conshohocken, PA, 2013.
[41] M. Duerrschnabel, E. Gaisina, R. Gaisin, M. Walter, J. Aktaa, M. Rieth, Nanoscale insights into the corrosion of EUROFER by lithium ceramics, Corrosion Science 199 (2022) 110190. https://doi.org/10.1016/j.corsci.2022.110190.
[42] J. Aktaa, M. Walter, E. Gaisina, M. Kolb, R. Knitter, Assessment of the chemical compatibility between EUROFER and ceramic breeder with respect to fatigue lifetime, Fusion Engineering and Design 157 (2020) 111732. https://doi.org/10.1016/j.fusengdes.2020.111732.
[43] E. Gaisina, M. Duerrschnabel, J. Leys, R. Knitter, J. Aktaa, M. Walter, Recent studies to the impact of a ceramic breeder environment on the mechanical properties of EUROFER97 under operating conditions, Journal of Nuclear Materials 564 (2022) 153677. https://doi.org/10.1016/j.jnucmat.2022.153677.
[44] K.P. Thiruppathi, D. Nataraj, Phase transformation from α-Fe2O3 to Fe3O4 and LiFeO2 by the self-reduction of Fe(iii) in Prussian red in the presence of alkali hydroxides: investigation of the phase dependent morphological and magnetic properties, CrystEngComm 19 (2017) 6170–6181. https://doi.org/10.1039/C7CE01342F.
[45] T. Chikada, M.H. Kolb, H. Fujita, K. Nakamura, K. Kimura, M. Rasinski, Y. Hishinuma, K. Mukai, R. Knitter, Compatibility of tritium permeation barrier coatings with ceramic breeder pebbles, Corrosion Science 182 (2021) 109288. https://doi.org/10.1016/j.corsci.2021.109288.
[46] E. Gaisina, R. Gaisin, J. Leys, R. Knitter, J. Aktaa, M. Walter, Comparative analysis of low cycle fatigue behavior of pre-corroded standard and sub-sized EUROFER97 specimens exposed to ceramic breeder environment, Nuclear Materials and Energy 36 (2023) 101497. https://doi.org/10.1016/j.nme.2023.101497.
[47] R.E. Melchers, Predicting long-term corrosion of metal alloys in physical infrastructure, npj Materials Degradation 3 (2019) 4. https://doi.org/10.1038/s41529-018-0066-x.
[48] C. Schroer, O. Wedemeyer, J. Novotny, A. Skrypnik, J. Konys, Performance of 9% Cr steels in flowing lead-bismuth eutectic at 450 and 550°C, and 10−6mass% dissolved oxygen, Nuclear Engineering and Design 280 (2014) 661–672. https://doi.org/10.1016/j.nucengdes.2014.01.023.
[49] Vicente Braz Trindade, Rodrigo Borin, Behzad Zandi Hanjari, Songlang Yang, Ulrich Krupp,Hans-Jürgen Christ, High-temperature oxidation of pure Fe and the ferritic steel 2.25Cr1Mo, Materials Research 8(4) (2005).
[50] W. Liu, J.Y. Lim, M.A. Saucedo, A.N. Hayhurst, S.A. Scott, J.S. Dennis, Kinetics of the reduction of wüstite by hydrogen and carbon monoxide for the chemical looping production of hydrogen, Chemical Engineering Science 120 (2014) 149–166. https://doi.org/10.1016/j.ces.2014.08.010.

[51] W. Mao, W.G. Sloof, Reduction Kinetics of Wüstite Scale on Pure Iron and Steel Sheets in Ar and H2 Gas Mixture, Metallurgical and Materials Transactions B 48 (2017) 2707–2716. https://doi.org/10.1007/s11663-017-1037-2.

[52] L. Cornish, Y. Eichhammer, D. Pavlyuchkov, E. Semenova, Materials Science International Team, MSIT®, Fe-Li Binary Phase Diagram Evaluation \textperiodcentered Phase diagrams, crystallographic and thermodynamic data: Datasheet from MSI Eureka in SpringerMaterials (https://materials.springer.com/msi/docs/sm_msi_r_20_018967_01), MSI Materials Science International Services GmbH, https://materials.springer.com/msi/docs/sm_msi_r_20_018967_01.

[53] M. Klimenkov, R. Lindau, E. Materna-Morris, A. Möslang, TEM characterization of precipitates in EUROFER 97, Progress in Nuclear Energy 57 (2012) 8–13. https://doi.org/10.1016/j.pnucene.2011.10.006.

[54] P. Fernández, M. García-Mazarío, A. Lancha, J. Lapeña, Grain boundary microchemistry and metallurgical characterization of Eurofer'97 after simulated service conditions, Journal of Nuclear Materials 329-333 (2004) 273–277. https://doi.org/10.1016/j.jnucmat.2004.04.055.

[55] P. Fernández, A. Lancha, J. Lapeña, M. Serrano, M. Hernández-Mayoral, Metallurgical properties of reduced activation martensitic steel Eurofer'97 in the as-received condition and after thermal ageing, Journal of Nuclear Materials 307-311 (2002) 495–499. https://doi.org/10.1016/S0022-3115(02)01013-9.

[56] Jaroslav Polák, Cyclic Plasticity and Low Cycle Fatigue Life of Metals, Elsevier Science Publishers B. V, PO Box 211, 1000 AE Amsterdam, The Netherlands, 1990.

[57] S. S. Manson, Behavior of materials under conditions of thermal stress: Heat Transfer Symposium, University of Michigan Engineering Research Institute, Ann Arbor, Mich,, 1953.

[58] L. F. Jr. Coffin, A Study of the Effects of Cyclic Thermal Stresses on a Ductile Metal, Transactions of the ASME, 1954.

[59] Jarir Aktaa, MAT-T.01.03-T004-D001. Report on test results and test methodology/guidelines for DFT, LCF and FCG, Karlsruhe, 2021.

[60] F. A. Hernández, F. Arbeiter, L. V. Boccaccini, E. Bubelis, V. P. Chakin, I. Cristescu, B. E. Ghidersa, M. González, W. Hering, T. Hernández, X. Z. Jin, M. Kamlah, B. Kiss, R. Knitter, M. H. H. Kolb, P. Kurinskiy, O. Leys, I. A. Maione, M. Moscardini, G. Nádasi, H. Neuberger, P. Pereslavtsev, S. Pupeschi, R. Rolli, S. Ruck, G. A. Spagnuolo, P. V. Vladimirov, C. Zeile, G. Zhou, Overview of the HCPB Research Activities in EUROfusion, IEEE Transactions on Plasma Science 46 (2018) 2247–2261. https://doi.org/10.1109/TPS.2018.2830813.

[61] T. Hernández, A. Moroño, F.J. Sánchez, C. Maffiotte, M.A. Monclús, R. González-Arrabal, Study of deuterium permeation, retention, and desorption in SiC coatings submitted to relevant conditions for breeder blanket applications: thermal cycling effect under electron irradiation and oxygen exposure, Journal of Nuclear Materials 557 (2021) 153219. https://doi.org/10.1016/j.jnucmat.2021.153219.

[62] T. Hernández, F.J. Sánchez, F. Di Fonzo, M. Vanazzi, M. Panizo, R. González-Arrabal, Corrosion protective action of different coatings for the helium cooled pebble bed breeder concept, Journal of Nuclear Materials 516 (2019) 160–168. https://doi.org/10.1016/j.jnucmat.2019.01.009.

[63] T. Hernández, F.J. Sánchez, A. Moroño, E. León-Gutiérrez, M. Panizo-Laiz, M.A. Monclus, R. González-Arrabal, Corrosion behavior of diverse sputtered coatings for the helium cooled pebbles bed (HCPB) breeder concept, Nuclear Materials and Energy 25 (2020) 100795. https://doi.org/10.1016/j.nme.2020.100795.

[64] Chandler W.T., Hydrogen Embrittlement and Its Control in Hydrogen-Fueled Engine Systems, NASA. Langley Res. Center Recent Advan. in Structures for Hypersonic Flight, Pt. 1, (1978).

[65] Jonathan A. Lee, Hydrogen Embrittlement. NASA/TM-2016–218602, National Aeronautics and Space Administration Marshall Space (2016).

[66] K. Splichal, J. Berka, J. Burda, M. Falcník, Hydrogen embrittlement and fracture mode of EUROFER 97 ferritic-martensitic steel, International Journal of Pressure Vessels and Piping 89 (2012) 42–47. https://doi.org/10.1016/j.ijpvp.2011.09.006.

[67] K. Splichal, J. Berka, J. Burda, M. Zmitko, Fracture toughness of the hydrogen charged EUROFER 97 RAFM steel at room temperature and 120°C, Journal of Nuclear Materials 392 (2009) 125–132. https://doi.org/10.1016/j.jnucmat.2009.03.053.

[68] Y. Yagodzinskyy, E. Malitckii, M. Ganchenkova, S. Binyukova, O. Emelyanova, T. Saukkonen, H. Hänninen, R. Lindau, P. Vladimirov, A. Moeslang, Hydrogen effects on tensile properties of EUROFER 97 and ODS-EUROFER steels, Journal of Nuclear Materials 444 (2014) 435–440. https://doi.org/10.1016/j.jnucmat.2013.10.026.

[69] E. Malitckii, Y. Yagodzinskyy, H. Hänninen, Hydrogen uptake from plasma and its effect on EUROFER 97 and ODS-EUROFER steels at elevated temperatures, Fusion Engineering and Design 98-99 (2015) 2025–2029. https://doi.org/10.1016/j.fusengdes.2015.05.049.

[70] M. Cauwels, R. Depraetere, W. de Waele, S. Hertelé, K. Verbeken, T. Depover, Effect of hydrogen charging on Charpy impact toughness of an X70 pipeline steel, Procedia Structural Integrity 42 (2022) 977–984. https://doi.org/10.1016/j.prostr.2022.12.123.

[71] P. Fassina, F. Bolzoni, G. Fumagalli, L. Lazzari, L. Vergani, A. Sciuccati, Influence of hydrogen and low temperature on mechanical behaviour of two pipeline steels, Engineering Fracture Mechanics 81 (2012) 43–55. https://doi.org/10.1016/j.engfracmech.2011.09.016.

[72] G. Golisch, G. Genchev, E. Wanzenberg, J. Mentz, H. Brauer, E. Muthmann, D. Ratke, Application of line pipe and hot induction bends in hydrogen gas, Journal of Pipeline Science and Engineering 2 (2022) 100067. https://doi.org/10.1016/j.jpse.2022.100067.

[73] M.-F. Maday, L. Pilloni, Hydrogen effects on the tensile and fatigue properties of Eurofer'97, Fusion Engineering and Design 75-79 (2005) 957–961. https://doi.org/10.1016/j.fusengdes.2005.06.024.

[74] M.-F. Maday, L. Pilloni, The influence of hydrogen on the fatigue behaviour of base and gas tungsten arc welded Eurofer, Journal of Nuclear Materials 367-370 (2007) 516–521. https://doi.org/10.1016/j.jnucmat.2007.03.107.

[75] G.E. Lucas, G.R. Odette, H. Matsui, A. Möslang, P. Spätig, J. Rensman, T. Yamamoto, The role of small specimen test technology in fusion materials development, Journal of Nuclear Materials 367-370 (2007) 1549–1556. https://doi.org/10.1016/j.jnucmat.2007.04.034.

[76] G.E. Lucas, G.R. Odette, M. Sokolov, P. Spätig, T. Yamamoto, P. Jung, Recent progress in small specimen test technology, Journal of Nuclear Materials 307-311 (2002) 1600–1608. https://doi.org/10.1016/S0022-3115(02)01171-6.

[77] T. Hirose, H. Sakasegawa, A. Kohyama, Y. Katoh, H. Tanigawa, ASTM SPT 1405, Americ Society for Testing and Materials (2001) 535.

[78] P. Marmy, T. Kruml, Low cycle fatigue of Eurofer 97, Journal of Nuclear Materials 377 (2008) 52–58. https://doi.org/10.1016/j.jnucmat.2008.02.054.

[79] I. Kuběna, T. Kruml, P. Spätig, N. Baluc, Z. Oksiuta, M. Petrenec, K. Obrtlík, J. Polák, Fatigue behaviour of ODS ferritic-martensitic Eurofer steel, Procedia Engineering 2 (2010) 717–724. https://doi.org/10.1016/j.proeng.2010.03.077.

[80] ASTM E647-15e1, Standard Test Method for Measurement of Fatigue Crack Growth Rates, ASTM International, 100 Barr Harbor Drive, PO Box C700, West Conshohocken, PA 19428-2959. United States, 2023.

[81] Anderson T. L., Fracture Mechanics: Fundamentals and Applications, Fourth Edition (4th ed.). CRC Press., Boca Raton, FL, 2017.

[82] J. Schijve (Ed.), Fatigue of Structures and Materials, Springer Netherlands, Dordrecht, 2009.

[83] R.G. Forman, V. Shivakumar, Growth behavior of surface cracks in the circumferential plane of solid and hollow cylinders, ASTM special technical publications (1986) 59–74.

[84] R.G. Forman, V. Shivakumar, S.R. Mettu, J.C. Newman, Jr., Fatigue Crack Growth Computer Program 'NASGRO' Version 3.00, Reference Manual: JSC-22267B, Johnson Space Center, Houston, TX., 1998.

[85] Peggy C. Miedlar, Alan P. Berens, Allan Gunderson, and J.P. Gallagher, USAF Damage Tolerant Design Handbook: Guidelines for the Analysis and Design of Damage Tolerant Aircraft Structures: AFRL-VA-WP-TR-2003-3002 ANALYSIS AND SUPPORT INITIATIVE FOR STRUCTURAL TECHNOLOGY (ASIST) Delivery Order 0016, Dayton, OH 45469, 2002.

[86] A. Athanassiadis, J.M. Boissenot, P. Brevet, D. Francois, A. Raharinaivo, Linear elastic fracture mechanics computations of cracked cylindrical tensioned bodies, International Journal of Fracture 17 (1981) 553–566. https://doi.org/10.1007/BF00681556.

[87] T. Kruml, P. Hutař, L. Náhlík, S. Seitl, J. Polák, Fatigue cracks in Eurofer 97 steel: Part II. Comparison of small and long fatigue crack growth, Journal of Nuclear Materials 412 (2011) 7–12. https://doi.org/10.1016/j.jnucmat.2011.01.018.
[88] Francisco A. Hernández, Pavel Pereslavtsev, Guangming Zhou, Qinlan Kang, Salvatore D'Amico, Anoop Retheesh, Heiko Neuberger, WPBB-DEL-BB-1.2.1-T006-D001. HCPB Design and Integration Studies 2019, Karlsruhe, 2019.
[89] I. S. Raju and J.C. Newman, Jr., Stress-Intensity Factors for Circumferential Surface Cracks in Pipes and Rods Under Tension and Bending Loads: Fracture Mechanics: Seventeenth Volume, Philadelphia, 1984.
[90] R.G. Forman, V. Shivakumar, J.C. Newman, Jr., Fatigue Crack Growth Computer Program – NASA/FLAGRO: JSC-22267, Houston, TX, 1989.
[91] J. Aktaa, M. Weick, M. Walter, High Temperature Creep-Fatigue Structural Design Criteria for Fusion Components Built from EUROFER 97: Final Report: TW2-TTMS-005b, D1 TW5-TTMS-005, D7. FZKA 7309, Forschungszentrum Karlsruhe, 2007.
[92] B.F. Langer, Design of Pressure Vessels for Low-Cycle Fatigue, Journal of Basic Engineering 84 (1962) 389–399.
[93] C. Bachmann, Plant Description Document: EFDA_D_2KVWQZ. V.1.9., Garching, 2020.
[94] Guangming Zhou, HCPB Design and Analysis – Interim Report 2021: Deliverable BB-S-02.01-T001-D001. EFDA_D_2Q4YMC, Karlsruhe, 2021.
[95] F.A. Hernández, P. Pereslavtsev, First principles review of options for tritium breeder and neutron multiplier materials for breeding blankets in fusion reactors, Fusion Engineering and Design 137 (2018) 243–256. https://doi.org/10.1016/j.fusengdes.2018.09.014.
[96] S.J. Piet, E.T. Cheng, S. Fetter, J. Herring, Initial integration of accident safety, waste management, recycling, effluent, and maintenance considerations for low-activation materials, Fusion Technology 19 (1991) 146–161. https://doi.org/10.13182/FST19-1-146.
[97] T. Chikada, K. Kimura, J. Mochizuki, S. Horikoshi, M. Matsunaga, H. Fujita, K. Okitsu, T. Tanaka, Y. Hishinuma, Y. Sakamoto, Y. Someya, H. Nakamura, Surface oxidation effect on deuterium permeation in reduced activation ferritic/martensitic steel F82H for DEMO application, Fusion Engineering and Design 146 (2019) 450–454. https://doi.org/10.1016/j.fusengdes.2018.12.089.
[98] T. Chikada, S. Naitoh, A. Suzuki, T. Terai, T. Tanaka, T. Muroga, Deuterium permeation through erbium oxide coatings on RAFM steels by a dip-coating technique, Journal of Nuclear Materials 442 (2013) 533–537. https://doi.org/10.1016/j.jnucmat.2013.05.072.
[99] I. Cristescu, M. Draghia, Developments on the tritium extraction and recovery system for HCPB, Fusion Engineering and Design 158 (2020) 111558. https://doi.org/10.1016/j.fusengdes.2020.111558.
[100] Ramil Gaisin, BB-T.01.02-T001-D002: Progress in manufacture, processing and characterization of NMM - 2022, 2022.
[101] J.-H. Kim, M. Nakamichi, Compatibility of advanced tritium breeders and neutron multipliers, Fusion Engineering and Design 156 (2020) 111581. https://doi.org/10.1016/j.fusengdes.2020.111581.
[102] Guangming Zhou, Design of HCPB BB (2QR4SG v1.0). HCPB BB Design: OB and IB, Karlsruhe, 2023.
[103] N. Khan, A. Sinha, V. Sudarsan, Lithium titanate foam for tritium breeding application, Journal of Nuclear Materials 583 (2023) 154491. https://doi.org/10.1016/j.jnucmat.2023.154491.
[104] S. Sharafat, N. Ghoniem, M. Sawan, A. Ying, B. Williams, Breeder foam: an innovative low porosity solid breeder material, Fusion Engineering and Design 81 (2006) 455–460. https://doi.org/10.1016/j.fusengdes.2005.06.374.
[105] Y. Zhong, L. Lin, H. Yang, H. Wang, G. Li, B. Liu, Bulk porous materials as an alternative to pebble beds in tritium breeding blankets, Fusion Engineering and Design 161 (2020) 112077. https://doi.org/10.1016/j.fusengdes.2020.112077.